Physics of Atomic Nuclei, Vol. 67, No. 10, 2004, pp. 1767–1775. From Yadernaya Fizika, Vol. 67, No. 10, 2004, pp. 1795–1803.

Proceedings of the International Conference "Nuclear Structure and Related Topics"

Extended $E(5)$ and $X(5)$ Symmetries: Series of Models Providing Parameter-Independent Predictions*

D. Bonatsos[1)], D. Lenis[1)***], N. Minkov[2)****], P. P. Raychev[2)*****], and P. A. Terziev[2)******]**

Received January 21, 2004

Abstract—The $E(5)$ symmetry describes nuclei related to the $U(5)-SO(6)$ phase transition, while the $X(5)$ symmetry is related to the $U(5)-SU(3)$ phase transition. First, a chain of potentials interpolating between the $U(5)$ symmetry of the five-dimensional harmonic oscillator and the $E(5)$ symmetry is considered. Parameter-independent predictions for the spectra and $B(E2)$ values of nuclei with $R_4 = E(4)/E(2)$ ratios of 2.093, 2.135, and 2.157 (compared to the ratio of 2.000 of the $U(5)$ case and the ratio of 2.199 of the $E(5)$ case) are derived numerically and compared to existing experimental data, suggesting several new experiments. The $X(5)$ symmetry describes nuclei characterized by $R_4 = 2.904$. Using the same separation of variables of the original Bohr Hamiltonian as in $X(5)$, an exactly soluble model with $R_4 = 2.646$ is constructed and its parameter-independent predictions are compared to existing spectra and $B(E2)$ values. In addition, a chain of potentials interpolating between this new model and the $X(5)$ symmetry is considered. Parameter-independent predictions for the spectra and $B(E2)$ values of nuclei with R_4 ratios of 2.769, 2.824, and 2.852 are derived numerically and compared to existing experimental data, suggesting several new experiments. © *2004 MAIK "Nauka/Interperiodica".*

1. INTRODUCTION

The recently introduced $E(5)$ [1] and $X(5)$ [2] models have attracted considerable interest, since they are considered to be related to the critical points of the phase transitions from $U(5)$ (vibrational) to $O(6)$ (γ-unstable) nuclei and from $U(5)$ to $SU(3)$ (prolate-deformed) nuclei, respectively. Both models originate (under certain simplifying assumptions) from the Bohr collective Hamiltonian [3], which is known to possess the $U(5)$ symmetry of the five-dimensional (5D) harmonic oscillator [4], while their spectra and $B(E2)$ transition rates are parameter-free (up to overall scale factors).

In Section 2 of the present paper, we study a sequence of potentials interpolating between $U(5)$ and $E(5)$, while in Section 3 a new exactly soluble model, to be called $X(5)$-β^2, is introduced. A sequence of potentials interpolating between $U(5)$ and $X(5)$ is considered in Section 4, while the conclusions and plans for further work are given in Section 5.

2. POTENTIALS INTERPOLATING BETWEEN $U(5)$ AND $E(5)$

The original Bohr Hamiltonian [3] is

$$H = -\frac{\hbar^2}{2B}\left[\frac{1}{\beta^4}\frac{\partial}{\partial\beta}\beta^4\frac{\partial}{\partial\beta} + \frac{1}{\beta^2\sin(3\gamma)}\frac{\partial}{\partial\gamma}\sin(3\gamma)\frac{\partial}{\partial\gamma} - \frac{1}{4\beta^2}\sum_{k=1,2,3}\frac{Q_k^2}{\sin^2\left(\gamma-\frac{2}{3}\pi k\right)}\right] + V(\beta,\gamma), \quad (1)$$

where β and γ are the usual collective coordinates describing the shape of the nuclear surface, Q_k ($k = 1, 2, 3$) are the components of angular momentum, and B is the mass parameter.

Assuming that the potential depends only on the variable β, i.e., $V(\beta,\gamma) = U(\beta)$, one can proceed to separation of variables in the standard way [3, 5], using the wave function $\Psi(\beta,\gamma,\theta_i) = f(\beta)\Phi(\gamma,\theta_i)$, where θ_i ($i = 1, 2, 3$) are the Euler angles describing the orientation of the deformed nucleus in space.

In the equation involving the angles, eigenvalues of the second-order Casimir operator of $SO(5)$ occur, having the form $\Lambda = \tau(\tau+3)$, where $\tau = 0, 1, 2, \ldots$

*This article was submitted by the authors in English.

[1)]Institute of Nuclear Physics, N.C.S.R. Demokritos, Attiki, Greece.
[2)]Institute for Nuclear Research and Nuclear Energy, Bulgarian Academy of Sciences, Sofia, Bulgaria.
**e-mail: bonat@inp.demokritos.gr
***e-mail: dlenis@lithos.culture.gr
****e-mail: nminkov@inrne.bas.bg
*****e-mail: raychev@inrne.bas.bg
******e-mail: terziev@inrne.bas.bg

is the quantum number characterizing the irreducible representations (irreps) of $SO(5)$, called the "seniority" [6]. This equation has been solved by Bes [7].

The "radial" equation can be simplified by introducing [1] reduced energies $\epsilon = 2BE/\hbar^2$ and reduced potentials $u = 2BU/\hbar^2$, as well as by making the transformation [1] $\phi(\beta) = \beta^{3/2} f(\beta)$, leading to

$$\phi'' + \frac{\phi'}{\beta} + \left[\epsilon - u(\beta) - \frac{(\tau+3/2)^2}{\beta^2}\right]\phi = 0. \quad (2)$$

For $u(\beta) = \beta^2/2$, one obtains the original solution of Bohr [3], which corresponds to a 5D harmonic oscillator characterized by the symmetry $U(5) \supset SO(5) \supset SO(3) \supset SO(2)$ [4], the eigenfunctions being proportional to Laguerre polynomials [8],

$$F_\nu^\tau(\beta) = \left[\frac{2\nu!}{\Gamma\left(\nu+\tau+\frac{5}{2}\right)}\right]^{1/2} \times \beta^\tau L_\nu^{\tau+3/2}(\beta^2) e^{-\beta^2/2}, \quad (3)$$

where $\Gamma(n)$ stands for the Γ function, and the spectrum having the simple form

$$E_N = N + \frac{5}{2}, \qquad N = 2\nu + \tau, \qquad \nu = 0, 1, 2, 3, \ldots. \quad (4)$$

For $u(\beta)$ being a 5D infinite well

$$u(\beta) = \begin{cases} 0, & \text{if } \beta \le \beta_W, \\ \infty, & \text{for } \beta > \beta_W, \end{cases} \quad (5)$$

one obtains the $E(5)$ model of Iachello [1], in which the eigenfunctions are Bessel functions $J_{\tau+3/2}(z)$ (with $z = \beta k$, $k = \sqrt{\epsilon}$), while the spectrum is determined by the zeros of the Bessel functions:

$$E_{\xi,\tau} = \frac{\hbar^2}{2B} k_{\xi,\tau}^2, \qquad k_{\xi,\tau} = \frac{x_{\xi,\tau}}{\beta_W}, \quad (6)$$

where $x_{\xi,\tau}$ is the ξth zero of the Bessel function $J_{\tau+3/2}(z)$. The relevant symmetry in this case is $E(5) \supset SO(5) \supset SO(3) \supset SO(2)$, where the Euclidean algebra in 5D $E(5)$ is generated by the 5D momenta π_μ and the $5D$ angular momenta $L_{\mu\nu}$, while $SO(5)$ is generated by the $L_{\mu\nu}$ alone [2]; τ, L, and M are the quantum numbers characterizing the irreps of $SO(5)$, $SO(3)$, and $SO(2)$, respectively. The values of angular momentum L contained in each irrep of $SO(5)$ (i.e., for each value of τ) are given by the algorithm [9]

$$\tau = 3\nu_\Delta + \lambda, \qquad \nu_\Delta = 0, 1, \ldots, \quad (7)$$

$$L = \lambda, \lambda+1, \ldots, 2\lambda-2, 2\lambda$$

(with $2\lambda - 1$ missing), where ν_Δ is the missing quantum number in the reduction $SO(5) \supset SO(3)$.

The spectra of the $u(\beta) = \beta^2/2$ potential and of the $E(5)$ model become directly comparable by establishing the formal correspondence $\nu = \xi - 1$, which allows one to continue using for the states the notation $L_{\xi,\tau}$, as in [1], although the notation $L_{\nu,\tau}$ would have been equally appropriate. The ground-state band corresponds to $\xi = 1$ (or, equivalently, $\nu = 0$).

The two cases mentioned above are the only ones in which Eq. (2) is exactly soluble, giving spectra characterized by $R_4 = E(4)/E(2)$ ratios of 2.00 and 2.20, respectively. However, the numerical solution of Eq. (2) for potentials other than the ones mentioned above is a straightforward task [10], in which one uses the chain $U(5) \supset SO(5) \supset SO(3) \supset SO(2)$ for the classification of the states.

Not all potentials can be used in Eq. (2), though, since they have to obey the restrictions imposed by the 24 transformations mentioned in [3] and listed explicitly in [11]. These restrictions allow the presence of even powers of β in the potentials, while odd powers of β should be accompanied by $\cos(3\gamma)$ [12].

A particularly interesting sequence of potentials is given by $u_{2n}(\beta) = \beta^{2n}/2$, with n being an integer. For $n = 1$, the Bohr case ($U(5)$) is obtained, while for $n \to \infty$ the infinite well of $E(5)$ is obtained [13]. Therefore this sequence of potentials provides a "bridge" between the $U(5)$ symmetry and the $E(5)$ model, using their common $SO(5) \supset SO(3)$ chain of subalgebras for the classification of the spectra.

Numerical results for the spectra of the β^4, β^6, and β^8 potentials have been obtained through two different methods. In one approach, the representation of the position and momentum operators in matrix form [14] has been used, while in the other the direct integration method [15] has been applied. In the latter, the differential equation is solved for each value of $\tau = 0, 1, 2, \ldots$ separately, the successive eigenvalues for each value of τ labeled by $\xi = 1, 2, 3, \ldots$ (or, equivalently, by $\nu = 0, 1, 2, \ldots$). The two methods give mutually consistent results, the second one appearing to have more general applicability. The results are shown in Table 1, where excitation energies relative to the ground state, normalized to the excitation energy of the first excited state, are exhibited.

In Table 1 the labels $E(5)$-β^4, $E(5)$-β^6, and $E(5)$-β^8 have been used for the above-mentioned potentials, their meaning being that $E(5)$-β^{2n} corresponds to the potential $\beta^{2n}/2$ plugged in the differential equation obtained in the framework of the $E(5)$

Table 1. Spectra of the $E(5)$-β^4, $E(5)$-β^6, and $E(5)$-β^8 models, compared to the predictions of the $U(5)$ [Eq. (4)] and $E(5)$ [Eq. (6)] models [for each value of τ, only the maximum value of L occurring for it, $L_{\max}$, is reported; the rest of the allowed values of L for each value of τ, indicating states having the same energy as the state with $L_{\max}$, can be found from the algorithm of Eq. (7)]

Band	τ	$L_{\max}$	$U(5)$	$E(5)$-β^4	$E(5)$-β^6	$E(5)$-β^8	$E(5)$
$\xi=1$	0	0	0.000	0.000	0.000	0.000	0.000
	1	2	1.000	1.000	1.000	1.000	1.000
	2	4	2.000	2.093	2.135	2.157	2.199
	3	6	3.000	3.265	3.391	3.459	3.590
	4	8	4.000	4.508	4.757	4.894	5.169
	5	10	5.000	5.813	6.225	6.456	6.934
	6	12	6.000	7.176	7.788	8.138	8.881
	7	14	7.000	8.592	9.442	9.935	11.009
	8	16	8.000	10.057	11.180	11.841	13.316
$\xi=2$	0	0	2.000	2.390	2.619	2.756	3.031
	1	2	3.000	3.625	4.012	4.255	4.800
	2	4	4.000	4.918	5.499	5.874	6.780
	3	6	5.000	6.266	7.075	7.607	8.967
	4	8	6.000	7.666	8.738	9.450	11.357
	5	10	7.000	9.115	10.483	11.400	13.945
$\xi=3$	0	0	4.000	5.153	5.887	6.364	7.577
	1	2	5.000	6.563	7.588	8.269	10.107
	2	4	6.000	8.015	9.363	10.274	12.854
	3	6	7.000	9.509	11.213	12.379	15.814
	4	8	8.000	11.043	13.134	14.580	18.983
	5	10	9.000	12.617	15.125	16.875	22.359
$\xi=4$	0	0	6.000	8.213	9.698	10.707	13.639
	1	2	7.000	9.764	11.661	12.966	16.928
	2	4	8.000	11.349	13.687	15.316	20.436
	3	6	9.000	12.967	15.776	17.753	24.161
	4	8	10.000	14.619	17.928	20.278	28.100
	5	10	11.000	16.304	20.141	22.888	32.250

model. In this notation, $E(5)$-β^2 coincides with the original $U(5)$ model of Bohr [3], while $E(5)$-β^{2n} with $n\to\infty$ is simply the original $E(5)$ model [1].

From Table 1, it is clear that, in all bands and for all values of the angular momentum L, the potentials β^4, β^6, and β^8 gradually lead from the $U(5)$ case to the $E(5)$ results in a smooth way.

In nuclear structure, it is well known that electromagnetic transition rates are quantities sensitive to the details of the underlying microscopic structure, as well as to details of the theoretical models, much more than the corresponding spectra. It is therefore a must to calculate $B(E2)$ ratios (normalized to $B(E2\colon 2_1^+\to 0_1^+)=100$) for the potentials mentioned above.

The quadrupole operator has the form [5]

$$T^{(E2)}_\mu = t\alpha_\mu = t\beta\Bigg[\mathcal{D}^{(2)}_{\mu,0}(\theta_i)\cos\gamma + \frac{1}{\sqrt{2}}(\mathcal{D}^{(2)}_{\mu,2}(\theta_i)+\mathcal{D}^{(2)}_{\mu,-2}(\theta_i))\sin\gamma\Bigg], \tag{8}$$

where t is a scale factor and $\mathcal{D}(\theta_i)$ denote Wigner functions of the Euler angles, while the $B(E2)$ transition rates are given by

$$B(E2;\varrho_i L_i\to\varrho_f L_f) = \frac{1}{2L_i+1}|\langle\varrho_f L_f||T^{(E2)}||\varrho_i L_i\rangle|^2, \tag{9}$$

where quantum numbers other than the angular momentum L are denoted by ϱ.

For the states with $\nu_\Delta=0$ and $L=2\tau$, one obtains

$$B(E2;L_{\xi,\tau}\to(L+2)_{\xi',\tau+1}) = \frac{(\tau+1)(4\tau+5)}{(2\tau+5)(4\tau+1)}t^2 I^2_{\xi',\tau+1;\xi,\tau}, \tag{10}$$

$$B(E2;(L+2)_{\xi',\tau+1}\to L_{\xi,\tau}) = \frac{\tau+1}{2\tau+5}t^2 I^2_{\xi',\tau+1;\xi,\tau}, \quad (11)$$

where

$$I_{\xi',\tau+1;\xi,\tau} = \int_0^\infty \beta f_{\xi'\tau+1}(\beta) f_{\xi\tau}(\beta)\beta^4 d\beta. \quad (12)$$

In the special case of the potential being a 5D infinite well, the eigenfunctions are

$$f_{\xi\tau}(\beta) = \frac{1}{\sqrt{C_{\xi,\tau}}}\beta^{-3/2} J_{\tau+3/2}\left(x_{\xi,\tau}\frac{\beta}{\beta_W}\right), \quad (13)$$

$$C_{\xi,\tau} = \frac{\beta_W^2}{2} J^2_{\tau+5/2}(x_{\xi,\tau}),$$

where $x_{\xi,\tau}$ is the ξth zero of the Bessel function $J_{\tau+3/2}(z)$, while the constants $C_{\xi,\tau}$ are obtained from the normalization condition $\int_0^{\beta_W} f^2_{\xi\tau}(\beta)\beta^4 d\beta = 1$. In this case, the integrals of Eq. (12) take the form

$$I_{\xi',\tau+1;\xi,\tau} = (C_{\xi',\tau+1}C_{\xi,\tau})^{-1/2}\beta_W^3 \times \int_0^1 z^2 J_{\tau+5/2}(x_{\xi',\tau+1}z) J_{\tau+3/2}(x_{\xi,\tau}z) dz. \quad (14)$$

The results of the calculations for intraband and interband transitions are shown in Table 2. In all cases, a smooth evolution from $U(5)$ to $E(5)$ is seen. The $E(5)$ results reported in Table 2 are in good agreement with the results given in [16].

It is interesting to examine whether there is any experimental evidence supporting the $E(5)$-β^{2n} predictions. It is clear that the first regions to be considered are the ones around the nuclei which have been identified as good candidates for $E(5)$, i.e., ^{134}Ba [17], ^{104}Ru [18], and ^{102}Pd [19]. A very preliminary search indicates that ^{98}Ru can be a candidate for $E(5)$-β^6, while ^{100}Pd can be a candidate for $E(5)$-β^4. However, much more detailed information on the spectra and $B(E2)$ transitions of these nuclei is required before final conclusions can be reached.

3. $X(5)$-β^2: A NEW EXACTLY SOLUBLE MODEL

The starting point is again the original Bohr Hamiltonian [3] of Eq. (1). One seeks solutions of the relevant Schrödinger equation having the form $\Psi(\beta,\gamma,\theta_i) = \phi^L_K(\beta,\gamma)\mathcal{D}^L_{M,K}(\theta_i)$, where θ_i $(i = 1, 2, 3)$ are the Euler angles, $\mathcal{D}(\theta_i)$ denote Wigner functions of them, L are the eigenvalues of angular momentum, and M and K are the eigenvalues of the projections of angular momentum onto the laboratory-fixed z axis and the body-fixed z' axis, respectively.

As pointed out in [2], in the case in which the potential has a minimum around $\gamma = 0$, one can write the last term of Eq. (1) in the form

$$\sum_{k=1,2,3} Q_k^2/\sin^2\left(\gamma - \frac{2\pi}{3}k\right) \approx \frac{4}{3}(Q_1^2+Q_2^2+Q_3^2) + Q_3^2\left(\frac{1}{\sin^2\gamma} - \frac{4}{3}\right). \quad (15)$$

Using this result in the Schrödinger equation corresponding to the Hamiltonian of Eq. (1), introducing reduced energies $\epsilon = 2BE/\hbar^2$ and reduced potentials $u = 2BV/\hbar^2$, and assuming that the reduced potential can be separated into two terms, one depending on β and the other depending on γ, i.e., $u(\beta,\gamma) = u(\beta) + u(\gamma)$, the Schrödinger equation can be separated into two equations [2]:

$$\left[-\frac{1}{\beta^4}\frac{\partial}{\partial\beta}\beta^4\frac{\partial}{\partial\beta} + \frac{1}{4\beta^2}\frac{4}{3}L(L+1) + u(\beta)\right]\xi_L(\beta) = \epsilon_\beta\xi_L(\beta), \quad (16)$$

$$\left[-\frac{1}{\langle\beta^2\rangle\sin(3\gamma)}\frac{\partial}{\partial\gamma}\sin(3\gamma)\frac{\partial}{\partial\gamma} + \frac{1}{4\langle\beta^2\rangle}K^2\left(\frac{1}{\sin^2\gamma} - \frac{4}{3}\right) + u(\gamma)\right]\eta_K(\gamma) = \epsilon(\gamma)\eta_K(\gamma), \quad (17)$$

where $\langle\beta^2\rangle$ is the average of β^2 over $\xi(\beta)$ and $\epsilon = \epsilon_\beta + \epsilon_\gamma$.

Equation (16) is solved exactly in [2] for the case in which $u(\beta)$ is an infinite-well potential [Eq. (5)]. The relevant exactly soluble model is labeled as $X(5)$ (which is not meant as a group label, although there is relation to projective representations of $E(5)$, the Euclidean group in five dimensions [2]). In particular, Eq. (16) in the case of $u(\beta)$ being an infinite well potential is transformed into a Bessel equation, the relevant eigenvalues being

$$\epsilon_{\beta;s,L} = (k_{s,L})^2, \qquad k_{s,L} = \frac{x_{s,L}}{\beta_W}, \quad (18)$$

where $x_{s,L}$ is the sth zero of the Bessel function $J_\nu(k_{s,L}\beta)$ with $\nu = (L(L+1)/3 + 9/4)^{1/2}$, while the relevant eigenfunctions are

$$\xi_{s,L}(\beta) = c_{s,L}\beta^{-3/2}J_\nu(k_{s,L}\beta), \quad (19)$$

where $c_{s,L}$ are normalization constants.

Equation (16) is exactly soluble also in the case in which $u(\beta) = \beta^2/2$. In this case, which we are going

Table 2. Intraband and interband $B(E2)$ transition rates for the $E(5)$-β^4, $E(5)$-β^6, and $E(5)$-β^8 models, compared to the predictions of the $U(5)$ and $E(5)$ models (see Section 2 for details)

Bands	$(L_{\xi,\tau})_i$	$(L_{\xi,\tau})_f$	$U(5)$	$E(5)$-β^4	$E(5)$-β^6	$E(5)$-β^8	$E(5)$
$(\xi=1)\to(\xi=1)$	$2_{1,1}$	$0_{1,0}$	100.00	100.00	100.00	100.00	100.00
	$4_{1,2}$	$2_{1,1}$	200.00	183.20	176.60	173.32	167.40
	$6_{1,3}$	$4_{1,2}$	300.00	256.37	239.80	231.64	216.88
	$8_{1,4}$	$6_{1,3}$	400.00	322.73	294.27	280.39	255.20
	$10_{1,5}$	$8_{1,4}$	500.00	384.12	342.57	322.51	286.01
	$12_{1,6}$	$10_{1,5}$	600.00	441.65	386.26	359.74	311.47
	$14_{1,7}$	$12_{1,6}$	700.00	496.11	426.36	393.25	332.95
	$16_{1,8}$	$14_{1,7}$	800.00	548.02	463.57	423.80	351.39
$(\xi=2)\to(\xi=2)$	$2_{2,1}$	$0_{2,0}$	140.00	112.64	98.97	91.24	75.22
	$4_{2,2}$	$2_{2,1}$	257.14	197.92	170.97	156.06	124.32
	$6_{2,3}$	$4_{2,2}$	366.67	271.04	230.57	208.71	161.52
	$8_{2,4}$	$6_{2,3}$	472.73	336.84	282.53	253.85	191.58
$(\xi=3)\to(\xi=3)$	$2_{3,1}$	$0_{3,0}$	180.00	126.58	103.69	91.64	65.73
	$4_{3,2}$	$2_{3,1}$	314.29	214.91	173.97	152.67	106.63
	$6_{3,3}$	$4_{3,2}$	433.33	288.38	230.96	201.40	137.44
	$8_{3,4}$	$6_{3,3}$	545.45	353.71	280.48	243.22	162.57
$(\xi=4)\to(\xi=4)$	$2_{4,1}$	$0_{4,0}$	220.00	140.44	109.56	94.03	60.68
	$4_{4,2}$	$2_{4,1}$	371.43	232.42	179.66	153.33	96.89
	$6_{4,3}$	$4_{4,2}$	500.00	306.70	235.08	199.63	123.79
	$8_{4,4}$	$6_{4,3}$	618.18	371.85	282.79	239.04	145.70
$(\xi=2)\to(\xi=1)$	$0_{2,0}$	$2_{1,1}$	200.00	141.77	118.98	107.57	86.79
	$2_{2,1}$	$4_{1,2}$	102.86	66.10	52.62	46.00	33.82
	$2_{2,1}$	$0_{1,0}$	0.00	0.16	0.30	0.38	0.47
$(\xi=3)\to(\xi=2)$	$0_{3,0}$	$2_{2,1}$	400.00	257.90	205.27	178.52	123.22
	$2_{3,1}$	$4_{2,2}$	205.71	123.14	94.54	80.50	51.57
	$2_{3,1}$	$0_{2,0}$	0.00	0.22	0.38	0.46	0.54
$(\xi=4)\to(\xi=3)$	$0_{4,0}$	$2_{3,1}$	600.00	358.53	273.82	232.05	144.02
	$2_{4,1}$	$4_{3,2}$	308.57	173.79	129.12	107.67	62.88
	$2_{4,1}$	$0_{3,0}$	0.00	0.26	0.43	0.51	0.56

to refer to as the $X(5)$-β^2 model, the eigenfunctions are [8]

$$F_n^L(\beta)=\left[\frac{2n!}{\Gamma\left(n+a+\frac{5}{2}\right)}\right]^{1/2}\beta^a L_n^{a+3/2}(\beta^2)e^{-\beta^2/2}, \tag{20}$$

where $\Gamma(n)$ stands for the Γ function, $L_n^a(z)$ denotes the Laguerre polynomials, and $a=\frac{1}{2}\left(-3+\sqrt{9+\frac{4}{3}L(L+1)}\right)$, while the energy eigenvalues are

$$E_{n,L}=2n+a+\frac{5}{2}=2n+1+\sqrt{\frac{9}{4}+\frac{L(L+1)}{3}}, \qquad n=0,1,2,\ldots. \tag{21}$$

In the above, n is the usual oscillator quantum number. One can see that a formal correspondence between the energy levels of the $X(5)$ model and the present $X(5)$-β^2 model can be established through the relation $n=s-1$. In the present notation, the ground-state band corresponds to $s=1$ ($n=0$). For the energy states, the notation $E_{s,L}=E_{n+1,L}$ of [2] will be kept.

In the original version of the $X(5)$ model [2], the potential $u(\gamma)$ in Eq. (17) is considered as a harmonic-oscillator potential. The energy eigenvalues turn out to be

$$E(s,L,n_\gamma,K,M)=E_0+B(x_{s,L})^2+An_\gamma+CK^2, \tag{22}$$

where n_γ and K come from solving Eq. (17) for $u(\gamma)$

Table 3. Spectra of the $X(5)$-β^4, $X(5)$-β^6, and $X(5)$-β^8 models, compared to the predictions of the $X(5)$ [Eq. (18)] and $X(5)$-β^2 [Eq. (21)] models (see Sections 3 and 4 for details)

Band	L	$X(5)$-β^2	$X(5)$-β^4	$X(5)$-β^6	$X(5)$-β^8	$X(5)$
$s=1$, $n_\gamma=0$, $K=0$	0	0.000	0.000	0.000	0.000	0.000
	2	1.000	1.000	1.000	1.000	1.000
	4	2.646	2.769	2.824	2.852	2.904
	6	4.507	4.929	5.125	5.230	5.430
	8	6.453	7.343	7.777	8.015	8.483
	10	8.438	9.954	10.721	11.151	12.027
	12	10.445	12.729	13.922	14.605	16.041
	14	12.465	15.647	17.359	18.355	20.514
	16	14.494	18.694	21.013	22.383	25.437
$s=1$, $n_\gamma=1$, $K=2$	2	0.000	0.000	0.000	0.000	0.000
	3	0.781	0.821	0.839	0.847	0.863
	4	1.646	1.769	1.824	1.852	1.904
	5	2.562	2.811	2.925	2.985	3.097
	6	3.507	3.929	4.125	4.230	4.430
$s=2$, $n_\gamma=0$, $K=0$	0	3.562	4.352	4.816	5.091	5.649
	2	4.562	5.602	6.232	6.619	7.450
	4	6.208	7.733	8.684	9.288	10.689
	6	8.069	10.248	11.629	12.527	14.751
	8	10.014	12.990	14.896	16.154	19.441
$s=3$, $n_\gamma=0$, $K=0$	0	7.123	9.384	10.823	11.758	14.119
	2	8.123	10.817	12.562	13.710	16.716
	4	9.769	13.228	15.520	17.054	21.271
	6	11.630	16.032	19.004	21.025	26.832
	8	13.576	19.050	22.802	25.385	33.103
$s=4$, $n_\gamma=0$, $K=0$	0	10.685	14.956	17.831	19.781	25.414
	2	11.685	16.536	19.842	22.105	28.805
	4	13.331	19.177	23.235	26.044	34.669
	6	15.192	22.225	27.189	30.667	41.717
	8	17.137	25.483	31.458	35.689	49.551

being a harmonic-oscillator potential,

$$n_\gamma=0, \quad K=0; \qquad n_\gamma=1, \quad K=\pm 2; \qquad (23)$$
$$n_\gamma=2, \quad K=0,\pm 4; \quad \ldots.$$

For $K=0$, one has $L=0,2,4,\ldots$, while, for $K\neq 0$, one obtains $L=K, K+1, K+2, \ldots$.

In the present $X(5)$-β^2 model, one also uses in Eq. (17) for $u(\gamma)$ a harmonic-oscillator potential, as in the $X(5)$ model. As a consequence, the full spectrum is given by

$$E(n,L,n_\gamma,K,M)=E'_0 \qquad (24)$$
$$+B'\left(2n+1+\sqrt{\frac{L(L+1)}{3}+\frac{9}{4}}\right)$$
$$+A'n_\gamma+C'K^2,$$

which is an analog of Eq. (22). Equation (23) and the discussion following it remain unchanged.

Numerical results for the β parts of the energy spectra (which correspond to no excitations in the γ variable, i.e., to $n_\gamma=0$) of the $X(5)$-β^2 and $X(5)$ models are shown in Table 3. All levels are normalized to the energy of the first excited state, $E_{1,2}-E_{1,0}=1.0$, where the notation $E_{s,L}=E_{n+1,L}$ is used. The model predictions for these bands are parameter-independent, up to an overall scale, as seen from Eqs. (18), (21). This is not the case for bands with $n_\gamma\neq 0$, since in this case, as seen from Eqs. (22), (24), the extra parameters A, C and A', C' enter, respectively. Therefore, in the case of the ($n_\gamma=1$, $K=2$) band, the energies are listed in Table 3 after subtracting from them the relevant $L=2$ bandhead, using the same normalization as above.

The quadrupole operator has the form of Eq. (8) [5], while the $B(E2)$ transition rates are given by Eq. (9). The matrix elements of the quadrupole operator involve an integral over the Euler angles, which is the same as in [2] and is performed by using the properties of the Wigner $\mathcal{D}$ functions, of which only $\mathcal{D}^{(2)}_{\mu,0}$ participates, since $\gamma\simeq 0$ in Eq. (8) [as mentioned before Eq. (15)], as well as an integral over β. After performing the integrations over the angles, one is left with $B(E2;L_s\rightarrow L'_{s'})=(L_s2L'_{s'}|000)^2 I^2_{s,L;s',L'}$, where the Clebsch–Gordan coefficient $(L_s2L'_{s'}|000)$ appears, which determines the relevant selection rules. In the case of $X(5)$, the integral over β is $I_{s,L;s',L'}=\int\beta\xi_{s,L}(\beta)\xi_{s',L'}(\beta)\beta^4 d\beta$, which, as can be seen from Eq. (19), involves Bessel functions, while in the case of $X(5)$-β^2 the integral has the form $I_{s,L;s',L'}=\int\beta F^L_n(\beta)F^{L'}_{n'}\beta^4 d\beta$, with $n=s-1$ and $n'=s'-1$, which involves Laguerre polynomials, as can be seen from Eq. (20).

The results for intraband and interband transitions are reported in Table 4. All transitions are normalized to $B(E2;2^+_1\rightarrow 0^+_1)=100$.

4. A SEQUENCE OF POTENTIALS LYING BETWEEN $U(5)$ AND $X(5)$

The two cases mentioned in the previous section are the only ones in which Eq. (16) is exactly soluble,

Table 4. Intraband and interband $B(E2)$ transition rates for the $X(5)$-β^4, $X(5)$-β^6, and $X(5)$-β^8 models, compared to the predictions of the $X(5)$ and $X(5)$-β^2 models (see Sections 3 and 4 for details)

Band	$(L_s)_i$	$(L_s)_f$	$X(5)$-β^2	$X(5)$-β^4	$X(5)$-β^6	$X(5)$-β^8	$X(5)$
$(s=1)\to(s=1)$	2_1	0_1	100.00	100.00	100.00	100.00	100.00
	4_1	2_1	177.90	169.03	165.31	163.41	159.89
	6_1	4_1	255.18	226.15	214.62	208.83	198.22
	8_1	6_1	337.06	279.88	258.09	247.31	227.60
	10_1	8_1	421.32	330.45	297.02	280.71	250.85
	12_1	10_1	506.85	378.25	332.37	310.24	269.73
	14_1	12_1	593.11	423.67	364.85	336.77	285.42
$(s=2)\to(s=2)$	2_2	0_2	155.69	121.99	106.03	97.23	79.52
	4_2	2_2	240.30	187.73	162.89	149.05	120.02
	6_2	4_2	316.27	239.86	205.80	187.08	146.75
	8_2	6_2	397.68	290.57	245.80	221.73	169.31
$(s=3)\to(s=3)$	2_3	0_3	211.85	144.41	116.82	102.55	72.52
	4_3	2_3	302.74	208.42	169.03	148.48	104.36
	6_3	4_3	377.38	256.28	206.61	180.79	124.81
	8_3	6_3	458.35	304.07	242.92	211.42	142.94
$(s=2)\to(s=1)$	0_2	2_1	121.92	93.21	81.03	74.66	62.41
	2_2	0_1	1.57	2.04	2.18	2.21	2.12
	2_2	2_1	13.40	11.34	10.28	9.66	8.22
	2_2	4_1	96.85	65.53	53.55	47.59	36.56
	4_2	2_1	0.06	0.48	0.72	0.84	0.94
	4_2	4_1	12.41	9.63	8.37	7.68	6.10
	4_2	6_1	96.68	59.53	46.23	39.78	27.87
$(s=3)\to(s=2)$	0_3	2_2	241.37	166.55	136.53	120.61	86.33
	2_3	0_2	2.74	3.20	3.19	3.11	2.66
	2_3	2_2	25.45	19.61	16.82	15.19	11.25
	2_3	4_2	193.64	120.83	94.54	81.36	54.01
	4_3	2_2	0.11	0.70	0.97	1.08	1.12
	4_3	4_2	23.75	17.14	14.27	12.67	8.83
	4_3	6_2	193.35	111.85	84.29	70.99	43.76

giving spectra characterized by R_4 ratios of 2.646 and 2.904 for $X(5)$-β^2 and $X(5)$, respectively. However, the numerical solution of Eq. (16) for other potentials is a straightforward task. The potentials to be used in Eq. (16) have to obey the restrictions imposed by the 24 transformations mentioned in [3] and listed explicitly in [11].

A particularly interesting sequence of potentials is given by $u_{2n}(\beta)=\beta^{2n}/2$, with n being an integer. For $n=1$, the $X(5)$-β^2 case is obtained, while for $n\to\infty$ the infinite well of $X(5)$ is obtained [13]. Therefore, this sequence of potentials interpolates between the $X(5)$-β^2 model and the $X(5)$ model, in the region lying between $U(5)$ and $X(5)$.

Numerical results for the spectra of the β^4, β^6, and

β^8 potentials have been obtained through the two different methods described in Section 2. The results are shown in Table 3, where excitation energies relative to the ground state, normalized to the excitation energy of the first excited state, are exhibited.

In Table 3, the model labels $X(5)$-β^4, $X(5)$-β^6, and $X(5)$-β^8 have been used for the above-mentioned potentials, their meaning being that the $X(5)$-β^{2n} model corresponds to the potential $\beta^{2n}/2$ plugged in the differential equation of Eq. (16) obtained in the framework of the $X(5)$ model. In this notation, $X(5)$-β^{2n} with $n \to \infty$ is simply the original $X(5)$ model [2].

From Table 3, it is clear that, in all bands and for all values of the angular momentum L, the potentials β^4, β^6, and β^8 gradually lead from the $X(5)$-β^2 case to the $X(5)$ results in a smooth way.

The calculation of the $B(E2)$ follows the steps described at the end of Section 3. The same general equation is still valid, the only difference being that, in the integral over β, the wave functions in the present cases are known only in numerical form and not in analytic form, as in the $X(5)$ and $X(5)$-β^2 cases.

The results of the calculations for intraband and interband transitions are shown in Table 4. In all cases, a smooth evolution from $X(5)$-β^2 to $X(5)$ is seen.

It is clear that the first place to look for nuclei exhibiting $X(5)$-β^{2n} behavior is the region close to nuclei showing the $X(5)$ structure. The best examples of nuclei corresponding to the $X(5)$ structure thus far are the $N = 90$ isotones ^{152}Sm [20], ^{150}Nd [21], and ^{156}Dy [22]. A preliminary search in the rare earths with $N < 90$ shows that ^{148}Nd can be a candidate for $X(5)$-β^2, ^{158}Er can be a candidate for $X(5)$-β^6, and ^{160}Yb can be a candidate for $X(5)$-β^4. However, much more detailed information on spectra and $B(E2)$ transitions is needed before final conclusions can be reached.

5. CONCLUSION

It has been proved that the potentials β^{2n} (with n being integer) provide a complete "bridge" between the $U(5)$ symmetry of the Bohr Hamiltonian with a harmonic oscillator potential (occurring for $n = 1$) and the $E(5)$ model of F. Iachello, which is obtained from the Bohr Hamiltonian when an infinite-well potential is plugged in it (materialized for $n \to \infty$). Parameter-free (up to overall scale factors) predictions for spectra and $B(E2)$ transition rates have been given for the potentials β^4, β^6, and β^8, called the $E(5)$-β^4, $E(5)$-β^6, and $E(5)$-β^8 models, respectively. Hints about nuclei showing this behavior have been briefly discussed.

In addition, an exactly soluble model, labeled as $X(5)$-β^2, has been constructed starting from the original Bohr collective Hamiltonian, separating the β and γ variables as in the $X(5)$ model of F. Iachello, and using a harmonic-oscillator potential for the β variable. Furthermore, it has been proved that the potentials β^{2n} (with n being integer) provide a "bridge" between this new $X(5)$-β^2 model (occurring for $n = 1$) and the $X(5)$ model of F. Iachello (which is obtained by putting in the Bohr Hamiltonian an infinite-well potential in the β variable, materialized for $n \to \infty$). Parameter-free (up to overall scale factors) predictions for spectra and $B(E2)$ transition rates have been given for the potentials β^2, β^4, β^6, and β^8, called the $X(5)$-β^2, $X(5)$-β^4, $X(5)$-β^6, and $X(5)$-β^8 models, respectively, lying between the $U(5)$ symmetry of the original Bohr Hamiltonian and the $X(5)$ model. Hints about nuclei showing this behavior have been given.

Concerning future theoretical work, one should try to find a sequence of potentials interpolating between $O(6)$ and $E(5)$, as well as between $SU(3)$ and $X(5)$. In other words, one should try to approach $E(5)$ and $X(5)$ "from the other side." From the classical limit of the $O(6)$ and $SU(3)$ symmetries of the interacting boson model [9], it is clear that, for this purpose, potentials with a minimum at $\beta \neq 0$ should be considered, the potentials $u^D_{2n}(\beta) = \beta^{2n} + \beta_0^{4n}/\beta^{2n}$ being strong candidates. The Davidson potential, corresponding to $n = 1$, is known to be exactly soluble [23, 24]. Work in these directions is in progress.

ACKNOWLEDGMENTS

We are grateful to Rick Casten (Yale), Jean Libert (Orsay), and Werner Scheid (Giessen) for illuminating discussions. Support through the NATO Collaborative Linkage (grant PST.CLG 978799) is gratefully acknowledged.

REFERENCES

1. F. Iachello, Phys. Rev. Lett. **85**, 3580 (2000).
2. F. Iachello, Phys. Rev. Lett. **87**, 052502 (2001).
3. A. Bohr, K. Dan. Vidensk. Selsk. Mat. Fys. Medd. **26** (14) (1952).
4. E. Chacón and M. Moshinsky, J. Math. Phys. (N.Y.) **18**, 870 (1977).
5. L. Wilets and M. Jean, Phys. Rev. **102**, 788 (1956).
6. G. Rakavy, Nucl. Phys. **4**, 289 (1957).
7. D. R. Bes, Nucl. Phys. **10**, 373 (1959).
8. M. Moshinsky, J. Math. Phys. (N.Y.) **25**, 1555 (1984).
9. F. Iachello and A. Arima, *The Interacting Boson Model* (Cambridge Univ. Press, Cambridge, 1987).

10. D. Troltenier, J. A. Maruhn, and P. O. Hess, in *Computational Nuclear Physics. 1. Nuclear Structure*, Ed. by K. Langanke, J. A. Maruhn, and S. E. Koonin (Springer, Berlin, 1991), p. 105.
11. T. M. Corrigan, F. J. Margetan, and S. A. Williams, Phys. Rev. C **14**, 2279 (1976).
12. W. Greiner and J. A. Maruhn, *Nuclear Models* (Springer, Berlin, 1996).
13. C. M. Bender, S. Boettcher, H. F. Jones, and V. M. Savage, J. Phys. A **32**, 6771 (1999).
14. H. J. Korsch and M. Glück, Eur. Phys. J. A **23**, 413 (2002).
15. N. Minkov and W. Scheid, Preprint INRNE (Sofia, 2003).
16. F. Iachello, AIP Conf. Proc. **638**, 1 (2002).
17. R. F. Casten and N. V. Zamfir, Phys. Rev. Lett. **85**, 3584 (2000).
18. A. Frank, C. E. Alonso, and J. M. Arias, Phys. Rev. C **65**, 014301 (2002).
19. N. V. Zamfir *et al.*, Phys. Rev. C **65**, 044325 (2002).
20. R. F. Casten and N. V. Zamfir, Phys. Rev. Lett. **87**, 052503 (2001).
21. R. Krücken *et al.*, Phys. Rev. Lett. **88**, 232501 (2002).
22. M. A. Caprio *et al.*, Phys. Rev. C **66**, 054310 (2002).
23. P. M. Davidson, Proc. R. Soc. London **135**, 459 (1932).
24. D. J. Rowe and C. Bahri, J. Phys. A **31**, 4947 (1998).

Physics of Atomic Nuclei, Vol. 67, No. 10, 2004, pp. 1776–1780. From Yadernaya Fizika, Vol. 67, No. 10, 2004, pp. 1804–1808.

Proceedings of the International Conference "Nuclear Structure and Related Topics"

Pairing Correlations in Finite Nuclear Systems*

D. Gambacurta[1] and M. Sambataro[2]**

Received January 21, 2004

Abstract—We discuss an approach for the treatment of correlations in finite nuclear systems. The approach is based on a boson formalism, the basic boson operators representing elementary particle–hole excitations. We show an application of the method within an exactly solvable multilevel pairing model. We calculate the correlation energy of the system and compare it with the exact results as well as with results obtained within other approaches. © *2004 MAIK "Nauka/Interperiodica".*

1. INTRODUCTION

Searching for an appropriate treatment of two-body correlations is among the basic goals of quantum many-body physics. Several approaches can be found on the market which deal with this problem, but, so far, none of them has received unanimous consensus. This justifies the great deal of effort which is still devoted to this subject.

Pairing correlations are among those which have traditionally attracted more interest because of the role that the pairing force plays in nuclear structure and, more in general, in quantum many-body physics. In recent years, in particular, the interest in nuclear pairing has been further stimulated by the shift of modern nuclear physics toward nuclei far from stability, where pairing has confirmed its key role in the understanding of nuclear properties. A very recent and accurate analysis of pairing in nuclear systems can be found in [1].

A model which has been often studied in the past for a theoretical analysis of pairing is the so-called picket fence model (PFM). This model was used long ago in nuclear physics as a model for a superfluid deformed nucleus [2, 3], but, in recent years, it has had a very interesting revival in the context of superconducting ultrasmall metallic grain [4]. Being exactly solvable and highly nontrivial, the PFM provides an ideal testing ground for any approach dealing with an approximate treatment of the correlations. As such, this model has been used to check the validity of methods like the random phase approximation (RPA) and its self-consistent extension [5], the coupled cluster theory (CCT) [6], as well as, of course, more specific approaches like BCS and its projected version [2, 6].

In this paper, we report on exploratory work that we have done to test, within the PFM, the validity of an approach which offers a treatment of correlations alternative to those already present in the literature. As we will see, this approach is based on a boson formalism, the basic boson operators representing elementary particle–hole excitations, and has some similarities with BCS without introducing, however, any violation of the particle number.

The plan of the paper is the following. In Section 2, we briefly discuss the model and its exact solutions. In Section 3, we illustrate the method and, in Section 4, compare the correlation energy calculated with this method with the exact one and with that obtained within other approximations like BCS, LN, and particle–particle RPA (ppRPA). Finally, in Section 5, we summarize the results and draw some conclusions.

2. THE PFM AND ITS EXACT SOLUTIONS

This model treats a system of particles distributed over a set of equidistant, doubly degenerate levels and interacting via a pairing force. The Hamiltonian of the model is

$$H = \sum_j \epsilon_j \hat{N}_j - g \sum_{ij} A_i^\dagger A_j, \qquad (1)$$

where

$$\hat{N}_j = \sum_\sigma a_{j\sigma}^\dagger a_{j\sigma}, \qquad A_j^\dagger = a_{j+}^\dagger a_{j-}^\dagger, \qquad (2)$$

$$A_j = (A_j^\dagger)^\dagger.$$

The operator $a_{j\sigma}^\dagger$ ($a_{j\sigma}$) creates (destroys) a fermion in the single-particle state (j, σ), where j identifies one

*This article was submitted by the authors in English.

[1]Dipartimento di Fisica e Astronomia dell'Università di Catania, Italy.

[2]Istituto Nazionale di Fisica Nucleare, Sezione di Catania, Italy.

**e-mail: samba@ct.infn.it

of the Ω levels of the model and $\sigma = \pm$ denotes one of the two allowed states on each level. For the single-particle energies ϵ_j, we assume the form

$$\epsilon_j = \epsilon j - \frac{\Omega + 1 - g}{2} \tag{3}$$

which guarantees a constant spacing ($\Delta\epsilon \equiv \epsilon_{j+1} - \epsilon_j = \epsilon$) and a particle–hole symmetry [5]. We only consider half-filled systems, i.e., systems with as many particles as levels. If N denotes the number of pairs, we therefore have $2N = \Omega$.

The derivation of the exact solutions of the Hamiltonian (1) dates back to the 1960s and, more precisely, to a series of works of R.W. Richardson, the first of which was published in 1963 [7]. According to this author, if $|\Psi_\nu\rangle$ is an exact eigenstate of (1), one can write

$$|\Psi_\nu\rangle = \prod_{i=1}^{N} B^\dagger_{\nu_i}|0\rangle, \tag{4}$$

where

$$B^\dagger_{\nu_i} = \sum_{k=1}^{\Omega} \frac{1}{2\epsilon_k - E_{\nu_i}} A^\dagger_k, \tag{5}$$

$|0\rangle$ is the vacuum of the $a_{j\sigma}$, and E_{ν_i} are N parameters which must satisfy the set of N coupled equations

$$1 - \sum_{k=1}^{\Omega} \frac{g}{2\epsilon_k - E_{\nu_i}} + \sum_{j(j\neq i)}^{N} \frac{2g}{E_{\nu_j} - E_{\nu_i}} = 0. \tag{6}$$

The eigenvalue E_ν associated with $|\Psi_\nu\rangle$ takes the form

$$E_\nu = \sum_{i=1}^{N} E_{\nu_i}. \tag{7}$$

In order to have the exact eigenvalues, one has therefore to solve the set of Eqs. (6). This requires, however, some further transformations in order to remove divergences and avoid complex solutions [2].

3. TREATMENT OF CORRELATIONS IN A BOSON FORMALISM

In the noninteracting case ($g = 0$), the lowest $\Omega/2$ levels are occupied by two particles in each level. We call $|\Phi\rangle$ this state of the system. As usual, we classify the states into particle states (p) for those levels above the Fermi energy and hole states (h) for those levels below the Fermi energy.

The formalism that we discuss in this work goes through four basic steps. At the first step, we introduce the fermion ph operators

$$B^\dagger_{i\sigma} = a^\dagger_{p_i\sigma} a_{h_i\sigma} \tag{8}$$

and, in correspondence, the boson operators $b^\dagger_{i\sigma}$. The last ones satisfy the following commutation relations:

$$[b_{i\sigma}, b^\dagger_{i'\sigma'}] = \delta_{ii'}\delta_{\sigma\sigma'}, \quad [b^\dagger_{i\sigma}, b^\dagger_{i'\sigma'}] = 0. \tag{9}$$

We notice that $|\Phi\rangle$ is the vacuum of the $B_{i\sigma}$ operators, i.e., $B_{i\sigma}|\Phi\rangle = 0$. The corresponding boson vacuum is denoted by $|\Phi)$ ($b_{i\sigma}|\Phi) = 0$).

As a second step, we construct a boson image of the pairing Hamiltonian (1) in the language of these boson operators. The basic boson Hamiltonian that we consider has the form

$$H_b = W^{(0)} + \sum_i W^{(1)}_i \sum_\sigma b^\dagger_{i\sigma} b_{i\sigma} \tag{10}$$
$$+ \sum_i W^{(2)}_i (b^\dagger_{i+} b^\dagger_{i-} + \text{h.c.}) + \sum_{ij} W^{(3)}_{ij} b^\dagger_{i+} b^\dagger_{i-} b_{j+} b_{j-}.$$

In order to derive the coefficients of this Hamiltonian, we first define the spaces

$$F = \left\{ |\Phi\rangle, B^\dagger_{i\sigma}|\Phi\rangle, B^\dagger_{i+}B^\dagger_{i-}|\Phi\rangle \right\}, \tag{11}$$

$$B = \left\{ |\Phi), b^\dagger_{i\sigma}|\Phi), b^\dagger_{i+}b^\dagger_{i-}|\Phi) \right\}. \tag{12}$$

The states which span these spaces are in a one-to-one correspondence and orthonormal. The coefficients of H_b are defined by requiring that corresponding matrix elements of F and B be equal. As a result of that, one gets

$$W^{(0)} = 2\sum_h \epsilon_h - gN, \tag{13}$$
$$W^{(1)}_i = \epsilon_{p_i} - \epsilon_{h_i} + g, \quad W^{(2)}_i = -g,$$
$$W^{(3)}_{ij} = -g(\delta_{p_ip_j} + \delta_{h_ih_j}).$$

As a third step, we introduce new operators $\beta^\dagger_{i\sigma}, \beta_{i\sigma}$ which are related to $b^\dagger_{i\sigma}, b_{i\sigma}$ through a Bogolyubov transformation:

$$\beta^\dagger_{i\sigma} = u_i b^\dagger_{i\sigma} - v_i b_{i-\sigma}. \tag{14}$$

Under the condition that

$$u_i^2 - v_i^2 = 1, \tag{15}$$

these new operators satisfy boson commutation relations of the type (9), i.e.,

$$[\beta_{i\sigma}, \beta^\dagger_{i'\sigma'}] = \delta_{ii'}\delta_{\sigma\sigma'}, \qquad [\beta^\dagger_{i\sigma}, \beta^\dagger_{i'\sigma'}] = 0. \tag{16}$$

If we call $|\Phi_\beta)$ the vacuum of the $\beta_{i\sigma}$ operators (i.e., $\beta_{i\sigma}|\Phi_\beta) = 0$), one can verify that it has the form

$$|\Phi_\beta) \propto \exp\left(\sum_i \frac{v_i}{u_i} b^\dagger_{i+} b^\dagger_{i-} \right) |\Phi). \tag{17}$$

The operator $b^\dagger_{i+}b^\dagger_{i-}$ which appears in the exponent of (17) creates, in the boson language, a $2p$–$2h$

state since it mimics the fermion operator $B^\dagger_{i+}B^\dagger_{i-} = a^\dagger_{p_i+}a_{h_i+}a^\dagger_{p_i-}a_{h_i-}$ which raises a pair of particles from the level h_i up to p_i. $|\Phi_\beta)$ is therefore a sum of states all carrying a different number of ph excitations.

As a fourth (and final, at least as far as ground-state energies are concerned) step, we assume $|\Phi_\beta)$ to be the ground state of the system and determine its energy by minimizing the expectation value

$$E_0^{(\beta)} = \frac{(\Phi_\beta|H_b|\Phi_\beta)}{(\Phi_\beta|\Phi_\beta)} \tag{18}$$

with respect to u_i, v_i and under the constraints (15). In the evaluation of the expectation value of H_b, we take advantage of the definition (14) by reversing it, i.e., by expressing $b^\dagger_{i\sigma}$, $b_{i\sigma}$ in terms of $\beta^\dagger_{i\sigma}$, $\beta_{i\sigma}$, and remembering that $|\Phi_\beta)$ is the vacuum of $\beta_{i\sigma}$.

It is interesting to note that, in the model under consideration, the minimization of $E_0^{(\beta)}$ leads to the set of equations

$$u_i^2 = \frac{1}{2}\left\{\frac{\tilde{\epsilon}_i}{[(\tilde{\epsilon}_i)^2 - (\widetilde{\Delta}_i)^2]^{1/2}} + 1\right\}, \tag{19}$$

$$v_i^2 = \frac{1}{2}\left\{\frac{\tilde{\epsilon}_i}{[(\tilde{\epsilon}_i)^2 - (\widetilde{\Delta}_i)^2]^{1/2}} - 1\right\}, \tag{20}$$

where

$$\tilde{\epsilon}_i = \epsilon_{p_i} - \epsilon_{h_i} + g(1 - 2v_i^2), \tag{21}$$
$$\widetilde{\Delta}_i = g + \Delta_{p_i} + \Delta_{h_i},$$

with

$$\Delta_{p_i} = g\sum_{h_i} u_i v_i, \qquad \Delta_{h_i} = g\sum_{p_i} u_i v_i. \tag{22}$$

These equations can be solved with a numerical iterative procedure. We also note that the boson Hamiltonian written in terms of the $\beta^\dagger_{i\sigma}$, $\beta_{i\sigma}$ operators takes the form

$$H_b = E_0^{(\beta)} + \sum_i E_{1,i}^{(\beta)} \sum_\sigma \beta^\dagger_{i\sigma}\beta_{i\sigma} + H_{\rm int}^{(\beta)}, \tag{23}$$

where

$$E_0^{(\beta)} = W^{(0)} + 2\sum_i (\tilde{\epsilon}_i + g v_i^2)v_i^2 \tag{24}$$
$$- \sum_i (g + \widetilde{\Delta}_i)u_i v_i,$$

$$E_{1,i}^{(\beta)} = [(\tilde{\epsilon})_i^2 - (\tilde{\Delta})_i^2]^{1/2}. \tag{25}$$

The previous equations evidence an interesting similarity between the present formalism and BCS, the basic difference being that our formalism makes use of a Bogolyubov transformation involving (boson) ph excitation operators rather than (fermion) particle operators as in BCS. This in turn implies that the ground state, although having in both cases an exponential form, has a very different nature and, in our formalism, it does not mix states with different particle number, as occurs instead in BCS. The ground state (17) looks, instead, equivalent, although in a boson formalism, to the CCT ground state in the SUB2 approximation [8].

A problem that one usually has to face when dealing with boson mapping procedures concerns the violation of the Pauli principle. Such a violation is strictly related to the need for truncating operators like the Hamiltonian at a finite order in the boson expansion. The Hamiltonian (10) already contains four-boson terms, and going to a higher order, especially when considering realistic systems, might be rather complicated. However, in order to examine the relevance of additional terms in (10), we have also studied the Hamiltonian

$$H'_b = H_b + g\sum_i (b^\dagger_{i+}b^\dagger_{i-}b^\dagger_{i+}b^\dagger_{i-}b_{i+}b_{i-} + \text{h.c.}). \tag{26}$$

The six-boson term appearing in H'_b has a quite important role: it guarantees that

$$(\Phi|b_{k+}b_{k-}H'_b b^\dagger_{j+}b^\dagger_{j-}b^\dagger_{j+}b^\dagger_{j-}|\Phi) = 0. \tag{27}$$

This is exactly what one would expect to obtain, as a result of the Pauli principle, when considering the corresponding fermion matrix element. The extra term of H'_b has therefore the effect of allowing for a better treatment of the Pauli principle at the boson level. It must also be noted that it has a repulsive behavior ($g > 0$). Of course, introducing this extra term in the Hamiltonian leads to some modifications in Eqs. (19)–(25) which, however, will not be discussed here for simplicity. What is important, the basic structure of the equations for u_i^2 and v_i^2 [Eqs. (19) and (20)] remains unchanged. In the following, we will examine calculations performed by using both H_b and H'_b.

4. CALCULATIONS

In the figure, we plot the correlation energy $E_{\rm corr}$ versus the strength g for a system with $\Omega = 24$ levels (and particles) with spacing $\epsilon = 1$. In the formalism of the previous section, it is $E_{\rm corr} = E_0^{(\beta)} - W^{(0)}$ [see Eqs. (13) and (24)]. For comparison, we also plot the results obtained within BCS, LN, and ppRPA.

Calculations referring to the Hamiltonians H_b and H'_b are labeled with the symbols "a" and "b," respectively. These calculations differ significantly. Calculations a lead to values of the correlation energy which are indistinguishable from the exact ones in the

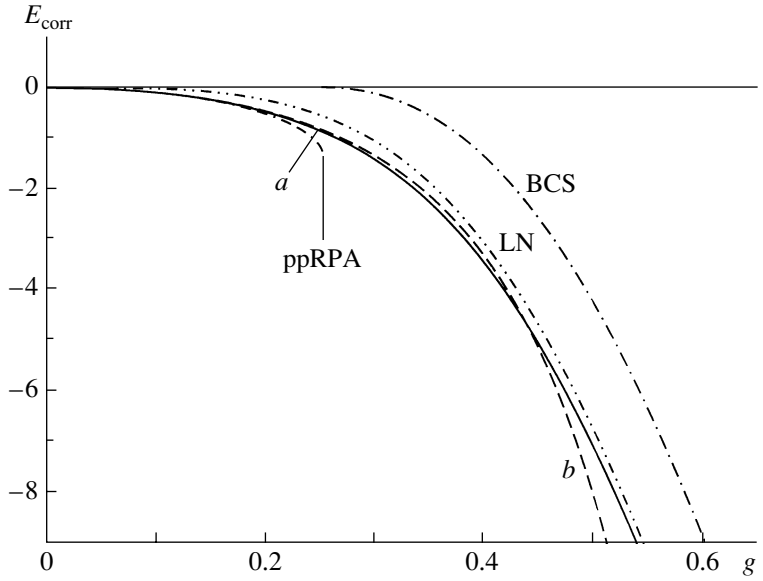

Correlation energy for a system of 24 particles distributed over 24 levels with spacing $\epsilon = 1$. The results obtained with the procedure illustrated in this work are indicated with the symbols "a" and "b" and refer to the use of different Hamiltonians (see text). Exact results are shown by the solid curve. For comparison, also results obtained within BCS, LN, and ppRPA are reported.

figure, but they undergo a collapse at $g \approx 0.25 \equiv g_{cr}$. This collapse occurs very close to the points where BCS and ppRPA also collapse. Calculations b lead to results which do not differ significantly from the previous one for $g \leq g_{cr}$. However, the inclusion of the repulsive term in the Hamiltonian has the important effect of shifting the collapse to a value of g considerably higher ($g \approx 0.68 \equiv g'_{cr}$). The correlation energy can therefore be calculated, in this case, also well inside the superfluid region. The quality of the agreement with the exact results remains optimal in the normal-fluid region, but it is also good around g_{cr} and, more generally, in the first part of the superfluid region. A progressive deterioration of the quality of the results is observed for values of g approaching g'_{cr}. The inclusion of the repulsive term in the boson Hamiltonian also has an important effect on the behavior of the energy of the first excited state. This point, however, will not be discussed in this paper.

Similar calculations have been performed also for systems with smaller and larger values of Ω, and they all qualitatively confirm the results of the figure.

5. SUMMARY AND CONCLUSIONS

In this paper, we have discussed an approach for the treatment of correlations in nuclear and, more generally, in quantum many-body systems. This approach is based on a boson formalism, the basic boson operators $b^\dagger_{i\sigma}$, $b_{i\sigma}$ representing elementary particle–hole excitations. A mapping of the original fermion Hamiltonian onto a boson one built in terms of these operators is therefore required. New boson operators $\beta^\dagger_{i\sigma}$, $\beta_{i\sigma}$ are also defined which are related to $b^\dagger_{i\sigma}$, $b_{i\sigma}$ through a Bogolyubov transformation. The ground state of the system is assumed to be the vacuum of the $\beta_{i\sigma}$ operators and its energy evaluated via a minimization procedure. In the case of the pairing model examined in this paper, this minimization leads to a set of equations whose structure closely resembles that of the BCS equations.

We have shown the results of a calculation of the correlation energy for a system of 24 particles distributed over 24 levels. These results have been performed by making use of two boson Hamiltonians, one truncated at four-boson terms and one which, instead, contains an extra (repulsive) six-boson term. The calculations with the reduced Hamiltonian undergo a collapse in proximity of the points, where also BCS and ppRPA crash. Up to this point (i.e., in the normal-fluid region), the approximate results obtained with our procedure are in very good agreement with the exact ones. The inclusion of the additional six-boson term in the Hamiltonian has the main effect of shifting the collapse to a considerably higher value of the pairing strength. The quality of the results remains good in the first part of the superfluid region and only deteriorates for values of the pairing strength approaching the new point of collapse. Calculations performed for systems with smaller and larger number of particles qualitatively confirm these results.

As a general conclusion, we believe that what has emerged from this preliminary work is interest-

ing enough to stimulate further investigations of the present formalism especially within realistic systems.

REFERENCES

1. D. J. Dean and M. Hjorth-Jensen, Rev. Mod. Phys. **75**, 607 (2003).
2. R. W. Richardson, Phys. Rev. **141**, 949 (1966).
3. J. Bang and J. Krumlinde, Nucl. Phys. **141**, 18 (1970).
4. F. Braun and J. von Delft, Phys. Rev. Lett. **81**, 4712 (1998).
5. J. Dukelsky and P. Schuck, Phys. Lett. B **464**, 164 (1999); J. G. Hirsch, A. Mariano, J. Dukelsky, and P. Schuck, Ann. Phys. (N.Y.) **296**, 187 (2002).
6. J. Dukelsky, G. G. Dussel, J. G. Hirsch, and P. Schuck, Nucl. Phys. A **714**, 63 (2003).
7. R. W. Richardson, Phys. Lett. **3**, 277 (1963); R. W. Richardson and N. Sherman, Nucl. Phys. **52**, 221, 253 (1964); R. W. Richardson, Phys. Lett. **14**, 325 (1965); J. Math. Phys. (N.Y.) **6**, 1034 (1965); **8**, 1802 (1967); Phys. Rev. **144**, 874 (1966); **159**, 792 (1967).
8. R. F. Bishop, Teor. Chim. Acta **80**, 95 (1991).

Physics of Atomic Nuclei, Vol. 67, No. 10, 2004, pp. 1781–1785. From Yadernaya Fizika, Vol. 67, No. 10, 2004, pp. 1809–1813.

Proceedings of the International Conference "Nuclear Structure and Related Topics"

Self-Consistent RPA with Multilevel Pairing Model at Finite Temperature*

A. N. Storozhenko[1)**], **A. I. Vdovin**[1)***], and **P. Schuck**[2)****]

Received January 21, 2004

Abstract—A self-consistent version of the thermal random phase approximation (TSCRPA) is developed within the Matsubara Green's function formalism. The TSCRPA is applied to the many-level pairing model, and the normal phase of the system is considered. The TSCRPA results are compared with the exact ones calculated for the grand canonical ensemble. Advantages of the TSCRPA over the thermal mean-field approximation and the standard thermal random phase approximation are demonstrated. Results for correlation functions, excitation energies, etc., as a function of temperature are presented.

1. INTRODUCTION

Almost all microscopic approximations used to describe excitations in hot finite Fermi systems such as the thermal Hartree–Fock and Hartree–Fock–Bogolyubov approximations or the thermal random phase approximation (TRPA) are based upon the single-particle or single-quasiparticle picture. Some approximations going beyond the TRPA were considered as well, but merely a coupling of thermal particle–hole or TRPA phonon excitations with more complex ones was studied [1]. Although these approaches are able to provide a qualitative description of some properties of highly excited nuclei, they have some drawbacks. The most evident difficulty is the description of the strongly correlated finite systems of fermions in the vicinity of the phase-transition point, where proper inclusion of two-body correlations is especially important.

There are different ways to construct a theory which can adequately treat two-body correlations. One of the greatest promising approaches providing such a consideration is the self-consistent RPA (SCRPA) theory [2], which grew out of the works by Ken-ji Hara and D. Rowe, who first suggested a way to generalize the RPA [3]. Recently, the SCRPA was successfully applied to various nontrivial models, where two-body correlations are of importance [4].

Extensions of the SCRPA to finite temperatures were studied as well. In [5], besides a general formulation of the new thermal approximation (TSCRPA) within the framework of thermofield dynamics, applications of TSCRPA to simple model systems with particle–hole correlations were considered. Advantages of TSCRPA over traditional approximations were found.

The main aim of this paper is an extension of SCRPA to finite temperature and investigation in this respect of the many-level pairing model [also known as the picket fence model (PFM)], which was initially introduced to describe deformed superfluid nuclei [6] and was recently used for investigation of ultrasmall superconducting metallic grains [7, 8].

We organize the paper in the following way. In Section 2, the approach is outlined in general. Then, in Section 3, the formalism is applied to the PFM. A comparison with the exact solutions as well as with the corresponding results of other approximations is made in Section 4. In Section 5, we summarize the results and draw some conclusions.

2. GENERAL FORMALISM

In treating a finite many-body system at finite temperature, it is convenient to use the grand canonical ensemble, although it violates number conservation. With the definition

$$K = H - \mu N,$$

the grand partition function and statistical operator read

$$Z_G = e^{-\beta\Omega} = \mathrm{Tr}(e^{-\beta K}),$$

$$\rho_G = Z_G^{-1} e^{-\beta K} = e^{\beta(\Omega - K)},$$

*This article was submitted by the authors in English.

[1)]Bogolyubov Laboratory of Theoretical Physics, Joint Institute for Nuclear Research, Dubna, Moscow oblast, 141980 Russia.
[2)]Institut de Physique Nucléaire, Orsay Cedex, France.
**e-mail: astorozh@thsun1.jinr.ru
***e-mail: vdovin@thsun1.jinr.ru
****e-mail: schuck@ipno.in2p3.fr

1063-7788/04/6710-1781$26.00

where $\beta = 1/T$. Then, for any Schrödinger operator A_α, the modified Heisenberg picture can be introduced,

$$A_\alpha(\tau) = e^{K\tau} A_\alpha e^{-K\tau},$$

and the temperature (or the Matsubara) Green's function (GF) is defined as [9]

$$\begin{aligned} G_{\alpha\beta}^{\tau-\tau'} &= -\langle T_\tau A_\alpha(\tau) A_\beta^+(\tau')\rangle \qquad (1)\\ &= -\mathrm{Tr}[e^{-\beta(K-\Omega)} T_\tau e^{\tau K} A_\alpha e^{-(\tau-\tau')K} A_\beta^+ e^{-\tau' K}]\\ &= -\mathrm{Tr}[\rho_G T_\tau e^{\tau K} A_\alpha e^{-(\tau-\tau')K} A_\beta^+ e^{-\tau' K}]. \end{aligned}$$

Here, the brackets $\langle\ \rangle$ mean the thermodynamic average; T_τ is a τ ordering operator, which arranges operators with the earliest τ (the closest to $-\beta$) to the right.

Let us consider a two-body Hamiltonian

$$H = \sum_{12} t_{12} a_1^+ a_2 + \frac{1}{4} \sum_{1234} \bar{v}_{1234} a_1^+ a_2^+ a_3 a_4, \qquad (2)$$

where a and a^+ are fermion annihilation and creation operators, and t_{12} and $\bar{v}_{1234} = v_{1234} - v_{1243}$ are the kinetic energy and the antisymmetrized matrix element of the two-body interaction. The GF $G_{\alpha\beta}^{\tau-\tau'}$ for an arbitrary operator A_α^+ obeys the following equation of motion:

$$\begin{aligned} -\frac{\partial}{\partial\tau} G_{\alpha\beta}^{\tau-\tau'} &= \delta_{\tau-\tau'} \langle [A_\alpha, A_\beta^+]\rangle\\ - \langle T_\tau [A_\alpha, K]^\tau A_\beta^+(\tau')\rangle &= \delta_{\tau-\tau'} N_{\alpha\beta}\\ &+ \sum_\gamma \int d\tau_1' \mathcal{H}_{\alpha\gamma}^{\tau-\tau_1'} G_{\gamma\beta}^{\tau_1'-\tau'}. \end{aligned}$$

In this expression, it is possible to split the effective Hamiltonian $\mathcal{H}_{\alpha\beta}^{\tau-\tau'}$ into an instantaneous and a dynamic (frequency dependent) part [2]:

$$\begin{aligned} \mathcal{H}_{\alpha\beta}^{\tau-\tau'} &= \sum_{\beta'} \{\delta_{\tau-\tau'} \langle [[A_\alpha, K], A_{\beta'}^+]\rangle\\ &- \langle T_\tau [A_\alpha, K]^\tau [K, A_{\beta'}^+]^{\tau'}\rangle_{\mathrm{irr}}\} N_{\beta'\beta}^{-1}\\ &= \mathcal{H}_{\alpha\beta}^{(0)} \delta_{\tau-\tau'} + \mathcal{H}_{\alpha\beta}^{(r)\tau-\tau'}. \end{aligned}$$

In the approximation of the instantaneous effective Hamiltonian, i.e., neglecting $\mathcal{H}_{\alpha\beta}^{(r)\tau-\tau'}$, the Dyson equation for the two-body Matsubara GF $G_{\alpha\beta}^{\tau-\tau'}$ can be written as

$$-\frac{\partial}{\partial\tau} G_{\alpha\beta}^{(0)\tau-\tau'} = \delta_{\tau-\tau'} N_{\alpha\beta} + \sum_\gamma \mathcal{H}_{\alpha\gamma}^{(0)} G_{\gamma\beta}^{(0)\tau-\tau'}. \quad (3)$$

3. APPLICATION TO THE PICKET FENCE MODEL

The so-called PFM consists of an equidistant multilevel pairing Hamiltonian. Each level is twofold degenerate; i.e., only spin up/down fermions of one kind can occupy it. The corresponding Hamiltonian is given by

$$H = \sum_{k=1}^{\Omega} e_k N_k - G \sum_{i,k=1}^{\Omega} P_i^+ P_k, \qquad (4)$$

where $N_k = c_k^+ c_k + c_{\bar{k}}^+ c_{\bar{k}}$, $P_k^+ = c_k^+ c_{\bar{k}}^+$; $\bar{k}$ means the time reversal of k; single-particle energies are $e_k = k\varepsilon - \lambda$, with level spacing ε chosen to be equal to 1; and Ω stands for the number of levels. The chemical potential λ will be chosen such as to conserve the average number of particles $N = \Omega$ of the system.

To study the model at finite temperature, we define in analogy to (1) the following set of two-body Matsubara GFs: $G_{ji}^\tau = -\langle T_\tau \bar{P}_j(\tau) \bar{P}_i^+(0)\rangle$, where $\bar{P}_j = P_j/\sqrt{\langle|1-N_j|\rangle}$. Applying the instantaneous approximation for a mass operator, we obtain expressions for the two-body SCRPA GFs:

$$i\omega_n G_{ji}^{\mathrm{SCRPA}} = \delta_{ji} + \sum_k \mathcal{H}_{jk}^{(0)} G_{ki}^{\mathrm{SCRPA}}, \qquad (5)$$

with

$$\begin{aligned} \mathcal{H}_{jk}^{(0)} &= 2\delta_{jk} \left(e_j + \frac{G}{\langle 1-N_j\rangle} \sum_{j'} \langle P_j^+ P_{j'}\rangle \right) \qquad (6)\\ &- G \frac{\langle (1-N_j)(1-N_k)\rangle}{\sqrt{|\langle 1-N_j\rangle\langle 1-N_k\rangle|}}. \end{aligned}$$

To find the correlation functions of the form $\langle(1-N_j)(1-N_k)\rangle$, we use the following approximation.

When $j \neq k$, we apply a simple factorization procedure, which has turned out to be accurate in the zero temperature limit,

$$\langle (1-N_j)(1-N_k)\rangle = \langle 1-N_j\rangle\langle 1-N_k\rangle, \qquad (7a)$$

but when $j = k$, we use the exact relation

$$\langle (1-N_j)^2\rangle = \langle 1-N_j\rangle + 2\langle P_j^+ P_j\rangle. \qquad (7b)$$

With this ansatz, a particle–particle RPA-like equation is obtained in the form

$$\begin{aligned} G_{ji}^{\mathrm{SCRPA}} &= \delta_{ji} \frac{1}{z-C_j} - \frac{G\sqrt{|D_j D_i|}}{(z-C_j)(z-C_i)} \qquad (8)\\ &\times \left[1 + G \sum_k \frac{D_k}{z-C_k} \right]^{-1}, \end{aligned}$$

where

$$z = i\omega_n, \qquad D_i = \langle 1 - N_i \rangle,$$

and

$$C_j = 2\left(e_j - Gn_j + \frac{G}{D_j} \sum_{j' \neq j} \langle P_j^+ P_{j'} \rangle \right).$$

From the above expression, one can easily find the excitation spectrum of the model by equating the denominator of (8) to zero:

$$1 + G \sum_k \frac{D_k}{z - C_k} = 0. \tag{9}$$

Knowing the poles of the GF (8), one can write down its spectral representation (we give it here as a function of imaginary time) with the corresponding residua.

In order to close the set of the SCRPA equations, it is necessary to find the so far unknown occupation numbers $n_k = \langle c_k^+ c_k \rangle$. They can be found from the single-particle Matsubara GF

$$G_{kk'}^{\tau} = \langle T_\tau a_k(\tau) a_{k'}^+(0) \rangle$$

as

$$n_k = \langle a_k^+ a_k \rangle = \lim_{\tau \to 0^-} G_k^{\tau}. \tag{10}$$

In general, the single-particle Matsubara GF $G_k^{\tau - \tau'}$ obeys the Dyson equation

$$\left(-\frac{\partial}{\partial \tau} + \varepsilon_k \right) G_{kk'}^{\tau} = \delta(\tau) + \int d\tau_1 M_k^{\tau - \tau_1} G_k^{\tau_1}. \tag{11}$$

In the frequency representation, we have

$$G_k^{\omega_n} = G_k^0 + G_k^0 M_k G_k^{\omega_n}, \tag{12}$$

where

$$G_k^0 = \frac{1}{i\omega_n - \varepsilon_k}. \tag{13}$$

Here, ε_k already contains the usual (instantaneous) mean field, so that M_k denotes only the dynamical part of the mass operator.

The problem is to find an approximation for the mass operator M_k consistent with the SCRPA. An appropriate approximation for the G_k^{τ} can be obtained if we remember that the single-particle mass operator M_k has in general an exact representation in terms of the two-body T matrix [10]. The needed approximation will be in calculation of the mass operator $\widetilde{M_k}$ through the T matrix found in the framework of SCRPA. As the relation between the T matrix and the sum of all irreducible Feynman graphs in the *pp* channel is also known, then the following expression for the single-particle mass operator can be obtained [2]:

$$\widetilde{M_k} = G \sum_{k_1 k_2} G_{\bar{k}}^{0(\tau_1' - \tau_1)} G_{k_1 k_2}^{(\tau_1' - \tau_1)} \widetilde{\mathcal{H}}_{k_2 k}^{(0)}. \tag{14}$$

The operator $\widetilde{\mathcal{H}}_{k_2 k}^{(0)}$ is expressed through the effective Hamiltonian (6) without the disconnected part:

$$\widetilde{\mathcal{H}}_{kk'}^{(0)} = \mathcal{H}_{kk'}^{(0)} - 2\delta_{kk'}\varepsilon_k, \tag{15}$$

where

$$\varepsilon_k = e_k - Gf_k, \qquad f_k = \frac{1}{1 + e^{\varepsilon_k \beta}}.$$

The system of SCRPA equations is fully closed now and represents a self-consistent problem for pair fluctuations.

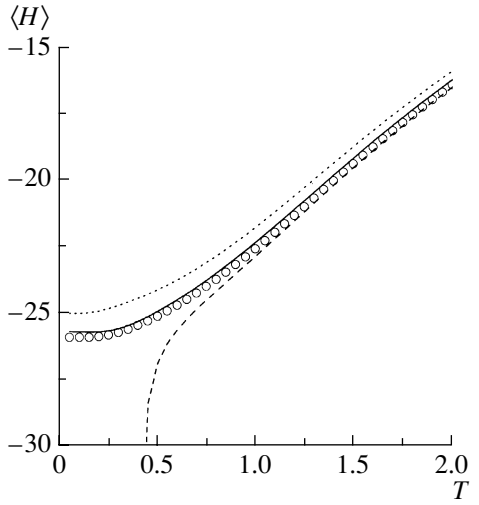

Fig. 1. The average energy $\langle H \rangle$ as a function of the temperature for $\Omega = N = 10$ and $G = 0.4$. The exact results (open circles), the TMFA results (dotted curve), the TRPA results (dashed curve), and the TSCRPA results (solid curve). Values $\langle H \rangle$ and T are given in units of ε.

4. RESULTS AND DISCUSSION

The numerical calculations are performed for the system with $N = 10$ particles distributed among $\Omega = 10$ levels. We compare the SCRPA results with the exact ones for the grand canonical ensemble as well as with the results of the standard TRPA and thermal mean-field approximation (TMFA).

Let us consider the behavior of the system near the phase-transition point. To make distinctions between different results more apparent, we not only show the full intrinsic energy $\langle H \rangle$ but also the correlation energy E_{corr}, which is defined as $E_{\mathrm{corr}} = \langle H \rangle - \langle H \rangle_0$,

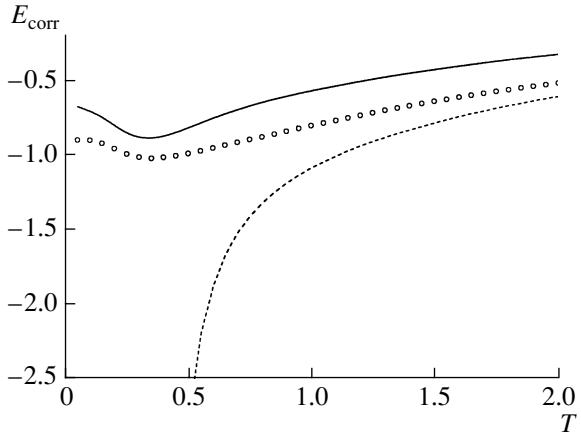

Fig. 2. The correlation energy E_{corr} as a function of the temperature for $\Omega = N = 10$ and $G = 0.4$. For notation, see Fig. 1. Values E_{corr} and T are given in units of ε.

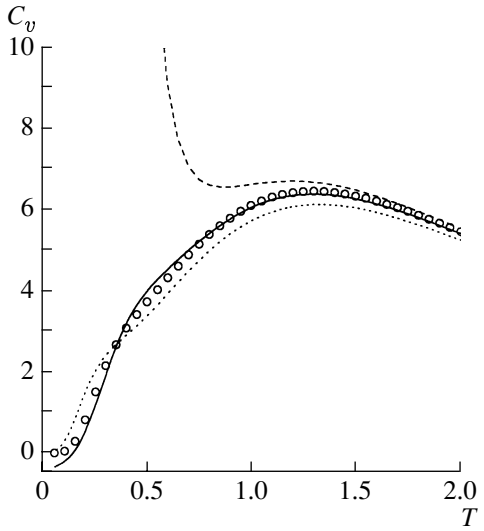

Fig. 3. The heat capacity C_v (dimensionless) as a function of T (in units of ε) for $\Omega = N = 10$ and $G = 0.4$. For notation, see Fig. 1.

where $\langle H\rangle_0$ is the average energy calculated in the TMFA.

In Figs. 1 and 2, the average energy $\langle H\rangle$ and correlation energy E_{corr} as functions of T are displayed for the interaction constant $G = 0.4$ (at $T = 0$, this value of G is larger than the critical value $G_{\mathrm{cr}} \simeq 0.33$). With increasing T, the mean-field rearrangement occurs and the system goes from the superfluid phase to the normal one at $T_{\mathrm{cr}} \simeq 0.38$. Note that, within the TRPA, the lowest excitation energy ω_1 vanishes when $T \to T_{\mathrm{cr}}$, whereas within the TSCRPA ω_1 stays finite. For both the correlation energy and the intrinsic energy, the TSCRPA gives more precise results as compared to the other approximations. It is remarkable that the TSCRPA results are accurate down to practical zero temperature, in spite of the fact that, within the standard BCS theory, one enters the superfluid regime. A quasiparticle formulation of SCRPA [11] will only be necessary for stronger G values driving the system more deeply into the symmetry-broken phase.

To analyze the region near the phase-transition point in more detail, the heat capacity is calculated as a partial derivative of the intrinsic energy with respect to T: $C_v = \partial\langle H\rangle/\partial T$. The results are shown in Fig. 3. The TRPA and TMFA give discontinuities of C_v at T_{cr} (we recall again that our results are obtained using a normal fluid approach and not transforming to quasiparticles). The heat capacity calculated in the TSCRPA has some kink near T_{cr}, but has no discontinuities and is quite similar to the exact result throughout the whole range of temperature.

Nevertheless, the TSCRPA and also the exact solution feel the phase transition to the superfluid phase. This can be seen in Fig. 2, where both the TSCRPA and the exact correlation energies show a depression near $T = 0.38$. This originates from strong pair fluctuations leading to the BCS phase transition in TMFA with the critical temperature $T_{\mathrm{cr}}^{\mathrm{BCS}} = 0.38$ for $G = 0.4$. However, one notices that the sharp phase transition of the mean field is in reality completely smeared out and only a faint, though clearly visible, signal survives.

5. CONCLUSION

In this work, we generalized the recent work [4] on the multilevel pairing model (PFM) within the SCRPA approach to finite temperature (TSCRPA). In our context, the SCRPA can be viewed as a self-consistent mean-field theory for pair fluctuations. Our comparison is done for the case of ten levels with ten particles, where it is still relatively easy to establish the exact partition function. We base our studies on the Matsubara one- and two-particle Green's functions, which allows us to calculate correlation and excitation energies, specific heat, level densities, etc. The quality of our results for the above-mentioned quantities turns out to be very good and it does not fail in any qualitative or quantitative aspect. Most of the time, the agreement with the exact solution is within a couple of percent.

In the present studies, we restricted ourselves to values of the coupling which are below or slightly above the critical value. In the future, we shall elaborate on the SCRPA for quasiparticles at finite T (TSCQRPA), which should allow us to consider the system deeply in the superfluid phase and to study the transition from one phase to the other in more detail.

REFERENCES

1. P. Ring and J. Egido, J. Phys. G **19**, 1 (1993); P. Schuck and S. Ayik, Nucl. Phys. A **687**, 230c (2001).
2. J. Dukelsky and P. Schuck, Phys. Lett. B **464**, 164 (1999); J. Dukelsky, G. Röpke, and P. Schuck, Nucl. Phys. A **628**, 17 (1998).
3. Ken-ji Hara, Prog. Theor. Phys. **32**, 88 (1964); D. J. Rowe, Phys. Rev. **175**, 1283 (1968); Rev. Mod. Phys. **40**, 153 (1968).
4. J. G. Hirsch, A. Mariano, J. Dukelsky, and P. Schuck, Ann. Phys. (N.Y.) **296**, 187 (2002).
5. A. I. Vdovin, D. S. Kosov, and W. Nawrocka, Theor. Math. Phys. **111**, 613 (1997); A. I. Vdovin and A. N. Storozhenko, Eur. Phys. J. A **5**, 263 (1999); Yad. Fiz. **64**, 1144 (2001) [Phys. At. Nucl. **64**, 1069 (2001)].
6. R. W. Richardson and N. Sherman, Nucl. Phys. A **52**, 221 (1964).
7. J. von Delft and D. C. Ralph, Phys. Rep. **345**, 61 (2001).
8. J. von Delft, Ann. Phys. (Leipzig) **10**, 219 (2001).
9. A. L. Fetter and J. D. Walecka, *Quantum Theory of Many-Particle Systems* (McGraw-Hill, New York, 1971).
10. A. B. Migdal, *Theory of Finite Fermi Systems and Application to Atomic Nuclei* (Intersci., New York, 1967).
11. A. Rabhi, R. Bennaceur, G. Chanfray, and P. Schuck, nucl-th/0208037.

Physics of Atomic Nuclei, Vol. 67, No. 10, 2004, pp. 1786–1793. From Yadernaya Fizika, Vol. 67, No. 10, 2004, pp. 1814–1821.

Proceedings of the International Conference "Nuclear Structure and Related Topics"

Double-Beta Decay and Neutrino Mass*

S. Stoica**

Department of Theoretical Physics,
Horia Hulubei National Institute for Physics and Nuclear Engineering, Bucharest, Romania

Received January 21, 2004

Abstract—Recent achievements in the study of double-beta ($\beta\beta$) decay are presented. We discuss the potential of this process to search, beyond Standard Model physics, for the QRPA-based methods used for the calculation of the relevant nuclear matrix elements and the derivation of the neutrino mass from both $\beta\beta$-decay calculations and neutrino oscillation and cosmological data. The key position of the $\beta\beta$-decay experiments in resolving the neutrino absolute mass is highlighted. © *2004 MAIK "Nauka/Interperiodica".*

1. INTRODUCTION

Nuclear double-beta decay is a natural decay of an even–even nucleus which transforms into another even–even nucleus keeping its total mass but modifying its charge by two units. This process occurs whenever single-beta decay cannot occur due to energy-conservation reasons, or if it is highly forbidden by angular-momentum selection rules. The $\beta\beta$-decay process by which a nucleus increases its charge by two units is the most accessible experimentally (and thus the most studied) due to larger $Q_{\beta\beta}$ values, and in this paper we will refer only to this process. Usually one speaks of the following decay modes:

$$\text{(a)}\quad (A,Z)\to(A,Z+2)+2e^-+2\bar{\nu},$$
$$\text{(b)}\quad (A,Z)\to(A,Z+2)+2e^-,$$
$$\text{(c)}\quad (A,Z)\to(A,Z+2)+2e^-+\chi.$$

The first process, called the $2\nu\beta\beta$-decay mode, is allowed within the Standard Model (SM), while the other two are only predicted within beyond SM theories which allow for lepton-number violation. The second process is called the neutrinoless double-beta ($0\nu\beta\beta$) decay mode, where one finds only two electrons in the final states, whereas the process (c) is another neutrinoless decay mode but with the emission of a particle called Majoron besides the two electrons.

It was demonstrated [1] that the occurrence of (b) implies that the neutrino is a Majorana particle with a nonzero mass. This is why the impact of eventual experimental evidence of the $0\nu\beta\beta$-decay mode will be crucial for understanding some of the neutrino properties. The developments in the field of $\beta\beta$ decay are well presented in several reviews [2–7].

After the first experimental evidence of the $2\nu\beta\beta$ decay [8], there has been a continuous effort to refine the theoretical calculations in order to get agreement with the experimental half-lives. Since the calculation of the phase-space factors entering the $\beta\beta$-decay half-lives causes no special problems, the nuclear matrix elements (NME) were considered the main source of errors. So, the nuclear structure methods used for their computation tried to adjust the model parameters in order to predict accurately other $2\nu\beta\beta$-decay half-lives. Agreement was obtained in the framework of the *pn*QRPA-type methods [9–16]. In parallel, there has been continuous progress of the $\beta\beta$-decay experiments in the attempt to get evidence for the $0\nu\beta\beta$-decay mode. The knowledge of the NME and phase factors, on one hand, and of experimental lower limits for the $0\nu\beta\beta$-decay half-lives, on the other hand, allows us to extract upper limits for the neutrino mass.

On the other hand, other scenarios for the occurrence of the $0\nu\beta\beta$-decay mode (than the usual decay mode by exchange of Majorana neutrinos between two nucleons inside the nucleus) may be considered. These reveal the broader potential of the $\beta\beta$-decay process to search beyond SM physics [17–19]. Recently, other neutrino-related experiments produced essential results in understanding the neutrino properties. Neutrino-oscillation experiments confirmed today that at least one flavor of neutrinos has nonzero mass. In addition, cosmological data coming from measurements of cosmic microwaves background provided us with very stringent limits for the neutrino masses. Making use of these data and of the knowledge of the NME, one can get information about the observability of the $0\nu\beta\beta$-decay mode. This

*This article was submitted by the author in English.

** e-mail: stoica@ifin.nipne.ro

is at present a crucial point, since only $\beta\beta$-decay experiments will be able in the near future to give us information about the absolute mass of the neutrino and about its nature: Dirac or Majorana? This places the $\beta\beta$-decay experiments in a key position among other experiments to resolve some of the neutrino properties.

The paper will be organized as follows. In Section 2, we discuss the broader potential of the $\beta\beta$ decay to search beyond SM physics, and Section 3 is devoted to the nuclear structure methods used to calculate the NME relevant for $\beta\beta$ decay. In Section 4, we refer to the neutrino-mass problem in connection with $\beta\beta$-decay and other ν-related experiments. Finally, in Section 5, we end up with some conclusions and perspectives on the field.

2. CONNECTIONS TO THEORIES BEYOND THE STANDARD MODEL

The occurrence of $0\nu\beta\beta$ decay by exchange of Majorana neutrinos is the most usual scenario. Even in this scenario, in the expression of the $0\nu\beta\beta$-decay half-lives, there are also contributions coming from RH components in the weak interaction. Combined studies of $0\nu\beta\beta$ decay to excited states and of $\beta^+\beta^+$-decay modes may provide us with information about the possible existence of such currents in the weak interaction. This extends the potential of $\beta\beta$ decay to check, besides neutrino properties, other physics beyond the SM. In addition, within other GUTs, where lepton-number violation is allowed, one can imagine alternative $0\nu\beta\beta$-decay mechanisms. In this way, the study of nuclear $\beta\beta$ decay may provide us with information about the correctness of various GUT hypotheses and set upper limits on the coupling constants and the masses of various exotic particles.

Within $L-R$ theories, $0\nu\beta\beta$ decay may be mediated by RH W bosons, and the absence of such a decay mode gives us lower limits for the mass of these bosons [20, 21].

In SUSY theories with R-parity violation ($R = (-1)^{3B+L+2S}$, B is baryon number, L is lepton number, and S is spin of a particle; $R = 1$ for particles and $R = -1$ for their superpartners), $0\nu\beta\beta$ decay appears via exchange of heavy supersymmetric particles such as squarks, gluinos, and neutralinos. Since the conservation of R parity is made on an ad hoc basis, the nonobservability of this decay mode can be used for restricting R-parity-violating SUSY models [17].

In some GUTs, new bosons, called Majorons, can play a significant role in cosmology, stellar evolution, supernovas, etc. They are associated with the spontaneous breaking of a global $B-L$ symmetry and can couple to the neutrinos, giving a contribution to the $0\nu\beta\beta$ decay [18]. The half-lives contain the neutrino–Majoron coupling constant, and the nonobservability of such a decay mode can put limits on this constant.

Leptoquarks, bosons carrying both lepton and baryon quantum numbers, which appear in some GUTs, can also mediate $0\nu\beta\beta$ decay, and one can put restrictions on their mass.

Compositeness, a possible substructure of quarks on a scale of $\sim$TeV, is another interesting hypothesis. $0\nu\beta\beta$ decay may be a possible low-energy manifestation of it, and the nonobservability of this decay mode gives us indications on the scale [19].

All these demonstrate the broader potential of nuclear $\beta\beta$ decay to search beyond SM physics than that related to the nature and mass of the neutrino. These are additional arguments for studying this process both theoretically and experimentally.

3. NUCLEAR STRUCTURE METHODS

In the theoretical estimations of the $\beta\beta$-decay half-lives, the evaluation of the involved NME plays an important role in extracting the neutrino mass. However, their calculation represents one source of uncertainty. This is because the nuclei undergoing such a decay are generally medium- and heavy-mass open-shell nuclei with a rather complicated nuclear structure. In addition, the sensitive part is connected to an accurate description of the intermediate odd–odd nuclei participating in the $\beta\beta$ decay, which is still more complicated.

Generally, there are two types of nuclear structure methods used in $\beta\beta$ decay: (i) QRPA- and (ii) shell-model-based methods. Shell-model-based methods are very attractive since they are more precise. Unfortunately, calculations of the NME with these methods remain unfeasible for the majority of nuclei undergoing $\beta\beta$ decay. Thus, there are few calculations performed with such methods [22].

The QRPA-based methods [9–16, 23–33] have been the most employed for computing NME for a wide class of nuclei.

The pnQRPA [9], a version of the usual QRPA but developed for the charge-exchange process, was the first method widely used for calculations of nuclear-charge-exchanging processes.

The phonon operators are defined as

$$\Gamma^{\dagger}_{1\mu}(k) = \sum_{l=(j_p,j_n)} \left[X^1_k(l) A^{\dagger}_{1\mu}(l) + Y^1_k(l) \tilde{A}_{1\mu}(l) \right]$$

such that

$$\Gamma_{1\mu}(k)|0\rangle_{i,f} = 0,$$

X and Y are the forward- and backward-going pnQRPA amplitudes, and k labels the positive solutions of the pnQRPA equations. The A, $A^\dagger$ are the bifermion quasiparticle operators coupled to angular momentum $J=1$ and projection μ,

$$A^\dagger_{1\mu}(l) = \sum_{m_p,m_n} C^{j_p j_n 1}_{m_p m_n \mu} a^\dagger_{j_p m_p} a^\dagger_{j_n m_n};$$

$$\tilde{A}_{1\mu} = (-1)^{1-\mu} A_{1,-\mu}.$$

In the quasiboson approximation (QBA), the operators $A^\dagger$, A as well as the phonon operators $\Gamma^\dagger$, Γ fulfill the boson-type commutator relations.

In the formalism, we also need the bifermion density-type operators

$$B^\dagger_{1\mu}(l) = \sum_{m_p,m_n} C^{j_p j_n J}_{m_p -m_n \mu} a^\dagger_{j_p m_p} a_{j_n m_n} (-1)^{j_n - m_n};$$

$$\tilde{B}_{1\mu}(l) = (-1)^{1-\mu} B_{1\mu}(l).$$

Using the equation-of-motion method, one can derive the pnQRPA equations, which may be written in the matrix representation as follows:

$$\begin{pmatrix} \mathcal{A} & \mathcal{B} \\ \mathcal{B} & \mathcal{A} \end{pmatrix}_{J^\pi} \begin{pmatrix} X^m \\ Y^m \end{pmatrix} = \Omega^m_{J^\pi} \begin{pmatrix} \mathcal{U} & 0 \\ 0 & -\mathcal{U} \end{pmatrix}_{J^\pi} \begin{pmatrix} X^m \\ Y^m \end{pmatrix}. \quad (1)$$

Solving this equation, one gets the X and Y amplitudes as well as the pnQRPA energies $\Omega^m_{J^\pi}$.

Further, in the particle representation, the transition operators of interest $\beta^\pm$ are defined as follows:

$$\beta^-_\mu(l) = \sum_{m_p m_n} \langle j_p m_p | \sigma_\mu | j_n m_n \rangle c^\dagger_{j_p m_p} c_{j_n m_n};$$

$$\beta^+_\mu(l) = (-1)^\mu \left(\beta^-_{-\mu}(l)\right)^\dagger,$$

where σ_μ denotes the μth spherical component of the Pauli spin operator. Their expressions in the quasiparticle representation read [6]

$$\beta^-_\mu(l) = \theta_l A^\dagger_{1\mu}(l) + \bar{\theta}_l \tilde{A}_{1\mu}(l) + \eta_l B^\dagger_{1\mu}(l) + \bar{\eta}_l \tilde{B}_{1\mu}(l),$$

$$\beta^+_\mu(l) = -(\bar{\theta}_l A^\dagger_{1\mu}(l) + \theta_l \tilde{A}_{1\mu}(l) + \bar{\eta}_l B^\dagger_{1\mu}(l) + \eta_l \tilde{B}_{1\mu}(l)),$$

where the following notation is used:

$$\theta_l = \frac{\hat{j}_p}{\sqrt{3}} \langle j_p || \sigma || j_n \rangle U_p V_n;$$

$$\bar{\theta}_l = \frac{\hat{j}_p}{\sqrt{3}} \langle j_p || \sigma || j_n \rangle U_n V_p; \quad \hat{j} = \sqrt{2j+1};$$

$$\eta_l = \frac{\hat{j}_p}{\sqrt{3}} \langle j_p || \sigma || j_n \rangle U_p U_n;$$

$$\bar{\eta}_l = \frac{\hat{j}_p}{\sqrt{3}} \langle j_p || \sigma || j_n \rangle V_p V_n.$$

The NME relevant for the $2\nu\beta\beta$-decay mode within pnQRPA has the expression

$$M^{2\nu}_{\mathrm{GT}} = \sum_{l,k} \frac{\langle 0^+_f || \sigma\tau^- || 1^+_k \rangle \langle 1^+_k | 1^+_l \rangle \langle 1^+_k || \sigma\tau^- || 0^+_i \rangle}{E_l + Q_{\beta\beta}/2 + m_e - E_0},$$

where the $|0^+_{i,f}\rangle$ are the ground states of the initial and final nuclei participating in the $\beta\beta$ decay, $|1^+_{k,l}\rangle$ and E_l are the intermediate states and their energies generated by two different pnQRPA procedures applied to the parent and the daughter nuclei, and E_0 is the initial ground-state energy.

The success of the pnQRPA method in explaining the suppression mechanism of the $2\nu\beta\beta$-decay matrix elements (ME) was achieved later on, by the inclusion of the particle–particle correlations [11–15]. However, this inclusion leads to a strong sensitivity of these NME related to the particle–particle component of the pn residual interaction. Namely, the $2\nu\beta\beta$-decay ME as functions of the particle–particle interaction strength (usually denoted by g_{pp}) decrease rapidly and change sign, within a very narrow interval of values of g_{pp}, and this causes difficulties for fixing this parameter adequately.

Trying to overcome this drawback, several improvements of this method have been proposed during the last decade: the appropriate treatment of the particle-number nonconservation [24], the inclusion of the pn pairing [29, 30], the double-commutator method [25], etc. However, more successful have been the extensions of the pnQRPA beyond the QBA developed in [23, 27, 31, 32]. Their main achievement is that the ME become more stable against g_{pp} and the instability of the pnQRPA is shifted towards the region of unphysical values of this parameter.

The first method including higher order corrections to pnQRPA was developed in [23, 26]. In this approach, the pnQRPA phonon operator and the transition $\beta^\pm$ operators were expressed as boson expansions of appropriate pair operators and the next order terms from these series beyond the QBA were retained:

$$A^\dagger_{1\mu}(pn) = \sum_k (A^{(1,0)}_{k_1} \Gamma^\dagger_{1\mu}(k) + A^{(0,1)}_{k_1} \tilde{\Gamma}^+_{1\mu}(k)), \quad (2)$$

$$B^\dagger_{1\mu}(pn) = \sum_{k_1 k_2} (B^{(2,0)}_{k_1 k_2}(pn) [\Gamma^\dagger_1(k_1) \Gamma^\dagger_2(k_2)]_{1\mu} + B^{(0,2)}_{k_1 k_2}(pn) [\Gamma_1(k_1) \Gamma_2(k_2)]_{1\mu}), \quad (3)$$

where

$$\Gamma^\dagger_{2\mu}(k')$$

$$= \sum_{l'=(j_p,j'_p;j_n,j'_n)} [X^2_{k'}(l')A^\dagger_{2\mu}(l') + Y^2_{k'}(l')\tilde{A}_{2\mu}(l')].$$

Retaining in the above series up to two-phonon states, we obtained the version of this method called SQRPA.

The boson expansion coefficients $A^{(1,0)}$, $A^{(1,0)}$, $B^{(2,0)}$, $B^{(0,2)}$ were determined, so that Eqs. (2), (3) are also valid for the corresponding ME in the boson basis.

Then, SQRPA was employed, with some extensions, for both $2\nu\beta\beta$ and $0\nu\beta\beta$ decays, for a wide class of isotopes of nuclei, as well as for transitions to excited states in [26–28].

An alternative approach for extending pnQRPA is based on the idea of partial restoration of the Pauli exclusion principle by taking into account the next terms in the commutator of the like-nucleon operators involved in the derivation of the QRPA equations,

$$[A_{\mu\nu}(k,l,J,M), A^\dagger_{\mu'\nu'}(k',l',J,M)] \qquad (4)$$
$$= \mathcal{N}(k\mu,l\nu)\mathcal{N}(k'\mu',l'\nu')(\delta_{\mu\mu'}\delta_{\nu\nu'}\delta_{kk'}\delta_{ll'} - \delta_{\mu\nu'}\delta_{\nu\mu'}\delta_{lk'}\delta_{kl'}(-1)^{j_k+j_l-J}).$$

Within the RQRPA method, the above commutator is calculated more precisely by adding in expression (4), besides the scalar term, the next terms which are just the proton and neutron number operators. The value of this commutator is replaced by its expectation values in the RPA ground state. Further, one observes that one can mimic the boson behavior of the A, $A^\dagger$ operators if one renormalizes them as follows [31, 32]:

$$\bar{A}_{\mu\mu'}(k,l,J,M) = D^{-1/2}_{\mu k\nu k' J^\pi}\, A_{\mu\mu'}(k,l,J,M),$$

where the $D_{\mu k\nu k'}$ matrices are defined as follows:

$$D_{\mu k\nu k' J^\pi} = \mathcal{N}(k\mu,l\nu)N(k'\mu',l'\nu')(\delta_{\mu\mu'}\delta_{\nu\nu'}\delta_{kk'}\delta_{ll'} - \delta_{\mu\nu'}\delta_{\nu\mu'}\delta_{lk'}\delta_{kl'}(-1)^{j_k+j_l-J}) \times [1 - j_l^{-1}\langle 0^+_{\rm RPA}|[a^\dagger_{\nu l}a_{\nu l'}]_{00}|0^+_{\rm RPA}\rangle - j_k^{-1}\langle 0^+_{\rm RPA}|[a^\dagger_{\mu k}a_{\mu k'}]_{00}|0{+}_{\rm RPA}\rangle].$$

By also renormalizing the QRPA amplitudes, the $\mathcal{A}$ and $\mathcal{B}$ matrices, and the QRPA phonon operator,

$$\bar{X}^m = D^{1/2}X^m; \quad \bar{Y}^m = D^{1/2}Y^m;$$
$$\bar{\mathcal{A}}^m = D^{-1/2}\mathcal{A}D^{-1/2}; \quad \bar{\mathcal{B}}^m = D^{-1/2}\mathcal{B}D^{-1/2};$$
$$\Gamma^{m\dagger}_{JM^\pi} = \sum_{k,l,\mu\le\mu'} [\bar{X}^m_{\mu\mu'}(k,l,J^\pi)\bar{A}^\dagger_{\mu\mu'}(k,l,J,M) + \bar{Y}^m_{\mu\mu'}(k,l,J^\pi)\tilde{\bar{A}}_{\mu\mu'}(k,l,J,M)],$$

one observes that the RQRPA equations have the same form as in the ordinary QRPA, but now the quantities of Eq. (1) are replaced by the renormalized ones.

To calculate $\bar{\mathcal{A}}$ and $\bar{\mathcal{B}}$, we need to determine the renormalization matrices D. This is done by solving numerically a system of nonlinear equations by an iterative procedure. As input values, one can use their expressions in which the averages of the number operators are replaced by the backward-going amplitudes obtained as initial solutions of the QRPA equation.

Before starting the QRPA procedure, we need the occupation amplitudes (u, v) and the quasiparticle energies in order to get the quasiparticle representation of the RPA operators. This is done by solving the HFB equations, in which one may include, in the general case, both like- and unlike-nucleon pairing interactions. When one includes only like-nucleon pairing in these equations, the QRPA procedure described above is called pnRQRPA [31, 32]. Later on this method was extended by the inclusion of both types of pairing interaction [33], and this version is called full-RQRPA.

However, one should note that the RQRPA-type methods face an undesirable drawback, namely, a significant degree of nonconservation of the Ikeda sum rule (ISR). Although refinements in the way of calculating the averages of the quasiparticle number operator were proposed [32], the result was a rather small reduction of the violation. Another challenging issue of this method is the dependence of the calculated NME on the size of the single-particle basis, especially for the neutrinoless mode.

Analyzing the calculations of the $\beta\beta$-decay ME existent in the literature, one still observes discrepancies between the values of the same ME, which may differ by up to a factor of three. On the other hand, it is difficult to compare results obtained with different versions of the QRPA-based methods and using different parameters and codes. In order to reduce such discrepancies and have an idea about the magnitude of the deviations between different calculations, we made a study of both two-neutrino and neutrinoless $\beta\beta$-decay NME for the experimentally interesting nuclei ^{82}Se, ^{96}Zr, ^{100}Mo, ^{116}Cd, ^{128,130}Te, and ^{136}Xe with the pnQRPA, pnRQRPA, full-RQRPA, and SQRPA methods [28]. For each method, two different single-particle bases are used in order to see the dependence of the results on the size of the Hilbert space. For a better comparison between the results, the calculations are performed for each method with the same set of parameters regarding all steps of the QRPA codes (the construction of the single-particle basis and of the BCS and QRPA wave functions, as well as the renormalization of the G-matrix elements).

Table 1. The neutrinoless NME and upper limits for the neutrino mass parameter calculated in this paper with *pn*QRPA, *pn*RQRPA, full-RQRPA, and SQRPA methods using the experimental limits given in Table 2 (the numbers in the first row of each nucleus are the NME, while the numbers in the second row are the neutrino mass parameters; the calculations are performed with the large basis or with the small one)

Nucleus	*pn*QRPA		*pn*RQRPA		Full-RQRPA		SQRPA	
	large	small	large	small	large	small	large	small
^{76}Ge	1.71	4.45	1.87	3.74	2.40	3.68	3.21	3.82
	0.84	0.33	0.79	0.40	0.62	0.41	0.46	0.39
^{82}Se	4.71	5.60	2.70	4.30	2.63	4.15	3.54	4.13
	6.75	5.67	11.71	7.38	12.04	7.64	8.96	7.68
^{96}Zr	2.75	4.16	2.72	3.01	2.42	2.99	2.12	2.70
	24.61	16.27	24.88	22.48	27.97	22.64	31.92	25.06
^{100}Mo	3.81	5.37	3.40	4.36	3.35	4.11	4.23	4.51
	1.75	1.24	1.96	1.53	1.63	1.53	1.58	1.48
^{116}Cd	2.85	3.99	3.39	3.61	2.35	2.62	2.29	2.67
	3.13	2.24	2.63	2.47	3.80	3.41	3.90	3.34
^{128}Te	3.43	4.84	2.83	4.29	2.85	3.75	2.85	3.38
	1.31	0.94	1.60	1.05	1.59	1.21	1.58	1.34
^{130}Te	3.77	4.73	3.00	4.55	2.61	3.49	2.42	2.53
	2.81	2.24	3.54	2.33	4.07	3.04	4.39	4.19
^{136}Xe	1.35	1.69	1.02	1.57	0.89	0.99	0.98	1.03
	2.17	2.73	3.6	2.35	4.14	3.72	3.76	3.57

Table 1 presents the results obtained for the $0\nu\beta\beta$ NME for several isotopes, calculated with four QRPA-based methods and for the two basis sets, at values of g_{pp} fixed, for each method, as was explained previously. By inspection, one observes that, in all cases, the differences between the results obtained with the same method but with different basis are not so large around the physical values of g_{pp}. With a few exceptions, one would say that the uncertainty in the calculations of the neutrinoless ME performed with all these methods, coming from the use of different single-particle bases, is within a factor of two. The largest discrepancies between the results occur for *pn*QRPA and RQRPA, and possible explanations for this may be related to the shortcomings of these methods which were already discussed previously. One also observes that the full-RQRPA and SQRPA values do not differ from each other by more that 50%. So, in the worst case, one may have confidence in the calculated NME for the $0\nu\beta\beta$-decay mode within a factor two, but, having in view that the SQRPA displays both a better stability against the change of the basis and a good fulfillment of the ISR, we may reduce the uncertainties in the predictions of these NME within QRPA-based methods (due to the uncertainties discussed above) to about 50%.

4. NEUTRINO MASS

Until recently, the most stringent limits for the neutrino mass were extracted from $\beta\beta$-decay calculations under the following procedure: the $0\nu\beta\beta$-decay half-lives are written in the usual factorized form (see, for instance, [6]):

$$\left[T^{0\nu}_{1/2}\right]^{-1} = C_{mm}\left(\frac{\langle m_\nu\rangle}{m_e}\right)^2 + C_{\lambda\lambda}\lambda^2 \qquad (5)$$
$$+ C_{\eta\eta}\eta^2 + C_{m\lambda}\frac{\langle m_\nu\rangle}{m_e}\lambda + C_{m\eta}\frac{\langle m_\nu\rangle}{m_e}\eta + C_{\lambda\eta}\lambda\eta,$$

where $\langle m_\nu\rangle$ is the effective neutrino mass and λ and η are parameters related to the possible existence of RH currents in the weak interaction. A value

$$\langle m_\nu\rangle = \sum_i |U_{ei}|^2 e^{\alpha_i} m_i$$

is an average over the neutrino mass eigenstates m_i and U_{ei} is the neutrino mixing matrix. The coefficients

Table 2. The integrated phase-space factors $F_1^{2\nu}$ and $F_1^{0\nu}$ [25], the recent experimental $2\nu\beta\beta$- and $0\nu\beta\beta$-decay half-lives, and the $0\nu\beta\beta$ half-lives estimated by the SQRPA for $m_\nu = 0.1$ eV (the experimental half-lives are taken from the references indicated in brackets)

Nucleus	$T^{2\nu}$, yr	$T^{0\nu}$, yr	$T^{0\nu}_{\mathrm{SQRPA}}$, yr
^{76}Ge	1.55×10^{21} [41]	$>1.9 \times 10^{25}$ [41]	$(2.83{-}4) \times 10^{26}$
^{82}Se	8.3×10^{19} [42]	$>9.5 \times 10^{21}$ [43]	$(5.6{-}7.6) \times 10^{25}$
^{96}Zr	2.1×10^{19} [42]	$>1.0 \times 10^{21}$ [42]	$(0.63{-}1.02) \times 10^{26}$
^{100}Mo	0.95×10^{19} [44]	$>5.2 \times 10^{22}$ [44]	$(1.14{-}1.29) \times 10^{25}$
^{116}Cd	2.6×10^{19} [45]	$>0.7 \times 10^{23}$ [45]	$(0.78{-}1.06) \times 10^{26}$
^{128}Te	7.7×10^{24} [46]	$>7.7 \times 10^{24}$ [46]	$(1.38{-}1.90) \times 10^{27}$
^{130}Te	2.6×10^{21} [47]	$>5.6 \times 10^{22}$ [47]	$(0.98{-}1.08) \times 10^{26}$
^{136}Xe	$>3.6 \times 10^{20}$ [48]	$>4.4 \times 10^{23}$ [48]	$(5.63{-}6.22) \times 10^{26}$

C_{ij} are products of phase space and combinations of NME. As an example, C_{mm} of the term giving the leading contribution to $0\nu\beta\beta$ by the mechanisms of exchange Majorana neutrinos between two nucleons inside the nucleus has the expression

$$C_{mm} = F_1^{0\nu}\left(M_{\mathrm{GT}}^{0\nu} - \left(\frac{g_V}{g_A}\right)^2 M_{\mathrm{F}}^{0\nu}\right)^2.$$

Here, $F_1^{0\nu}$ is the phase-space integral and $M_{\mathrm{GT}}^{0\nu}$ and $M_{\mathrm{F}}^{0\nu}$ are Gamow–Teller and Fermi NME. If one neglects the effects of RH weak currents (see, e.g., [4]), the only term that remains in (5) is the first one, and the corresponding (simplified) expression for the $0\nu\beta\beta$-decay half-life can be used to set limits on the neutrino mass. Once we calculated the NME for $0\nu\beta\beta$, we used the best presently available half-lives for this decay mode and deduced upper limits for the neutrino mass parameter. The results are presented in Table 1.

Alternatively, one can derive $\langle m_\nu \rangle$ from ν-related experiments and compare the obtained values with those from $\beta\beta$-decay calculations. In this way, one can make predictions on the observability of the $0\nu\beta\beta$-decay mode. Such a procedure became very frequently employed after the recent claim for positive evidence of the $0\nu\beta\beta$-decay mode observed in the Heidelberg–Moscow experiment [34].

Before doing this, we recall the main results reported recently by the neutrino oscillation experiments and from cosmological experiments.

From atmospheric ν-oscillation experiments, the recent results of Super-Kamiokande (SK) concerning the existence of an up–down asymmetry between muon events coming from the reactions [35]

$$\pi \to \mu + \nu_\mu, \quad \mu \to \nu_\mu + \nu_e$$

strengthen the previous results of the same experiment (1996–2000) in favor of ν oscillations in the channel $\mu \to \tau$. This result was confirmed by the K2K reactor experiment [36]. The best fit for the ν-oscillation parameters is found to be

$$\Delta m^2 \sim 2.6 \times 10^{-3}; \quad \sin^2(2\theta) \sim 1.0.$$

Also, solar neutrino experiments provide us with interesting results. The SNO experiment [37] has performed a careful analysis of solar neutrinos through the charge–charge, neutral–charge, and elastic-scattering neutrino reactions.

The results obtained confirmed the SK results [38], and a combined analysis of both experiments allows us to eliminate several possible scenarios of solar ν oscillations admitted so far. Moreover, the results from the KamLAND reactor experiment impose the LMA solution as the only valid one, finding the best fit parameters [39]

$$\Delta m^2 \sim 2.6 \times 10^{-5}; \quad \sin^2(2\theta) \sim 1.0.$$

Thus, there is now compelling evidence that at least one flavor of neutrinos has mass.

In parallel, there was impressive progress in cosmological data. Experiments aiming at measuring the cosmic microwave background (CMB) gave, by combining their data (WMAP, 2dFGRS, CMI, etc.), very stringent limits for neutrino masses, namely [40],

$$\sum_i m_i = 0.71 \text{ eV}.$$

To deduce the $\langle m_\nu \rangle$ from all these recent data, one proceeds as follows: (i) write the neutrino mixing matrix (U) in a convenient form; (ii) choose a hierarchy neutrino mass spectrum; (iii) make use of ν-oscillation data to fix as many parameters as possible from the U matrix; (iv) determine $\langle m_\nu \rangle$ as function of

the remaining parameters and determine the range of its values such that they fit the present data.

According to the present data, doing that one obtains the following lower limits of the $\langle m_\nu \rangle$:

(i) normal hierarchy ($m_1 \ll m_2 < m_3$):

$$\langle m_\nu \rangle > \text{several meV};$$

(ii) inverse hierarchy ($m_1 \gg m_2 \sim m_3$):

$$\langle m_\nu \rangle > \text{several tens of meV}.$$

Looking to these results and to the limits that future direct experiments propose to reach for $0\nu\beta\beta$-decay half-lives, one can conclude the following: single-beta-decay experiments (the most ambitious being KATRIN) will not be able to reach such sensibilities. However, the most ambitious $\beta\beta$-decay experiments will reach such values. These are exciting results for these experiments, which put them in a key position for determining the scale of the neutrino mass. In addition, such experiments are the only ones able to say something about the nature of neutrinos: Dirac or Majorana?

Now, with these lower and upper limits for $\langle m_\nu \rangle$ and using our calculated NME, we also estimated time scales for neutrinoless half-lives that experiments should reach to measure neutrino masses of about 0.1 eV. These results are presented in Table 2 together with the present limits reached by the corresponding experiments.

5. CONCLUSIONS

We reviewed the recent results obtained in $\beta\beta$-decay research in connection with the neutrino properties. First, we showed the broader potential of this process to provide us with information beyond SM physics. Then, we presented the QRPA-based methods and their extensions beyond the QBA, which are the most widely employed nuclear structure methods for the computation of the NME relevant for $\beta\beta$ decay. The error in calculation of the NME within these methods was estimated to be $\sim 50\%$. Further, using our calculated values for the NME, we derived upper limits for the neutrino masses from experimental $0\nu\beta\beta$-decay half-lives. Alternatively, using data from ν-related experiments (ν oscillations, cosmological data) and also using the calculated NME, one can predict lower and upper limits for the observability of $0\nu\beta\beta$-decay mode. It turns out that some planned future $\beta\beta$-decay experiments will be able to reach the range of these predictions. This places the $\beta\beta$-decay experiments in a key position among the other ν-related experiments in resolving some fundamental properties of the neutrino like its nature (Dirac or Majorana) and its absolute mass.

REFERENCES

1. S. M. Bilenky and S. T. Petcov, Rev. Mod. Phys. **59**, 671 (1987).
2. W. C. Haxton and G. J. Stephenson, Prog. Part. Nucl. Phys. **12**, 409 (1984).
3. M. Doi and T. Kotani, Prog. Theor. Phys. Suppl. **83**, 1 (1985).
4. K. Muto and H. V. Klapdor, *Neutrinos*, Ed. by H. V. Klapdor (Springer, Heidelberg, 1988), p. 183.
5. A. Faessler, Prog. Part. Nucl. Phys. **24**, 409 (1989).
6. J. Suhonen and O. Civitarese, Phys. Rep. **300**, 123 (1998).
7. V. Tretyak and Y. Zdesenko, At. Data Nucl. Data Tables **61**, 43 (1995); **80**, 83 (2002).
8. S. R. Elliot, A. A. Hann, and M. K. Moe, Phys. Rev. Lett. **59**, 2020 (1987).
9. J. A. Halbleib and R. A. Sorensen, Nucl. Phys. A **98**, 542 (1967).
10. H. V. Klapdor and K. Grotz, Phys. Lett. B **142B**, 323 (1984); K. Grotz and H. V. Klapdor, Phys. Lett. B **153B**, 1 (1985); Nucl. Phys. A **460**, 395 (1986).
11. P. Vogel and M. R. Zirnbauer, Phys. Rev. Lett. **57**, 3148 (1986).
12. T. Tomoda and A. Faessler, Phys. Lett. B **199**, 475 (1987).
13. J. Suhonen, A. Faessler, T. Taigel, and T. Tomoda, Phys. Lett. B **202**, 174 (1988).
14. K. Muto, E. Bender, and H. V. Klapdor, Z. Phys. A **334**, 177, 187 (1989).
15. A. Staudt, T. T. S. Kuo, and H. V. Klapdor-Kleingrothaus, Phys. Lett. B **242**, 17 (1990).
16. A. Staudt, K. Muto, and H. V. Klapdor-Kleingrothaus, Europhys. Lett. **13**, 31 (1990).
17. M. Hirsch, H. V. Klapdor-Kleingrothaus, and S. G. Kovalenko, Phys. Rev. Lett. **75**, 17 (1995).
18. G. B. Gelmini and M. Roncadelli, Phys. Lett. **99**, 411 (1981).
19. O. Panela, *Double-Beta Decay and Related Topics*, Ed. by S. Stoica and H. V. Klapdor-Kleingrothaus (World Sci., Singapore, 1996), p. 145.
20. R. N. Mohapatra, Phys. Rev. D **34**, 3457 (1986).
21. M. Doi and T. Kotani, Prog. Theor. Phys. **89**, 139 (1993).
22. E. Caurier, F. Nowacki, A. Poves, and J. Retamosa, Phys. Rev. Lett. **77**, 1954 (1996).
23. A. A. Raduta, A. Faessler, S. Stoica, and W. A. Kaminski, Phys. Lett. B **254**, 7 (1991).
24. O. Civitarese, A. Faessler, J. Suhonen, and X. R. Wu, Phys. Lett. B **251**, 333 (1990).
25. J. Suhonen, Nucl. Phys. A **563**, 205 (1993).
26. S. Stoica and W. A. Kaminski, Phys. Rev. C **47**, 867 (1993); S. Stoica, Phys. Rev. C **49**, 2240 (1994).
27. S. Stoica, Phys. Lett. B **350**, 152 (1995).
28. S. Stoica and H. V. Klapdor-Kleingrothaus, Nucl. Phys. A **694**, 769 (2001).
29. M. K. Cheoun *et al.*, Nucl. Phys. A **587**, 301 (1995).
30. G. Pantis, F. Simcovic, J. D. Vergados, and A. Faessler, Phys. Rev. C **53**, 695 (1996).
31. J. Toivanen and J. Suhonen, Phys. Rev. Lett. **75**, 410 (1995).

32. J. Schwieger, F. Simcovic, and A. Faessler, Nucl. Phys. A **600**, 179 (1996).
33. J. Schwieger, F. Simcovic, A. Faessler, and W. A. Kaminski, Phys. Rev. C **57**, 1738 (1998).
34. H. V. Klapdor-Kleingrothaus, A. Dietz, H. L. Harney, and I. V. Krivosheina, Mod. Phys. Lett. A **16**, 2409 (2001).
35. S. Fukuda *et al.* (Super-Kamiokande Collab.), Phys. Rev. Lett. **86**, 5651 (2001).
36. M. H. Ahn *et al.* (K2K Collab.), hep-ex/0212007.
37. Q. R. Ahmad *et al.* (SNO Collab.), Phys. Rev. Lett. **89**, 011302 (2002).
38. S. Fukuda *et al.* (Super-Kamiokande Collab.), Phys. Lett. B **539**, 179 (2002).
39. K. Eguchi *et al.*, hep-ex/0212021.
40. C. L. Bennet *et al.*, astro-ph/0302207.
41. H. V. Klapdor-Kleingrothaus, *60 Years of Double-Beta Decay—From Nuclear Physics to Beyond the Standard Model* (World Sci., Singapore, 2001); A. Dietz, Diploma Thesis (MPI, Heidelberg, 2000).
42. R. Arnold *et al.*, Nucl. Phys. A **636**, 209 (1998); **658**, 299 (1999).
43. A. S. Barabash, Nucl. Phys. A **629**, 517c (1998).
44. D. Dassie *et al.*, Phys. Rev. D **51**, 2090 (1995).
45. F. A. Danevich *et al.*, nucl-ex/0003001.
46. T. Bernatowicz *et al.*, Phys. Rev. Lett. **69**, 2341 (1992); Phys. Rev. C **47**, 806 (1993).
47. A. Alessandrello *et al.*, Nucl. Phys. B (Proc. Suppl.) **35**, 366 (1994); Phys. Lett. B **433**, 156 (1998).
48. R. Luescher, Nucl. Phys. B (Proc. Suppl.) **66**, 195 (1998).

Physics of Atomic Nuclei, Vol. 67, No. 10, 2004, pp. 1794–1798. From Yadernaya Fizika, Vol. 67, No. 10, 2004, pp. 1822–1826.

Proceedings of the International Conference "Nuclear Structure and Related Topics"

Weak Isoscalar Response of ^{11}B*

T. Kawabata[1)], H. Akimune[2)], H. Fujimura[3)], H. Fujita[3)], Y. Fujita[4)], M. Fujiwara[3)], K. Hara[3)], K. Y. Hara[2)], K. Hatanaka[3)], T. Ishikawa[5)], M. Itoh[3)], J. Kamiya[3)], M. Nakamura[5)], H. Sakaguchi[5)], Y. Shimbara[3)], H. Takeda[5)], A. Tamii[3)], T. Noro[6)], H. Toyokawa[7)], M. Uchida[3)], T. Wakasa[6)], Y. Yasuda[5)], H. P. Yoshida[3)], and M. Yosoi[5)]**

Received January 21, 2004

Abstract—Weak-interaction responses of ^{11}B were studied by measuring the ^{11}B(^{3}He, t) and ^{11}B(p, p') reactions. Obtained nuclear transition matrix elements B(GT), $B(\sigma\tau)$, and $B(\sigma)$ were compared with the shell-model calculations. The shell-model calculations, which explained the isovector parts B(GT) and $B(\sigma\tau)$ reasonably well if the quenching factors of 0.5–0.7 were taken into account, did not describe the isoscalar part $B(\sigma)$. © *2004 MAIK "Nauka/Interperiodica".*

1. INTRODUCTION

The properties of neutrinos and neutrino-induced phenomena play an important role in nuclear physics, astrophysics, and cosmology, as well as in particle physics. For example, the solar-neutrino problem was a long-standing unsolved problem for modern physics. This problem is now explained in terms of the solar-neutrino oscillation, which has been recently concluded from an analysis combining KAMIOKA and SNO results [1]. However, in order to understand the neutrino-oscillation mechanism at deeper levels, it is still important to continue the precise measurement of solar neutrinos.

Raghavan *et al.* [2] pointed out that the ^{11}B isotope can be used as a detector to investigate the solar-neutrino problem. High-energy neutrinos from the β decays of ^{8}B yielded in the proton–proton fusion chain in the Sun excite low-lying states in ^{11}B and ^{11}C by $M1$ and Gamow–Teller (GT) transitions via the neutral-current (NC) and charged-current (CC) processes as seen in Fig. 1. Such neutrinos are detected by measuring emitted electrons from the CC reactions and γ rays from the deexcitations of the low-lying states. Since there is a mirror-symmetrical relation between ^{11}B and ^{11}C and both the NC and the CC reactions can be measured in the same experimental setup, the systematic uncertainty for the strength ratio of the electron–neutrino flux to the entire neutrino flux from the Sun is expected to be small. It should be noted that a precise measurement of the relative strength is indispensable to tackle the solar-neutrino problem.

Since there is one excess neutron in the ^{11}B nucleus, the low-lying states in ^{11}B are excited by both the isovector and the isoscalar transitions. Therefore, both the isoscalar and the isovector responses are needed for estimating the ^{11}B(ν, ν') cross section. The cross sections of hadronic reactions provide

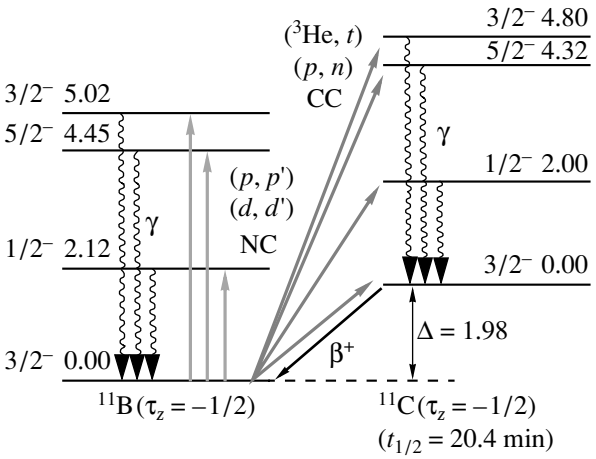

Fig. 1. Level scheme for the low-lying states in ^{11}B and ^{11}C (the energies are in MeV).

*This article was submitted by the authors in English.

[1)]Center for Nuclear Study, Graduate School of Science, University of Tokyo, Tokyo, Japan.
[2)]Department of Physics, Konan University, Kobe, Japan.
[3)]Research Center for Nuclear Physics, Osaka University, Osaka, Japan.
[4)]Department of Physics, Osaka University, Osaka, Japan.
[5)]Department of Physics, Kyoto University, Kyoto, Japan.
[6)]Department of Physics, Kyushu University, Fukuoka, Japan.
[7)]Japan Synchrotron Radiation Research Institute, Sayo, Japan.
**e-mail: kawabata@cns.s.u-tokyo.ac.jp

a good measure for the weak-interaction response since the relevant operators in the hadronic reactions are identical with those in the β-decay and neutrino-capture processes. The cross section for the (^{3}He, t) reaction can be written in terms of the GT operator $\sigma\tau_-$. On the other hand, the cross section for (p, p') can be described by a coherent sum of the isoscalar (σ) and isovector ($\sigma\tau_z$) $M1$ operators. It is, therefore, possible to obtain both the isoscalar and the isovector response by comparing the (^{3}He, t) and (p, p') cross sections.

In this article, we will report our recent results on the weak-interaction response of ^{11}B studied via the ^{11}B(^{3}He, t) and ^{11}B(p, p') reactions.

2. EXPERIMENT AND RESULTS

The experiment was performed at the Research Center for Nuclear Physics, Osaka University, using 450-MeV ^{3}He and 392-MeV proton beams. The proton and ^{3}He beams extracted from the ring cyclotron were achromatically transported to the target. The beam intensity on target was in the range of 1–10 enA. Scattered protons and tritons were momentum analyzed by the high-resolution spectrometer Grand Raiden [3]. Trajectories of the scattered protons and tritons were determined using a focal-plane detector system consisting of two multiwire drift chambers and plastic scintillation detectors. In case of the (p, p') reaction, a focal plane polarimeter (FPP) was also used to measure the polarization of protons scattered from the ^{11}B target. The FPP consisted of an analyzer target of a 12-cm-thick carbon slab, four multiwire proportional chambers, and scintillator hodoscopes [4]. An energy resolution of 300 keV full width at half maximum (FWHM) was obtained in the ^{11}B(^{3}He, t) measurement. Since the magnetic spectrometer was operated near the maximum magnetic field in the ^{11}B(^{3}He, t) measurement, the aberration due to the magnetic saturation determined the energy resolution. In the ^{11}B(p, p') measurement, an energy resolution of 200 keV (FWHM) was obtained, which was dominated by the energy spread of the cyclotron beam. Typical spectra of the ^{11}B(^{3}He, t) and ^{11}B(p, p') reactions are shown in Fig. 2. The cross section for the ^{11}B(^{3}He, t) reaction was measured at several angles between $\theta_{\rm lab} = 0°$ and 14.5° as shown in Fig. 3. For the ^{11}B(p, p') reaction, the cross section, analyzing power (A_y), induced polarization (P), and depolarization parameter (D_{NN}) were measured between $\theta_{\rm lab} = 2°$ and 11°. The results are shown in Fig. 4.

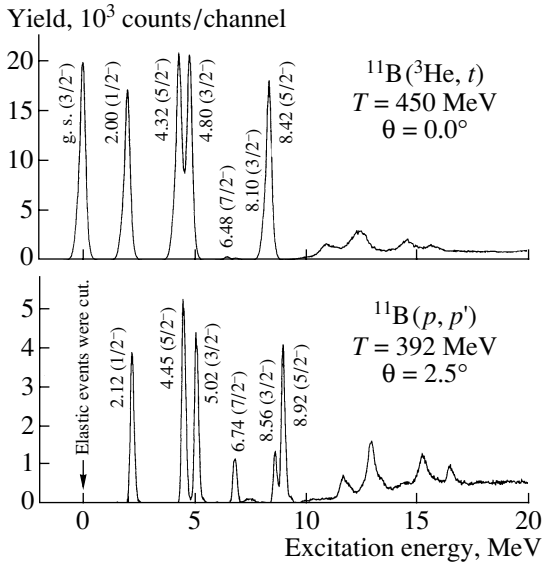

Fig. 2. Spectra for the ^{11}B(^{3}He, t) and ^{11}B(p, p') reactions.

3. DISCUSSION

The ^{11}B(^{3}He, t) cross section was compared with the results of the distorted-wave Born approximation (DWBA) calculations. The Cohen–Kurath wave functions (CKWFs) [5] were used in the DWBA calculations. An effective ^{3}He–N potential with isospin (V_τ), spin–isospin ($V_{\sigma\tau}$), and isospin-tensor (V_τ^T) terms represented by a Yukawa potential was employed to describe the projectile–target interaction. The values of V_τ, $V_{\sigma\tau}$, and V_τ^T were 0.73 MeV, −2.1 MeV, and −2.0 MeV/fm^2, respectively [6]. The calculated cross section is given by an incoherent sum over the cross sections of the different multipole contributions,

$$\frac{d\sigma}{d\Omega} = \sum_{\Delta J} \frac{d\sigma}{d\Omega}_{\Delta J}.$$

The angular distribution of each multipole cross section is well described by the DWBA calculation, but the relative strength between the different multipole contributions is not. To obtain a better description of the experimental data, we introduced scaling parameters $A_{\Delta J}$ defined by

$$\frac{d\sigma}{d\Omega}_{\rm fit} = \sum_{\Delta J} A_{\Delta J} \frac{d\sigma}{d\Omega}_{\Delta J}$$

and performed a least-χ^2 search for the $A_{\Delta J}$. The result is shown in Fig. 3. The dotted, dash-dotted, and dashed curves show the scaled cross sections of the $\Delta J = 0$, 1, and $2 + 3$ contributions, respectively. The solid curves are the sum of all possible multipole contributions. As seen from Fig. 3, the experimental

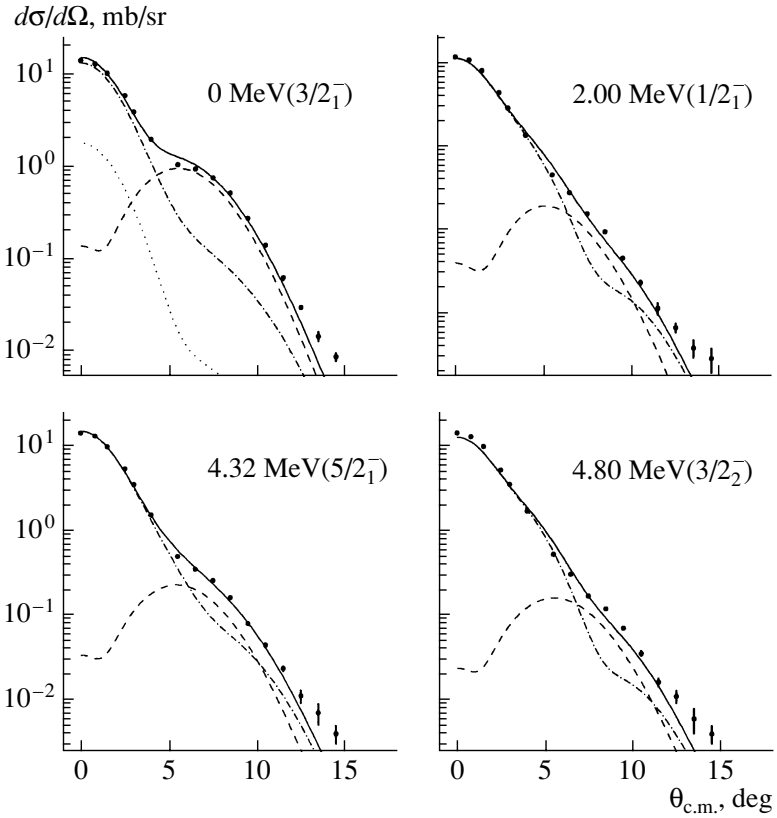

Fig. 3. Measured cross sections of the ^{11}B(^{3}He, t) reaction for the transitions to $3/2_1^-$ (0.00), $1/2_1^-$ (2.00), $5/2_1^-$ (4.32), and $3/2_2^-$ (4.80) states in ^{11}C compared with the DWBA calculations. The dotted, dash-dotted, and dashed curves show the cross sections of the $\Delta J = 0$, 1, and $2 + 3$ contributions. The solid curves represent the sum of all the possible ΔJ contributions.

results are well reproduced by the fits. Since there is a good linear proportional relation between the GT transition strength B(GT) and the (^{3}He, t) cross section at a small momentum transfer, where the $\Delta L = 0$ process is dominant [7], we extrapolated the cross section to the zero-momentum transfer using the DWBA result and normalized by the β-decay strength from ^{11}C. The obtained B(GT) values are compared with those from the earlier ^{11}B(p, n) measurement [8] in the table. The present result is consistent with the (p, n) result within the measurement uncertainty, although the $5/2_1^-$ and $3/2_2^-$ states at $E_x = 4.32$ and 4.80 MeV were not resolved separately in the (p, n) measurement. Theoretical B(GT) values from the CKWFs are also listed in the table. The B(GT) values using the CKWFs explain the experimental result reasonably well if the quenching factors of 0.5–0.7 are taken into account.

For the (p, p') data, the Franey–Love (FL) interaction [9] was used for the nucleon–nucleon effective interaction in the DWBA calculation. In similar fashion to the (^{3}He, t) analysis, we performed a least-χ^2 search for the multipole strengths. The dashed curves in Fig. 4 show the results. The DWBA calculation reasonably explains the ^{11}B(p, p') cross section, analyzing power, and induced polarization, but fails to describe the depolarization parameter. To solve the problem, we modified the isoscalar ($\alpha_{\Delta J}^{\Delta T=0}$) and isovector ($\alpha_{\Delta J}^{\Delta T=1}$) one-body transition densities in the DWBA calculation by introducing the isospin

Comparison between the Gamow–Teller transition strengths obtained in the experiment and the shell-model calculation (the experimental values are normalized by the β-decay strength from ^{11}C)

E_x, MeV	B(GT)$^{a}_{exp}$	B(GT)$^{b}_{exp}$	B(GT)$_{SM}$
0.00	0.345[c]	0.345[c]	0.514
2.00	0.405 ± 0.009	0.399 ± 0.008	0.791
4.32	0.491 ± 0.008	0.961 ± 0.017	0.647
4.82	0.481 ± 0.008		0.845

[a] Obtained from the present (^{3}He, t) analysis.

[b] Obtained from the (p, n) analysis [8].

[c] Obtained from β-decay strength.

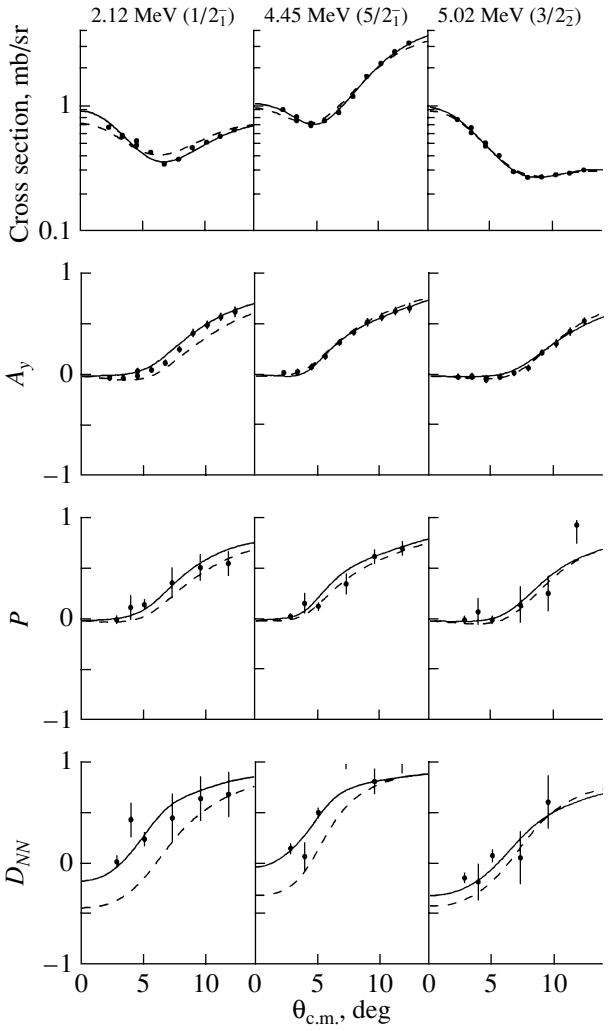

Fig. 4. Measured cross section, analyzing power (A_y), induced polarization (P), and depolarization parameter (D_{NN}) for the ^{11}B(p, p') reaction. The experimental data for the $1/2_1^-$ (2.12), $5/2_1^-$ (4.45), and $3/2_2^-$ (5.02) states in ^{11}B are compared with the DWBA calculations. The dashed curves are the results from the least-χ^2 search for the multipole strengths, while the solid curves are from the least-χ^2 search for the strengths and isospin mixing parameter (see the text).

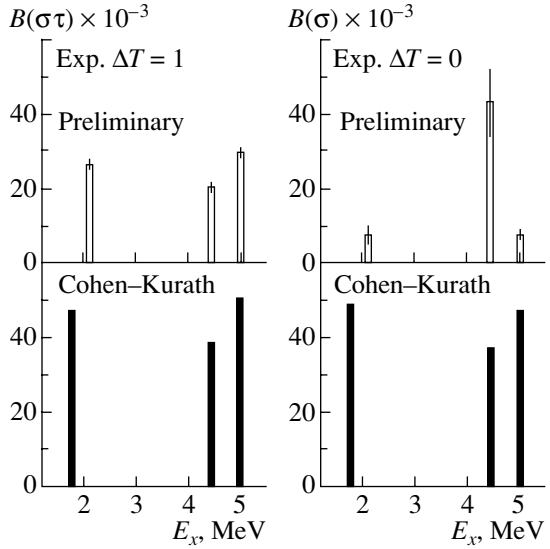

Fig. 5. Measured transition matrix elements for the σ and $\sigma\tau$ operators compared with the shell-model predictions.

mixing parameter $\theta_{\Delta J}$:

$$\alpha'^{\Delta T=0}_{\Delta J} = \sqrt{\frac{1}{2}}\alpha^{\Delta T=0}_{\Delta J}\cos\theta_{\Delta J},$$

$$\alpha'^{\Delta T=1}_{\Delta J} = \sqrt{\frac{1}{2}}\alpha^{\Delta T=1}_{\Delta J}\sin\theta_{\Delta J}.$$

The mixing parameters for $\Delta J = 1$ and 2 transitions were determined by the least-χ^2 fit to the experimental data, while the mixing parameters for other ΔJ transitions were fixed at 45°. The results of the least-χ^2 search for the multipole strengths and the isospin mixing parameters are shown by the solid curves in Fig. 4. All the observables, including the depolarization parameter, were reasonably well explained by the DWBA calculation. Finally, the transition matrix elements for the σ and $\sigma\tau_z$ operators $B(\sigma)$ and $B(\sigma\tau)$ were obtained from the modified one-body transition densities. The obtained $B(\sigma)$ and $B(\sigma\tau)$ are compared with the shell-model predictions in Fig. 5. It is clearly seen that the isoscalar matrix elements $B(\sigma)$ for the $1/2_1^-$ and $3/2_2^-$ states are strongly quenched by a factor of 0.15 in comparison with those of the shell-model predictions. Bernabéu *et al.* [10] deduced $B(\sigma) = 0.037$ and $B(\sigma\tau) = 0.024$ for the $1/2_1^-$ state from the γ-decay width under the assumption of charge independence. The $B(\sigma)$ value by Bernabéu is almost 50% of the shell-model predictions, but 3 times larger than the present result. Thus, the present $B(\sigma)$ value is very small in comparison with that by Bernabéu too. The reason for this $B(\sigma)$ quenching is still unclear. One of the reasons could be attributed to the fact that the result for the isoscalar strength from the (p, p') experiment has a large systematic uncertainty because the proton scattering amplitude in the $M1$ transition is dominated by the isovector component due to the large $|V_{\sigma\tau}/V_\sigma|$ value in the effective interaction around $E_p = 400$ MeV. Thus, we recently measured deuteron inelastic scattering at forward angles to study the isoscalar $M1$ excitations in ^{11}B. Because the deuteron inelastic scattering has a selectivity for the isoscalar transition, an exclusive measurement of the isoscalar transition becomes possible. The analysis of this experiment is still going on. The result will be reported elsewhere soon [11].

4. SUMMARY

In the present ^{11}B(^{3}He, t) and ^{11}B(p, p') experiments, nuclear transition matrix elements B(GT), $B(\sigma\tau)$, and $B(\sigma)$ were obtained to study the weak-interaction response of ^{11}B. The obtained matrix elements were compared with the shell-model calculations and other work. The shell-model calculation explained the isovector parts B(GT) and $B(\sigma\tau)$ reasonably well if the quenching factors of 0.5–0.7 were taken into account, but did not describe the isoscalar part $B(\sigma)$. $B(\sigma)$ for the transitions to the $1/2^-_1$ and $3/2^-_2$ states were found to be quenched by a factor of 0.15 in comparison with those obtained in the shell-model. The present $B(\sigma)$ value is also 3 times smaller than the estimate by Bernabéu *et al.* [10] for the $1/2^-_1$ state. This large quenching of $B(\sigma)$ in the present study might be due to the fact that our analysis on the isoscalar strength could have a large systematic uncertainty. Recently, we measured the ^{11}B(d, d') reaction to obtain $B(\sigma)$ values with small systematic uncertainties. The analysis of the (d, d') experiment is still going on. The result will be reported elsewhere soon.

ACKNOWLEDGMENTS

We are grateful to the RCNP cyclotron crew for preparing a stable and clean beam.

This research was supported in part by the Grant-in-Aid for Scientific Research no. 15740136 from the Japanese Ministry of Education, Sports, Culture, Science, and Technology.

REFERENCES

1. Q. R. Ahmad *et al.*, Phys. Rev. Lett. **87**, 071301 (2001).
2. R. S. Raghavan, Sandip Pakvasa, and B. A. Brown, Phys. Rev. Lett. **57**, 1801 (1986).
3. M. Fujiwara *et al.*, Nucl. Instrum. Methods Phys. Res. A **422**, 484 (1999).
4. M. Yosoi *et al.*, AIP Conf. Proc. **343**, 157 (1995).
5. S. Cohen and D. Kurath, Nucl. Phys. **73**, 1 (1965).
6. R. G. T. Zegers *et al.*, Phys. Rev. Lett. **90**, 202501 (2003).
7. M. Fujiwara *et al.*, Nucl. Phys. A **599**, 223c (1996).
8. T. N. Taddeucci *et al.*, Phys. Rev. C **42**, 935 (1990).
9. M. A. Franey and W. G. Love, Phys. Rev. C **31**, 488 (1985).
10. J. Bernabéu *et al.*, Nucl. Phys. B **378**, 131 (1992).
11. T. Kawabata *et al.*, Phys. Rev. (in press).

Physics of Atomic Nuclei, Vol. 67, No. 10, 2004, pp. 1799–1803. From Yadernaya Fizika, Vol. 67, No. 10, 2004, pp. 1827–1831.

Proceedings of the International Conference "Nuclear Structure and Related Topics"

Schiff Moment of the Mercury Nucleus and the Proton Dipole Moment*

V. F. Dmitriev[1)]** **and** **R. A. Sen'kov**[1),2)]***

Received January 21, 2004

Abstract—The Schiff moment of the ^{199}Hg nucleus is calculated using finite range P- and T-violating weak nucleon–nucleon interaction. Both the contributions of the P- and T-odd interaction and of internal nucleon electric dipole moments to the Schiff moment of ^{199}Hg are calculated. The contribution of the proton electric dipole moment is obtained via core-polarization effects treated in the framework of RPA with effective residual interactions. We derive a new upper bound $|d_p| < 5.4 \times 10^{-24}\ e$ cm for the proton electric dipole moment. © *2004 MAIK "Nauka/Interperiodica".*

1. INTRODUCTION

The interest in electric dipole moments (EDM) of elementary particles and more complex systems like nuclei and atoms has existed since 1950, when it was first suggested that there was no experimental evidence for symmetry of nuclear forces under parity transformation [1].

The experimental upper limit on the neutron EDM [2] is

$$d_n < 0.63 \times 10^{-25}\ e\ \text{cm}. \tag{1}$$

The measured value for the proton EDM [2] is

$$d_p = (-4 \pm 6) \times 10^{-23}\ e\ \text{cm} \tag{2}$$

and is compatible with zero. This corresponds to an upper limit which is three order of magnitude weaker than the one for a neutron.

The best upper limit on EDM ever obtained was in an atomic experiment with ^{199}Hg [3]. The result for the dipole moment of this atom is

$$d(^{199}\text{Hg}) < 2.1 \times 10^{-28}\ e\ \text{cm}. \tag{3}$$

Unfortunately, the implications of this result are somewhat less impressive, due to the electrostatic screening of the nuclear EDM in this essentially Coulomb system. The point is that, in a stationary state of such a system, the total electric field acting on each particle must vanish. Thus, an internal rearrangement of the system's constituents gives rise to an internal field $\mathbf{E}_{\text{in}}$ that exactly cancels external field $\mathbf{E}_{\text{ex}}$ at each charged particle; the external field is effectively switched off, and an EDM feels nothing [1, 4].

Still, some P- and T-odd component of the electrostatic potential survives due to final nuclear size. It is created by the next moment in the nuclear electric dipole density distribution. This is the Schiff moment defined as [5]

$$\mathbf{S} = \frac{1}{10}\sum_q e_q \left(r_q^2 \mathbf{r}_q - \frac{5}{3}\langle r^2\rangle_{\text{ch}} \mathbf{r}_q \right). \tag{4}$$

The Schiff moment generates a P- and T-odd electrostatic potential in the form

$$\phi(\mathbf{r}) = 4\pi\, \mathbf{S}\cdot\boldsymbol{\nabla}\delta(\mathbf{r}). \tag{5}$$

Interaction of atomic electrons with the potential given by Eq. (5) produces an atomic dipole moment

$$d_{\text{atom}} = \sum_n \frac{\langle 0| - e\sum_i^Z \phi(\mathbf{r}_i)|n\rangle\langle n| - e\sum_i^Z z_i|0\rangle}{E_n - E_0} + \text{h.c.} \tag{6}$$

Due to the contact origin of the potential, only the electrons in s and p atomic orbitals contribute to the dipole moment given by Eq. (6).

Equation (4) is valid for any system of pointlike charges e_q. Let us split the sum in Eq. (4) into the sum over coordinates of nucleons and the sum over coordinates of charges inside the nucleons:

$$\mathbf{S} = \frac{1}{10}\sum_N \sum_i e_i \left((\mathbf{r}_N + \boldsymbol{\rho}_i)^2 - \frac{5}{3}\langle r^2\rangle_{\text{ch}} \right) \times (\mathbf{r}_N + \boldsymbol{\rho}_i). \tag{7}$$

Here, $\mathbf{r}_N$ is a nucleon position and $\boldsymbol{\rho}_i$ is the position of the ith charge inside the nucleon. Combining the terms of the zeroth and first order in $\boldsymbol{\rho}$ and using $\sum_i e_i = e_N$, $\sum_i e_i\boldsymbol{\rho}_i = \mathbf{d}_N$, we obtain an expression

*This article was submitted by the authors in English.

[1)]Budker Institute of Nuclear Physics, Siberian Division, Russian Academy of Sciences, Novosibirsk, 630090 Russia.
[2)]Novosibirsk State University, Novosibirsk, Russia.
**e-mail: v.f.dmitriev@inp.nsk.su
***e-mail: r.a.senkov@inp.nsk.su

for the Schiff moment as a sum of two terms. The first of them is similar to (4):

$$\mathbf{S}_1 = \frac{1}{10}\sum_N^A e_N \left(r_N^2 \mathbf{r}_N - \frac{5}{3}\langle r^2\rangle_{\rm ch}\mathbf{r}_N \right), \quad (8)$$

where e_N is equal to $|e|$ for a proton and zero for a neutron. The mean value of this operator is nonzero only in the presence of the P- and T-invariance-violating nucleon–nucleon interaction.

The second term is related to the internal dipole moments of the nucleons

$$\mathbf{S}_2 = \frac{1}{6}\sum_N^A \mathbf{d}_N \left(r_N^2 - \langle r^2\rangle_{\rm ch}\right) \quad (9)$$
$$+ \frac{1}{5}\sum_N^A \left(\mathbf{r}_N(\mathbf{r}_N\cdot\mathbf{d}_N) - \mathbf{d}_N r_N^2/3\right).$$

The previous calculations of the Schiff moment of a heavy nucleus [5, 6] were performed in a simplified manner, without taking into account the residual interaction between a valence nucleon and the core nucleons. Only recently did more microscopic studies of the Schiff moment of ^{199}Hg [7] and ^{225}Ra [8] appear, where effects of the core polarization with the effective forces for ^{199}Hg and the octupole deformation for ^{225}Ra based on the Skyrme–Hartree–Fock method were discussed. In this work, we discuss both the contribution of the P- and T-odd interaction and the nucleon EDM contribution to the Schiff moment of the ^{199}Hg nucleus. In the picture of an independent-particle model, only a valence nucleon contributes to the Schiff moment. In the case of ^{199}Hg, it is a neutron. However, when a residual quasiparticle interaction between the valence neutron and the protons in the core is taken into consideration, the proton contribution to the nuclear Schiff moment becomes nonzero. We calculated this contribution using a random phase approximation (RPA) with effective forces. From the relation between the Schiff moment and the electric dipole moment of the Hg atom [9], a new upper limit on the proton EDM was obtained.

2. OUTLINE OF THE THEORY

2.1. Nuclear Mean Field

In our calculations, we used a full single-particle spectrum including continuum. The single-particle basis was obtained using the partially self-consistent mean-field potential of [10]. The potential includes four terms. The isoscalar term is the standard Woods–Saxon potential

$$U_0(r) = -\frac{V}{1+\exp[(r-R)/a]}, \quad (10)$$

with the parameters $V = 52.03$ MeV, $R = 1.2709A^{1/3}$ fm, and $a = 0.742$ fm. Two other terms $U_{ls}(r)$ and $U_\tau(r)$ were obtained in a self-consistent way using the two-body Landau–Migdal-type interaction of [11] for the spin–orbit and isovector parts of the potential. The last term is the Coulomb potential of a uniformly charged sphere with $R_{\rm C} = 1.18A^{1/3}$ fm. The mean-field potential obtained in this way fits well single-particle energies and rms radii of nuclei in the region around ^{208}Pb.

2.2. Nucleon–Nucleon P- and T-Odd Interaction

We use the interaction generated by P- and T-violating pion exchange [12–14]:

$$W(\mathbf{r}_1-\mathbf{r}_2) = -\frac{g}{8\pi m_p}[(g_0\boldsymbol{\tau}_1\cdot\boldsymbol{\tau}_2 \quad (11)$$
$$+ g_2(\boldsymbol{\tau}_1\cdot\boldsymbol{\tau}_2 - 3\tau_1^3\tau_2^3))(\boldsymbol{\sigma}_1-\boldsymbol{\sigma}_2)$$
$$+ g_1(\tau_1^3\boldsymbol{\sigma}_1 - \tau_2^3\boldsymbol{\sigma}_2)]\cdot\boldsymbol{\nabla}_1\frac{e^{-m_\pi r_{12}}}{r_{12}},$$

where g is the usual strong pion–nucleon pseudoscalar coupling constant; g_0, g_1, and g_2 correspond to isoscalar, isovector, and isotensor P- and T-odd couplings; and m_p is the proton mass. In contrast to P-odd and T-even interaction, in Eq. (11) the exchange of π^0 is allowed. This term produces the direct contribution to the P- and T-odd part of the nuclear mean field, while the other terms produce the exchange contribution only. Since the direct contribution dominates for finite-range potentials, we can expect that the interaction (11) is the leading one and the exchange of heavier mesons can be omitted.

2.3. Core Polarization

The effects of the core polarization for a single-particle operator can be treated by introducing a renormalized operator $\tilde{\mathbf{S}}$ satisfying the equation

$$\tilde{\mathbf{S}}_{\nu'\nu} = \mathbf{S}_{\nu'\nu} \quad (12)$$
$$+ \sum_{\mu'\mu}\tilde{\mathbf{S}}_{\mu\mu'}\frac{n_\mu - n_{\mu'}}{\epsilon_\mu - \epsilon_{\mu'}+\omega}\langle\nu'\mu'|F+W|\mu\nu\rangle,$$

where $\mathbf{S}$ is the bare Schiff moment operator given by (4), (8), or (9), and n_μ and ϵ_μ are single-particle occupation numbers and energies. For static moments, the external frequency $\omega \to 0$. The value of the Schiff moment is given by the diagonal matrix element of the z component of the renormalized operator (12) between mean-field states of the last unpaired nucleon with a maximal angular-momentum projection:

$$S = \langle \mu jm = j|\tilde{\mathbf{S}}_z|\mu jm = j\rangle. \quad (13)$$

For the residual interaction F, we use the phenomenological Landau–Migdal interaction of the form

$$F = C(f(r) + f'(\boldsymbol{\tau}_1 \cdot \boldsymbol{\tau}_2) + g_s(\boldsymbol{\sigma}_1 \cdot \boldsymbol{\sigma}_2) + g'_s(\boldsymbol{\sigma}_1 \cdot \boldsymbol{\sigma}_2)(\boldsymbol{\tau}_1 \cdot \boldsymbol{\tau}_2))\delta(\mathbf{r}_1 - \mathbf{r}_2), \quad (14)$$

where $C = 300$ MeV fm^3 and $f(r) = f_{\rm ex} + (f_{\rm in} - f_{\rm ex})\dfrac{\rho(r)}{\rho(0)}$. The values of the empirical interaction constants g_s and g'_s are crucial for our calculations. The proton contribution is proportional to the proton–neutron interaction $g_s - g'_s$. The constant g'_s is determined from magnetic properties of nuclei and the position of a Gamow–Teller resonance. Its adopted value varies between $g'_s = 0.9$–1.0 depending on details of the mean-field potential used [15–17]. The constant g_s is not so well defined. The magnetic moments and $M1$ transitions are to a great extent isovector and they do not fix g_s. An attempt to fix it from the structure of high-spin states in ^{208}Pb has been done in [18]. They found that $g_s = 0.25$ had to be used in order to reproduce the excitation energies of the $M12$ and $M14$ states. Another value $g_s = 0.19$ was quoted in the review paper [17]. A value close to zero was found in [19].

Let us demonstrate the RPA effects on the Schiff moment operator of Eq. (9). In the coordinate space, the operator can be represented in the form

$$S_{1m} = \sum_{i=1}^{2} S^i(r) T^{(i)}_{1m}, \quad (15)$$

where we introduced the set of linearly independent tensor operators

$$T^{(1)}_{JM} = \boldsymbol{\sigma} \cdot \mathbf{Y}^{J-1}_{JM}(\mathbf{n}), \quad (16)$$
$$T^{(2)}_{JM} = \boldsymbol{\sigma} \cdot \mathbf{Y}^{J+1}_{JM}(\mathbf{n})$$

(here, $\mathbf{Y}^L_{JM}(\mathbf{n})$ is the vector spherical harmonic). For $J = 1$, we have $T^{(1)}_{1m} \sim \sigma_m$ and $T^{(2)}_{1m} \sim n_m(\mathbf{n} \cdot \boldsymbol{\sigma}) - \dfrac{1}{3}\sigma_m$. For a spherical nucleus, we can separate the angular variables and solve the obtained equations in coordinate space. The equations are

$$S^{ai}(r) = S^{ai}_0(r) + \int_0^\infty A^{aibj}(r, r') S^{bj}(r') dr', \quad (17)$$

where $a = p, n$ and $S^{ai}_0(r)$ is the radial part of the Schiff moment operator (9) multiplied by r. The kernel of the integral equation $A^{aibj}(r, r')$ was calculated by means of the Green's functions of the radial Schrödinger equation:

$$A^{aibj}(r, r') \quad (18)$$

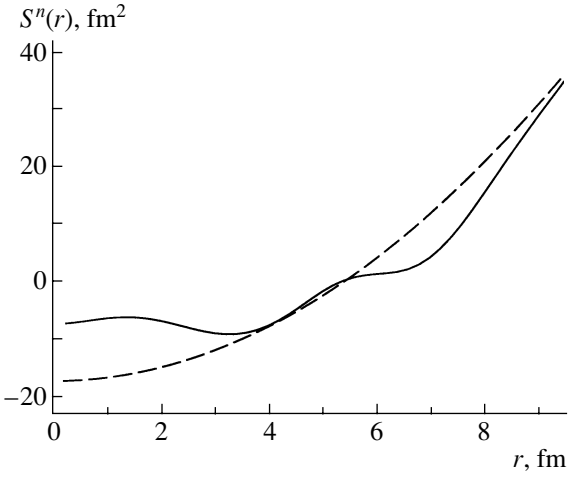

Fig. 1. Core-polarization effects in the neutron Schiff moment operator. The solid curve is $S^{n1}(r)$. The dashed curve is the bare operator $S^{n1}_0(r)$.

$$= \frac{Cg^{ab}}{3} \sum_{\kappa jl} n^b_\kappa \langle jl||T^{(i)}_1||\kappa\rangle\langle jl||T^{(j)}_1||\kappa\rangle r R^b_\kappa(r) \times r' R^b_\kappa(r') \left(G^b_{jl}(r, r'|\epsilon_\kappa + \omega) + G^b_{jl}(r, r'|\epsilon_\kappa - \omega)\right),$$

where $g^{pp} = g^{nn} = g_s + g'_s$, $g^{pn} = g^{np} = g_s - g'_s$, $R^b_\kappa(r)$ are the radial wave functions, and n^b_κ are the occupation numbers.

The solutions of Eq. (12) for $S^{ai}(r)$ are shown in Fig. 1 and Fig. 2.

Figure 1 demonstrates the magnitude of the core-polarization effects. The repulsive residual interaction (14) leads to a not very significant decrease in the mean value of the Schiff moment. Figure 2 shows the radial dependence of the proton contributions induced by the core polarization. Note the one order of magnitude difference in the scales in Fig. 1 and Fig. 2. The solid curve in Fig. 2 is the radial dependence at the first operator $T^{(1)}_{1m}$ and the dashed curve is the radial dependence at the second operator $T^{(2)}_{1m}$. The function $S^{p1}(r)$ changes sign inside the nucleus; therefore, its mean value is smaller than the mean value of $S^{p2}(r)$, which is mostly negative inside the nucleus.

3. RESULTS

All the contributions can be summarized as a sum of two parts. The first part corresponds to the bare operator given by Eq. (8). Its contribution to the Schiff moment is (see [7])

$$S = -0.0004 g g_0 - 0.055 g g_1 + 0.009 g g_2 \ [e\,\text{fm}^3]. \quad (19)$$

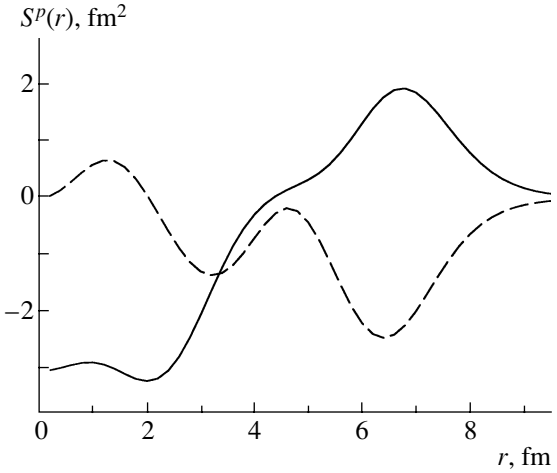

Fig. 2. Radial dependence of the proton effective Schiff moment operators induced by the core polarization. The solid curve is $S^{p1}(r)$, the dashed curve is $S^{p2}(r)$.

The obtained value for the Schiff moment in Eq. (19) cannot be compared directly with the previous calculations, where the contact interaction has been used. To perform the comparison, we redefine the constants g_i:

$$g_i = \frac{Gm_\pi^2}{\sqrt{2}}\tilde{g}_i. \tag{20}$$

With this factor, the integration over space of the Yukawa function gives 1, exactly as the integration of a delta function $\delta(\mathbf{r})$. Introducing this factor, we obtain

$$S = (-0.01g\tilde{g}_0 - 0.86g\tilde{g}_1 + 0.14g\tilde{g}_2) \times 10^{-8}\,[e\,\mathrm{fm}^3]. \tag{21}$$

This value should be compared with $S = -1.4 \times 10^{-8}\eta_{np}$ [20] and $S \approx -1.6 \times 10^{-8}\eta_{np}$ [6], where $\eta_{np} \sim g(\tilde{g}_0 + \tilde{g}_1 - 2\tilde{g}_2)$. We conclude that the difference between our result and previous calculations is significant for the $T = 0$ and $T = 2$ channels. Our values are smaller in absolute value. In order to trace the origin of this difference, we repeated our calculations using the contact interaction and omitting the core polarization. The contact interaction was obtained by replacing the Yukawa function in Eq. (11) by the delta function. The result is

$$S = -0.96 \times 10^{-8} g(\tilde{g}_0 + \tilde{g}_1 - 2\tilde{g}_2)\,[e\,\mathrm{fm}^3]. \tag{22}$$

If we completely omit the effect of the core polarization in calculations with the finite-range interaction Eq. (11), then the only nonzero contribution

$$S = -0.086g(g_0 + g_1 - 2g_2)\,[e\,\mathrm{fm}^3],$$

which corresponds to

$$S = -1.35 \times 10^{-8} g(\tilde{g}_0 + \tilde{g}_1 - 2\tilde{g}_2)\,[e\,\mathrm{fm}^3]. \tag{23}$$

Comparing Eqs. (22) and (23), we conclude that the effect of the finite weak-interaction range is not very significant. The main effect bringing the value of the Schiff moment from that in Eq. (23) to the value in Eq. (21) comes from the core polarization.

The value of the Schiff moment of ^{199}Hg corresponding to the bare operator of Eq. (9) can be represented as a sum of proton and neutron contributions

$$S = s_p d_p + s_n d_n, \tag{24}$$
$$s_p = 0.20 \pm 0.02\ \mathrm{fm}^2,$$
$$s_n = 1.895 \pm 0.035\ \mathrm{fm}^2,$$

where the uncertainties reflect differences in values of the interaction constants g and g'. The main contribution to s_p and s_n comes from the second term in Eq. (9). The contribution of the first term is only -0.7 fm^2 in s_n and 0.006 fm^2 in s_p.

The constraint for the Schiff moment of the mercury nucleus from the experiment [3] can be obtained using the results of [9]. They calculated EDM of an atom created by the nuclear Schiff moment. For ^{199}Hg, they found

$$d = -2.8 \times 10^{-17} S.$$

From (3), we obtain the following upper bound for the Schiff moment:

$$|S(^{199}\mathrm{Hg})| < 0.75 \times 10^{-11}\ e\,\mathrm{fm}^3. \tag{25}$$

From (25), we can give the following constraints for EDM of nucleons:

$$|d_p| < 3.8 \times 10^{-24}\ e\,\mathrm{cm}, \tag{26}$$
$$|d_n| < 4.0 \times 10^{-25}\ e\,\mathrm{cm}.$$

The constraint for the neutron EDM is worse than the existing result $d_n < 0.63 \times 10^{-25}\ e$ cm [2]; therefore, we shall not discuss it below. For proton EDM, the estimate (26) is one order of magnitude lower than the existing experiment, $d_p = (-4 \pm 6) \times 10^{-23}\ e$ cm [2]. In these circumstances, the question about a real theoretical accuracy of our approach becomes important. It is clear that the value ± 0.02 cited in Eq. (24) does not reflects the real accuracy of the theory. It just came from the difference in adopted values of g_s and g'_s. The theoretical uncertainty appears from two sources. First, there is an uncertainty in the atomic calculations that couple the nuclear Schiff moment and EDM of an atom. We shall not discuss it here, referring to the work [9]. Second, there is an uncertainty in calculations of the core-polarization effects using RPA with effective forces. The latter can be estimated from the following considerations. Using RPA with the effective forces, we can fit different nuclear moments in one nucleus. Then, in neighboring nuclei, the calculated moments will differ from the data. This

difference can be regarded as an uncertainty in the theory. In our experience, this difference is of the order of 20% on the average, sometimes reaching a value of 30% [21]. To be safe, we can adopt a conservative 30% uncertainty in calculations of s_p. Therefore, instead of (24), we would prefer to write for s_p

$$s_p = 0.2 \pm 0.06 \text{ fm}^2. \quad (27)$$

Since the error in (27) is not statistical, we cannot give a probability distribution for s_p. If one takes 0.14 fm^2 as a minimal value of s_p, then it gives the following value for the proton EDM upper bound:

$$|d_p| < 5.4 \times 10^{-24}\, e \text{ cm}. \quad (28)$$

In summary, we calculated different contributions of the protons and neutrons to the Schiff moment of ^{199}Hg. The effects of core polarization were accounted for in the scope of RPA with effective residual forces. A new upper bound of the proton EDM has been obtained from the upper bound on the atomic EDM of the ^{199}Hg atom.

ACKNOWLEDGMENTS

We are grateful to I.B. Khriplovich for bringing our attention to this problem and for useful discussions.

REFERENCES

1. E. M. Purcell and N. F. Ramsey, Phys. Rev. **78**, 807 (1950).
2. K. Hagiwara *et al.*, Phys. Rev. D **66**, 010001 (2002).
3. M. V. Romalis, W. C. Griffith, and E. N. Fortson, Phys. Rev. Lett. **86**, 2505 (2001).
4. L. I. Schiff, Phys. Rev. **132**, 2194 (1963).
5. V. V. Flambaum, I. B. Khriplovich, and O. P. Sushkov, Zh. Éksp. Teor. Fiz. **87**, 1521 (1984) [Sov. Phys. JETP **60**, 873 (1984)].
6. V. V. Flambaum and J. S. M. Ginges, Phys. Rev. A **65**, 032113 (2002).
7. V. F. Dmitriev and R. A. Sen'kov, nucl-th/0304048.
8. J. Engel, M. Bender, J. Dobaczewski, *et al.*, nucl-th/0304075.
9. V. A. Dzuba, V. V. Flambaum, J. S. M. Ginges, and M. G. Kozlov, Phys. Rev. A **66**, 012111 (2002).
10. B. L. Birbrair and V. A. Sadovnikova, Yad. Fiz. **20**, 645 (1974) [Sov. J. Nucl. Phys. **20**, 347 (1975)].
11. A. B. Migdal, *Theory of Finite Fermi Systems* (Wiley, New York, 1967).
12. G. Barton, Nuovo Cimento **19**, 512 (1961).
13. W. C. Haxton and E. M. Henley, Phys. Rev. Lett. **51**, 1937 (1983).
14. P. Herczeg, Hyperfine Interact. **43**, 77 (1988).
15. J. Speth, E. Werner, and W. Wild, Phys. Rep. **33**, 127 (1977).
16. V. F. Dmitriev and V. B. Telitsin, Nucl. Phys. A **402**, 581 (1983).
17. F. Osterfeld, Rev. Mod. Phys. **64**, 491 (1992).
18. S. Krewald and J. Speth, Phys. Rev. Lett. **45**, 417 (1980).
19. I. N. Borzov, S. V. Tolokonnikov, and S. A. Fayans, Sov. J. Nucl. Phys. **40**, 732 (1984).
20. V. V. Flambaum, I. B. Khriplovich, and O. P. Sushkov, Nucl. Phys. A **449**, 750 (1986).
21. V. F. Dmitriev and R. A. Sen'kov, Nucl. Phys. A **706**, 351 (2002).

Physics of Atomic Nuclei, Vol. 67, No. 10, 2004, pp. 1804–1809. From Yadernaya Fizika, Vol. 67, No. 10, 2004, pp. 1832–1837.

Proceedings of the International Conference "Nuclear Structure and Related Topics"

"Alpha Decays" of $^{10}_{\Lambda}$Be and $^{10}_{\Lambda}$B Hypernuclei: Phenomenological Analysis and Role of Nuclear Structure*

L. Majling[1)], **V. A. Kuz'min[2)]**, and **T. V. Tetereva[3)]**

Received January 21, 2004

Abstract—Hypernuclei are used to study the baryon–baryon weak interaction and associated effective weak Hamiltonian. We will show how the proper choice of hypernucleus can be used to pick out components of the effective weak Hamiltonian. It is well known that removing one nucleon from ^{9}Be or ^{9}B results in ^{8}Be* with a subsequent $\alpha\alpha$ decay. Through this unique process, it would be possible to identify final states of the residual nucleus. So, due to these specific properties of the core nuclei ^{9}Be and ^{9}B, it may be possible to measure the branching fractions $\Gamma^{n(p)}_{\alpha\alpha i}$ for the exclusive decays of the $^{10}_{\Lambda}$Be ($^{10}_{\Lambda}$B) hypernuclei.

1. INTRODUCTION: HYPERNUCLEI

Λ hypernucleus $^A_\Lambda Z$ is a bound system of Z protons, $A-Z-1$ neutrons, and one Λ hyperon. This is a best example of a nucleus with a new flavor—strangeness. The lifetime of a hypernucleus is about 2×10^{-10} s.

Hypernuclei are formed in any reaction of an elementary particle with nucleons of a nucleus in which hyperons are produced. They were discovered by Danysz and Pniewski [1] in a balloon-flown emulsion stack, where salient pictures, namely, "twin stars" corresponding to strong production of the primary hypernucleus and weak decay of the hyperfragment connected with a path ($\sim 50\ \mu$m), were easily recognized.

The large-scale systematic studies of hypernuclei began with the advent of separated K^- beams, which permitted the use of a counter technique and confirmed the brilliant suggestion of Podgoretsky [2]: instead of hunting down decays of random fragments, to study hypernuclear production in the strangeness exchange reaction

$$K^- + {}^AZ \to {}^A_\Lambda Z + \pi^-, \quad p_K \approx 530\ \text{MeV}/c, \quad \theta_\pi \approx 0 \quad (q_\Lambda \approx 0),$$

where the π^- momenta can be used to determine spectra of hypernuclear resonances. The pioneering work of groups led by T. Bressani [3] and B. Povh at CERN [4] and R. Chrien at BNL [5] established the existence of hypernuclei and allowed a clear assignment of hypernuclear states. The achievements of hypernuclear spectroscopy using the in-flight (K^-,π^-) reaction stimulated the study of the associated-production reaction $\pi^+ + n \to \Lambda + K^+$. The different production reactions are complementary and are required for a complete study of hypernuclear spectra [6]. From these studies, the Λ-nucleus potential was derived and strength of spin–orbit interaction was obtained.

The **weak nonmesonic decay** of Λ hypernuclei is of top physical interest, since it gives access to the weak-decay process $\Lambda N \to nN$, which is only achievable through the observation of hypernuclear ground-state decays. The field of weak decay of Λ hypernuclei has experienced impressive progress in the last few years [7, 8]. Among weak-decay observables, the total decay width (or lifetime) can be measured most accurately [9] and is now available from different experiments.

The main problem concerning the weak decay of Λ hypernuclei is the disagreement between the theoretical and experimental values for the ratio Γ^n/Γ^p. The results of the calculations lie below the data points for all considered hypernuclei, although large experimental error bars do not permit any definitive conclusion. In order to solve the Γ^n/Γ^p puzzle, many attempts have been made up to now, but without success (see [8] for details).

One has to point out that present experiments cannot identify the final state of the residual $(A-2)$

*This article was submitted by the authors in English.

[1)]Nuclear Physics Institute, Academy of Sciences of Czech Republic, Řež.
[2)]Bogolyubov Laboratory of Theoretical Physics, Joint Institute for Nuclear Research, Dubna, Moscow oblast, 141980 Russia.
[3)]Institute of Nuclear Physics, Moscow State University, Moscow, 119992 Russia.
**e-mail: majling@ujf.cas.cz

nucleus in the case of nonmesonic decays

$$ {}^{A}_{\Lambda}Z \to {}^{A-2}Z + n + n \qquad \text{and} $$
$$ {}^{A}_{\Lambda}Z \to {}^{A-2}(Z-1) + n + p, $$

and an average over many nuclear final states has to be performed.

Below, we focus our attention on one peculiar case which makes it possible to detect some of such final states.

2. "ALPHA DECAYS" OF ${}^{10}_{\Lambda}$Be AND ${}^{10}_{\Lambda}$B HYPERNUCLEI

It was proposed recently [10] to use the unique feature of the ^{9}Be nucleus—namely, the fact that, after removing a neutron from its ground state, several groups of α particles appear from different excited states of a residual nucleus ^{8}Be. Due to their specific cluster structure—$\alpha\alpha N\Lambda$—it may be possible to measure in the ${}^{10}_{\Lambda}$Be and ${}^{10}_{\Lambda}$B hypernuclei the partial "alpha widths" $\Gamma^{\tau}_{\alpha\alpha i}$, corresponding to states of the residual nucleus ^{8}Be decaying through the $\alpha\alpha$ channel. In the figure, the relevant states of $A = 8$ isotopes are displayed [11], as well as the probabilities of their feeding, spectroscopic factors S^{n}_{i}.

The partial widths $\Gamma^{\tau}_{\alpha\alpha i}$ can be determined through detection of tagged α particles. Such tagged α particles were recognized as "hammer tracks" in the emulsion and were efficiently used for identification of ${}^{8}_{\Lambda}$Li ($\to \pi^{-}\,{}^{8}$Be*) [12]. The points of the production and decay of **relativistic hypernuclei** [13] are separated by many centimeters and this situation offers a great advantage, a possibility of observing and studying independently the production and decay of hypernuclei. With the new trigger tuned to search for two tagged α particles, $\Gamma^{n}_{\alpha\alpha 2}({}^{10}_{\Lambda}\mathrm{Be})$, $\Gamma^{n}_{\alpha\alpha 1}({}^{10}_{\Lambda}\mathrm{Be})$, $\Gamma^{p}_{\alpha\alpha 2}({}^{10}_{\Lambda}\mathrm{B})$, and $\Gamma^{p}_{\alpha\alpha 1}({}^{10}_{\Lambda}\mathrm{B})$ could be measured at the Dubna Nuclotron [14, 15].

In such a way, we can determine not only a partial rate (including neutron ones), but also an exactly one-nucleon stimulated process $\Lambda N \to nN$. The study of four $\Gamma^{\tau}_{\alpha\alpha i}$ offers a unique possibility of determining all needed matrix elements of the weak interaction $\Lambda N \to nN$.

3. PARTIAL DECAY WIDTHS OF ${}^{10}_{\Lambda}$Be AND ${}^{10}_{\Lambda}$B

In our contribution to the problem of Γ^{n}/Γ^{p} ratio, we have benefited from previous efforts, mainly from the detailed analysis given by Parreño *et al.* [16]. We consider two decay channels, $\Lambda n \to nn\,(\Gamma^{n})$ and $\Lambda p \to np\,(\Gamma^{p})$, in which the Λ hyperon picks up one p-shell nucleon of the core nucleus. Employing the technique of fractional-parentage coefficients (FPC), the ground-state wave function of the initial hypernucleus is decomposed [16] into a complete set of wave functions of excited states in the residual $(A-2)$ nucleus $\Psi^{(A-2)}(E_i, J_i, T_i, \tau_i)$ coupled to the complete set of wave function of states of an ΛN pair, $|\tau l, s_\Lambda : L = lSJ\rangle$. So, the wave function of the initial state of the hypernucleus is

$$ |I\rangle = \sum_{\tau,j,l} \sum_{E_i,J_i,T_i} \sum_{J,S} \sqrt{k} \left(T_i \tau_i \frac{1}{2} \tau \middle| T_c \tau_c \right) \qquad (1) $$
$$ \times U\left(J_i j \mathcal{J} \frac{1}{2} : J_c J \right) U\left(l \frac{1}{2} J \frac{1}{2} : jS \right) $$
$$ \times g^{E_c J_c T_c}_{E_r J_r T_r} \left[|k^{k-1} E_i J_i T_i \tau_i\rangle \otimes |\tau l, s_\Lambda : L = lSJ\rangle \right]^{\mathcal{J}} $$

and the total rate Γ_{nm} [16],

$$ \Gamma_{\mathrm{nm}} = \sum_{\tau=n,p} \sum_{E_i,J_i,T_i,J,T} \left| \left\langle \left[\Psi^{(A-2)}(\{i\}) \Psi^{(NN)}(JT) \right]^{\mathcal{J}} \middle| V_w \middle| \left[\Psi^{(A-1)}(\{c\}) \psi^{\Lambda}\left(\frac{1}{2}\right) \right]^{\mathcal{J}} \right\rangle \right|^2, \qquad (2) $$

is a sum of partial rates Γ^{τ}_{i}:

$$ \Gamma^{\tau}_{i} = \left| \sum_{SJ} G_{\mathcal{J}}(\{c\}, \{i\}, \tau LSJ) w^{SJ}_{l\tau} \right|^2. \qquad (3) $$

We use the shorthand notation $\{c\} \equiv \{E_c, J_c, T_c, \tau_c\}$ and $\{i\} \equiv \{E_i, J_i, T_i, \tau_i\}$ for sets of quantum numbers describing the states of initial and final nuclei. Here,

$$ w^{SJ}_{\ell\tau} = \sum_{L',S'} \langle l_1 l_2 : L'S'JT \big| V_w \big| \tau l, s_\Lambda : L = lSJ \rangle \qquad (4) $$

are **unknown** matrix elements of "weak interaction" to be extracted from partial transition widths. The factor $G_{\mathcal{J}}$, the ΛN pair FPC, is equal to

$$ G_{\mathcal{J}}(\{c\}, \{i\}, \tau lSJ) \qquad (5) $$

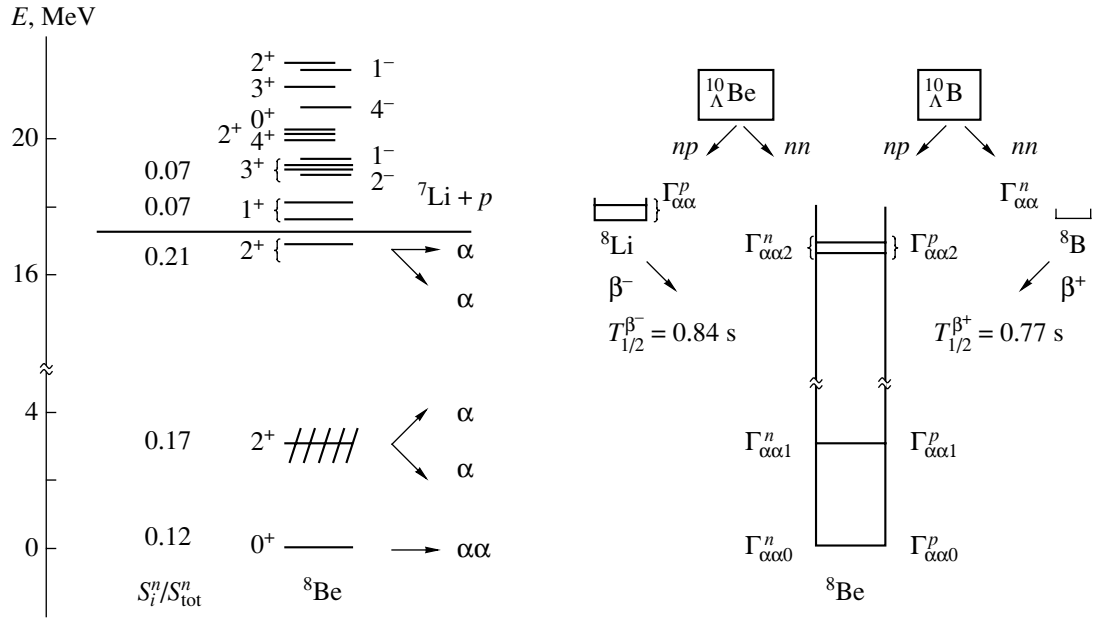

(Left panel) Pattern of the ^{8}Be spectra produced in the ^{9}Be$(p,d)^8$Be* reaction. (Right panel) $\alpha\alpha$ decay of $^{10}_{\Lambda}$Be and $^{10}_{\Lambda}$B hypernuclei and notation of $\Gamma^{\tau}_{\alpha\alpha i}$.

$$= \sum_j U\left(Jj\mathcal{J}\frac{1}{2} : J_cJ\right) U\left(l\frac{1}{2}J\frac{1}{2} : jS\right) S_i(\tau lj),$$

where $S_i(\tau lj)$ are spectroscopic amplitudes for the separation of one nucleon from the ground state of the nucleus: $S_i(\tau lj) = \sqrt{k}\left(T_i\tau_i\frac{1}{2}\tau\middle|T_c\tau_c\right) g^{E_cJ_cT_c}_{E_iJ_iT_i}(lj)$, and $g^c_i(lj)$ is a one-nucleon FPC in the intermediate coupling:

$$g^c_i(lj) = \sum_{f_cL_cS_c}\sum_{f_iL_iS_i} a^{E_cJ_cT_c}_{f_cL_cS_c} a^{E_iJ_iT_i}_{f_iL_iS_i} \qquad (6)$$

$$\times \langle l^k[f_c]L_cS_cT_c\{|l^{k-1}[f_i]L_iS_iT_i\rangle \begin{pmatrix} L_i & S_i & J_i \\ l & \frac{1}{2} & j \\ L_c & S_c & J_c \end{pmatrix}.$$

The coefficients $a^{E_cJ_cT_c}_{f_cL_cS_c}$ are results of the shell-model Hamiltonian diagonalization [17].

There are only four $|p_js_\Lambda : J\rangle$ states, $p_{\frac{1}{2}}s_\Lambda$ with $J = 0$, 1 and $p_{\frac{3}{2}}s_\Lambda$ with $J = 1$, 2, or, in an LS coupling scheme, $^1P_1$, $^3P_0$, $^3P_1$, and $^3P_2$. Hence, the partial widths of nonmesonic decay of p-shell hypernuclei for transition into natural parity states are linear combinations of four matrix elements $w^{10}_{1\tau}$ ($^3P_0$), $w^{01}_{1\tau}$ ($^1P_1$), $w^{11}_{1\tau}$ ($^3P_1$), and $w^{12}_{1\tau}$ ($^3P_2$) only. From Eqs. (3) and (5), one can easily see that partial widths corresponding to different J_i values are determined by quite definite (and different) combinations of matrix elements $w^{SJ}_{1\tau}$. The coefficients of these combinations for our case $\left(J_c = \frac{3}{2},\ \mathcal{J} = 1\right)$ are given in Table 1.

As a result, in an ideal case when the transitions to final states with $J_i = 0$, 1, 2, and 3 are observed, one can unambiguously determine all four matrix elements $w^{SJ}_{1\tau}$. The nuclear residual interaction accounted for by the many-particle shell model influences the relative $g_{\frac{1}{2}}$ and $g_{\frac{3}{2}}$ quantities.

Now we should discuss one important question: What is the role of nuclear structure in the partial widths $\Gamma^{\tau}_{\alpha\alpha i}$, or how do the obtained matrix elements depend on the nuclear "residual" interaction employed in calculations of the wave functions for $A = 9$ and $A = 8$ nuclei? To answer this question, we will use standard approaches of the many-particle nuclear shell model: the spectra and wave functions

Table 1. The spin structure of the fractional parentage coefficient of ΛN pair

J_i	$^3P_0$	$^1P_1$	$^3P_1$	$^3P_2$
0		$\sqrt{\frac{2}{3}}g_{\frac{3}{2}}$	$\sqrt{\frac{1}{3}}g_{\frac{3}{2}}$	
1	$\sqrt{\frac{2}{3}}g_{\frac{1}{2}}$	$-\sqrt{\frac{1}{9}}g_{\frac{1}{2}} + \sqrt{\frac{5}{9}}g_{\frac{3}{2}}$	$\sqrt{\frac{2}{9}}g_{\frac{1}{2}} + \sqrt{\frac{5}{18}}g_{\frac{3}{2}}$	$\sqrt{\frac{1}{6}}g_{\frac{3}{2}}$
2		$-\sqrt{\frac{1}{3}}g_{\frac{1}{2}} + \sqrt{\frac{1}{3}}g_{\frac{3}{2}}$	$\sqrt{\frac{2}{3}}g_{\frac{1}{2}} + \sqrt{\frac{1}{6}}g_{\frac{3}{2}}$	$\sqrt{\frac{1}{2}}g_{\frac{3}{2}}$
3				$g_{\frac{3}{2}}$

Table 2. FPC of Λn pair in $^{10}_{\Lambda}$Be, Eq. (7), calculated with different parametrizations of the Hamiltonian of the many-particle nuclear shell model (the states of ^{8}Be are labeled by $J^{\pi}_{i}T_{i}$ and E_{i} [MeV])

Nuclear model		$0^{+}0, 0.0$		$2^{+}0, 3.0$		$2^{+}0+1, 16.7$	
		ν_0	G_0	ν_1	G_1	ν_2	G_2
CK_I	[18]	0.580	0.667	0.726	0.515	0.930	0.096
CK_{II}	[18]	0.581	0.667	0.728	0.515	0.970	0.105
Barker	[17]	0.549	0.667	0.753	0.458	0.937	0.091
PBA_I	[19]	0.591	0.667	0.705	0.537	0.923	0.096
WB	[20]	0.549	0.667	0.776	0.458	0.936	0.103
					≈ 0.5		≈ 0.1

of nuclear excited states are obtained by the diagonalization of the Hamiltonian matrix. The parameters of the residual two-body interaction used were determined by the fit of a large amount of experimental spectroscopic data on a range of p-shell nuclei [18]. Table 2 illustrates the influence of a nuclear model on the calculated spectroscopic factors. We present there

$$G^2_{\mathcal{J}}(\{c\},\{i\},{}^1P_1) = \nu_i G_i \qquad (7)$$

with G_i for weight of the singlet state of the ΛN pair and ν_i for normalization factor ($\sum_i \nu_i = 5(1+1/8)$ is the effective number of $1p$-shell nucleons). The models used employ the full $1p$-shell space and differ only in the nuclear residual interactions. We have selected several models usually used in the calculations of characteristics of $1p$-shell nuclei. The calculations were performed with the many-particle shell-model code `OXBASH` [21].

4. WHAT "ALPHA-DECAY" WIDTHS TELL US

As we pointed out above, the detection of correlated $\alpha\alpha$ pairs from the decay of $^{10}_{\Lambda}$Be and $^{10}_{\Lambda}$B allows one to determine all necessary matrix elements $w^{SJ}_{l\tau}$ and describe the nonmesonic decay of p-shell hypernuclei.

This is very complicated task and several complementary experiments should be carried out. However, measurement of even a few partial widths opens the way for the phenomenological analysis of matrix elements of weak interaction and reveals its peculiarities.

Here, we discuss that one can obtain information about nonmesonic weak interaction from the α decay of $^{10}_{\Lambda}$Be and $^{10}_{\Lambda}$B, which will be measured in the experiment approved at the Nuclotron in the Joint Institute for Nuclear Research, Dubna, Russia.

Table 3. The possible $\Lambda N \to nN$ transitions in s-shell hypernuclei

Transition	T_f	ΔS	Parity
${}^1S_0 \to {}^1S_0$	1	0	PC
${}^1S_0 \to {}^3P_0$	1	1	PV
${}^3S_1 \to {}^3S_1$	0	0	PC
${}^3S_1 \to {}^1P_1$	0	1	PV
${}^3S_1 \to {}^3P_1$	1	0	PV
${}^3S_1 \to {}^3D_1$	0	0	PC tensor

Our starting point is phenomenological analysis developed forty years ago by Block and Dalitz [22] for the study of nonmesonic decay of the s-shell hypernuclei. In the s-shell hypernuclei, the pair ΛN can be in the state with total orbital moment $L=0$ only. The total angular moment J, which is conserved by the weak interaction, is equal to the pair total spin, S. The final states of nucleons produced in the nonmesonic weak decay are shown in Table 3. We would like to stress that the weak interaction Λ hyperon with a neutron with production of two neutrons ($T_f = 1$) is possible for certain states only. For example, the neutron yield will be suppressed for one-pion exchange, where the ${}^3S_1 \to {}^3D_1$ transition dominates. Total widths of nonmesonic decays of four s-shell hypernuclei $^{3}_{\Lambda}$H, $^{4}_{\Lambda}$H, $^{4}_{\Lambda}$He, and $^{5}_{\Lambda}$He have been expressed by Block and Dalitz [22] as the sums of four rates $R_{\tau S}$:

$$\Gamma_{\rm nm}(^{3}_{\Lambda}{\rm H}) = (\rho_3/8)\ (3R_{n0} + 1R_{n1} + 3R_{p0} + 1R_{p1}), \qquad (8)$$

$$\Gamma_{\rm nm}(^{4}_{\Lambda}{\rm H}) = (\rho_4/6)\ (1R_{n0} + 3R_{n1} + 2R_{p0}) \equiv \Gamma^n_{\rm H} + \Gamma^p_{\rm H},$$

$$\Gamma_{\rm nm}(^{4}_{\Lambda}{\rm He}) = (\rho_4/6)\ (2R_{n0} + 1R_{p0} + 3R_{p1}) \equiv \Gamma^n_{\rm He} + \Gamma^p_{\rm He},$$

$$\Gamma_{\rm nm}(^{5}_{\Lambda}{\rm He}) = (\rho_5/8)\ (1R_{n0} + 3R_{n1} + 1R_{p0} + 3R_{p1}),$$

where ρ_A is the nucleon density of the nuclear core. The $R_{\tau J}$ are simply connected with the rates of associated partial wave transitions from Table 3:

$$R_{n0} = R_n({}^1S_0) + R_n({}^3P_0),$$
$$R_{p0} = R_p({}^1S_0) + R_p({}^3P_0),$$
$$R_{n1} = R_n({}^3P_1),$$
$$R_{p1} = R_p({}^1S_1) + R_p({}^1P_1) + R_p({}^3P_1) + R_p({}^3D_1).$$

From (8), some simple relations between the widths

Table 4. Ratios $\gamma_i^{n/p}$ ($A = 10$) and R_{n0}/R_{p0} ($A = 4$) calculated for different models of weak interaction

	OME [23]			TPE [24]			HQ [25]			PH [26]	
	π	PS	+PV	V_π	$+V_{2\pi/\rho}$	$+V_{2\pi/\sigma}$	$\pi + K$	DQ	all	AG1	AG2
$\gamma_1^{n/p}$	0.25	0.56	3.22	0.14	0.25	0.63	0.50	1.12	0.65	0.87	1.07
$\gamma_2^{n/p}$	0.13	0.51	3.26	0.08	0.19	0.28	0.44	1.41	0.75	1.06	0.90
R_{n0}/R_{p0}	2.0	2.0	2.0	2.0	2.5	2.0	1.8	0.85	0.13	0.6	2.0

of nonmesonic decays of s-shell hypernuclei follow:

$$\frac{R_{n0}}{R_{p0}} = \frac{\Gamma^n_{\rm He}}{\Gamma^p_{\rm H}}, \quad \frac{R_{n1}}{R_{n0}} = \frac{1}{3}\left(2\frac{\Gamma^n_{\rm H}}{\Gamma^n_{\rm He}} - 1\right), \quad (9)$$
$$\frac{R_{p1}}{R_{p0}} = \frac{1}{3}\left(2\frac{\Gamma^p_{\rm He}}{\Gamma^p_{\rm H}} - 1\right).$$

Recently, the values of $\Gamma^\tau({}^4_\Lambda{\rm H})$ and $\Gamma^\tau({}^4_\Lambda{\rm He})$ were calculated with several models of weak interactions (one-meson exchange [23], two-pion exchange [24], hybrid quark [25]) between hyperons and nucleons. And it is possible now to extract ratios of $R_{\tau S}$ from theoretical $\Gamma^\tau({}^4_\Lambda{\rm H})$ and $\Gamma^\tau({}^4_\Lambda{\rm He})$ values.

In order to compensate the small number of quantities measured at the Nuclotron, we have to simplify expression (3) for partial width Γ^τ_i. The authors of recent calculations [16, 24] show that the contribution of the decay rates from ΛN in the state with relative $l = 1$ is only $\approx 5\%$ of the total rates for the ${}^{12}_\Lambda$C hypernucleus, so we neglect them for a moment. Now we can write an extremely simple expression for $\tilde\Gamma^\tau_i$:

$$\tilde\Gamma^\tau_i = \kappa[G_i R_{\tau 0} + (1 - G_i)R_{\tau 1}]. \quad (10)$$

Here, κ absorbs all radial dependences and G_i is from Table 2. The benefit of such an oversimplification is a possibility of relating decay rates for $A = 10$ hypernuclei to decay rates for s-shell hypernuclei ${}^4_\Lambda$H and ${}^4_\Lambda$He. The ratios

$$\gamma_i^{n/p} \equiv \frac{\tilde\Gamma^n_{\alpha\alpha i}({}^{10}_\Lambda{\rm Be})}{\tilde\Gamma^p_{\alpha\alpha i}({}^{10}_\Lambda{\rm B})} = \frac{R_{n0}}{R_{p0}}\frac{G_i + (1 - G_i)(R_{n1}/R_{n0})}{G_i + (1 - G_i)(R_{p1}/R_{p0})} \quad (11)$$

depend on single structure characteristic G_i. However, G_i differs strongly for two states in ^{8}Be: $G_1 = 0.5$ for the state at $E = 3$ MeV and $G_2 = 0.1$ for states at $E = 16.7$ MeV (Table 2). This opens the way to estimate the possibility of the Nuclotron experiment to select the proper model of weak interaction. In Table 4, we display ratios $\gamma_1^{n/p}$ and $\gamma_2^{n/p}$ with $R_{\tau S}$ calculated within different models [23–25] or obtained from phenomenological analysis [26].

5. CONCLUSION

It is shown that the spin structure of the weak nonmesonic process $\Lambda N \to nN$ can be studied in partial $\alpha\alpha$ decays of hypernuclei ${}^{10}_\Lambda$Be and ${}^{10}_\Lambda$B due to specific cluster properties of core nuclei ^{9}Be and ^{9}B. The ratio $\gamma_i^{n/p}$, introduced in this paper, is very sensitive to the model of the weak interaction $\Lambda N \to nN$. Also, this ratio reveals a small sensitivity to the choice of nuclear residual interaction employed in the calculations. For this reason, even the first results expected in the planned experiment at the JINR Nuclotron can play a decisive role in selecting the proper model of weak $\Lambda N \to nN$ interaction.

ACKNOWLEDGMENTS

The present investigation was supported by the Votruba–Blokhintsev Program. The work of L.M. has been supported in part by the Grant Agency of the Czech Republic, grant no. 2002/02/0930.

REFERENCES

1. M. Danysz and J. Pniewski, Philos. Mag. **44**, 348 (1953).
2. M. I. Podgoretsky, Zh. Éksp. Teor. Fiz. **44**, 695 (1963).
3. G. C. Bonazzola, T. Bressani, *et al.*, Phys. Lett. B **53B**, 297 (1974).
4. B. Povh, Annu. Rev. Nucl. Part. Sci. **28**, 1 (1978).
5. R. E. Chrien and C. B. Dover, Annu. Rev. Nucl. Part. Sci. **39**, 113 (1989).
6. H. Bandō, T. Motoba, and J. Žofka, Int. J. Mod. Phys. A **5**, 4021 (1990).
7. E. Oset and A. Ramos, Prog. Part. Nucl. Phys. **41**, 191 (1998).
8. W. M. Alberico and G. Garbarino, Phys. Rep. **369**, 1 (2002).
9. H. Bhang *et al.,* Phys. Rev. Lett. **81**, 4321 (1998).
10. L. Majling and Yu. Batusov, Nucl. Phys. A **691**, 185c (2001).
11. F. Ajzenberg-Selove, Nucl. Phys. A **490**, 1 (1988).
12. G. Bohm *et al.,* Nucl. Phys. B **74**, 237 (1974).
13. M. I. Podgoretsky, in *Nuclotron and Relativistic Nuclear Physics* (Dubna, 1974), JINR-8309, p. 81.

14. J. Lukstins, Nucl. Phys. A **691**, 491c (2001).
15. L. Majling *et al.,* Czech. J. Phys. **53**, 667 (2003).
16. A. Parreño, A. Ramos, and C. Bennhold, Phys. Rev. C **56**, 339 (1997); A. Parreño and A. Ramos, Phys. Rev. C **65**, 015204 (2002).
17. F. C. Barker, Nucl. Phys. **83**, 418 (1966).
18. S. Cohen and D. Kurath, Nucl. Phys. **73**, 1 (1965).
19. F. C. Barker, Aust. J. Phys. **34**, 7 (1981).
20. E. K. Warburton and B. A. Brown, Phys. Rev. C **46**, 923 (1992).
21. B. A. Brown *et al.*, MSUCL-524 (Michigan, USA, 1986).
22. M. M. Block and R. H. Dalitz, Phys. Rev. Lett. **11**, 96 (1963).
23. F. Krmpotić and T. Tadić, Braz. J. Phys. **33**, 187 (2003); nucl-th/0212040.
24. K. Itonaga, T. Ueda, and T. Motoba, Phys. Rev. C **65**, 034617 (2002).
25. K. Sasaki, T. Inoue, and M. Oka, Nucl. Phys. A **707**, 477 (2002).
26. W. M. Alberico and G. Garbarino, Phys. Lett. B **486**, 362 (2000).

Physics of Atomic Nuclei, Vol. 67, No. 10, 2004, pp. 1810–1817. From Yadernaya Fizika, Vol. 67, No. 10, 2004, pp. 1838–1844.

Proceedings of the International Conference "Nuclear Structure and Related Topics"

Structures and Decay of Deep-Hole States in Light Nuclei Populated by the $(p, 2p)$ Reactions*

M. Yosoi[1)], H. Akimune[2)], I. Daito[3)], H. Ejiri[4)], H. Fujimura[3)], M. Fujiwara[3)], K. Hara[3)], K. Y. Hara[2)], T. Ishikawa[1),5)], M. Itoh[3)], Y. Itow[6)], T. Kawabata[3),7)], K. Kobayashi[6)], M. Nakamura[1)], T. Noro[8)], E. Obayashi[3)], H. Sakaguchi[1)], Y. Sakemi[3)], M. Shiozawa[6)], H. Takeda[1),9)], T. Taki[1)], A. Tamii[3)], H. Toyokawa[4)], N. Tsukahara[1)], M. Uchida[3)], T. Yamada[10)], Y. Yasuda[1)], H. P. Yoshida[3)], and R. G. T. Zegers[3),11)]**

Received January 21, 2004

Abstract—Decay particles from the s-hole states in ^{11}B and ^{15}N have been measured in coincidence with the quasifree ^{12}C$(p, 2p)$ and ^{16}O$(p, 2p)$ reactions at $E_p = 392$ MeV. Triton decay is found to be dominant for the ^{11}B(s-hole) state and also found to be larger than α decay for the ^{15}N(s-hole) state despite its smaller Q value compared to α decay. Measured decay branching ratios are discussed in comparison with the results of statistical-model, $SU(3)$-model, and shell-model calculations. The energy spectra around the s-hole states in both ^{11}B and ^{15}N exhibit some bumplike structures, which can be qualitatively explained by recent shell-model calculations for both nuclei. © *2004 MAIK "Nauka/Interperiodica"*.

1. INTRODUCTION

Quasifree scattering is one of the most direct ways of investigating both the single-particle properties in a nucleus and the nature of the strong interaction in the nuclear medium. The first kind of quasifree scattering reaction to be studied extensively was of the form $^{A}Z(p, 2p)^{A-1}(Z-1)$, which is then interpreted as a direct knockout of a proton bound in the ^{A}Z nucleus by a fast incident proton, and the $^{A-1}(Z-1)$ remains in a one-hole state. After the first $(p, 2p)$ experiment by Chamberlain and Segrè [1], quasifree proton knockout reactions were systematically measured using proton beams at medium energies [2, 3] and, later, plenty of quasifree $(e, e'p)$ investigations were also performed [4]. However, for deep-hole states, only the macroscopic structures like separation energies ($E_{\rm sep}$) and total widths (Γ) are obtained. Detailed structures and fragmentation mechanisms of deep-hole states have been little known even for light nuclei until now, while interests in decay characters of s-hole states in light nuclei have been newly aroused through the study of the production of hypernuclei [5, 6] and the relation to the nucleon decay search [7, 8].

The $1s$-hole states are observed as broad bumps in the highly excited energy region above 20 MeV. It is estimated that the ratio of the nuclear radius to the mean free path of a $1s$ hole is about or less than 1 in p-shell nuclei and larger than 1 in heavy nuclei [9]. These results indicate that the s-hole states in light nuclei may have large escape widths ($\Gamma^{\uparrow}$) and that the spreading widths ($\Gamma^{\downarrow}$) are dominant in heavy nuclei. Yamada *et al.* [9] recently calculated spectroscopic factors and partial decay widths for two-body cluster decay processes from the doorway s-hole states of ^{11}B and ^{15}N in the framework of the microscopic cluster model with $SU(3)$ wave functions. The description of the s-hole state is based on the fact that the doorway s-hole state produced by the

*This article was submitted by the authors in English.

[1)]Department of Physics, Kyoto University, Kyoto, Japan.
[2)]Department of Physics, Konan University, Kobe, Japan.
[3)]Research Center for Nuclear Physics, Osaka University, Osaka, Japan.
[4)]Japan Synchrotron Radiation Research Institute, Sayo, Hyogo, Japan.
[5)]Present address: Laboratory of Nuclear Science, Tohoku University, Sendai, Japan.
[6)]Institute for Cosmic Ray Research, University of Tokyo, Kashiwa, Japan.
[7)]Present address: Center for Nuclear Study, University of Tokyo, Hongo, Tokyo, Japan.
[8)]Department of Physics, Kyushu University, Fukuoka, Japan.
[9)]Present address: RI Beam Science Laboratory, RIKEN, Wako, Japan.
[10)]Laboratory of Physics, Kanto Gakuin University, Yokohama, Japan.
[11)]Present address: NSCL/MSU, East Lansing, USA.
[**]e-mail: yosoi@ne.scphys.kyoto-u.ac.jp

quasifree knockout reactions should have the same spatial symmetry as the ground state of the target nucleus, whose wave function is well described by the $SU(3)$-cluster model in light nuclei. The authors showed in their $SU(3)$-model calculation that a selection rule owing to the spatial symmetry is valid for fragmentation of s-hole states in light nuclei: n, p, d, t, and ^{3}He fragments are allowed, while fragments such as the α particle and heavier particles are forbidden. On the other hand, since the Q values for α fragments in most light nuclei are larger than those for other cluster decay channels, α decay is favored in the statistical decay process.

In the present work, particle decays from the quasifree proton-knockout reactions on ^{12}C and ^{16}O are studied to understand the structures and fragmentation mechanisms of the s-hole states in ^{11}B and ^{15}N. The $(p, 2p)$ reaction at intermediate energies is well described by the direct reaction picture and is flexible enough to choose the proper kinematics to enhance the s-hole state.

2. EXPERIMENTAL PROCEDURE AND RESULTS

The experiment was carried out at the Research Center for Nuclear Physics (RCNP), Osaka University, by using a 392-MeV proton beam accelerated by the AVF and Ring cyclotrons. The quasifree $(p, 2p)$ reaction was measured with the dual spectrometer system consisting of the high-resolution spectrometer Grand Raiden (GR) [10] and the large-acceptance spectrometer (LAS) [11]. GR was set at the most possible forward angle (25.5°) for the $(p, 2p)$ mode and detected protons with higher energies, taking into account the difference of the momentum acceptance of GR (5%) and LAS (30%). The laboratory angle of LAS and the magnetic fields of the spectrometers were determined to satisfy the zero-recoil momentum condition at the central energy of the $1s_{1/2}$-knockout bump, where the cross section leading to the s-hole state is maximal. Two multiwire drift chambers in each focal plane of both spectrometers determined the positions and the incidence angles of particles. Particle identification was provided by the ΔE signals from plastic scintillation counters, which were also used for trigger signals. We separated the experiment into two parts. In the first beam time, charged particle decay of the s-hole states in both ^{11}B and ^{15}N was measured in coincidence with the quasifree ^{12}C$(p, 2p)$ and ^{16}O$(p, 2p)$ reactions, and neutron decay of the s-hole state in ^{15}N was measured in the second beam time.

In the measurements of charged-particle decay, one generally needs a thin target because the energy losses of the emitted particles like α in the target are not negligible. We used a natural carbon target with a thickness of 0.5 mg/cm^2 for the ^{12}C$(p, 2p)$ reaction. A quartz glass (SiO_2) target and a natural silicon (Si) target each with thickness of about 2 mg/cm^2 were employed for the ^{16}O$(p, 2p)^{15}$N reaction, and the cross section was obtained after subtracting the Si target runs from the SiO_2 runs. Charged particles decaying from the highly excited states in ^{11}B and ^{15}N were measured in sixteen telescopes of ΔE–E Si solid-state detectors (SSD) in coincidence with the two protons of the $(p, 2p)$ reaction. Each telescope consisted of a thin (20, 50, or 100 μm) ΔE SSD and a thick (5000 μm) E Si(Li) detector. Eight 20-μm ΔE detectors were used for the identification of α particles with $E_\alpha \geq 4.5$ MeV. The 50-μm and 100-μm ΔE detectors were used for identification of protons, deuterons, and tritons. The SSD telescopes were mounted on a copper frame of a hemispherical shape and placed in the scattering chamber at backward angles. The total solid angle of the SSD array was 3.5% of 4π. In order to reduce the leakage current, the SSD system was cooled to about −20°C with four Peltier elements. The experimental details and the results for the charged-particle decay of the ^{11}B(s-hole) state were already reported in [12].

In the measurements of neutron decay, we used a newly constructed small scattering chamber made of thin stainless steel with a 4-mm thickness and a neutron multidetector array system previously developed at RCNP [13], which consisted of, at maximum, 48 BC-501A liquid scintillators. In the present experiment, 30 scintillators were employed and placed at a distance of 2 m from the target. The energy of each neutron was determined with the time-of-flight (TOF) methods. The neutron-decay measurements were carried out only for the ^{16}O$(p, 2p)$ reaction. In the detection of decay neutrons, the thickness of the target is not a serious problem, but the detection efficiency and the solid angle are small compared to the charged-particle decay measurements. Therefore, we adopted an H_2O ice sheet as a background-free oxygen target, which was recently developed by Kawabata *et al.* [14]. The ice target with a thickness of 40 mg/cm^2 was cooled down to below 140 K by liquid nitrogen, where the loss of the target material by the sublimating process is negligible.

Excitation energy spectra of the hole states obtained by summing up the energies of two emitted protons are shown in Fig. 1*a* for the ^{12}C$(p, 2p)^{11}$B reaction and in Fig. 2*a* for the ^{16}O$(p, 2p)^{15}$N reaction. The differential cross sections are calculated with $\Delta\Omega_1 = 4.3$ msr, $\Delta\Omega_2 = 20.0$ msr, and $\Delta E_1 = 12.5$ MeV. The systematic errors of the absolute cross sections are estimated to be 10 to 15%, which are due

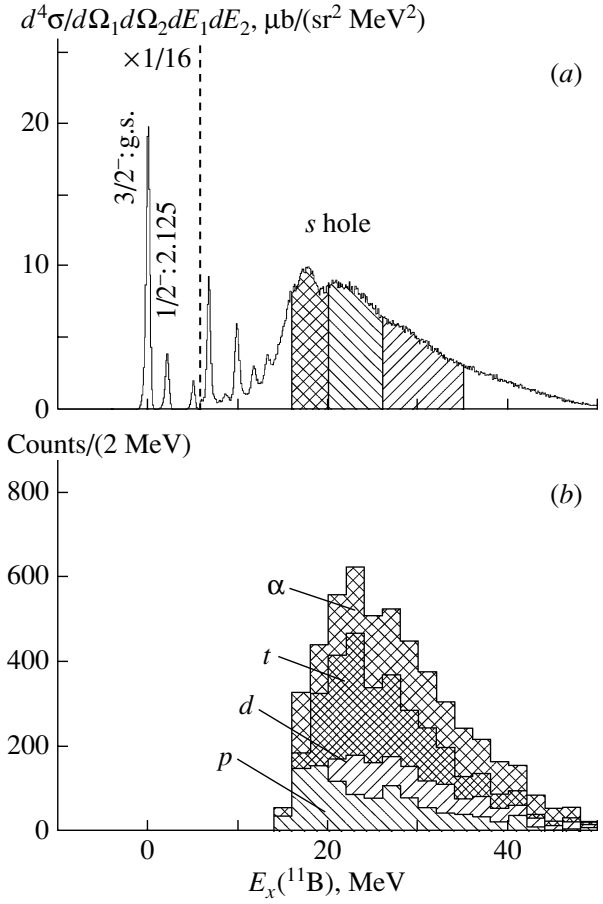

Fig. 1. (*a*) Energy spectrum of the differential cross section of ^{11}B produced by the ^{12}C$(p, 2p)^{11}$B* reaction at $E_p = 392$ MeV. (*b*) Excitation energy spectra of ^{11}B in coincidence with decay charged particles. The contributions of the p, d, t, and α decays are shown separately.

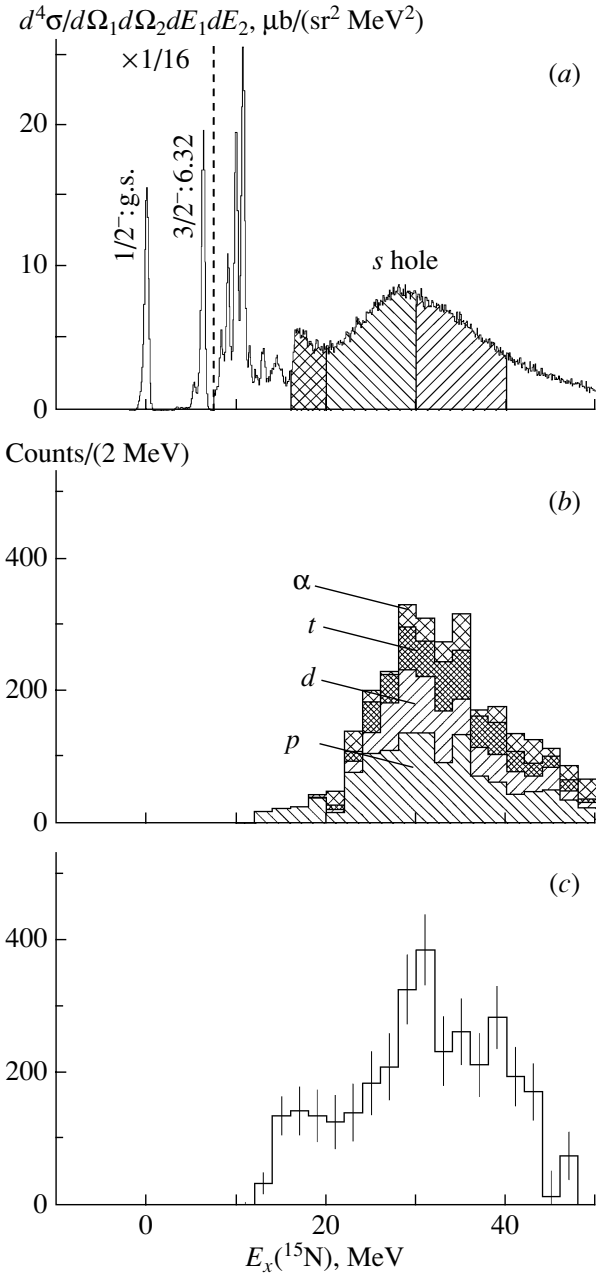

Fig. 2. (*a*) Energy spectrum of the differential cross section of ^{15}N produced by the ^{16}O$(p, 2p)^{15}$N* reaction at $E_p = 392$ MeV. (*b*) Excitation energy spectra of ^{15}N in coincidence with decay charged particles. The contributions of the p, d, t, and α decays are shown separately. (*c*) Excitation energy spectrum of ^{15}N in coincidence with decay neutrons.

to the uncertainties of the target thickness (including contaminant subtractions) and charge collections and the acceptance normalization. Several discrete p-hole states, such as the ground state ($3/2^-$) and the first excited state (2.125 MeV, $1/2^-$) in ^{11}B and the ground state ($1/2^-$) and the third excited state (6.32 MeV, $3/2^-$) in ^{15}N, are observed with an energy resolution of 450 keV (FWHM). The s-hole states are strongly excited in the higher excitation energy region. The bump corresponding to the s-hole state in both ^{11}B and ^{15}N obviously splits into several components.

In the higher end of excitation energies, the detection efficiencies decrease gradually in both reactions due to the finite momentum acceptance of the spectrometers. Moreover, in the decay measurements, the decay particles were detected mostly for excitation energy above ~ 16 MeV. Therefore, the hatched regions of the s-hole states in both Fig. 1*a* and Fig. 2*a* are studied in the decay analysis, which are further separated into three regions in order to investigate the substructures of the s-hole states.

The coincidence spectra with decay charged particles for the ^{12}C$(p, 2p)$ reaction are shown in Fig. 1*b*. Accidental coincidence events were subtracted. The

threshold energies of two-body decay from ^{11}B to the channels $^{10}\mathrm{B}+n$, $^{10}\mathrm{Be}+p$, $^{9}\mathrm{Be}+d$, $^{8}\mathrm{Be}+t$, $^{8}\mathrm{Li}+{}^{3}\mathrm{He}$, and $^{7}\mathrm{Li}+\alpha$ are 11.5, 11.2, 15.8, 11.2, 27.2, and 8.7 MeV, respectively. The ^{3}He-decay events, which are hardly expected due to its large threshold energy, are included in the α-decay portion. It is apparent in Fig. 1*b* that the triton contribution is the largest, although the Q value is smaller than that of α decay. The branching ratios are calculated under the assumption that the decay from the s-hole state is isotropic:

$$\mathrm{Br}_i = \frac{\int n_i(4\pi/\Delta\Omega_{\mathrm{SSD}})dE_x}{\int N dE_x}, \qquad (1)$$
$$i = (n), p, d, t, \text{ and } \alpha,$$

where N is the number of events of the $(p,2p)$ reaction, n_i is the number of particles detected for i decay, and E_x is the excitation energy of the s-hole state.

From the projection of two-dimensional spectra of the energies of decay particles versus the excitation energy E_x of ^{11}B, the peaks populating low-lying states up to the excitation energy of about 5 MeV in each residual daughter nucleus indicate that those events occur mainly through a binary decay process. We define the two-body decay region in each decay channel of the ^{11}B(s-hole) state as $E_x(\mathrm{res}) \leq \max(5\ \mathrm{MeV}, E_{\mathrm{th}}(3\text{-body}))$, where E_x(res) indicates the excitation energy relative to the ground state and E_{th}(3-body) denotes the threshold energy of particle decay in the residual nucleus. The branching ratio of the two-body decay to the low-lying states of the residual nucleus is calculated for this region. Events outside of the two-body decay region consist of mainly the three-body decay and sequential decay processes. It should be noted that, for particles with small E_{th}(3-body), the three-body decay and sequential decay processes are partially included in the two-body decay region defined above.

The coincidence spectra with decay particles for the $^{16}\mathrm{O}(p,2p)$ reaction are shown in Figs. 2*b* and 2*c* for charged particles and neutrons, respectively. The threshold energies of two-body decay from ^{15}N to the channels $^{14}\mathrm{N}+n$, $^{14}\mathrm{C}+p$, $^{13}\mathrm{C}+d$, $^{12}\mathrm{C}+t$, $^{12}\mathrm{B}+{}^{3}\mathrm{He}$, and $^{11}\mathrm{B}+\alpha$ are 10.8, 10.2, 16.2, 14.8, 28.2, and 11.0 MeV, respectively. The ^{3}He-decay events are also included in the α-decay portion. In Fig. 2*b*, it is found that the α-decay contribution is very small. The branching ratios are calculated using Eq. (1) for the range between 16 and 40 MeV. In the region of $E_x \leq 20$ MeV, however, d and t decays could not be measured due to the lower limits of the detectable energies. The branching ratios of the decay to the low-lying states of the residual nuclei are calculated similarly in the case of ^{11}B. The two-body decay region in each decay channel is defined as $E_x(\mathrm{res}) \leq \max(8\ \mathrm{MeV}, E_{\mathrm{th}}(3\text{-body}))$. The three-body decay and sequential decay processes are almost excluded in the two-body decay region, except for d decay with the three-body decay threshold energy of 5.0 MeV.

3. COMPARISON WITH THEORETICAL CALCULATIONS

In Fig. 3, the experimental branching ratios of decay particles from the excitation energy region of 16–35 MeV in ^{11}B and of 20–40 MeV in ^{15}N are shown, respectively, together with the results of a statistical-model calculation with the code CASCADE [15]. The transmission coefficients were calculated with the global optical potential parameters of [16–20], which are well suited for light nuclei. Energy levels known below 12-MeV excitation energy were explicitly included for all nuclei ($6 \leq A \leq 16$) necessary for the calculation, while the levels of higher excitation energies were calculated using level-density parameters given in the code. In the CASCADE calculations, decay particles above the experimental detection thresholds were only employed to obtain the branching ratios. The branching ratios of the decay onto the two-body decay regions are also indicated in Fig. 3 with dark areas.

In the case of the ^{11}B(s-hole) state, the measured branching ratios of both t decay and α decay are much larger than those of the statistical-model calculations. The experimental α decay in the two-body decay region is about one-half of the total α decay, indicating that contributions of the sequential decay and three-body decay processes are large in this channel. Actually, the $\alpha+\alpha+t$ three-body decay channel has a very low threshold energy of 11.2 MeV and may compete against the two-body decay process, while the statistical-model calculations include only the two-body decay and sequential decay processes. This suggests that the three-body decay process could contribute significantly to the branching ratios of α decay. However, even in the two-body decay regions, the t-decay strength is still dominant. Furthermore, the relative ratio of the t decay to the α decay in the experiment is opposite to that of the statistical calculations as well as the ratio of the p decay to the d decay.

In the case of the s-hole state in ^{15}N, the three-body decay threshold is higher than those of the two-body n, p, d, t, and α decay. Moreover, the ground state of ^{16}O is more purely described as the $SU(3)(\lambda\mu) = (00)$ state. Thus, ^{15}N is more suitable to understand the microscopic structure and fragmentation mechanism of the s-hole state. In Fig. 3

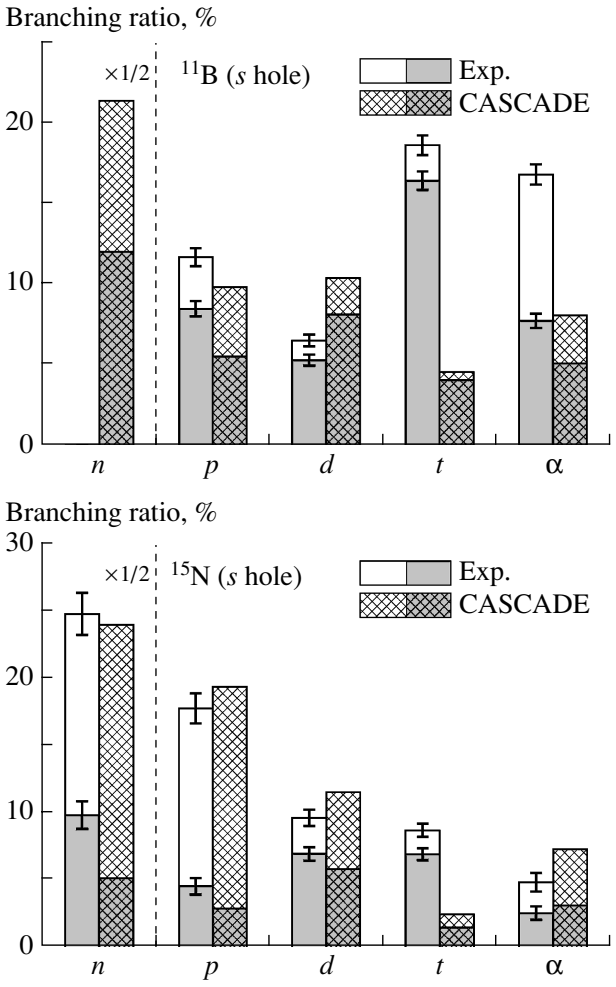

Fig. 3. Comparisons of the measured branching ratios of the n, p, d, t, and α decays from the excitation energy region of 16–35 MeV in ^{11}B and of 20–40 MeV in ^{15}N with those of the statistical-model calculation using the code CASCADE. The error bars shown include only statistical errors. The experimental branching ratio of the n decay is measured only for the ^{15}N(s-hole) state. The branching ratios of the decay onto the two-body decay regions are indicated with dark areas (see text).

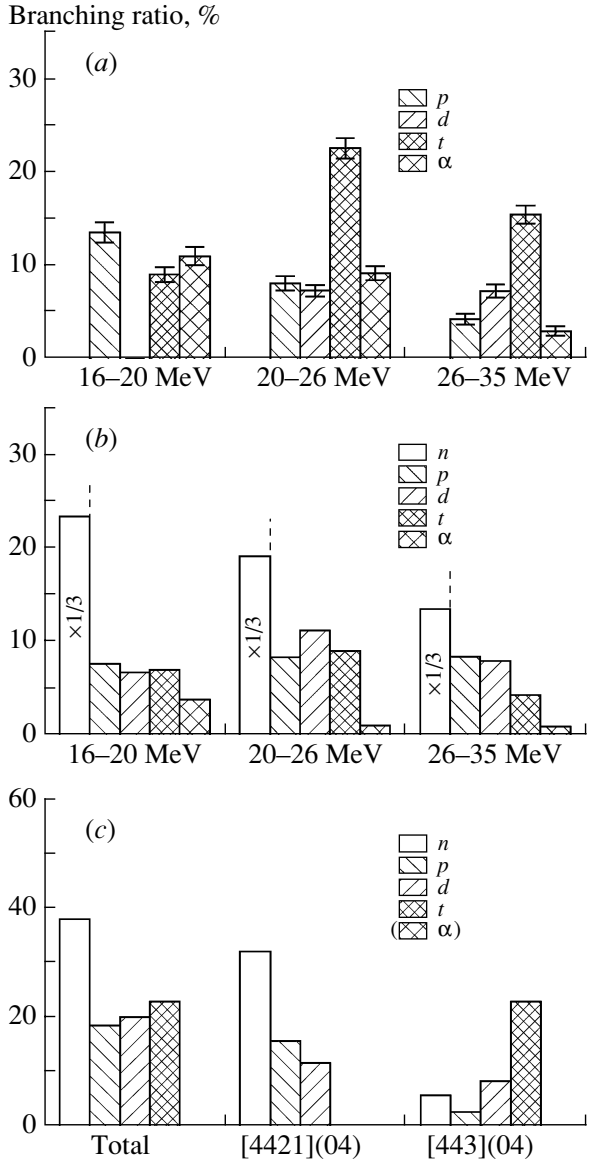

Fig. 4. (a) Experimental branching ratios of the p, d, t, and α decays onto the two-body decay regions from the three excitation energy regions of 16–20, 20–26, and 26–35 MeV in ^{11}B. (b) Branching ratios of the n, p, d, t, and α decays from the three excitation energy regions of 16–20, 20–26, and 26–35 MeV in ^{11}B obtained by the $1\hbar\omega$ shell-model calculations [21]. (c) Branching ratios of the n, p, d, t, and α decays from the doorway s-hole state in ^{11}B calculated by the $SU(3)$ model [9]. Branching ratios for the states with $[f](\lambda\mu) = [4421](04)$ and $[f](\lambda\mu) = [443](04)$ and total branching ratios are shown.

(bottom), the neutron fragments account for about half of the total decay fragments in both the measurements and the statistical-model calculations. Only the measured branching ratio of t decay is much larger than that of the statistical-model calculations. The n decay and p decay are considerably reduced in the two-body decay regions, suggesting the sequential decay processes are large in these channels. In the two-body decay regions, the measured n decay and t decay are larger than those of the statistical-model calculations, while the measured p, d, and α decays are reasonably well explained by the calculations. Although the large t decay compared to α decay supports the selection rule coming from the $SU(3)$ spatial symmetry, the portion of the statistical decay may be considerable for the ^{15}N(s-hole) state.

Figure 4a shows the branching ratios of p, d, t, and α decays in the two-body decay regions from the three excitation energy regions of 16–20, 20–

26, and 26–35 MeV in ^{11}B. The decay patterns from the respective regions suggested by the substructures are very different, indicating that the s-hole state in ^{11}B splits into some components with different microscopic structures. Owing to the detection threshold, the measured deuteron branching ratio is zero in the low-energy region. Predictions from the $SU(3)$ model [9] are shown in Fig. 4c, where the ^{11}B(s-hole) state has the same spatial symmetry as the ground state of ^{12}C, $SU(3)(\lambda\mu) = (04)$, and has two degenerated partition symmetries $[f] = [443]$ and $[4421]$. When the branching ratios of α decay are neglected, the experimental decay pattern of the 26–35 MeV region is similar to that of the $SU(3)[f](\lambda\mu) = [443](04)$ component. The first and second regions may have both the $SU(3)[f](\lambda\mu) = [4421](04)$ and $[443](04)$ components, whereas the mixing of the $[4421](04)$ component seems to decrease with increasing excitation energy.

Yamada [21] has recently made new calculations within the framework of the $1\hbar\omega$ shell model. The excitation spectrum of the ^{12}C$(p, 2p)$ and ^{16}O$(p, 2p)$ reaction was formulated within the impulse approximation, where calculated energy-dependent spectroscopic factors for the ^{12}C(g.s.) $\rightarrow p + {}^{11}$B(s-hole) and ^{16}O(g.s.) $\rightarrow p + {}^{15}$N(s-hole) processes were folded by a Lorentzian function. The result of the shell-model calculation shows that the s-hole state in ^{11}B splits into three parts. Although the calculated strength ratios of the three regions are different from the experimental results, the substructure of the s-hole state is reasonably well explained by the shell-model calculation. The energy dependence of the branching ratios for n, p, d, t, and α decays from the ^{11}B(s-hole) state was also calculated using the separation-energy method [22], where the partial decay width is defined as the product of the penetration factor and reduced width. As shown in Fig. 4b, the calculated branching ratio of the t decay is larger than that of the α decay, reflecting the selection rule as mentioned above. The enhancement of the t decay observed in the present experiment, however, is not reproduced by the shell-model calculation. Calculations including the direct three-body decay process will be needed to explain the experimental decay pattern.

Figure 5a shows the experimental branching ratios of n, p, d, t, and α decays in the two-body decay regions from the three excitation energy regions of 16–20, 20–30, and 30–40 MeV in ^{15}N. The decay patterns between the lower region and higher region of the bump with the mean energy of 28 MeV are very different, indicating that this s-hole bump in ^{15}N includes a few components with different microscopic

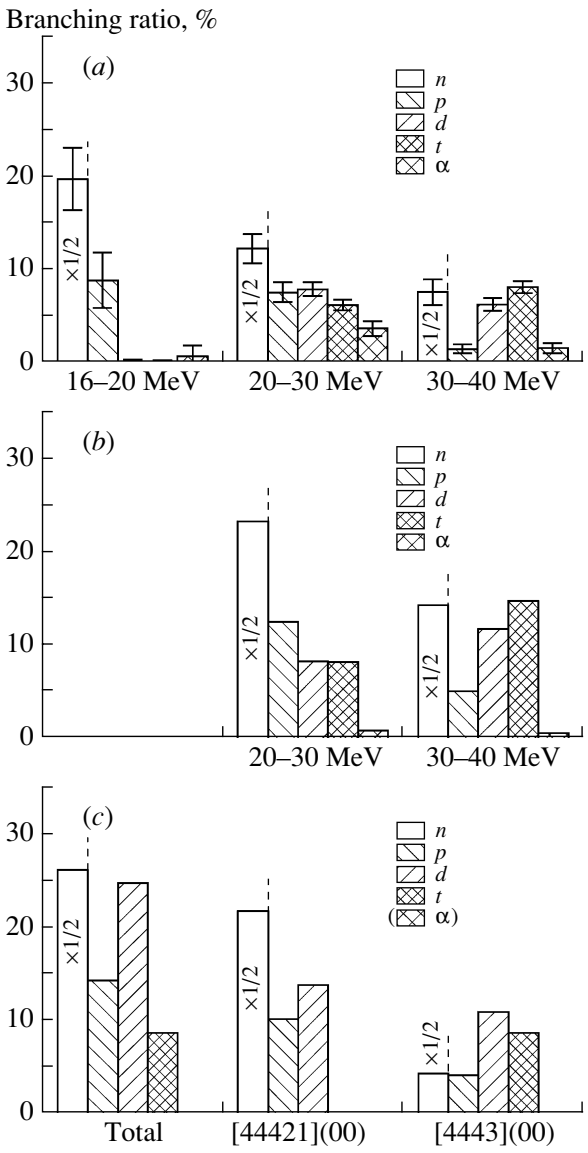

Fig. 5. (a) Experimental branching ratios of the n, p, d, t, and α decays onto the two-body decay regions from the three excitation energy regions of 16–20, 20–30, and 30–40 MeV in ^{15}N. (b) Branching ratios of the n, p, d, t, and α decays from the two excitation energy regions of 20–30, and 30–40 MeV in ^{15}N obtained by the $1\hbar\omega$ shell-model calculations [21]. (c) Branching ratios of n, p, d, t, and α decays from the doorway s-hole state in ^{15}N calculated by the $SU(3)$ model [9]. Branching ratios for the states with $[f](\lambda\mu) = [44421](00)$ and $[f](\lambda\mu) = [4443](00)$ and total branching ratios are shown.

structures. Predictions from the $SU(3)$ model [9] are shown in Fig. 5c, where the ^{15}N(s-hole) state has the same spatial symmetry as the ground state of ^{16}O, $SU(3)(\lambda\mu) = (00)$, and has two degenerated partition symmetries $[f] = [4443]$ and $[44421]$. The branching ratio of α decay is exactly zero in the calcu-

lations of the $SU(3)$ model due to the selection rule. The experimental decay pattern of the 30–40 MeV region strongly supports the selection rule and is similar to that of the $SU(3)[f](\lambda\mu) = [4443](00)$ component. However, the large branching ratios of d decay in the $SU(3)$-cluster model calculations do not agree with the experimental branching ratio, even taking into account the rather large lower limit of the detection energy. The second region may have both the $SU(3)[f](\lambda\mu) = [44421](00)$ and $[4443](00)$ components.

The branching ratios for two energy regions calculated with the shell model are shown in Fig. 5*b* for n, p, d, t, and α decays from ^{15}N(s-hole) state. The branching ratio of the α decay is very small owing to the selection rule as mentioned above. The agreement between the experimental branching ratios onto the two-body decay regions and calculated ones is fairly good in both regions, implying that the main part of the binary fragmentation is the direct decay of the doorway s-hole state. At first sight, this seems to be inconsistent with the results obtained from the comparison with the statistical-decay calculations, where some (not small) amounts of the statistical decay are considered to contribute to the total branching ratios. However, if we estimate the direct decay parts of the experimental branching ratios by subtracting the calculated statistical-decay ratios multiplied by 0.5 from the experimental ones in the two-body decay regions and compare it with the result of the shell-model calculations of Fig. 5*b* multiplied by 0.5, the agreement between two branching ratios is very good not only for the decay patterns but also for the absolute values. This indicates that the ratio of the escape width ($\Gamma^{\uparrow}$) to the spreading width ($\Gamma^{\downarrow}$) of the ^{15}N(s-hole) state is about 1.

4. SUMMARY

We presented the first measurements of the decay particles from the s-hole state in ^{11}B and ^{15}N excited by the ^{12}C$(p, 2p)$ and ^{16}O$(p, 2p)$ reactions at $E_p =$ 392 MeV. The measured excitation energy spectra show that both s-hole states split into some substructures. These splittings agree qualitatively with the results of recent shell-model calculations [21]. For the s-hole state in ^{11}B, the triton decay probability was found to be larger compared to any other decay, although the Q value of the α-decay channel is larger. The present results for the decay branching ratios of the ^{11}B(s-hole) state cannot be reproduced by statistical model calculations. $SU(3)$-model calculations [9] explain the experimental decay character qualitatively in the higher excitation region, while the $SU(3)(\lambda\mu) = [443](04)$ feature in the $SU(3)$-model calculations becomes unclear in the shell-model calculations.

In the case of the s-hole state in ^{15}N, the suppression of α decay is clearly recognized in the binary decay process, which supports the selection rule due to the spatial $SU(3)$ symmetry. The shell-model calculation explains the experimental two-body decay patterns better than the $SU(3)$-model calculations. From a comparison between the experimental results and both the statistical-model and the shell-model calculations, nearly half of the total fragmentation of the ^{15}N(s-hole) state is concluded to be the direct decay of the doorway s-hole state.

ACKNOWLEDGMENTS

We are grateful to the RCNP cyclotron staff for preparing a stable and clean beam. We thank K. Ikeda for fruitful discussions and encouragement.

This research was supported in part by the Grant-in-Aid for Scientific Research no. 09440105 and for the 21st Century COE "Center for Diversity and Universality in Physics" from the Japanese Ministry of Education, Sports, Culture, Science, and Technology.

REFERENCES

1. O. Chamberlain and E. Segrè, Phys. Rev. **87**, 81 (1952).
2. G. Jacob and T. A. J. Maris, Rev. Mod. Phys. **45**, 6 (1973), and references therein.
3. S. L. Belostotskii *et al.*, Yad. Fiz. **41**, 1425 (1985) [Sov. J. Nucl. Phys. **41**, 903 (1985)]; S. S. Volkov *et al.*, Yad. Fiz. **52**, 1339 (1990) [Sov. J. Nucl. Phys. **52**, 848 (1990)].
4. S. Frullani and J. Mougey, Adv. Nucl. Phys. **14**, 1 (1984), and references therein.
5. H. Bando, T. Yamada, and J. Žofka, Phys. Rev. C **36**, 1640 (1987).
6. T. Yamada and K. Ikeda, Prog. Theor. Phys. Suppl. **117**, 445 (1994).
7. H. Ejiri, Phys. Rev. C **48**, 1442 (1993).
8. Y. Hayato *et al.* (The Super-Kamiokande Collab.), Phys. Rev. Lett. **83**, 1529 (1999).
9. T. Yamada, M. Takahashi, and K. Ikeda, Phys. Rev. C **53**, 752 (1996).
10. M. Fujiwara *et al.*, Nucl. Instrum. Methods Phys. Res. A **422**, 484 (1999).
11. N. Matsuoka *et al.*, RCNP Annual Report (1991), p. 186.
12. M. Yosoi *et al.*, Phys. Lett. B **551**, 255 (2003).
13. T. Inomata *et al.*, Phys. Rev. C **57**, 3153 (1998).
14. T. Kawabata *et al.*, Nucl. Instrum. Methods Phys. Res. A **459**, 171 (2001).
15. F. Pühlhofer, Nucl. Phys. A **280**, 267 (1977); M. N. Harakeh, *Extended Version of Code CASCADE* (1983) (unpublished).

16. D. Wilmore and P. E. Hodgson, Nucl. Phys. **55**, 673 (1964).
17. B. A. Watson, P. P. Singh, and R. E. Segel, Phys. Rev. **182**, 977 (1969).
18. F. Michel *et al.*, Phys. Rev. C **28**, 1904 (1983).
19. M. Ermer *et al.*, Nucl. Phys. A **533**, 71 (1991).
20. J. B. A. England *et al.*, Nucl. Phys. A **475**, 422 (1987).
21. T. Yamada, Nucl. Phys. A **687**, 297c (2001).
22. H. Horiuchi, K. Ikeda, and Y. Suzuki, Prog. Theor. Phys. Suppl. **52**, 89 (1972).

Physics of Atomic Nuclei, Vol. 67, No. 10, 2004, pp. 1818–1822. From Yadernaya Fizika, Vol. 67, No. 10, 2004, pp. 1845–1849.

Proceedings of the International Conference "Nuclear Structure and Related Topics"

Two-Step Cascades of ^{117}Sn$(n, 2\gamma)$ Reaction and Problems of Describing Main Nuclear Properties below B_n*

V. A. Khitrov[1)], C. Panteleev[1)]***, A. M. Sukhovoj[1)]****, J. Honzátko[2)]*****, and I. Tomandl[2)]******

Received January 21, 2004

Abstract—Main properties of the excited states of ^{118}Sn manifesting themselves in cascade γ decay of its compound state are studied. As in heavier nuclei studied earlier, qualitative interpretation of the whole set of observed properties of the nucleus appears to be impossible without accounting for coexistence and interaction of quasiparticle and collective nuclear excitations and their considerable influence on the main parameters of the process under study. © *2004 MAIK "Nauka/Interperiodica".*

1. INTRODUCTION

The study of the two-step γ cascades following a thermal-neutron capture in more than 50 nuclei from ^{28}Al to ^{200}Hg in Dubna, Riga, and Řež allowed us to obtain unique information on nuclear properties in the energy range from the ground state up to, practically, the neutron binding energy B_n. Analysis of this information provided the following conclusions:

1. Experimental intensities of the cascades to groups of low-lying levels E_f cannot be reproduced in calculations with a precision achieved in experiments if one explores standard ideas of nuclear models. This cannot be done either within the simplest models like the noninteracting Fermi gas model or in the framework of the well-elaborated generalized model of superfluid nucleus [1].

2. A quite reliable energy dependence of the level density as well as radiative strength functions of dipole γ transitions can be extracted from experimentally obtained dependences of the cascade intensities on the energy of their primary transition E_1 (or the energy of their intermediate level $E_i = B_n - E_1$).

A practical possibility of solving this problem is determined by the following factors:

(i) A cascade intensity distribution (Fig. 1) is extracted [2] from the mass of γ–γ coincidences by means of the sum coincidence method. This experimental distribution contains a number of pairs of sufficiently narrow [3] full-energy peaks corresponding to intense cascades, a continuous distribution formed by a number of low-intensity cascades, and a "noise line" with zero mean value—a result of background subtraction. The local specific deviations of the normal distribution of events in a noise line can be partially or completely rejected numerically [4].

(ii) The main part (more than 95–99%) of the intensity of cascades with $E_1 > 0.5B_n$ can be extracted from these spectra in the form of energetically resolved pairs of peaks, quanta ordering in which is determined [5] with a high reliability using the maximum likelihood method. However, this requires a modern [6] spectrometer for registration of coincidences.

Using only these data, we determined (Fig. 2) the most probable energy dependence of all two-step cascades terminating at the ground and first excited states of ^{118}Sn. This permits one to make, according to the method [7], quite unambiguous (in the limits of existing notions and possibilities of studying this process) conclusions about both the density of the states excited at a thermal neutron capture and a reduced probability of their population by γ quanta.

2. ESTIMATION OF THE MOST PROBABLE LEVEL DENSITY ρ AND RADIATIVE STRENGTH FUNCTIONS k

A radiative strength function $k = \Gamma_{\lambda i}/(E_\gamma^3 A^{2/3} \times D_\lambda)$ (here, $\Gamma_{\lambda i}$ is a partial width of γ transition with the energy E_γ, A is the nucleus mass, and D_λ is the

*This article was submitted by the authors in English.

[1)]Frank Laboratory of Neutron Physics, Joint Institute for Nuclear Research, Dubna, Moscow oblast, 141980 Russia.
[2)]Nuclear Physics Institute, Academy of Sciences of Czech Republic, Řež, Czech Republic.
**e-mail: khitrov@nf.jinr.ru
***e-mail: cvet@nf.jinr.ru
****e-mail: suchovoj@nf.jinr.ru
*****e-mail: honzatko@ujf.cas.cz
******e-mail: tomandl@ujf.cas.cz

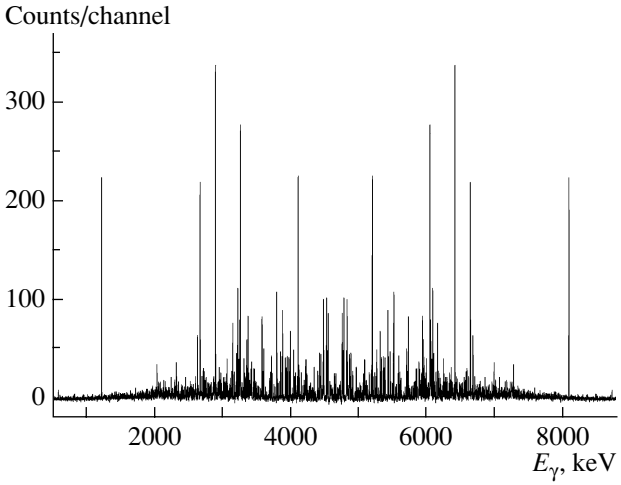

Fig. 1. The intensity distribution of two-step cascades with the total energy $E_1 + E_2 = 9326$ keV in ^{118}Sn (after background subtraction and corrections for efficiency of the registration of cascades).

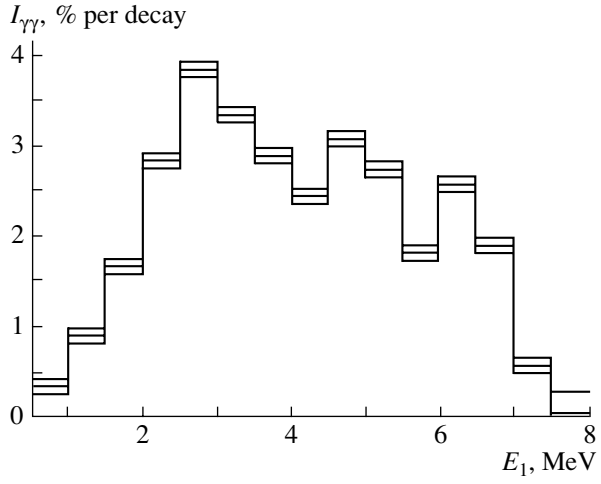

Fig. 2. Experimental distribution of the total intensity of two-step cascades terminating at the ground and first excited states in ^{118}Sn as a function of the energy of their primary transitions E_1. Ordinary statistical errors are shown.

spacing between decaying levels λ) and a level density ρ determine the total radiative width of a compound state Γ_λ and a cascade intensity $I_{\gamma\gamma}$ [8] in the following way:

$$\Gamma_\lambda = \langle\Gamma_{\lambda i}\rangle m_{\lambda i}, \tag{1}$$

$$I_{\gamma\gamma} = \sum_{\lambda,f}\sum_i \frac{\Gamma_{\lambda i}}{\Gamma_\lambda}\frac{\Gamma_{if}}{\Gamma_i} \tag{2}$$

$$= \sum_{\lambda,f} \frac{\Gamma_{\lambda i}}{\langle\Gamma_{\lambda i}\rangle m_{\lambda i}} n_{\lambda i} \frac{\Gamma_{if}}{\langle\Gamma_{if}\rangle m_{if}}.$$

Here, the values of the total and partial γ widths are set for the compound state λ and the cascade intermediate level i, respectively; m is the total number of excited levels; and n is the number of excited levels in the energy interval ΔE of averaging of the cascade intensity.

These equations do not allow one to determine k and ρ unambiguously and independently. A deviation of, for example, ρ from its real value is inevitably compensated by deviations of strength functions of the corresponding magnitude and sign. However, as was shown in [7], possible values of these deviations are rather small. Nevertheless, the results obtained in analysis [7] can be used to verify nuclear models and, if necessary, to point out a direction of their further development. The main argument in favor of this statement is relatively weak dependence of final results on the initial values of k and ρ (even if they are absolutely unreal) in the iterative process [7]. The most serious assumption of the method [7] of determination of k and ρ is the equality in the energy dependence of radiative strength functions for the primary and secondary transitions. If it is not true, then in the extracted values of k and ρ uncontrolled and, probably, significant systematic error can appear. Depending on the sign of this error, a discrepancy between the model and experimental values of k and ρ can decrease or increase.

Although calculations of the total γ-ray spectra with the use of a level density [7] and different (but, in principle, possible) radiative strength functions have showed [9] that the main properties of a level density are extracted with high confidence and the probable error reduces the discrepancy between the experimental and model [10, 11] values of k and ρ, an independent complementary test of the method [7] for every studied nucleus is required.

The values of k and ρ shown in Figs. 3 and 4 reflect the common features of their energy dependences. This conclusion is achieved by comparison of the experimental data with the results of calculations within different assumptions on the intensities of cascades terminating at higher lying levels (see table). Since the k and ρ values shown in Figs. 3 and 4 allow one to reproduce simultaneously

(i) the total radiative width Γ_λ of the compound state,

(ii) the energy dependence of the intensity $I_{\gamma\gamma}$ of cascades to the ground and first excited states of ^{118}Sn, and

(iii) the total intensity of cascades to different final levels with energy up to 2.8 MeV, one can consider the strength functions and the level density obtained in ^{118}Sn by the method [7] as the most probable ones. These data, of course, contain some systematic

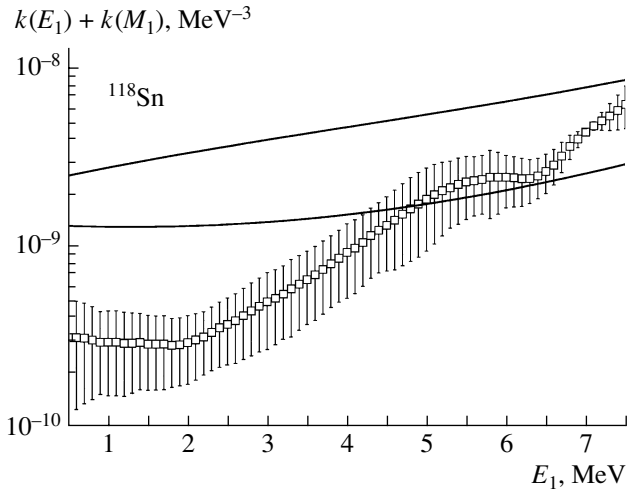

Fig. 3. The sum of probable radiative $E1$ and $M1$ strength functions (with estimated errors). The upper and lower solid curves represent predictions of the models [13] and [10], respectively (the value $k(M1) = \text{const}$ normalized to the experimental data at $E_\gamma \approx B_n$ is added).

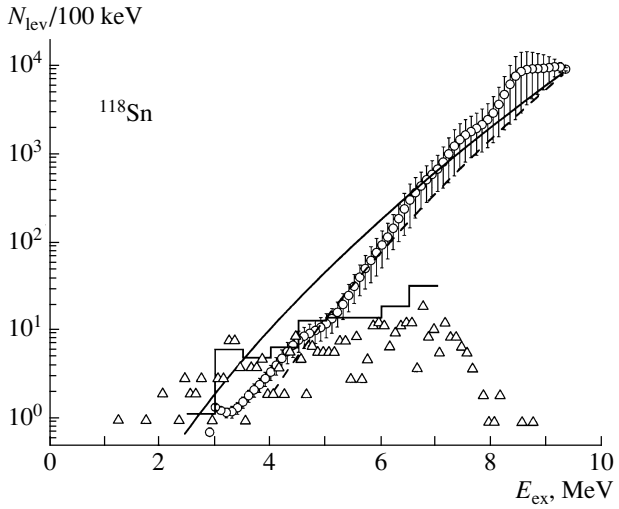

Fig. 4. The number of levels with $0^\pm \le J^\pi \le 2^\pm$ and its dispersion (circles with bars). The histogram represents the results of analysis [14]; triangles show the observed number of intermediate levels of intense cascades. Solid and dashed curves are the predictions of the models [11] and [12], respectively.

errors owing to errors in determination of $I_{\gamma\gamma}$ and incompleteness of information on the intensity of the two-step and larger multiplicity cascades.

The results of the analysis are compared with predictions of theoretical calculations of the level density [11, 12] and radiative widths [10, 13]. In the case of radiative strength functions, a comparison is performed in the following manner: the $k(E1)$ values calculated according to [13] and [10] (upper and lower curves in Fig. 3, respectively) are summed with $k(M1) = \text{const}$, which is normalized so that the ratio $\Gamma(M1)/\Gamma(E1)$ would be approximately equal to the experimental value at $E_\gamma \simeq B_n$.

A comparison of the results of the analysis with predictions of [10–13], which are often used to this end, shows the following:

1. The energy dependence of the function $k(E1) + k(M1)$ in ^{118}Sn differs strongly from predictions of [10, 13] as in even–even compound nuclei from the region of the $4s$ resonance of a neutron strength function.

2. The probable level density conforms to the picture obtained in previous experiments [7, 14]: up to the excitation energy $\simeq$3.5 MeV, our data do not contradict the exponential extrapolation of $\rho(E_{\text{ex}})$ predicted by the Fermi gas back-shift model [11]. The level density at $E_{\text{ex}} > 3$ MeV is considerably less than that predicted by this model. Above $E_{\text{ex}} \approx 5$ MeV, the level density is in better agreement with the predictions of the generalized model of the superfluid nucleus in its simplest version [12]. The values of ρ^{mod} predicted by the latter reduce the parameter $\chi^2 = ((\rho^{\text{mod}} - \rho^{\text{best}})/\delta\rho^{\text{best}})^2$ by a factor of about 3 as compared with the predictions of [11] for $E_{\text{ex}} \ge 4$ MeV.

A very fast exponential increase in the level density at $E_{\text{ex}} \simeq 5$ MeV points out [12] probably a dominant influence of many-quasiparticle structure of these states involving inner subshells.

3. DISCUSSION

The above conclusion is true only to an extent determined by contemporary (and included in the analysis [7]) notions of properties of nuclear excited states and dynamics of the γ-cascade process from a neutron resonance.

The main notions are the following:

(a) The branching coefficients at depopulation of any level i do not depend on the way of its feeding.

(b) All levels in a given excitation energy interval follow a sole statistical distribution. That is, the mean reduced probability of their population by primary $E1$ and $M1$ transitions is equal for any level in the spin window determined by the selection rule and does not depend on the structure of wave functions of a neutron resonance and an intermediate cascade level E_i. Therefore, by the theorem of the average, any sum of the widths is represented in calculation of $I_{\gamma\gamma}$ (2) by the product of their number and the mean partial width (determined through the corresponding wave function).

(c) Energy dependence of k (but not its absolute value) is the same for the primary and secondary transitions of cascades.

It is not known how close the notions (a) and (b) of the γ-decay process in a heavy nucleus are to reality. This should be found from the experiment. The analysis of spectra of intermediate levels of the most intense cascades in ^{118}Sn testifies [15] to their equidistancy. Below, it will be shown that the population of levels above $\simeq$3 MeV in ^{118}Sn strongly differs from the theoretical calculation. These two facts allow one to assume a very strong violation of the notion (c). If the interpretation of the results [15] as an existence of "vibrational bands" built on states with a complicated structure corresponds to reality, then enhanced γ transitions with energies of several hundred keV or higher inside the bands and between them are quite possible. A discrepancy of the results obtained according to [7] (see Fig. 4) and estimations [14] of the number of omitted levels admits the violation of notion (c) as one of the possible explanations.

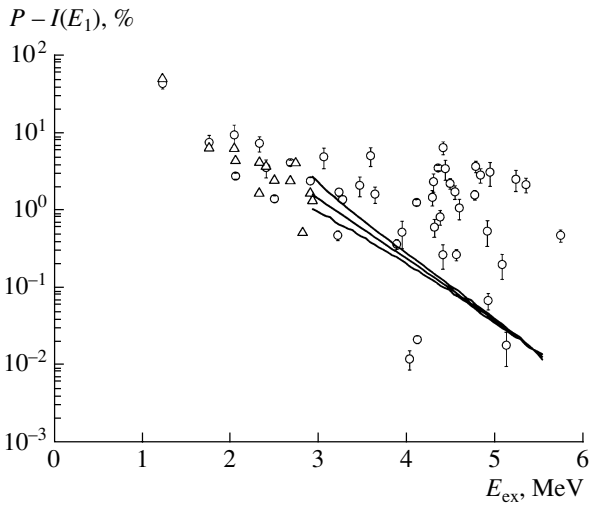

Fig. 5. Experimental populations of different levels in ^{118}Sn (points with bars) in comparison with the calculated ones for levels with $J^\pi = 0^+, 1^+, 2^+$. The calculations are made within model assumptions [10] (curves) and [11] (triangles) using $k(M1) = \text{const}$.

4. CASCADE POPULATION OF LEVELS IN ^{118}Sn

Obvious deviations of the level density and radiative strength functions from predictions of the simplest models [10, 11] show that the notions of the cascade γ-decay process need to be improved and corrected. It follows from the comparison between the experimental and calculated values of the population of high-lying levels of a nucleus under study. The equation for the intensity of individual cascade $i_{\gamma\gamma}$ proceeding via a given intermediate level reads

$$i_{\gamma\gamma} = i_1 i_2 / \sum i_2. \qquad (3)$$

The sum $P = \sum i_2$ in (3) is nothing more than the total population of a given level by the direct primary transitions and any possible cascade. It is seen from (3) that P can be determined if one has reliable information on $i_{\gamma\gamma}$ and intensities of their primary and secondary transitions i_1 and i_2, respectively. To diminish fluctuations of P, it is appropriate to subtract the primary transition intensity from it. The populations obtained in this way for the levels with positive parity are compared with the calculated values in Fig. 5. It should be noted that the difference between the calculated populations of levels with the same spin but different parities is insignificant. Otherwise, the complete correspondence between the experimental and calculated population of the levels above ≈ 3 MeV cannot be achieved. On one hand, this result confirms the above conclusion on the presence of the excitation-energy range where a drastic change in properties of excited states in both deformed and spherical nuclei occurs. On the other hand, it points out the necessity to develop more precise nuclear models for the states in the wide energy range at $E_m \simeq B_n$.

Energies $E_1 + E_2$ of cascades and their absolute intensities $I_{\gamma\gamma}$ [% per decay]

$E_1 + E_2$, keV	E_f, keV	$I_{\gamma\gamma}^{\text{exp}}$	$I_{\gamma\gamma}^{\text{cal}}$ [10, 11]	$I_{\gamma\gamma}^{\text{best}}$
9326.30	0	16.0(34)	6.7	15.7
8096.63	1230	15.3(11)	7.2	15.5
7568.00	1758	2.4(7)	1.1	2.5
7283.42	2042	3.3(16)	2.4	5.5
7269.39	2057	2.8(9)	0.8	1.7
7000.36	2325 + 2328	5.6(9)	2.8	5.4
6923.08	2403	2.8(2)	1.5	3.0
6829.42	2497	[2]	0.5	0.7
6648.95	2677	[1.5]	1.0	2.0
6588.29	2738	[4]	1.7	5.5
Sum		55.8(43)	25.7	57.5

Note: E_f is the energy of the final level of cascade; $I_{\gamma\gamma}^{\text{best}}$ is the calculated mean value for ensembles of random parameters ρ and k (their mean values and dispersions are shown in Figs. 3 and 4 by points with bars) allowing a reproduction [7] of the cascade intensity distribution (Fig. 2) with the experimental precision. The mean-square scatter of each of these parameters for each final level of cascades equals 5 to 15%.

5. CONCLUSIONS

The results of the comparison between the experimental and calculated cascade intensities in ^{118}Sn (as for the nuclei studied earlier) indicate a necessity to modify theoretical notions of excited-state properties in heavy nuclei. In particular, the models of a level density and radiative strength functions which are explored in calculations of nuclear parameters with a precision of about 10% must take into account the influence of nuclear structure up to $E_{\rm ex} \approx 0.5B_n$.

In the framework of modern theoretical notions, a qualitative explanation of the discrepancy between experiments and theory can be removed only within a more detailed treatment of coupling of nuclear excitations of both the fermionic and the bosonic type [1, 12]. Otherwise, it seems to be impossible to achieve a complete correspondence between the observed and calculated parameters of nuclear reactions, for instance, neutron-induced reaction. This concerns, partially, the total radiative widths of neutron resonances, γ spectrum, and cross sections of neutron–nucleus interactions.

ACKNOWLEDGMENTS

This work was supported by GACR under contract no. 202/03/0891 and by the Russian Foundation for Basic Research (project no. 99-02-17863).

REFERENCES

1. E. M. Rastopchin, M. I. Svirin, and G. N. Smirenkin, Yad. Fiz. **52**, 1258 (1990) [Sov. J. Nucl. Phys. **52**, 799 (1990)].
2. S. T. Boneva, E. V. Vasilieva, Yu. P. Popov, *et al.*, Fiz. Élem. Chastits At. Yadra **22**, 479 (1991) [Sov. J. Part. Nucl. **22**, 232 (1991)]; S. T. Boneva *et al.*, Fiz. Élem. Chastits At. Yadra **22**, 1433 (1991) [Sov. J. Part. Nucl. **22**, 698 (1991)].
3. A. M. Sukhovoj and V. A. Khitrov, Instrum. Exp. Tech. **27**, 1071 (1984).
4. V. A. Bondarenko, J. Honzátko, V. A. Khitrov, *et al.*, Fizika B (Zagreb) **11**, 83 (2002).
5. Yu. P. Popov, A. M. Sukhovoj, V. A. Khitrov, and Yu. S. Yazvitsky, Izv. Akad. Nauk SSSR, Ser. Fiz. **48**, 1830 (1984).
6. J. Honzátko *et al.*, Nucl. Instrum. Methods Phys. Res. A **376**, 434 (1996).
7. E. V. Vasilieva, A. M. Sukhovoj, and V. A. Khitrov, Yad. Fiz. **64**, 195 (2001) [Phys. At. Nucl. **64**, 153 (2001)]; V. A. Khitrov and A. M. Sukhovoj, nucl-ex/0110017.
8. S. T. Boneva, V. A. Khitrov, and A. M. Sukhovoj, Nucl. Phys. A **589**, 293 (1995).
9. A. M. Sukhovoj, V. A. Khitrov, and E. P. Grigor'ev, INDC(CCP) (Vienna) **432**, 115 (2002).
10. S. G. Kadmenskii, V. P. Markushev, and W. I. Furman, Yad. Fiz. **37**, 280 (1983) [Sov. J. Nucl. Phys. **37**, 165 (1983)].
11. W. Dilg, W. Schantl, H. Vonach, and M. Uhl, Nucl. Phys. A **217**, 269 (1973).
12. A. V. Ignatyuk, in *Proceedings of the IAEA Consultants Meeting on the Use of Nuclear Theory in Neutron Nuclear Data Evaluation, Trieste, Italy, 1975*, IAEA-190 (Vienna, 1976), Vol. 1, p. 211.
13. P. Axel, Phys. Rev. **126**, 683 (1962).
14. A. M. Sukhovoj and V. A. Khitrov, Yad. Fiz. **62**, 24 (1999) [Phys. At. Nucl. **62**, 19 (1999)].
15. J. Honzatko, V. A. Khitrov, C. Panteleev, *et al.*, Preprint No. E3-2003-88, JINR (Joint Inst. for Nucl. Res., Dubna, 2003); nucl-ex/0305020.

Physics of Atomic Nuclei, Vol. 67, No. 10, 2004, pp. 1823–1828. From Yadernaya Fizika, Vol. 67, No. 10, 2004, pp. 1850–1855.

Proceedings of the International Conference "Nuclear Structure and Related Topics"

On the Isotopic Dependence of the Mean Spin–Orbit Field in Nuclei*

V. I. Isakov[1)], K. I. Erokhina[2)], B. Fogelberg[3)], H. Mach[3)], and M. Sanchez-Vega[3)]**

Received January 21, 2004

Abstract—An analysis has been made of experimental data on level spectra, single-nucleon transfer reactions near closed shells, and data on the polarization effects in charge-exchange (p, n) reactions between isoanalog states of nuclei with even A. The analysis has allowed us to conclude that there is a significant difference between the spin–orbit splittings of neutrons and protons in identical orbitals. This conclusion is confirmed in a framework of different theoretical approaches. © *2004 MAIK "Nauka/Interperiodica".*

1. INTRODUCTION

Spin–orbit splitting of the mean-field orbitals is one of the main factors which determine the nuclear structure in nuclei both near and far from the closed shells. While the global characteristics of the spin–orbit splitting are well known, this cannot be said about the isotopic dependence of the splitting. However, new experimental results obtained recently [1–3] on nuclei close to ^{132}Sn has allowed one to define a nearly complete set of neutron and proton single-particle orbitals in the new region of "magicity" formed by the extremely strong $Z = 50$, $N = 82$ shells. Our current aim is to review the situation regarding the magnitude of spin–orbit splittings of neutrons and protons in identical orbits and to determine their isospin dependence based on the results of [1–3] and on the available data concerning other nuclei near the closed shells.

2. DEFINITION OF SINGLE-PARTICLE ENERGIES FROM THE EXPERIMENT

To define the values of single-particle energies from the experiments, we must remember that in nuclei there is a mixing of the single-particle and the more complicated modes of excitation (configuration mixing). Such mixing is small in nuclei of the type "magic ± nucleon" if the energy gaps between the shells are large (in "good" double-magic nuclei, such as ^{132}Sn and ^{208}Pb), though even in these cases one can see the spreading of the single-particle strength over states of the type "quasiparticle + phonon." However, if the energy gaps between the shells are small, the configuration mixing becomes very strong, which becomes obvious from the large cross sections for single-particle transfer reactions leading to levels having the J^π values of the single-particle states located on the other side of the Fermi level. This phenomenon happens because of the strong modification (decrease) of the Fermi step in the distribution of the occupancies of the single-particle levels vs. energy due to the ground-state correlations. The formula for definition of the single-particle energies ε_α from the experiment on the single-particle transfer reactions has the form [4]

$$\sum_{a\in(A+1)} [B_A(\text{g.s.}) - B_{A+1}(\text{g.s.}) + E_a^{\text{exc}}]s_{a\alpha}^{(+)} \quad (1)$$
$$+ \sum_{a'\in(A-1)} [B_{A-1}(\text{g.s.}) - B_A(\text{g.s.}) - E_{a'}^{\text{exc}}]s_{a'\alpha}^{(-)}$$
$$= \langle\alpha|\hat{t}|\alpha\rangle + \left\langle A;(0)\left|\sum_{i,k} {}_a\langle\alpha i|\hat{\vartheta}|\alpha k\rangle_a a_i^+ a_k\right|A;(0)\right\rangle$$
$$= \langle\alpha|\hat{t} + \hat{\Sigma}_{\text{s.p}}|\alpha\rangle \equiv \varepsilon_\alpha,$$

where

$$s_{a\alpha}^{(+)} = |\langle A+1;(a)|a_\alpha^+|A;(0)\rangle|^2, \quad (2)$$
$$s_{a'\alpha}^{(-)} = |\langle A-1;(a')|a_\alpha|A;(0)\rangle|^2,$$

and

$$\sum_{a\in(A+1)} s_{a\alpha}^{(+)} + \sum_{a'\in(A-1)} s_{a'\alpha}^{(-)} = 1. \quad (3)$$

In Eqs. (1)–(3), $s^\pm$ are spectroscopic factors normalized by relation (3); $|A;(0)\rangle$ is the ground-state vector of the target even–even nuclei; $|A+1;(a)\rangle$ and $|A-1;(a')\rangle$ are the vectors of the $\{a\}$ or $\{a'\}$

*This article was submitted by the authors in English.

[1)]Petersburg Nuclear Physics Institute, Russian Academy of Sciences, Gatchina, 188300 Russia.
[2)]Physical Technical Institute, Russian Academy of Sciences, St. Petersburg, 194021 Russia.
[3)]Department of Radiation Sciences, Uppsala University, Nyköping, Sweden.
**e-mail: visakov@thd.pnpi.spb.ru

Table 1. Single-particle states of ^{208}Pb [experimental single-particle energy marked by an asterisk, here and in Table 3, represents a mean value weighted by spectroscopic factors; theoretical values of the single-particle energies were calculated by using the following values of the parameters entering into formula (6): $V_0 = -52.0$ MeV, $V_{ls} = 32.7$ MeV fm^2, $a(\pi) = 0.73$ fm, $a(\nu) = 0.72$ fm, $\beta = 1.36$, $\beta_{ls} = -0.6$, $R = r_0 A^{1/3}$ with $r_0 = 1.27$ fm]

nlj	$\varepsilon_{\rm exp}$	$\varepsilon_{\rm th}$	nlj	$\varepsilon_{\rm exp}$	$\varepsilon_{\rm th}$
$\nu 3d3/2$	-1.40	-0.96	$\pi 3p1/2$	0.17^*	0.29
$\nu 2g7/2$	-1.44	-0.89	$\pi 3p3/2$	-0.68	-0.58
$\nu 4s1/2$	-1.90	-1.63	$\pi 2f5/2$	-0.97	-1.03
$\nu 1j15/2$	-2.09^*	-2.23	$\pi 1i13/2$	-2.19	-1.94
$\nu 3d5/2$	-2.37	-2.35	$\pi 2f7/2$	-2.90	-3.21
$\nu 1i11/2$	-3.16	-2.71	$\pi 1h9/2$	-3.80	-4.71
$\nu 2g9/2$	-3.94	-4.24	$\pi 3s1/2$	-8.01	-7.87
$\nu 3p1/2$	-7.37	-7.59	$\pi 2d3/2$	-8.36	-8.59
$\nu 2f5/2$	-7.94	-8.17	$\pi 1h11/2$	-9.36	-8.60
$\nu 3p3/2$	-8.27	-8.59	$\pi 2d5/2$	-10.04^*	-9.96
$\nu 1i13/2$	-9.00	-8.84	$\pi 1g7/2$	-12.18^*	-12.08
$\nu 2f7/2$	-10.07^*	-10.72			
$\nu 1h9/2$	-10.78	-10.60			

states, belonging to the $(A+1)$ or $(A-1)$ nuclei, that contain the fragmentation effects; $E^{\rm exc}_{a,a'}$ are the corresponding excitation energies; and B are the ground-state binding energies. Note that the values of J^π for the $\{a\}$, $\{a'\}$ states in (1)–(3) are the same as for the single-particle state $\{\alpha\}$.

The ε_α value defined by relation (1) represents the energy of the *true* single-particle state that corresponds to the eigenvalue of the single-particle Hamiltonian operator $\hat{t} + \hat{\Sigma}_{\rm s.p}$, where $\hat{t}$ is the kinetic energy, while $\hat{\Sigma}_{\rm s.p}$ is that contribution to the self-energy of the single-particle Green's function $G(\varepsilon_\alpha, \varepsilon)$ which does not depend on the energy ε (see [4] for details). We note that summation over the $\{a\}$ and $\{a'\}$ in (1) includes the isospin indices. It means that, if the N, Z values refer to the target nuclei with the ground-state isospin $T_0 = (N-Z)/2$, then, for proton stripping and neutron pickup reactions, we must include in (1) together with the low-lying, $T = T_0 - 1/2$, also the high-lying isoanalog states of the final nuclei with $T = T_0 + 1/2$, with transition probabilities $\sim 1/(2T_0+1)$. This factor is small for heavy nuclei ($1/45$ for ^{208}Pb), but equals $1/9$ for ^{48}Ca.

Careful definition of the values of single-particle energies at ^{208}Pb, made by us in [5], performed by averaging over the values of spectroscopic factors, leads to the result that the spin–orbit splittings of the neutron $2f$ and $3p$ orbitals are larger than those for similar proton orbitals. In this way, we obtain $\Delta^\nu_{ls}(2f) = 2.13$ MeV and $\Delta^\nu_{ls}(3p) = 0.90$ MeV, while $\Delta^\pi_{ls}(2f) = 1.93$ MeV and $\Delta^\pi_{ls}(3p) = 0.85$ MeV. In contrast, neutron and proton splittings are practically equal to each other in the ^{16}O and the ^{40}Ca nuclei, thus reflecting the fact of the isobaric symmetry in nuclei.

Recent experimental results [1–3] obtained for odd nuclei close to ^{132}Sn give evidence that the spin–orbit splitting of the neutron $2d$ orbit, $\Delta^\nu_{ls}(2d) = 1.65$ MeV, is also substantially larger than that for protons, $\Delta^\pi_{ls}(2d) = 1.48$ MeV. Here, some additional explanation is needed since there are, at present, no data on the single-nucleon transfer reactions for unstable nuclei at ^{132}Sn, and all the experimental data were obtained from the investigation of β and γ decays. Thus, we cannot perform the averaging procedure here. However, ^{132}Sn is a much more rigid nucleus than ^{208}Pb (see [6]); therefore, the configuration mixing is also much less pronounced here. An additional argument follows from the fact that ^{132}Sn and ^{208}Pb are in some respect "twins" having similar shell structures and properties with the correspondence $l \to l+1$ and $j \to j+1$ for most of the single-particle orbitals in these regions of the nuclide chart (see [7]). A different piece of evidence in favor of our statement comes from our theoretical modeling of the configuration mixing in the regions of ^{208}Pb and ^{132}Sn. Our calculations demonstrated that the configuration mixing leads to the result that the ratios $\Delta^\nu_{ls}/\Delta^\pi_{ls}$ for the starting *true* single-particle orbits $2f$ and $2d$ in ^{208}Pb and ^{132}Sn are *larger* than the mentioned ratios, but for the corresponding mixed states obtained after the diagonalization. These states contain the *true* single-particle states as main components. However, in the absence of experimental data on the direct reactions at ^{132}Sn, we used for this nucleus splittings that do not include averaging over spectroscopic factors.

The experimental values of the single-particle energies in the ^{208}Pb, ^{132}Sn, and the ^{48}Ca nuclei are shown in Tables 1–3. We mention here that the fragmentation of the single-particle states near ^{48}Ca is extremely strong, so for the correct definition of their *true* energies we took into account both the contribution of isoanalog states and the ground-state correlations [mixing of the $\{a\}$ and $\{a'\}$ terms in formula (1)]. The result is that the spin–orbit splitting

Table 2. Single-particle states of ^{132}Sn (the values of the parameters are $V_0 = -51.55$ MeV, $V_{ls} = 32.4$ MeV fm^2, $a(\pi) = 0.63$ fm, $a(\nu) = 0.66$ fm, $\beta = 1.31$, $\beta_{ls} = -0.6$, $r_0 = 1.27$ fm)

nlj	ε_{exp}	ε_{th}	nlj	ε_{exp}	ε_{th}
$\nu 2f5/2$	-0.58	0.22	$\pi 3s1/2$	-6.83	-6.64
$\nu 3p1/2$	-0.92	-0.55	$\pi 1h11/2$	-6.84	-6.77
$\nu 1h9/2$	-1.02	-0.47	$\pi 2d3/2$	-7.19	-7.07
$\nu 3p3/2$	-1.73	-1.42	$\pi 2d5/2$	-8.67	-9.04
$\nu 2f7/2$	-2.58	-2.84	$\pi 1g7/2$	-9.63	-10.60
$\nu 2d3/2$	-7.31	-7.63	$\pi 1g9/2$	-15.71	-14.57
$\nu 1h11/2$	-7.55	-7.33	$\pi 2p1/2$	-16.07	-16.14
$\nu 3s1/2$	-7.64	-8.03			
$\nu 2d5/2$	-8.96	-9.98			
$\nu 1g7/2$	-9.74	-9.51			

of the neutron $1d$, $1f$, and $2p$ orbitals are larger than the corresponding splittings for protons.

3. THEORETICAL APPROACH

Turning to the theoretical interpretation [5] of the experimental values of the spin–orbit splitting discussed above, we shall first recall that, from the point of view of many-body theory, the average spin–orbit potential has its origin in the pair spin–orbit interaction between nucleons (with tensor forces providing a minor contribution as well). On the level of qualitative arguments, it was noted by Bohr and Mottelson [8] that, due to the symmetry properties, one should expect the neutron spin–orbit splitting to be somewhat larger than that for protons in heavier nuclei, simply due to a higher number of like particles in the neutron case. However, at that time, the absence of experimental data did not permit a meaningful comparison with measurements. With the presently available data, we can fill this gap, providing also some quantitative considerations.

The two-body spin–orbit interaction differs from zero only in the states with a total spin $S = 1$. The neutron–neutron and proton–proton systems have the total isospin $T = 1$ and thus due to the Pauli principle have odd values of the relative orbital momentum L (in fact, $L = 1$). At the same time, the neutron–proton system is composed of the $T = 0$ and $T = 1$ states with equal weights, having $L = 0$ and $L = 1$, respectively. Due to the absence of spin–orbit interaction in states with $L = 0$, the pair spin–orbit np interaction is half as strong as that in pp or nn systems.

Table 3. Single-particle states of ^{48}Ca [the values of the parameters involved are the following: $V_0 = -52.0$ MeV, $V_{ls} = 33.2$ MeV fm^2, $a(\pi) = a(\nu) = 0.60$ fm, $\beta = 1.39$, $\beta_{ls} = -0.6$, $r_0 = 1.27$ fm]

nlj	ε_{exp}	ε_{th}	nlj	ε_{exp}	ε_{th}
$\nu 1g9/2$	$\sim 0.6^*$	0.32	$\pi 2p1/2$	-2.40^*	-3.07
$\nu 1f5/2$	-1.20^*	-1.97	$\pi 1f5/2$	-3.20^*	-3.58
$\nu 2p1/2$	-2.86^*	-2.90	$\pi 2p3/2$	-3.40^*	-5.22
$\nu 2p3/2$	-4.64^*	-5.07	$\pi 1f7/2$	-9.40^*	-10.09
$\nu 1f7/2$	-10.23^*	-9.22	$\pi 2s1/2$	-14.92^*	-15.87
$\nu 1d3/2$	-13.09^*	-14.03	$\pi 1d3/2$	-16.18^*	-16.32
$\nu 2s1/2$	-13.28^*	-14.48	$\pi 1d5/2$	-20.43^*	-20.28
$\nu 1d5/2$	-17.97^*	-18.56			

If $U_{ls}(\nu)$ and $U_{ls}(\pi)$ represent the magnitudes of the mean spin–orbit field for neutrons and protons and $\vartheta(T = 1, S = 1, L = 1)$ is a quantity representing the parameter of the pair spin–orbit interaction in a state with $T = 1$, $S = 1$, $L = 1$, then the above discourse leads to

$$U_{ls}(\nu) \sim \vartheta(1,1,1)\left(N + \frac{1}{2}Z\right) \equiv \vartheta\left(A - \frac{Z}{2}\right),$$
$$U_{ls}(\pi) \sim \vartheta(1,1,1)\left(\frac{N}{2} + Z\right) \equiv \vartheta\left(A - \frac{N}{2}\right). \quad (4)$$

As the spin–orbit splitting $\Delta_{ls}^{\nu,\pi} \sim U_{ls}(\nu,\pi)$, the relative difference γ of the neutron and proton spin–orbit splittings is given by the expression

$$\gamma = \frac{\Delta_{ls}^{(\nu)} - \Delta_{ls}^{(\pi)}}{(\Delta_{ls}^{(\nu)} + \Delta_{ls}^{(\pi)})/2} = \frac{2}{3}\frac{N-Z}{A}. \quad (5)$$

On the other hand, we can express the mean nuclear potential in the following form, which contains isospin dependences in both the central and the spin–orbit terms:

$$\hat{U}(r,\hat{\sigma}) = U_0(\tau_3)f(r) + U_{ls}(\tau_3)\frac{1}{r}\frac{df(r)}{dr}\hat{\mathbf{l}}\cdot\hat{\mathbf{s}}, \quad (6)$$
$$f(r) = \left[1 + \exp\left(\frac{r-R}{a}\right)\right]^{-1},$$
$$U_0(\tau_3) = V_0\left(1 + \beta\frac{T_3}{A}\tau_3\right),$$
$$U_{ls}(\tau_3) = V_{ls}\left(1 + \beta_{ls}\frac{T_3}{A}\tau_3\right),$$
$$T_3 = \frac{N-Z}{2}.$$

Here, $\tau_3 = -1$ for neutrons, $\tau_3 = +1$ for protons, and β_{ls} is the parameter which defines the isospin dependence of the mean spin–orbit field. Then we easily obtain, this time in terms of Eq. (6), an expression for the relative difference between the spin–orbit splittings of neutrons and protons in identical orbits:

$$\gamma = -\beta_{ls}\frac{N-Z}{A}. \qquad (7)$$

It follows from a comparison of Eqs. (5) and (7) that $\beta_{ls} = -2/3$.

Strictly speaking, this derivation was performed for the two-body spin–orbit interaction. However, as mentioned above, tensor forces also provide some contribution to the spin–orbit splitting. This noncentral interaction is proportional to S_{12} with

$$S_{12} = 3(\hat{\boldsymbol{\sigma}}_1 \cdot \mathbf{n})(\hat{\boldsymbol{\sigma}}_2 \cdot \mathbf{n}) - \hat{\boldsymbol{\sigma}}_1 \cdot \hat{\boldsymbol{\sigma}}_2 \qquad (8)$$
$$= \sqrt{24\pi}[[\hat{\boldsymbol{\sigma}}_1 \otimes \hat{\boldsymbol{\sigma}}_2]^2 \otimes Y_2(\mathbf{n})]^0_0;$$
$$\mathbf{n} = (\mathbf{r}_1 - \mathbf{r}_2)/|\mathbf{r}_1 - \mathbf{r}_2|.$$

One can easily see from (8) that the diagonal matrix elements of this interaction are different from zero only for states with $S = 1$ and $L \geq 1$, of which the $S = T = L = 1$ one is of the main importance. It is just the state which was already considered in this section in the case of spin–orbit interaction. Consequently, the diagonal part of tensor forces also provides a contribution of the type given by Eq. (6) with $\beta_{ls} = -2/3$, and thus it leads only to a renormalization of the V_{ls} value. However, as the spatial part of tensor operator is proportional to $Y_2(\mathbf{n})$ and due to the spin structure of S_{12}, this renormalization equals zero in cases of spin-saturated spherical nuclei. Thus, in ^{16}O and ^{40}Ca, tensor forces give a contribution to the isoscalar part of the spin–orbit splitting, which is mediated by their nondiagonal part and caused by admixtures that appear out of the Hartree–Fock-type ground state. As was shown in [9], tensor forces may really lead to a substantial contribution to the isoscalar part of spin–orbit splitting. On the other hand, in nuclei that are not spin saturated, such as ^{48}Ca, tensor forces can contribute to the spin–orbit splitting even in the "diagonal" scheme (i.e., a scheme without admixtures), if the antisymmetrization is properly included. Our numerical calculations for seniority one states of ^{47}Ca and ^{47}K, both having one neutron or proton hole, performed in the framework of the multiparticle shell model with tensor forces taken from our previous works [10–12] have demonstrated that the inclusion of a tensor component of the interaction leads to energy shifts that correspond to some variation of the spin–orbit splittings Δ_{ls}, such that, in ^{48}Ca, $\Delta^{(\nu)}_{ls}(1d) - \Delta^{(\pi)}_{ls}(1d) = 0.34$ MeV. This shift arises from neutrons filling the $\nu 1f_{7/2}$ subshell and is mainly due to charge-exchange two-body matrix elements of the np interaction mediated by the isovector part of the tensor force ($\sim \boldsymbol{\tau}_1 \cdot \boldsymbol{\tau}_2$). Thus, the inclusion of tensor forces does not change the pattern of spin–orbit splitting, which also leads to negative values of β_{ls} of about -0.5. These results qualitatively agree with those presented in [13], where, in the framework of the Brueckner–Hartree–Fock method with Reid potential (containing both the spin–orbit and tensor components), a substantially larger neutron than proton splitting was obtained for the $1d$ orbital in ^{48}Ca with β_{ls} about -1.0. We note that the experimental data on spin–orbit splittings in the ^{208}Pb, ^{132}Sn, and ^{48}Ca nuclei in each case lead to *negative* values of β_{ls} with the *average* magnitude of $\beta_{ls} \sim -1$, which is a number in good qualitative agreement with the prediction of Eq. (7).

It is thus of substantial interest to evaluate to what extent the isotopic dependence of the spin–orbit splittings is reproduced by standard model calculations. For this aim, we use the microscopic approach based on the meson–nucleon phenomenology in the framework of the Walecka model [14]. Then one obtains (see, for example, [15–22] and references therein) a Skyrme-type single-particle equation for a nucleon having the effective mass m^*_N. This approach explains well the magnitude of spin–orbit splitting in nuclei. Here, we concentrate only on the *difference* between the proton and neutron splittings of spin–orbit partners in the same nuclei, resulting from a spin–orbit potential having the form (see, for example, [18–21]; note that the pseudoscalar π mesons do not contribute to the model in the Hartree approach due to symmetry)

$$\hat{U}_{ls} = \frac{\lambda^2_N}{2}\frac{1}{r}\left\{\left(\frac{m_N}{m^*_N}\right)^2 \frac{d}{dr}[(V^0_\omega - S^0_{\sigma,\sigma_0}) \right. \qquad (9)$$
$$\left. - (V^1_\rho - S^1_{\delta,\sigma,\sigma_0}) \cdot \tau_3] - 2k\frac{m_N}{m^*_N}\frac{d}{dr}V^1_\rho \cdot \tau_3\right\}\hat{\mathbf{l}} \cdot \hat{\mathbf{s}},$$

where $V = V^0 - \tau_3 \cdot V^1$ and $S = S^0 - \tau_3 \cdot S^1$ are the vector and scalar fields related to corresponding mesons, $m^*_N = m_N + \frac{1}{2}(S - V)$, and k is the ratio of tensor to vector coupling constants of the ρ meson. Various approaches have been used to determine the coupling constants. In [21], the meson–nucleon coupling constants, defining the V and S fields, were taken from the Bonn NN boson exchange potential [23], where σ and σ_0 are scalar mesons imitating the 2π exchange in the NN systems with $T = 1$ and $T = 0$, respectively. In other works (see, for example, [18–20]), the constants were defined from the description of global nuclear properties, with

inclusion of the σ^3 and σ^4 terms in the Lagrangian density (one σ meson with the same characteristics for the $T = 1$ and $T = 0$ channels was used, which leads to zero contribution of this meson to S^1 in Eq. (9); note also that the tensor term was not included in the ρ-meson vertex in [18–20]).

Taking into account that the radial dependence of m_N/m_N^* is much weaker than that of V and S, which are considered to be proportional to the density in the form of a Fermi function, one can approximately represent the spin–orbit term (9) in the form of (6). Calculating then the V and S magnitudes in the center of nuclei at the values of vector and scalar densities $\rho_v = 0.17$, $\rho_s = 0.16$, $\rho_v^- = 0.17(N - Z)/A$, and $\rho_s^- = 0.16(N - Z)/A$ (all in fm^{-3}), using the coupling parameters from [21, 23] and taking into account the isotopic dependence of m_N/m_N^*, we obtain $V_{ls} \approx 34$ MeV fm^2 and $\beta_{ls} \approx -0.40$. If we use the NL2 set of parameters from [19, 20], then we have $V_{ls} \approx 31$ MeV fm^2 and $\beta_{ls} \approx -0.43$. At the same time, the set NL1 from [18, 20], giving small values of effective masses, leads to $V_{ls} \sim 50$ MeV fm^2 and $\beta_{ls} \sim -1.3$. As the V^1 and S^1 magnitudes are proportional to ρ_v^- and ρ_s^-, both formulas (6) and (9) give equal spin–orbit splitting for protons and neutrons in the $N = Z$ nuclei. It should be noted that the value of β_{ls} is always negative and is determined mainly, or entirely, by the ρ-meson contribution.

4. POLARIZATION EFFECTS IN THE (p, n) REACTIONS

A spin–orbit term in a potential leads to polarization effects in scattering. Making in Eq. (6) the substitutions $\tau_3 \to -2t_3$ and $T_3 \cdot t_3 \to \hat{\mathbf{T}} \cdot \hat{\mathbf{t}}$, where $\hat{\mathbf{T}}$ and $\hat{\mathbf{t}}$ are isospin vector operators for the core and nucleon, we obtain the nuclear part of potential (6) in the isotopic-invariant form (Lane potential, [24]), suitable for description of both the diagonal in t_3 (single-particle spectra and elastic scattering) and the nondiagonal ((p, n) reactions leading to isobaric analog states) processes. While the polarization in elastic scattering depends on the parameter combination of the form $V_{ls}\left(1 - \beta_{ls}\dfrac{(N-Z)}{A}t_3\right) \approx V_{ls}$, similar effects in charge-exchange reactions with excitation of isoanalog states are proportional to $\beta_{ls}V_{ls}$ and are thus defined by the isovector mean spin–orbit field parameter β_{ls}, as the V_{ls} parameter is well known. Thus, we can check [25] the above conclusions concerning the β_{ls} value and based on nuclear spectra using the data from (p, n) quasielastic scattering. One can find corresponding information about the polarization effects in the ^{48}Ca region in [26], where the $^{48}\mathrm{Ca}(p, n)\ ^{48}\mathrm{Sc}^*$ reaction with polarized protons leading to the 0^+ (6.67 MeV) isoanalog state was studied, but with theoretical analysis based on a microscopic approach for description of nuclear structure and in terms of nucleon–nucleon amplitudes (DWIA). Here, we proceed in terms of the Lane model on the basis of spin–orbit parameters defined before and using the Born approximation for the description of scattering. It is well known that, in the Born approximation, polarization effects arising from the spin–orbit potential disappear. Thus, to describe these effects, one needs to introduce an imaginary part (absorption) into the optical potential, which really means accounting for effects beyond the Born approach. We must also include in the real and imaginary parts of the potential the dependence on the incident energy, which was rather high ($E = 134$ MeV) in [26]. In [8], the following proposition in the case of volume absorption is presented for the V_0 parameter: $V_0 = V_0'(1 - 0.0058E)$ with $V_0' = -52$ MeV, which is rather close to the values used by us in the description of bound states (see Tables 1–3). The corresponding absorption term in the optical potential was proposed in [27] in the form of $iW_V f(r)$ with $W_V[\mathrm{MeV}] = -3.3(1 + 0.03E)$. Surface absorption is usually given as $iW_S(df/dr)$. For small values of transferred momentum (small angles), both variants of absorption must result in similar descriptions of the scattering process. In the case of $a \ll R$, this leads to $W_S \approx -(R/3)W_V$. So, as an absorption term, we use the combination of the form

$$iW_V\left[\alpha - (1-\alpha)\frac{R}{3}\frac{d}{dr}\right] f(r) \qquad (10)$$

with $0 \le \alpha \le 1$, which leads to polarization effects independent of α at small scattering angles, but strongly dependent on α at large values of transferred momentum. Thus, for the description of polarization effects, we use the optical potential of the form (6), but with

$$V_o \to -52(1 - 0.0058E) \qquad (11)$$
$$- i \cdot 3.3(1 + 0.03E)\left[\alpha - (1-\alpha)\frac{R}{3}\frac{d}{dr}\right],$$

adopting similar energy dependences for isoscalar and isovector terms of the central nuclear potential.

In the figure, one can see the results of our calculations for the analyzing power A in the case of the (p, n) reaction on ^{48}Ca leading to the isoanalog state,

$$A_{\mathrm{th}} = \frac{d\sigma_{\uparrow\uparrow}/d\omega - d\sigma_{\uparrow\downarrow}/d\omega}{d\sigma_{\uparrow\uparrow}/d\omega + d\sigma_{\uparrow\downarrow}/d\omega}, \quad |A| \le 1, \qquad (12)$$

together with experimental data and results of microscopic calculations from [26]. Here, $\sigma_{\uparrow\uparrow}$ and $\sigma_{\uparrow\downarrow}$ are cross sections with the polarization vector $\boldsymbol{\varepsilon}$ of

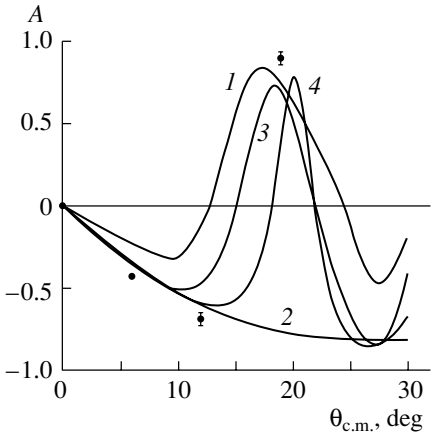

Experimental data (•) on analyzing power A [26] and the results of different calculations: (*1*) DWIA microscopic calculation [26]; (*2*) our calculation with $\alpha = 1$ (volume absorption), the other parameters being the same as for Table 3, including $\beta_{ls} = -0.6$; (*3*) our calculation with $\alpha = 0$ (surface absorption), the other parameters being from Table 3; (*4*) calculation with $\alpha = 0.5$ (surface–volume absorption).

protons parallel or antiparallel to $[\mathbf{k}_i \times \mathbf{k}_f]$. We see that, in the case of surface absorption ($\alpha \leq 0.5$), our calculations that use the spin–orbit parameters obtained from spin–orbit splitting demonstrate good agreement with the experiment up to high values of the scattering angle.

5. CONCLUSIONS

Using the available spectroscopic information on nuclei near the closed shells and the data on the (p, n) reactions, we for the first time defined the isotopic dependence of the spin–orbit average nuclear field. This dependence, consisting in more spin–orbit splitting for neutrons than for protons in the case of $N > Z$ nuclei, has received an explanation in the framework of different theoretical approaches. More precise knowledge of the spin–orbit splitting may be important in prediction of properties of an extreme neutron excess and superheavy nuclei, where the possible change of the ordering of levels and their spacings may lead to substantial variation of their properties.

ACKNOWLEDGMENTS

This work was supported by the Swedish National Research Council, the Royal Swedish Academy of Sciences, and the Russian Foundation for Basic Research (project no. RSGSS-1124.2003.2).

REFERENCES

1. P. Hoff, P. Baumann, A. Huck, *et al.*, Phys. Rev. Lett. **77**, 1020 (1996).
2. M. Sanchez-Vega, B. Fogelberg, H. Mach, *et al.*, Phys. Rev. Lett. **80**, 5504 (1998).
3. N. J. Stone, D. Doran, M. Lindroos, *et al.*, Phys. Rev. Lett. **78**, 820 (1997).
4. V. I. Isakov, Preprint No. 2510, PNPI (Gatchina, 2003); Phys. At. Nucl. **67**, 911 (2004).
5. V. I. Isakov, K. I. Erokhina, H. Mach, *et al.*, Eur. Phys. J. A **14**, 29 (2002).
6. B. Fogelberg, M. Hellström, D. Jerrestam, *et al.*, Phys. Scripta T **56**, 79 (1995).
7. J. Blomqvist, in *Proceedings of the 4th International Conference on Nuclei Far from Stability, Helsingor, 1981*; CERN Report No. 81-09 (1981), p. 536.
8. A. Bohr and B. R. Mottelson, *Nuclear Structure* (Benjamin, New York, 1969), Vol. 1.
9. S. C. Pieper and V. R. Pandharipande, Phys. Rev. Lett. **70**, 2541 (1993).
10. K. I. Erokhina and V. I. Isakov, Yad. Fiz. **57**, 212 (1994) [Phys. At. Nucl. **57**, 198 (1994)].
11. K. I. Erokhina and V. I. Isakov, Yad. Fiz. **59**, 621 (1996) [Phys. At. Nucl. **59**, 589 (1996)].
12. V. I. Isakov and K. I. Erokhina, Phys. At. Nucl. **65**, 1431 (2002).
13. K. T. R. Davies and R. J. McCarthy, Phys. Rev. C **4**, 81 (1971).
14. J. D. Walecka, Ann. Phys. (N.Y.) **83**, 491 (1974).
15. R. Brockmann, Phys. Rev. C **18**, 1510 (1978).
16. J. V. Noble, Nucl. Phys. A **329**, 354 (1979).
17. B. L. Birbrair, L. N. Savushkin, and V. N. Fomenko, Yad. Fiz. **35**, 1134 (1982) [Sov. J. Nucl. Phys. **35**, 664 (1982)].
18. P.-G. Reinhardt, M. Rufa, J. Martin, *et al.*, Z. Phys. A **323**, 13 (1986).
19. Suk-Joon Lee, J. Fink, A. B. Balantekin, *et al.*, Phys. Rev. Lett. **57**, 2916 (1986).
20. W. Koepf and P. Ring, Z. Phys. A **339**, 81 (1991).
21. B. L. Birbrair, Preprint No. 2234, PNPI (Gatchina, 1998).
22. S. Yoshida and H. Sagawa, Nucl. Phys. A **658**, 3 (1999).
23. R. Macleidt, K. Holinde, and Ch. Elster, Phys. Rep. **149**, 1 (1987).
24. A. M. Lane, Nucl. Phys. **35**, 676 (1962).
25. V. I. Isakov, Yad. Fiz. **66**, 1279 (2003) [Phys. At. Nucl. **66**, 1239 (2003)].
26. B. D. Anderson, T. Chittrakarn, A. R. Baldwin, *et al.*, Phys. Rev. C **34**, 422 (1986).
27. A. G. Sitenko, *Theory of Nuclear Reactions* (Énergoatomizdat, Moscow, 1983) [in Russian].

Physics of Atomic Nuclei, Vol. 67, No. 10, 2004, pp. 1829–1833. From Yadernaya Fizika, Vol. 67, No. 10, 2004, pp. 1856–1860.

Proceedings of the International Conference "Nuclear Structure and Related Topics"

The $X(5)$ Critical Point Nuclei and the Interacting Boson Model Symmetry Triangle*

N. V. Zamfir, E. A. McCutchan, and R. F. Casten**

WNSL, Yale University, New Haven, USA

Received January 21, 2004

Abstract—Shape/phase transitions in low-energy nuclear spectra, the new critical point symmetries $E(5)$ and $X(5)$, and their empirical realization have recently been the subject of many experimental and theoretical investigations. With a set of polar coordinates, the precise location of the critical phase transition region and of $X(5)$-type nuclei can be mapped in the interacting boson model symmetry triangle. An empirical mapping of the symmetry triangle for the $N = 82-104$ rare-earth nuclei is also obtained.

1. INTRODUCTION

Collectivity in low-energy nuclear motion is usually described relative to the geometrical models of harmonic vibrator [1], deformed symmetric rotor [2], and γ-unstable nuclei [3], or in terms of the dynamical symmetries of the interacting boson model [4]: $U(5)$, $SU(3)$, and $O(6)$, respectively. The nuclear shape depends strongly on the number of valence nucleons: it evolves from spherical near closed shells to quadrupole deformed towards the middle of the shells. It has been shown [5, 6] that spherical-deformed transition regions in the interacting boson approximation (IBA) model from $U(5)$ to $SU(3)$ and from $U(5)$ to $O(6)$ behave as first- and second-order phase transitions, respectively. The pronounced β softness of the phase/shape transition region inspired F. Iachello to introduce a square well potential in the Bohr Hamiltonian to describe this region. By solving analytically the Schrödinger equation, he developed new solutions called critical point symmetries, $E(5)$ [7] (for a spherical vibrator to a deformed γ-soft second-order phase transition) and $X(5)$ [8] (for a spherical vibrator to axially symmetric rotor first-order phase transition). Empirical examples close to these symmetries were found in nuclei: ^{134}Ba [9, 10], ^{102}Pd [11], and ^{104}Ru [12] as $E(5)$ examples and ^{152}Sm [13], ^{150}Nd [14], and ^{156}Dy [15] as $X(5)$ examples. In fact, the search for new examples of $X(5)$ symmetry continues to be the focus of many experimental and theoretical studies [16–19].

In this work, by introducing a set of polar coordinates, we will perform a mapping of the IBA symmetry triangle with a precise location of the phase/shape transition regions, of the $X(5)$-type nuclei, and of the "empirical" trajectories corresponding to the fit of each isotopic chain with $Z = 62-72$.

2. PHASE/SHAPE TRANSITION IN THE IBA AND THE $X(5)$-TYPE NUCLEI

We use the following IBA Hamiltonian in the extended consistent-Q formalism [20, 21]:

$$H(\zeta) = c\left[(1-\zeta)\hat{n}_d - \frac{\zeta}{4N_B}\hat{Q}^\chi\cdot\hat{Q}^\chi\right], \quad (1)$$

where N_B is the total number of bosons, $\hat{n}_d = d^\dagger\tilde{d}$, and $\hat{Q}^\chi = (s^\dagger\tilde{d} + d^\dagger s) + \chi(d^\dagger\tilde{d})^{(2)}$. This Hamiltonian contains two parameters, ζ and χ (c is only a scaling factor), and can describe all three IBA dynamical symmetries: $\zeta = 0$, any χ for $U(5)$; $\zeta = 1$, $\chi = -\sqrt{7}/2$ for $SU(3)$; and $\zeta = 1$, $\chi = 0$ for $O(6)$. The Hamiltonian also describes, by numerical diagonalization, a large variety of transitional structures.

It is possible to provide a quantitative description of the IBA parameter space of Eq. (1) in the symmetry triangle by representing each set of parameters (ζ, χ) by polar coordinates (ρ, θ) [22]:

$$\rho = \frac{\zeta\sqrt{3}}{\sqrt{3}\cos\theta_\chi - \sin\theta_\chi}, \quad (2)$$
$$\theta = \frac{\pi}{3} + \theta_\chi,$$

where $\theta_\chi = \dfrac{2}{\sqrt{7}}\chi\dfrac{\pi}{3}$.

*This article was submitted by the authors in English.

**e-mail: victor.zamfir@yale.edu

1063-7788/04/6710-1829$26.00

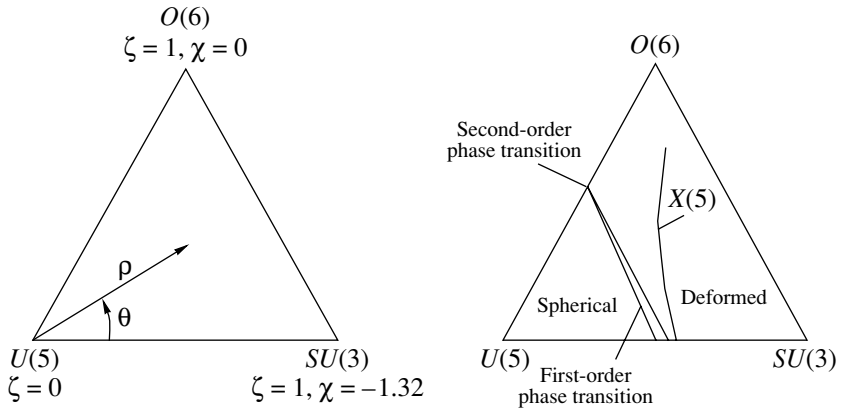

Fig. 1. The IBA symmetry triangle: (Left) Definition of the polar coordinates ρ, θ from Eq. (2). (Right) The phase transition region and the loci of $X(5)$-type spectra (trajectories labeled $X(5)$) [i.e., those IBA parameters which produce $R_{4/2} = 2.90$ and $E(0_2^+)/E(2_1^+) \sim 6$] for $N_B = 10$.

These coordinates allow for a convenient description of the entire IBA symmetry triangle. For example, $\rho = 0$ for $U(5)$ and $\rho = 1, \theta = \pi/3$ for $O(6)$ and $\rho = 1, \theta = 0$ for $SU(3)$. Figure 1 (left) represents the IBA symmetry triangle showing the definition of these polar coordinates and the three dynamical symmetries in terms of the Hamiltonian parametrization in Eq. (1).

The total energy corresponding to the IBA Hamiltonian can be obtained using the intrinsic state formalism and is expressed in terms of the intrinsic shape variables β, γ [23]. The study of the functional form for the total energy has shown that there is a phase/shape transition as a function of the control parameters ζ and χ. For fixed χ, a phase transition occurs in the ground-state energy at a critical value of the parameter $\zeta = \zeta_{\text{crit}}$: for $\chi \neq 0$, there is a first-order phase transition, and for $\chi = 0$, there is a second-order phase transition.

In the first-order phase transition, there is a region where two minima, spherical and deformed, occur in the total energy. This is a region of phase/shape coexistence [24]. The phase/shape coexistence region starts, with increasing ζ, where the deformed

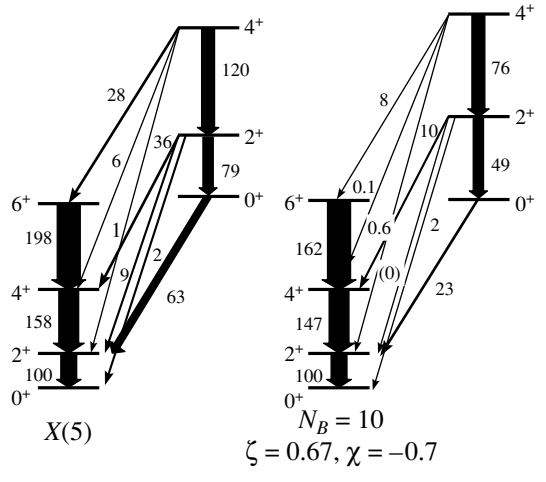

Fig. 2. Comparison of the IBA results for $N_B = 10$, $\chi = -0.7$, $\zeta = 0.67$ with the $X(5)$ predictions. The thickness of the arrows is approximately proportional to the respective $B(E2)$ values.

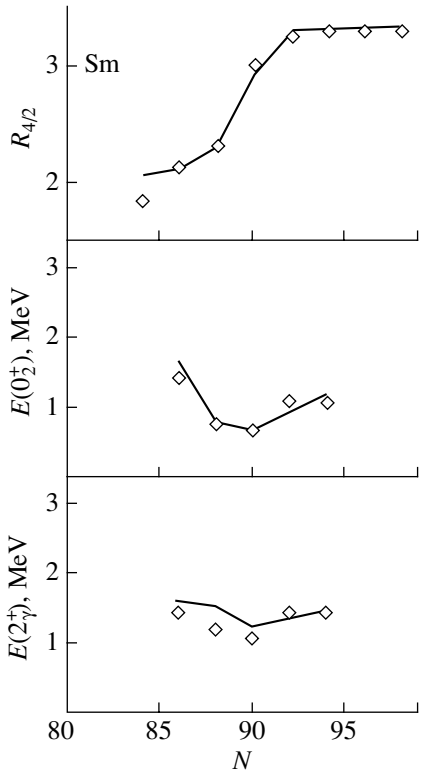

Fig. 3. The evolution of $R_{4/2}$, $E(0_2^+)$, and $E(2_\gamma^+)$ for the Sm isotopic chain with $N > 82$ compared with the IBA results [25].

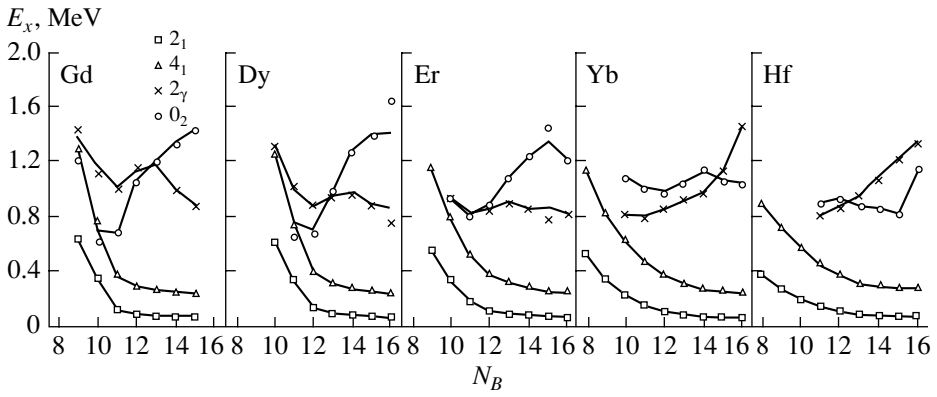

Fig. 4. Comparison between empirical level energies (symbols) and the IBA calculations (solid lines) for Gd–Hf isotopes.

minimum develops in addition to the spherical one and ends where the spherical minimum disappears. The critical point, where the first derivative is discontinuous, is $\zeta_{\rm crit} = 16N_B/(34N_B - 27)$. For example, for $\chi = -\sqrt{7}/2$ and $N_B = 10$, the three values of ζ characteristic of this phase/shape transition are 0.507, 0.542, and 0.512, respectively. The range of ζ corresponding to the region of coexistence becomes smaller for smaller $|\chi|$ [24] and for $\chi = 0$ ($U(5)$–$O(6)$ transition) converges to one point, the critical point of the second-order phase transition. This critical point is given by $\zeta = N_B/(2N_B - 2)$ and is equal to 0.556 for $N_B = 10$. We refer to these ranges of ζ and χ as the "phase transition region" and they are illustrated in Fig. 1 (right) for $N_B = 10$. Different observables related to the order parameter β should be discontinuous in the phase transition region. The discontinuities appear only for $N_B \to \infty$, and for finite N_B, the transition is smoothed out, exhibiting an abrupt change rather than a discontinuity (see below).

As was mentioned in the Introduction, a potential in the Bohr Hamiltonian very similar to the flat-bottomed potential in the phase/shape transition region, namely, a square well potential, generates the new critical point symmetries which give parameter-free predictions, except for scale. In the axially symmetric case, the solution, called $X(5)$, gives predictions for two important structural signatures, $R_{4/2} \equiv E(4_1^+)/E(2_1^+) = 2.90$ and $R_{0_2} \equiv E(0_2^+)/E(2_1^+) = 5.65$. A detailed comparison (presented in Fig. 2) of the $X(5)$ predictions with IBA calculations, using $N_B = 10$, $\chi \sim -0.7$, and $\zeta \sim 0.67$, shows that, while the values for these two ratios can be reproduced exactly in the IBA, some transition probabilities between the levels of the 0_2^+-based sequence and the quasi-ground band are poorly reproduced. IBA calculations which reproduce the $X(5)$ values of $R_{4/2}$ and R_{0_2} are very close to the phase/shape transition region. Figure 1 also shows the locus of the IBA parameters for $N_B = 10$, which reproduce exactly the $X(5)$ value for $R_{4/2}$, i.e., 2.90, and, within a reasonable deviation, the other characteristic energy ratio $E(0_2^+)/E(2_1^+)$ (labeled here the $X(5)$ trajectory).

3. EMPIRICAL TRAJECTORIES OF PHASE/SHAPE TRANSITIONAL NUCLEI

A well-known example of an $U(5)$–$SU(3)$ transition is the $N \sim 90$ region. In fact, the Sm isotopes were well described in the framework of the IBA [25] and $^{152}{\rm Sm}_{90}$ was the first empirical example of a nucleus very close to the $X(5)$ solution [13]. In Fig. 3, empirical basic observables, $R_{4/2} \equiv E(4_1^+)/E(2_1^+)$ and the energies of the head of 0_2^+ and γ quasi-bands for the Sm isotopic chain, are compared with the IBA results. The $R_{4/2}$ ratio evolves from $\sim$2.0, characteristic for the $U(5)$ symmetry, to $\sim$3.33, characteristic for $SU(3)$ symmetry, with a sharp rise at $N = 90$. The energies of the intrinsic excitations 0_2^+ and 2_γ^+ have a minimum also at $N = 90$. This point corresponds in the IBA to a calculation very near the critical point of the phase/shape $U(5)$–$SU(3)$ transition [26] (see below).

The Gd and Dy isotopic chains exhibit a similar evolution [26], while the Yb and Hf isotopic chains show a different behavior. A detailed fit for the Gd, Dy, Er, Yb, and Hf isotopes with $82 < N \leq 104$ was performed considering the basic observables, energies of the 2_1^+, 4_1^+, 2_γ^+, and 0_2^+ states and available transition probabilities [27]. In Fig. 4, a comparison is presented of the empirical energies of these states with the IBA results. The agreement is impressive, including the description of the 0_2^+ states, which were poorly described in previous fits [28]. The other excited states are reproduced quite well. (The main exceptions are the $2_{K=0}^+$–0_2^+ relative energies for $N \sim$

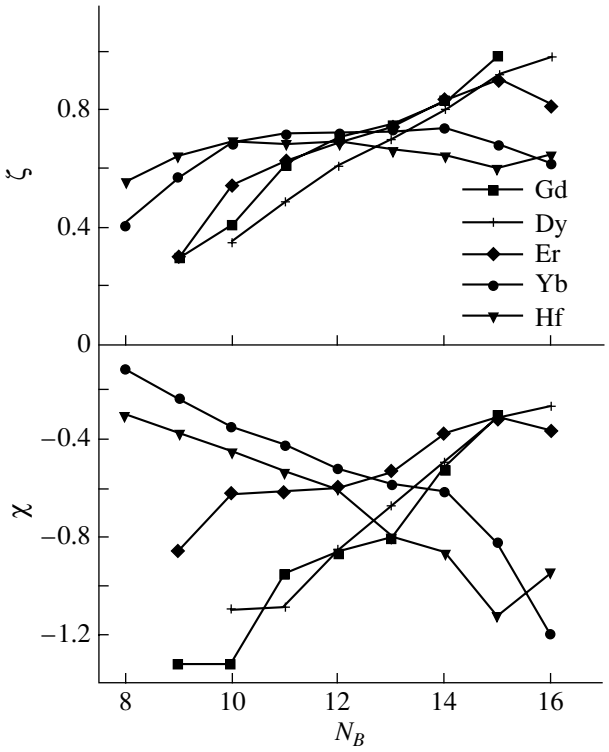

Fig. 5. The parameters ζ and χ for the IBA Hamiltonian in Eq. (1) describing the Gd–Hf isotopic chains with $84 < N \leq 104$.

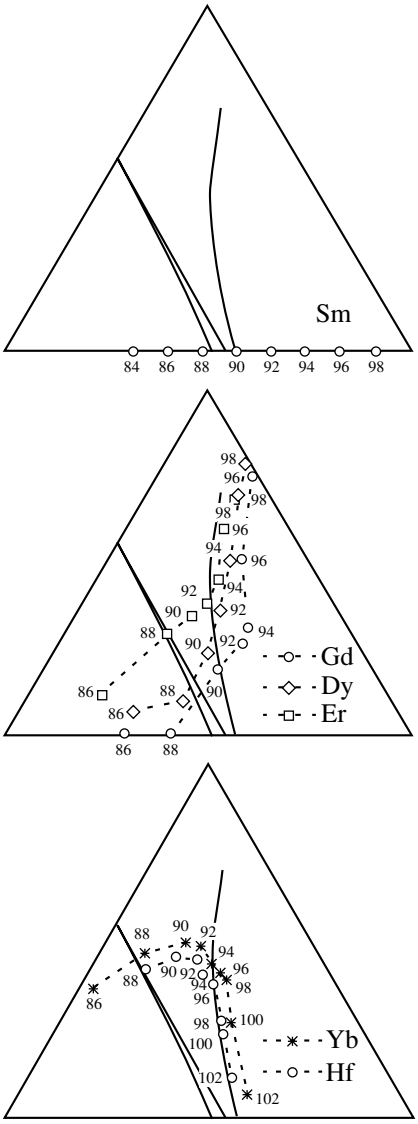

Fig. 6. The trajectories corresponding to the IBA fits for $^{146-160}Sm_{84-98}$, $^{150-162}Gd_{86-98}$, $^{152-164}Dy_{86-98}$, $^{154-166}Er_{86-98}$, $^{156-172}Yb_{86-102}$, and $^{160-174}Hf_{88-102}$ isotopic chains (N is shown for each individual point) in the IBA symmetry triangle. In each case are also shown the critical phase transition region and the $X(5)$ trajectory from Fig. 1 (right).

90 nuclei, which are larger in the calculations than the empirical values.) Electromagnetic transitions are also reproduced reasonably well.

The fitted parameters vary smoothly along each isotopic chain, as can be seen in Fig. 5. The trajectories in the symmetry triangle corresponding to these fitted parameters are shown in Fig. 6 in terms of the polar coordinates defined in Eq. (2). All isotopic chains are, as expected, transitional from $U(5)$ for N just above 82, toward the $SU(3)$–$O(6)$ leg (large ζ) with increasing N. The Sm isotopic chain corresponds to a $U(5)$–$SU(3)$ transition (which corresponds to a minimum of $V(\gamma)$ at 0°). The higher Z chains show an increasing γ softness for low N (≤ 90), but for higher N there are two different behaviors: the Gd, Dy, and Er isotopes show an increasing γ softness (closer to the $U(5)$–$O(6)$ leg), while the Yb and Hf isotopes with $N > 90$ present an increased γ rigidity. Each isotopic chain crosses the critical phase transition region and the $X(5)$ trajectory (corresponding to the fit of the $R_{4/2}$ and R_{0_2} ratios) at $N \sim 90$. Other basic observables are also very close to the $X(5)$ predictions. In Fig. 7, the yrast band's $B[E2; J \to (J-2)]$ values, normalized to the $2_1^+ \to 0_1^+$ transition, are shown for the best candidates for $X(5)$ nuclei: ^{152}Sm [13], ^{154}Gd, ^{156}Dy [15], and ^{162}Yb [19].

4. CONCLUSION

Comparison of the predictions of the $X(5)$ symmetry for different observables with the results of the extended consistent-Q formalism of the IBA shows that the former are never exactly reproduced in this IBA space of the Hamiltonian of Eq. (1) and that the best agreement is close to but does not coincide with the phase transition region defined by the intrinsic

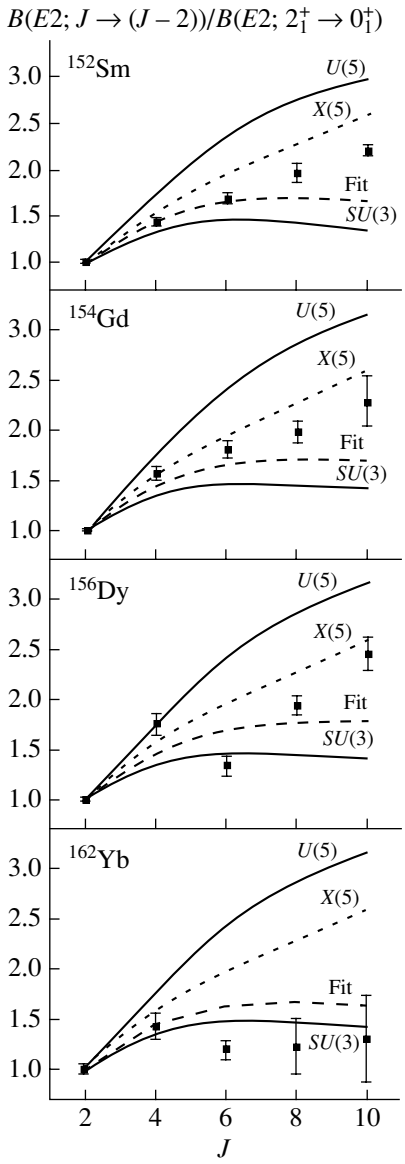

Fig. 7. Empirical yrast band $B(E2)$ values for the closest candidates for $X(5)$-type nuclei compared with the dynamical symmetries $U(5)$, $X(5)$, and $SU(3)$ predictions and with the results of the present IBA fit.

state formalism for a finite number of bosons. A set of polar coordinates allows a precise location of the nuclear critical phase transition region and of $X(5)$-type nuclei in the IBA symmetry triangle.

Empirical trajectories in the symmetry triangle corresponding to IBA fits to basic observables reveal two main evolutions of the $Z = 64-72$, $N = 82-104$ nuclei from spherical to deformed shapes: for N approaching mid shell Gd–Er nuclei show a pronounced γ softness relative to the Yb–Hf nuclei. A general feature of all trajectories is that they cross the critical phase/shape transition region at $N \sim 90$.

ACKNOWLEDGMENTS

We would like to thank F. Iachello and G. Fernandes for valuable discussions.

This work was supported by US DOE grant no. DE-FG02-91ER-40609.

REFERENCES

1. G. Sharff-Goldhaber and J. Weneser, Phys. Rev. **98**, 212 (1955).
2. A. Bohr, K. Dan. Vidensk. Selsk. Mat. Fys. Medd. **26** (14) (1952).
3. L. Wilets and M. Jean, Phys. Rev. **102**, 788 (1956).
4. F. Iachello and A. Arima, *The Interacting Boson Model* (Cambridge University Press, Cambridge, 1987).
5. A. E. L. Dieperink, O. Scholten, and F. Iachello, Phys. Rev. Lett. **44**, 1747 (1980); Nucl. Phys. A **346**, 125 (1980).
6. D. H. Feng, R. Gilmore, and S. R. Deans, Phys. Rev. C **23**, 1254 (1981).
7. F. Iachello, Phys. Rev. Lett. **85**, 3580 (2000).
8. F. Iachello, Phys. Rev. Lett. **87**, 052502 (2001).
9. R. F. Casten and N. V. Zamfir, Phys. Rev. Lett. **85**, 3584 (2000).
10. J. M. Arias, Phys. Rev. C **63**, 034308 (2001).
11. N. V. Zamfir *et al.*, Phys. Rev. C **65**, 044325 (2002).
12. A. Frank, C. E. Alonso, and J. M. Arias, Phys. Rev. C **65**, 014301 (2002).
13. R. F. Casten and N. V. Zamfir, Phys. Rev. Lett. **87**, 052503 (2001).
14. R. Krücken *et al.*, Phys. Rev. Lett. **88**, 232501 (2002).
15. M. A. Caprio *et al.*, Phys. Rev. C **66**, 054310 (2002).
16. P. G. Bizzeti and A. M. Bizzeti-Sona, Phys. Rev. C **66**, 031301(R) (2002).
17. C. Hutter *et al.*, Phys. Rev. C **67**, 054315 (2003).
18. R. M. Clark *et al.*, Phys. Rev. C **68**, 037301 (2003).
19. E. A. McCutchan *et al.*, Phys. Rev. C **69**, 024308 (2004).
20. D. D. Warner and R. F. Casten, Phys. Rev. Lett. **48**, 1385 (1982).
21. P. O. Lipas, P. Toivonen, and D. D. Warner, Phys. Lett. B **155B**, 295 (1985).
22. E. A. McCutchan, N. V. Zamfir, and R. F. Casten, Phys. Rev. C **69**, 064306 (2004).
23. J. N. Ginocchio and M. W. Kirson, Nucl. Phys. A **350**, 31 (1980).
24. F. Iachello, N. V. Zamfir, and R. F. Casten, Phys. Rev. Lett. **81**, 1191 (1998).
25. O. Scholten, F. Iachello, and A. Arima, Ann. Phys. (N.Y.) **115**, 325 (1978).
26. N. V. Zamfir, P. von Brentano, R. F. Casten, and J. Jolie, Phys. Rev. C **66**, 021304(R) (2002).
27. Nucl. Data Sheets **97** (1, 2, 3/4) (2002).
28. W. T. Chou, N. V. Zamfir, and R. F. Casten, Phys. Rev. C **56**, 829 (1997).

Physics of Atomic Nuclei, Vol. 67, No. 10, 2004, pp. 1834–1839. From Yadernaya Fizika, Vol. 67, No. 10, 2004, pp. 1861–1866.

Proceedings of the International Conference "Nuclear Structure and Related Topics"

An Importance Sampling Algorithm for Diagonalizing the Nuclear Shell-Model Hamiltonian*

F. Andreozzi, N. Lo Iudice, and A. Porrino**

Dipartimento di Scienze Fisiche, Università di Napoli Federico II, and Istituto Nazionale di Fisica Nucleare, Complesso Universitario di Monte S. Angelo, Napoli, Italy

Received January 21, 2004

Abstract—We have developed an iterative algorithm for generating exact eigensolutions of large matrices and endowed it with an importance sampling which allows for a reduction of the sizes of the matrices while keeping full control of the accuracy of the eigensolutions. We illustrate the potential of the method through its application to the nuclear shell-model eigenproblem. © *2004 MAIK "Nauka/Interperiodica".*

1. INTRODUCTION

The solution of the exact eigenvalue problem of complex systems is a challenging task even with modern computers. In nuclear structure, several roots have been followed for solving the shell-model (SM) problem in complex nuclei. One, of stochastic nature, is the Monte Carlo technique [1, 2]. This, however, is of rather limited applicability because of the well-known minus-sign problem and, in any case, can be adopted effectively only for generating the ground state. Other algorithms, like Lanczos [3] and Davidson [4], deal with the direct diagonalization of the SM Hamiltonian. Even in their most sophisticated versions, they reach a critical limit in the exceedingly large amount of memory needed and the time spent in the process of diagonalizing the huge SM Hamiltonian matrices, especially in heavy nuclei.

A more recent strategy, devoted to reconciling the two extreme approaches and therefore overcoming the limitations of each separate method, consisted in including a stochastic methodology in the standard diagonalization approaches [5–10]. A notable one is the so-called quantum Monte Carlo diagonalization method (QMCD), which turned out to be quite efficient in reducing the dimension of the SM space by using the auxiliary field Monte Carlo technique to select the relevant basis states [9, 10]. Though successful, the method has to deal with the redundancy of the basis states, which may slow considerably the convergence of the procedure, and with the problem of restoring the symmetries generally broken in the process of stochastically searching the basis.

We developed an iterative algorithm for determining a set of eigenvectors of a large matrix [11]. This is faster than the other, currently adopted, approaches and extremely simple to implement. We have further endowed the algorithm with an importance sampling, which allows one to reduce the sizes of the matrix while keeping under full control the accuracy of the eigensolutions [12].

For an exhaustive test, we adopted the method to solve the SM problem for a few typical nuclei. In order to enhance its efficiency, we used a correlated basis obtained from partitioning the SM space [13]. We computed a selected set of eigenvalues and eigenvectors as well as the $E2$ transition probabilities. In this paper, we outline the importance sampling algorithm and discuss the most meaningful results.

2. THE IMPORTANCE SAMPLING ALGORITHM

Although of more general validity, the algorithm, for illustrative purposes, is applied here to a symmetric matrix $A = \{(a_{ij}) = \langle i|\hat{A}|j\rangle\}$ representing a self-adjoint operator $\hat{A}$ in an orthonormal basis $\{|1\rangle, |2\rangle, \ldots, |N\rangle\}$. The method consists of several iteration loops. The first loop goes through the following steps:

(a) Diagonalize the two-dimensional matrix (a_{ij}) $(i, j = 1, 2)$.

(b) Select the lowest eigenvalue λ_2 and the corresponding eigenvector

$$|\phi_2\rangle = c_1^{(2)}|1\rangle + c_2^{(2)}|2\rangle.$$

(c) For $j = 3, \ldots, N$ diagonalize the matrix

$$\begin{pmatrix} \lambda_{j-1} & b_j \\ b_j & a_{jj} \end{pmatrix}, \qquad (1)$$

*This article was submitted by the authors in English.

**e-mail: loiudice@na.infn.it

where $b_j = \langle\phi_{j-1}|\hat{A}|j\rangle$ and select the lowest eigenvalue λ_j together with the corresponding eigenvector $|\phi_j\rangle$. This zero approximation loop yields the approximate eigenvalue and eigenvector

$$E^{(1)} \equiv \lambda_N, \qquad (2)$$
$$|\psi^{(1)}\rangle \equiv |\phi_N\rangle = \sum_{i=1}^{N} c_i^{(N)}|i\rangle.$$

With these new entries, we start an iterative procedure which goes through $n = 2, 3, \ldots$ refinement loops, consisting of the same steps with the following modification. At each step $j = 1, 2, \ldots, N$ of the nth loop ($n > 1$), we have to solve an eigenvalue problem of general form, since the states $|\phi_{j-1}\rangle$ and $|j\rangle$ are no longer orthogonal. The eigenvalue $E^{(n)} \equiv \lambda_N$ and eigenvector $|\psi^{(n)}\rangle \equiv |\phi_N\rangle$ obtained after the nth loop are proven to converge to the exact eigenvalue E and eigenvector $|\psi\rangle$, respectively [11].

The algorithm has been shown to be completely equivalent to the method of optimal relaxation [14] and has therefore a variational foundation. Because of its matrix formulation, however, it can be generalized with minimal changes so as to generate at once an arbitrary number n_v of eigensolutions. Indeed, we have to replace the two dimensional matrix (1) with a multidimensional one

$$\begin{pmatrix} \lambda_{j-1} & b_j \\ b_j & a_{jj} \end{pmatrix} \rightarrow \begin{pmatrix} \Lambda_k & B_k \\ B_k^T & A_k \end{pmatrix}, \qquad (3)$$

where Λ_k is a n_v-dimensional diagonal matrix whose nonzero entries are the eigenvalues $\lambda_1^{(k-1)}, \lambda_2^{(k-1)}, \ldots, \lambda_{n_v}^{(k-1)}$, $A_k = \{a_{ij}\}(i, j = (k-1)p+1, \ldots, kp)$ is a p-dimensional submatrix, and B_k and its transpose are matrices composed of the matrix elements $b_{ij}^{(k)} = \langle\phi_i^{(k-1)}|\hat{A}|j\rangle$ $(i = 1, \ldots, n_v;\ j = (k-1)p + 1, \ldots, kp)$. A loop procedure similar, though more general, to the one adopted in the one-dimensional case yields a set of n_v eigenvalues $E_1, \ldots, E_{n_v}$ and corresponding eigenvectors $\psi_1, \ldots, \psi_{n_v}$.

As proven and illustrated through typical numerical tests in [11], the algorithm is robust, being numerically stable and converging always to the extremal eigenvalues. It yields ghost-free solutions and generates orthogonal eigenvectors. It is also easy to implement and is fast, requiring $O(N^2)$ operations. Like the other methods, however, it requires the storage of at least one eigenvector. Since for many complex systems the dimensions of the Hamiltonian matrix become prohibitively large, one must rely on some importance sampling which allows for a truncation of the space by selecting only the basis states which actually enter into the exact eigensolutions.

Our algorithm offers a simple and efficient strategy. Being solutions that are quite accurate already in the first approximation loop, we can devise a sampling which exploits this first loop only. This, however, is to be accordingly modified as follows:

(1a) Diagonalize the v-dimensional principal submatrix $\{a_{ij}\}(i, j = 1, \ldots, v)$.

(1b) For $j = v+1, \ldots, N$, diagonalize the $(v+1)$-dimensional matrix

$$A = \begin{pmatrix} \Lambda_v & \mathbf{b}_j \\ \mathbf{b}_j^T & a_{jj} \end{pmatrix}, \qquad (4)$$

where $\mathbf{b}_j = \{b_{1j}, \ldots, b_{2j}, \cdot, b_{vj}\}$.

(1c) Select the lowest v eigenvalues $\lambda_i'(i = 1, \ldots, v)$ and accept the new set only if

$$\sum_{i=1,v} |\lambda_i' - \lambda_i| > \epsilon, \qquad (5)$$

otherwise restart from point (1b) with a new j.

We can avoid the explicit diagonalization of matrix (4) by carrying on a similarity transformation. This allows us to meet condition (5) upon the solution of a dispersion relation [12] and, therefore, avoids the $(N-v)$-fold iterated diagonalization of $(v+1)$-dimensional matrices. In the one-dimensional eigenspace ($v = 1$), the dispersion relation is simply

$$\Delta\lambda = \sum_j \Delta\lambda_j = \sum_j (\lambda_j' - \lambda_j) \qquad (6)$$
$$= -\sum_j \frac{b_{1j}^2}{a_{jj} - \lambda_j - \Delta\lambda_j}.$$

3. CORRELATED BASIS THROUGH MULTIPARTITIONING

The truncation induced by the sampling is more and more severe as the eigenvectors are more and more localized. In order to approach a condition of maximal localization, we used a correlated basis obtained by the following multipartitioning method [13]: (i) partition the SM space for N valence nucleons into orthogonal subspaces $P = P_1 + P_2$; (ii) distribute N_1 and N_2 nucleons ($N_1 + N_2 = N$) among these subspaces in all possible ways; (iii) decompose the Hamiltonian H into $H = H_1 + H_2 + H_{12}$; (iv) solve the eigenvalue equations

$$H_i|\alpha_i N_i\rangle = E_{\alpha_i}|\alpha_i N_i\rangle, \qquad (7)$$

obtaining the eigenstates $|\alpha_1 N_1\rangle$ and $|\alpha_2 N_2\rangle$ of H_1 and H_2, respectively, in P_1 and P_2. Once this is done, we replace the standard SM basis with the correlated one

$$|\alpha N\rangle = |\alpha_1 N_1 \alpha_2 N_2\rangle. \qquad (8)$$

4. APPLICATIONS TO TYPICAL NUCLEI

We applied the sampling algorithm to three typical nuclei, the semimagic ^{108}Sn, the $N = Z$ even–even ^{48}Cr, and the $N > Z$ odd–even ^{133}Xe. We chose the following model spaces:

(i) $P \equiv \{2d5/2, 1g7/2, 2d3/2, 3s1/2, 1h11/2\}$ for the eight valence neutrons of ^{108}Sn and for the four valence protons and three valence neutron holes of ^{133}Xe,

(ii) $P \equiv \{1f7/2, 1f5/2, 2p3/2, 2p1/2\}$ for the four valence protons and neutrons of ^{48}Cr.

We adopted a realistic effective interaction deduced from the Bonn-A potential [15] for ^{108}Sn and ^{133}Xe and the KB3 interaction [16] for ^{48}Cr. We deduced the single particle from a fit of properly selected experimental data.

We partitioned the SM space for ^{108}Sn according to the following prescriptions:

$$P \equiv \{2d5/2, 1g7/2, 2d3/2, 3s1/2, 1h11/2\} \quad \nearrow P_1 \equiv \{2d5/2, 1g7/2\}, \quad + \quad \searrow P_2 \equiv \{2d3/2, 3s1/2, 1h11/2\}. \tag{9}$$

This partition is dictated by the large energy gap (~ 2 MeV) between the two corresponding sets of single-particle energies.

For ^{48}Cr and ^{133}Xe, we simply decompose the space into a proton and neutron subspace

$$P = P_p + P_n. \tag{10}$$

We generated a new correlated basis

$$|j\rangle = |\alpha N\rangle \tag{11}$$

by the multipartitioning method [13] and used this new basis to implement the importance sampling.

4.1. Eigenvalues

We discuss only a few of the lowest states of ^{108}Sn and ^{48}Cr as illustrative examples. As shown in the plot of Fig. 1, the sampling parameter ϵ varies very smoothly with the dimensions n of the reduced matrices. In these, as in all other states considered, it scales according to

$$\epsilon = b\frac{N}{n^2}\exp\left[-c\frac{N}{n}\right]. \tag{12}$$

In virtue of this law, the increment of the dimensions of the matrix is modest for large values of ϵ, but grows dramatically as ϵ gets smaller and smaller. This behavior reflects the density of the unperturbed levels, which is very low at low energy and rises steeply around a centroid at high energy. This is shown in Fig. 2. It is important to point out that this is the distribution of our unperturbed correlated states defined by Eq. (8). The partitioning of the SM space is responsible for the squeezing of their energies around a centroid. Had we adopted the standard SM basis, the state distribution would have been more spread out.

Figure 3 plots the eigenvalues versus the dimensions n of the matrices resulting from decreasing values of the sampling parameter ϵ for some low-lying states of ^{108}Sn and ^{48}Cr, respectively. The eigenvalues decrease monotonically and smoothly with n in all nuclei and for all states, with the few meaningful exceptions represented by the curves of the first excited $J^\pi = 0^+$ and $J^\pi = 2^+$ and a few other, similarly behaving, high-lying states of ^{48}Cr. These undergo a jump from an upper to a lower curve at some small value of the sampling parameter ϵ, a signal of energy crossing. Even in these cases, however, the subsequent behavior of the energies is smooth as for the other states. It follows that, in all cases, starting from a sufficiently small ϵ, the energies scale with the dimensions n according to the law

$$E = E_0 + b\frac{N}{n}\exp\left[-c\frac{N}{n}\right], \tag{13}$$

where b, c, and E_0 are constants specific to each state and the full dimension N provides the scale. This fit allows for an extrapolation to asymptotic eigenvalues which differ from the exact ones in the second or third decimal. This law is somewhat different from the one proposed in [7, 8]. On the other hand, it is valid for all states and nuclei examined and follows directly from the sampling, as can be inferred from the following heuristic argument.

Expanding $\Delta\lambda_j$ in Eq. (6), we get a solution whose

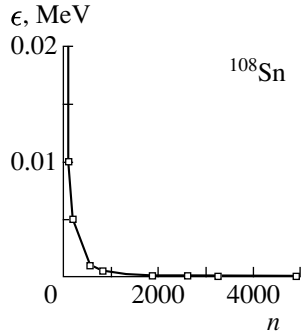

Fig. 1. Importance sampling parameters vs. the dimensions n of the truncated matrices resulting from the sampling.

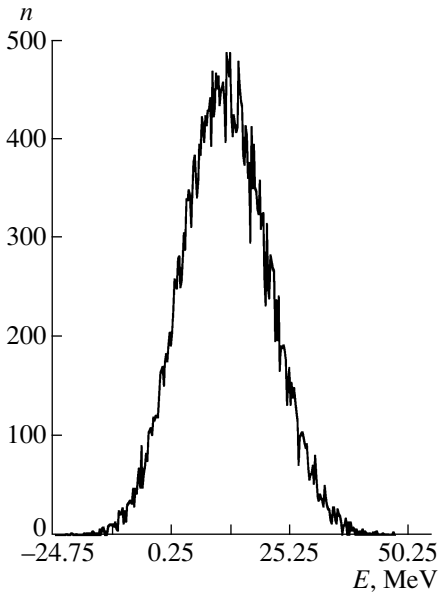

Fig. 2. Energy distribution of the unperturbed eigenvalues.

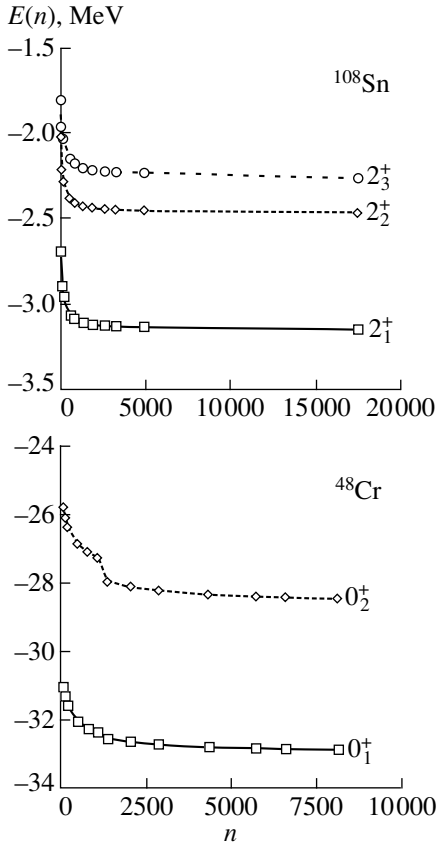

Fig. 3. Eigenvalues vs. the dimensions n of the truncated matrices resulting from the sampling.

leading term is

$$\Delta\lambda_j = \frac{b_{1j}^2}{a_{jj} - \lambda}. \qquad (14)$$

From the plots, it is clear that the extrapolation law holds for an energy range of 1–2 MeV in proximity of the exact eigenvalue. It accounts, therefore, for small contributions coming from a small fraction of the basis states in the $\sum_j$ in the high-density region around the peak, as shown in Fig. 2. Since, in this range, the energies E_j of our correlated basis states are closely packed and approach the E_n value, we can set $(a_{jj} - \lambda) \propto n$ in the first approximation. It remains to analyze the matrix elements b_{1j}^2. These are given by $\langle\phi_j|v|j\rangle^2$, where

$$|\phi_j\rangle = \sum_{i=1}^{j} c_i^j |i\rangle. \qquad (15)$$

For the lowest eigenvalue, the dominant c_i components of $|\phi_j\rangle$ are the low-energy ones with small i values. It follows that the probability, b_{1j}^2, that the interaction couples $|\phi_j\rangle$ to $|j\rangle$ is small and random for $j \leq n$ and vanishes for $j > n$, as prescribed by the sampling criterion. This implies that the dimension n represents the range of the allowed *events*. We can therefore set $b_{1j}^2 \propto \exp(-\bar{j}/n)$, where $\bar{j}$ is a label representative of the small fraction of j terms of the sum $\sum_j$. We used the factor N to fix the scale. The scaling law (12) for ϵ follows from the one for the energy E since ϵ is essentially the derivative of E with respect to n.

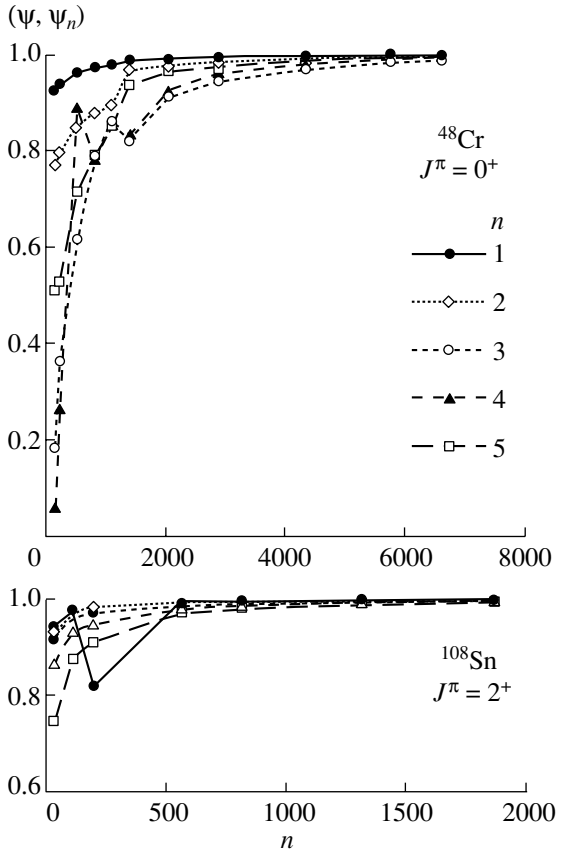

Fig. 4. Overlap of sampled wave functions with the corresponding exact ones.

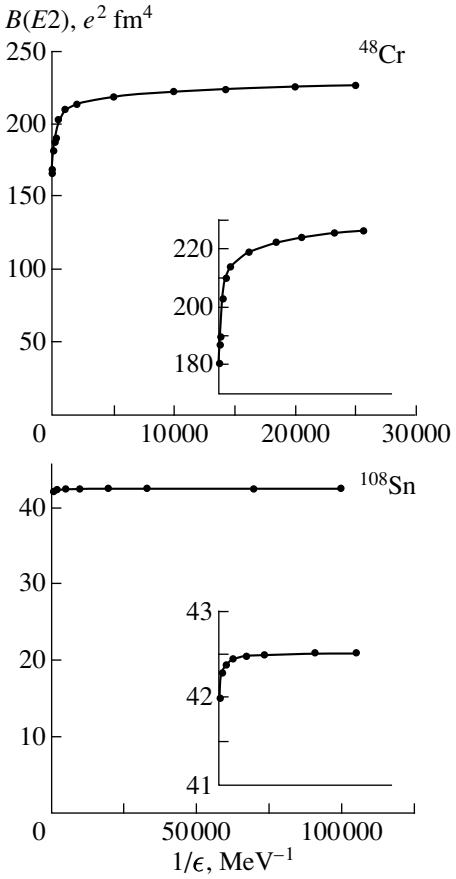

Fig. 5. Strengths of $E2$ transitions between some low-lying states vs. $1/\epsilon$.

4.2. Eigenvectors and E2 Transitions

The sampling guarantees an accuracy of the same quality also for the eigenstates

$$\psi_n = \sum_{i=1}^{n} c_i^{(n)} |i\rangle, \tag{16}$$

where $|i\rangle$ are the correlated basis states obtained by the partitioning method.

In Fig. 4, we give the overlap of ψ_n with the exact eigenvector ψ for the first five $J^\pi = 2^+$ states of ^{108}Sn and $J^\pi = 0^+$ of ^{48}Cr. The convergence to unity is fast for all five states, even if, for some of them, the overlap is very small at small n. Small fluctuations are noticeable at small n values. They reflect the interference between the components of different wave functions in correspondence with partial energy crossings. The above two features represent further proof of the *robustness* of the iterative algorithm.

To complete the analysis, we studied the behavior versus $1/\epsilon$ of the strengths of the $E2$ transitions between some low-lying states (Fig. 5). In all cases, the strengths soon reach a plateau and, then, undergo very small variations, appreciable only on a very small scale (see inset). This fine tuning analysis shows that each strength has smooth behavior which allows for an extrapolation to asymptotic values through a formula having the same structure as the scaling law adopted for the energies [Eq. (13)]. In any case, the strengths computed at a relatively large ϵ differ very little from the extrapolated ones, which in turn practically coincide with the exact values. This rapid convergence is quite significant in view of the extreme sensitivity of the transition strengths to even very small components of the wave function.

5. CONCLUDING REMARKS

The algorithm developed in [11] has several virtues. It has variational foundation and yields ghost-free solutions. Typical numerical tests have proven that it is robust, being numerically stable and converging always to the extremal eigenvalues. It is, moreover, easy to implement and is fast, requiring $O(N^2)$ operations.

Moreover, it can be naturally endowed with an importance sampling, which promotes a reduction of the sizes of the matrices. The truncation is not

only kept under strict control but also becomes quite severe when the eigenvectors are highly localized. For the SM nuclear Hamiltonian, we achieved this localization by adopting a correlated basis obtained by partitioning the SM space into two or more subspaces. As illustrated here for some typical nuclei, the sampling so implemented allows one to reduce the sizes of the Hamiltonian matrix by at least an order of magnitude with no detriment of the accuracy. We get in fact very accurate energies, wave functions, and $E2$ reduced strengths. Moreover, it generates extrapolation laws to asymptotic eigenvalues and $E2$ transition probabilities which practically coincide with the exact corresponding quantities.

In [12], we showed that the method is especially effective when applied to ^{133}Xe, having a neutron excess. On the basis of this result, we feel confident that the sampling, combined with the use of the correlated basis, will enable us to face successfully the eigenvalue problem in heavier nuclei, all having a neutron excess. We also would like to stress that the partition method is especially suitable for enlarging the standard SM valence space through the inclusion of n-particle–n-hole correlated configurations. We plan to make such an implementation in order to study the intruder states in light as well as heavy nuclei.

Although adopted here for solving the nuclear SM eigenproblem, the sampling algorithm is of general applicability. It is of simple and useful implementation in all many-body systems whenever a subset of eigensolutions is needed, as is often the case.

ACKNOWLEDGMENTS

The work was partly supported by the Prin 01 of the Italian MURST.

REFERENCES

1. A comprehensive account of the existing techniques can be found in *Quantum Monte Carlo Methods in Physics and Chemistry,* Ed. by M. P. Nightingale and C. J. Umrigar (Kluwer Acad., The Netherlands, 1999).
2. J. A. White, S. E. Koonin, and D. J. Dean, Phys. Rev. C **61**, 034303 (2000).
3. G. H. Golub and C. F. Van Loan, *Matrix Computations* (John Hopkins Univ. Press, Baltimore, 1996).
4. E. R. Davidson, J. Comput. Phys. **17**, 87 (1975).
5. K. Varga and R. J. Liotta, Phys. Rev. C **50**, 1292(R) (1994).
6. M. Horoi, B. A. Brown, and V. Zelevinsky, Phys. Rev. C **50**, R2274 (1994).
7. M. Horoi, A. Volya, and V. Zelevinsky, Phys. Rev. Lett. **82**, 2064 (1999).
8. M. Horoi, B. A. Brown, and V. Zelevinsky, Phys. Rev. C **67**, 034303 (2003).
9. M. Honma, T. Mizusaki, and T. Otsuka, Phys. Rev. Lett. **75**, 1284 (1995).
10. T. Otsuka, M. Honma, and T. Mizusaki, Phys. Rev. Lett. **81**, 1588 (1998).
11. F. Andreozzi, A. Porrino, and N. Lo Iudice, J. Phys. A **35**, L61 (2002).
12. F. Andreozzi, N. Lo Iudice, and A. Porrino, J. Phys. G **29**, 2319 (2003).
13. F. Andreozzi and A. Porrino, J. Phys. G **27**, 845 (2001).
14. I. Shavitt, C. F. Bender, A. Pipano, and R. P. Hosteny, J. Comput. Phys. **11**, 90 (1973).
15. R. Machleidt, Adv. Nucl. Phys. **19**, 189 (1989).
16. E. Caurier, A. P. Zuker, A. Poves, and G. Martinez-Pinedo, Phys. Rev. C **50**, 225 (1994).

Physics of Atomic Nuclei, Vol. 67, No. 10, 2004, pp. 1840–1845. From Yadernaya Fizika, Vol. 67, No. 10, 2004, pp. 1867–1871.

Proceedings of the International Conference "Nuclear Structure and Related Topics"

np Pairing Correlations in Low-Density Region of Nuclear Matter*

A. A. Isayev[1)], **S. I. Bastrukov[2),3),4)]**, and **J. Yang[2),3)]*****

Received January 21, 2004

Abstract—In the framework of Green's function formalism at finite temperatures, superfluidity of nuclear matter with np pairing correlations is studied. It is shown that, at low densities, equations for the energy gap in the spectrum of quasiparticles and chemical potentials of protons and neutrons allow solutions with negative chemical potential, which corresponds to appearance of Bose–Einstein condensation of deuterons in the low-density region of nuclear matter. In this region, np pairing correlations survive even for large isospin asymmetry. Interaction between nucleons is described by the effective zero range force, developed to reproduce the energy gap in the isospin singlet pairing channel, calculated with the use of the Paris NN potential. The obtained results may be of importance for description of thermal properties of outer low-density regions of neutron stars. © *2004 MAIK "Nauka/Interperiodica".*

1. INTRODUCTION

It is known that the magnitude of the pairing gap is of paramount relevance for the description of thermal evolution of neutron stars. Different values of the pairing gap correspond to drastically different scenarios of cooling process [1]. In this study, we would like to examine pairing properties of isospin asymmetric nuclear matter in the region of low densities. In an ordinary situation (for not overly low densities), isospin asymmetry effectively destroys a condensate with neutron–proton (np) Cooper pairs [2, 3]. However, for low densities, np pairing correlations survive and exist in the form of a Bose–Einstein condensate of deuterons, in spite of the fact that the isospin asymmetry may be very large. This conclusion may be of importance for description of thermodynamic properties of neutron stars, especially in their outer low-density regions. In addition, the appearance of deuterons can essentially modify magnetic properties of neutron stars, and, hence, it is relevant for determination of the neutrino mean free path [4].

The transition from BCS superconductivity to Bose–Einstein condensation (BEC) occurs in a Fermi system, either if the density is decreased or an attractive interaction between fermions is increased sufficiently. This transition was studied, first, in excitonic semiconductors [5] and then in an attractive Fermi gas [6]. Later it was realized that an analogous phase transition takes place in symmetric nuclear matter, when np Cooper pairs at higher densities go over to a Bose–Einstein condensate of deuterons at lower densities [7, 8]. During this transition, the chemical potential changes its sign at a certain critical density (Mott transition), approaching half of the deuteron binding energy at ultralow densities. In [7], crossover from np superfluidity to BEC of deuterons was studied in the T-matrix approach, where the pole in the T matrix determines the critical temperature of BEC of bound states in the case of negative chemical potential and the critical temperature of appearance of np Cooper pairs in the case of positive chemical potential.

Here, for studying the corresponding phase transition in superfluid nuclear matter, we shall use the formalism of Green's functions at finite temperatures. This will allow us to give an analysis beyond linear on the energy gap approximation. As a potential of NN interaction, we choose an effective zero range interaction, developed in [9] to reproduce the energy gap in symmetric nuclear matter for the Paris potential in the $S = 1$, $T = 0$ pairing channel. In addition, we shall discuss the influence of finite temperature and isospin asymmetry effects on peculiarities of the transition from np superfluidity to BEC of deuterons in nuclear matter.

Note that we do not consider here $T = 1$ np pairing correlations. The reason is that the coupling constant for np pairing correlations in the isospin singlet pairing channel is larger than that in the isospin triplet pairing channel and $T = 0$ np pairing is more

*This article was submitted by the authors in English.

[1)]Kharkov Institute of Physics and Technology, Kharkov, Ukraine.
[2)]Department of Physics and Center for Space Science and Technology, Ewha Womans University, Seoul, Korea.
[3)]Center for High Energy Physics, Kyungpook National University, Daegu, Korea.
[4)]Laboratory of Information Technologies, Joint Institute for Nuclear Research, Dubna, Moscow oblast, 141980 Russia.
**e-mail: isayev@mail-x-change.com
***e-mail: jyang@ewha.ac.kr

preferable for all relevant densities [10, 11]. Moreover, we do not consider $T = 1$ *nn* and *pp* pairing correlations, which will play a major role at sufficiently large asymmetry for not overly low densities. However, at ultralow densities, as we will see, the suppression mechanism for $T = 0$ *np* pair correlations will be ineffective and one can expect that this type of pairing will dominate over other channels for a wide range of isospin asymmetry parameter values.

2. SELF-CONSISTENT EQUATIONS

Superfluid states of nuclear matter can be described in terms of normal and anomalous Green's functions [12]

$$iG_{\kappa\kappa'}(\mathbf{k}, t - t') = \langle T[\psi_\kappa(\mathbf{k}, t)\psi^+_{\kappa'}(\mathbf{k}, t')]\rangle, \quad (1)$$

$$iF_{\kappa\kappa'}(\mathbf{k}, t - t') = \langle T[\psi_\kappa(\mathbf{k}, t)\psi_{\kappa'}(\mathbf{k}, t')]\rangle, \quad (2)$$

where T is the time ordering operator, $\kappa \equiv (\sigma, \tau)$, σ, τ being projections of spin and isospin on the third axis. Using the Fourier representation

$$G_{\kappa\kappa'}(\mathbf{k}, t) = \frac{1}{\beta}\sum_l e^{-i\omega_l t} G_{\kappa\kappa'}(\mathbf{k}, \omega_l), \quad (3)$$

$$F_{\kappa\kappa'}(\mathbf{k}, t) = \frac{1}{\beta}\sum_l e^{-i\omega_l t} F_{\kappa\kappa'}(\mathbf{k}, \omega_l), \quad (4)$$

where $\omega_l = (2l + 1)\pi T$; $l = 0, 1, 2, \ldots$; and $\beta = 1/T$ is the inverse temperature, the Gorkov equations can be written in the form

$$\begin{pmatrix} D(\mathbf{k}, \omega_l) & \Delta(\mathbf{k}) \\ \Delta^+(\mathbf{k}) & -D(\mathbf{k}, -\omega_l) \end{pmatrix} \begin{pmatrix} G(\mathbf{k}, \omega_l) \\ F^+(\mathbf{k}, \omega_l) \end{pmatrix} = \begin{pmatrix} \mathbf{1} \\ \mathbf{0} \end{pmatrix}, \quad (5)$$

where

$$D(\mathbf{k}, \omega_l) = \begin{pmatrix} i\omega_l - \varepsilon_{p\uparrow}(\mathbf{k}) & 0 & 0 & 0 \\ 0 & i\omega_l - \varepsilon_{p\downarrow}(\mathbf{k}) & 0 & 0 \\ 0 & 0 & i\omega_l - \varepsilon_{n\uparrow}(\mathbf{k}) & 0 \\ 0 & 0 & 0 & i\omega_l - \varepsilon_{n\downarrow}(\mathbf{k}) \end{pmatrix}$$

and functions Δ, G, F are matrices on spin and isospin variables. The single-particle energies can be written as

$$\varepsilon_{p\sigma}(\mathbf{k}) = \varepsilon_k + U_p(\mathbf{k}) - \mu_{03},$$
$$\varepsilon_{n\sigma}(\mathbf{k}) = \varepsilon_k + U_n(\mathbf{k}) + \mu_{03},$$
$$\varepsilon_k = \frac{k^2}{2m} - \mu_{00},$$

$\mu_{00} = (\mu_p + \mu_n)/2$ and $\mu_{03} = (\mu_p - \mu_n)/2$ being half of the sum and half of the difference of proton and neutron chemical potentials [3], and $U_{p,n}$ are the single-particle potentials, which in a consistent microscopic approach should be derived from the Brueckner theory. However, for simplicity, we shall consider that the effects of potentials $U_{p,n}$ result in the renormalization of a nucleon mass and chemical potentials and further simply drop the corresponding terms. The order parameter in the $S = 1, T = 0$ pairing channel has the structure

$$\Delta = \begin{pmatrix} 0 & 0 & 0 & i\Delta \\ 0 & 0 & i\Delta & 0 \\ 0 & -i\Delta & 0 & 0 \\ -i\Delta & 0 & 0 & 0 \end{pmatrix}.$$

The structure of the anomalous propagator is analogous to that of Δ, while the normal propagator G is the diagonal matrix in spin and isospin spaces. Taking this into account, solutions of Eq. (5) can be written as

$$G_p(\mathbf{k}, \omega_l) = \frac{i\omega_l + \varepsilon_n(\mathbf{k})}{(i\omega_l - E^-_k)(i\omega_l + E^+_k)}, \quad (6)$$

$$G_n(\mathbf{k}, \omega_l) = \frac{i\omega_l + \varepsilon_p(\mathbf{k})}{(i\omega_l - E^+_k)(i\omega_l + E^-_k)},$$

$$F^+_{pn}(\mathbf{k}, \omega_l) = \frac{\Delta(\mathbf{k})}{(i\omega_l - E^+_k)(i\omega_l + E^-_k)},$$

$$F^{+}_{np}(\mathbf{k},\omega_l) = -\frac{\Delta(\mathbf{k})}{(i\omega_l - E^{-}_k)(i\omega_l + E^{+}_k)},$$

where

$$E^{\pm}_k = E_k \pm \mu_{03} = \sqrt{\varepsilon^2_k + \Delta^2(\mathbf{k})} \pm \mu_{03}.$$

After analytical continuation of the normal and anomalous propagators in the complex z plane ($z_l = i\omega_l$), one can obtain equations determining the particle number densities of protons and neutrons,

$$\varrho_\tau = -\frac{2}{V}\sum_{\mathbf{k}}\int\frac{dz}{2\pi}\mathrm{Im}G_\tau(\mathbf{k},z)f(z) \qquad (7)$$
$$= \frac{1}{V}\sum_{\mathbf{k}}\left[\left(1+\frac{\varepsilon_k}{E_k}\right)f(E^{\mp}_k) + \left(1-\frac{\varepsilon_k}{E_k}\right)[1-f(E^{\pm}_k)]\right] \quad (\tau = p,n),$$

and the energy gap,

$$\Delta(\mathbf{k}) = -\frac{2}{V}\sum_{\mathbf{k}'}V(\mathbf{k},\mathbf{k}')\int\frac{dz}{2\pi}\mathrm{Im}F^{+}_{pn}(\mathbf{k},z)f(z) \qquad (8)$$
$$= -\frac{1}{V}\sum_{\mathbf{k}'}V(\mathbf{k},\mathbf{k}')\frac{\Delta(\mathbf{k}')}{2E_{k'}}(1-f(E^{+}_{k'})-f(E^{-}_{k'})),$$

where $f(E) = \{1+\exp(\beta E)\}^{-1}$. It is convenient to rewrite Eq. (7) for the total density $\varrho = \varrho_p + \varrho_n$ and neutron excess $\delta\varrho = \varrho_n - \varrho_p \equiv \alpha\varrho$ ($\alpha = (\varrho_n - \varrho_p)/\varrho$ being the asymmetry parameter):

$$\varrho = \frac{2}{V}\sum_{\mathbf{k}}\Big(1-\frac{\varepsilon_k}{E_k}[1-f(E^{+}_k)-f(E^{-}_k)]\Big) \qquad (9)$$
$$\equiv \frac{2}{V}\sum_{\mathbf{k}} n_k,$$

$$\alpha\varrho = \frac{2}{V}\sum_{\mathbf{k}}\Big(f(E^{+}_k)-f(E^{-}_k)\Big). \qquad (10)$$

Then, introducing the anomalous density

$$\psi(\mathbf{k}) = \langle a^{+}_{p,k}a^{+}_{n,-k}\rangle = \frac{\Delta(\mathbf{k})}{2E_k}\Big(1-f(E^{+}_k)-f(E^{-}_k)\Big)$$

and using Eq. (9), one can represent Eq. (8) for the energy gap in the form

$$\frac{k^2}{m}\psi(\mathbf{k}) + (1-n_k)\sum_{\mathbf{k}'}V(\mathbf{k},\mathbf{k}')\psi(\mathbf{k}') = 2\mu_{00}\psi(\mathbf{k}). \qquad (11)$$

In the limit of vanishing density, $n_k \to 0$, Eq. (11) goes over into the Schrödinger equation for the deuteron bound state [8, 13]. The corresponding energy eigenvalue is equal to $2\mu_{00}$.

3. PHASE TRANSITIONS IN NUCLEAR MATTER WITH *np* PAIRING CORRELATIONS

Further, for numerical calculations, we shall use the effective zero range force, developed in [9] to reproduce the pairing gap in $S = 1, T = 0$ pairing channel with Paris *NN* potential:

$$V(\mathbf{r}_1,\mathbf{r}_2) = v_0\left\{1-\eta\left(\frac{\varrho((\mathbf{r}_1+\mathbf{r}_2)/2)}{\varrho_0}\right)^{\gamma}\right\}\delta(\mathbf{r}_1-\mathbf{r}_2), \qquad (12)$$

where ϱ_0 is the nuclear saturation density ($\varrho_0 = 0.16\ \mathrm{fm}^{-3}$), and v_0, η, β are some adjustable parameters. In addition, in the gap equation (8), Eq. (12) must be supplemented with a cutoff parameter ε_c. In [9], the following sets of parameters were used to fit the density dependence of the energy gap, calculated with Paris NN potential: (i) $\eta = -0.1$, $\gamma = 0.2$, $v_0 = -480\ \mathrm{MeV\ fm}^3$, $m = m_\mathrm{G}$; (ii) $\eta = 0.4$, $\gamma = 0.9$, $v_0 = -480\ \mathrm{MeV\ fm}^3$, $m = m_0$; (iii) $\eta = 0$, $v_0 = -530\ \mathrm{MeV\ fm}^3$, $m = m_\mathrm{G}$, where m_G is the effective mass, corresponding to the Gogny force D1S [14], and m_0 is the bare mass of a nucleon. For all parametrizations, $\varepsilon_c = 60$ MeV was used. The first two sets of parameters correspond to formation of a bound state at zero energy, and the third set is chosen to produce the bound state between two extreme values: at zero energy and at the deuteron binding energy. Because we are mainly interested in studying the formation of bound states in the low-density region of nuclear matter, we will choose the third set of parameters. Note also that it is important that the gap equation (8) should be solved self-consistently with Eqs. (9), (10) for the chemical potentials μ_{00}, μ_{03}.

First, we consider the case of symmetric nuclear matter ($\alpha = 0$). In Fig. 1*a*, the density dependence of the energy gap at zero temperature is displayed. The maximum value of the energy gap is equal to 7.6 MeV at density $\varrho \approx 0.1\ \mathrm{fm}^{-3}$. The energy gap vanishes at density larger than the saturation density.

Figure 1*b* shows the zero temperature behavior of the chemical potential μ_{00}. It is seen that the chemical potential at some density ϱ_b ($\varrho_b \approx 3\times10^{-4}\ \mathrm{fm}^{-3}$) changes its sign, which, according to Eq. (11), corresponds to the appearance of deuteron-like bound states in nuclear matter. When density tends to zero, the chemical potential approaches its asymptotic value $\mu_{00} = -\varepsilon_b/2$, ε_b being the binding energy of a bound state. Therefore, we can conclude that, under lowering density, np superfluidity smoothly evolves into the BEC of np bound states (deuterons).

In Fig. 2, we present the results of numerical determination of the temperature dependence of the chemical potential μ_{00} for fixed values of density. If

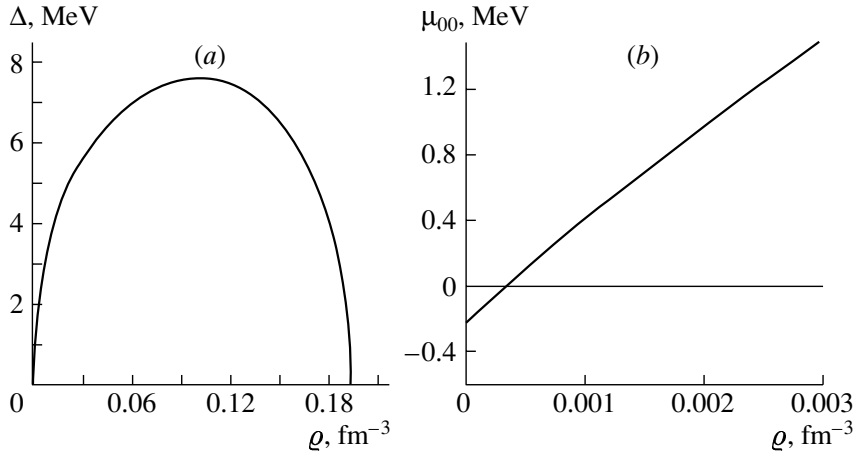

Fig. 1. Density dependence at zero temperature of (*a*) the energy gap and (*b*) the chemical potential (low-density region).

the density is low enough, then under a decrease in temperature the chemical potential becomes negative (curve *2*), which corresponds to formation of bound states. At very low densities, *np* condensate exists only in the form of a Bose–Einstein condensate of deuteron-like bound states (curve *3*). If densities are, however, high enough, *np* Cooper pairs survive even at zero temperature (curve *1*).

Now we consider asymmetric nuclear matter. It is known, that *np* pairing correlations are the strongest in the isospin symmetric case, when protons and neutrons lie on the Fermi surfaces of the same radius. If densities of protons and neutrons differ, then neutrons and protons lie on Fermi surfaces of different radii and *np* pairing correlations become weaker. At some critical asymmetry, *np* pairing correlations are destroyed. In fact, even a small asymmetry strongly suppresses *np* pairing correlations [3, 7]. However, this picture may be wrong in the low-density limit, when the chemical potential becomes negative and the Fermi surface drops into the unphysical region. As we shall see, at low densities, *np* condensate can exist in the form of a Bose condensate of deuterons even for a large excess of neutrons.

For nonzero asymmetry, we should solve Eqs. (8)–(10) simultaneously. The results of numerical calculations for the energy gap as a function of density for different asymmetries at zero temperature are shown in Fig. 3. As one can see, with increasing asymmetry, the value of the energy gap decreases and the density interval where *np* pairs exist shrinks in the direction of zero density. In reality, solutions exist for any $\alpha < 1$ (the phase curves for larger values of α are not shown in Fig. 3) and the corresponding density interval contracts more and more to the point $\varrho = 0$ when asymmetry increases. To understand why the isospin asymmetry loses its efficiency in destroying

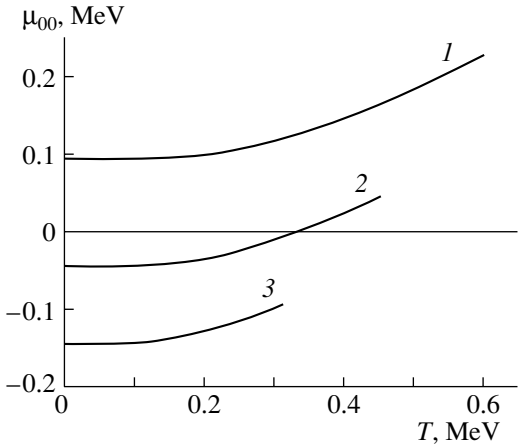

Fig. 2. Chemical potential as a function of temperature at fixed values of density: $\varrho = 0.00045$ fm^{-3} (curve *1*), 0.00024 fm^{-3} (curve *2*), and 0.0001 fm^{-3} (curve *3*).

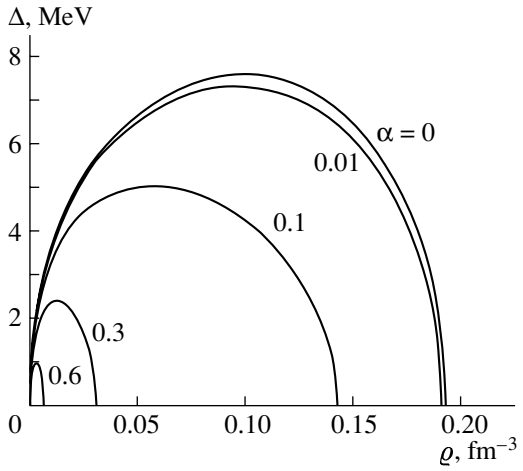

Fig. 3. Energy gap as a function of density at zero temperature and different asymmetries.

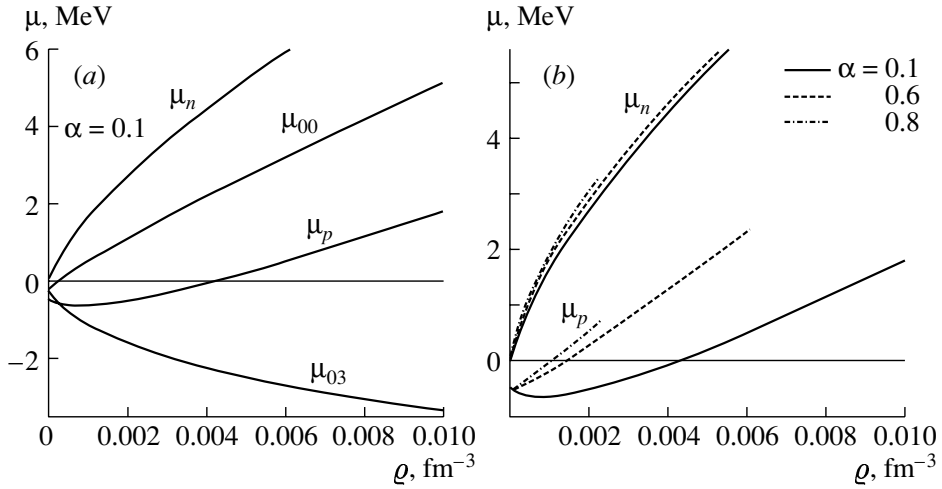

Fig. 4. Various chemical potentials as functions of density at zero temperature and different asymmetries: (*a*) $\mu_{00}, \mu_{03}, \mu_p, \mu_n$; (*b*) μ_p (lower curves), μ_n (upper curves).

np pairing correlations in the low-density region, let us note that, at zero temperature, the contribution to the integral in the gap equation gives the interval $[0, \varepsilon_c]$, excluding the domain $[\mu_{00} - \Delta\varepsilon, \mu_{00} + \Delta\varepsilon]$, where $\Delta\varepsilon = \sqrt{\mu_{03}^2 - \Delta^2}$. In the weak-coupling regime ($\mu_{00} \gg \Delta$) with increasing asymmetry, the width of this domain also increases, which results in considerable reduction of the energy gap magnitude, until it completely vanishes. However, when the chemical potential passes through zero ($\mu_{00} \approx 0$, Mott transition regime) and becomes negative ($\mu_{00} < 0$, strong-coupling regime), only part of the window participates in suppressing the energy gap, with the right end of the blocking interval going to zero at $\varrho \to 0$.

Figure 4*a* shows the zero temperature behavior of chemical potentials μ_{00}, μ_{03}, μ_p, μ_n as functions of density at very low densities of nuclear matter and finite isospin asymmetry. One can see that, at some critical density, the chemical potential μ_{00} changes its sign and np Cooper pairs smoothly go over into deuteron bound states. The asymptotic behavior of chemical potentials at $\varrho \to 0$ is $\mu_{00}, \mu_{03} \to -\varepsilon_b/2$, and, hence, $\mu_p \to -\varepsilon_b$, $\mu_n \to 0$. The latter behavior can be understood from the following considerations. At very low densities, nuclear matter consists of deuterons and unbound excess neutrons. The Bose-condensed deuterons occupy the energy state with $E \approx -\varepsilon_b$ and free neutrons occupy the positive energy states. According to the Pauli principle, the wave function of the system is antisymmetric with respect to interchange of unbound neutrons and neutrons bound in deuterons. Hence, with increasing asymmetry, excess neutrons populate the next positive energy states on the top of their Fermi sea. Therefore, the chemical potential of neutrons, which is the change in the system energy under addition of a neutron, is always the one of unbound neutrons and goes to zero at vanishing density. The chemical potential of protons will be equal to the binding energy of the system per half the number of particles bound in deuterons, i.e., $\mu_p \to -\varepsilon_b$ at $\varrho \to 0$. This asymptotic behavior does not depend on isospin asymmetry, which is confirmed by the results of numerical calculations, shown in Fig. 4*b*, where the density dependence of chemical potentials μ_p, μ_n is depicted for different values of the asymmetry parameter.

ACKNOWLEDGMENTS

A.I. is grateful for support of the Topical Program of APCTP during his stay in Seoul. He also acknowledges partial financial support of INTAS.

REFERENCES

1. S. Tsuruta, Phys. Rep. **292**, 1 (1998).
2. A. I. Akhiezer, A. A. Isayev, S. V. Peletminsky, and A. A. Yatsenko, in *Proceedings of the International Workshop on Hot Points in Astrophysics, Dubna, Russia, 2000*, p. 300.
3. A. I. Akhiezer, A. A. Isayev, S. V. Peletminsky, and A. A. Yatsenko, Phys. Rev. C **63**, 021304(R) (2001).
4. S. Reddy, M. Prakash, J. M. Lattimer, and J. A. Pons, Phys. Rev. C **59**, 2888 (1999).
5. L. V. Keldysh and Yu. V. Kopaev, Sov. Phys. Solid State **6**, 2219 (1965).
6. P. Nozieres and S. Schmitt-Rink, J. Low Temp. Phys. **59**, 195 (1985).
7. T. Alm, B. L. Friman, G. Röpke, and H.-J. Schulze, Nucl. Phys. A **551**, 45 (1993).
8. M. Baldo, U. Lombardo, and P. Schuck, Phys. Rev. C **52**, 975 (1995).

9. E. Garrido, P. Sarriguren, E. Moya de Guerra, *et al.*, Phys. Rev. C **63**, 037304 (2001).
10. A. I. Akhiezer, A. A. Isaev, S. V. Peletminsky, *et al.*, Zh. Éksp. Teor. Fiz. **112**, 3 (1997) [JETP **85**, 1 (1997)].
11. A. I. Akhiezer, A. A. Isayev, S. V. Peletminsky, and A. A. Yatsenko, Phys. Lett. B **451**, 430 (1999).
12. A. A. Abrikosov, L. P. Gorkov, and I. E. Dzyaloshinskii, *Methods of Quantum Field Theory in Statistical Physics* (Prentice-Hall, Englewood Cliffs, 1963).
13. U. Lombardo, P. Nozieres, P. Schuck, *et al.*, Phys. Rev. C **64**, 064314 (2001).
14. J. F. Berger, M. Girod, and D. Gogny, Comput. Phys. Commun. **63**, 365 (1991).

Physics of Atomic Nuclei, Vol. 67, No. 10, 2004, pp. 1846–1850. From Yadernaya Fizika, Vol. 67, No. 10, 2004, pp. 1872–1876.

Proceedings of the International Conference "Nuclear Structure and Related Topics"

New Data on Nuclear Subshells Obtained from the Analysis of the Information from the International Database on Nuclear Structure ENSDF*

I. N. Boboshin[1)], B. S. Ishkhanov[1),2)], and V. V. Varlamov[1)]**

Received January 21, 2004

Abstract—In the last decade, a large amount of experimental nuclear spectroscopy data was obtained. This is good progress really, but a new very serious problem appears. Due to significant systematic errors of the data, one is often forced to deal with very discrepant data and often it is difficult to obtain reliable information from them. To solve this problem and to remove the systematic errors, new technologies in working with the data were developed. Using these new technologies, one can obtain information with a high accuracy and reliability, and in many cases, new information has not been or could not be obtained experimentally. Below, an approach of this kind is presented concerning spectroscopic data on Ca and Zr isotopes. It is shown that the behavior of the energy of the first 2^+ level in Zr isotopes can be explained in the framework of a shell-model approach. A separation of the $2d_{5/2}$ subshell in ^{96}Zr (as is for the $1f_{7/2}$ subshell in ^{48}Ca) is found, so that the neutron number $N = 56$ becomes like a magic number for $Z = 40$. To explain a similarity in decaying properties of ^{48}Ca and ^{96}Zr, an additional interaction between closed structures consisting of 20 and 28 nucleons is proposed. Irregularities of the ground-state spin values in the K isotopic chain are explained in the framework of the shell-model approach by the inversion of the proton $1d_{3/2}$ and $2s_{1/2}$ orbitals. © *2004 MAIK "Nauka/Interperiodica".*

1. DATABASE ENSDF

Contemporary large and complete databanks give real possibilities to solve the problem mentioned in the abstract. The oldest, large, and complete data bank on nuclear spectroscopy is the ENSDF (Evaluated Nuclear Structure Data File) [1]. This file contains nuclear structure and decay data for all known nuclides. For each nucleus, there is an adopted data set containing the recommended values of characteristics of the levels and gamma rays observed and data sets containing the "best" values obtained from various types of experiments. It has to be pointed out that new physical information can appear even at the stage of forming an evaluated "data set." For example, if an experiment gives two possible spin values 1/2 or 3/2 for a given level and another experiment gives 3/2 or 5/2 for the same level, an evaluator assigns unambiguously to this level the spin value 3/2, etc.

An important feature of nucleon stripping and pickup experiments is that, as a rule, the total transferred momentum value j cannot be measured. The only exception is experiments with polarized particles. However, if spin and parity of the initial nucleus are equal to 0^+, the total transferred angular momentum is equal to that of a level feeding in the final nucleus. So it is very important to have accurate, reliable, and full data on spins of nuclides, and ENSDF provides this possibility.

2. THE METHOD OF PUTTING DATA ON NUCLEON PICKUP AND STRIPPING EXPERIMENTS IN ACCORDANCE TO EACH OTHER

The main idea of the method [2] is to correct the experimental data so that the constraints

$$S^+_{nlj} + S^-_{nlj} = 2j + 1 \qquad (1)$$

will be fulfilled for three single-particle orbitals closest to the Fermi energy, for which experimental data are presented with a maximum of completeness [3]. Moreover, the constraint

$$S^+_{nlj} + S^-_{nlj} \le 2j + 1 \qquad (2)$$

should hold for the remaining subshells, and

$$\left| \sum_{nlj} S^-_{nlj} - \sum_{nlj} S^+_{nlj} - A \right| \to 0 \qquad (3)$$

*This article was submitted by the authors in English.

[1)]Institute of Nuclear Physics, Moscow State University, Moscow, Russia.
[2)]Physics Faculty, Moscow State University, Moscow, Russia.
**e-mail: boboshin@depni.sinp.msu.ru

1063-7788/04/6710-1846$26.00

Table 1. Energies of the first 2^+ states in even–even Zr isotopes

Nucleus	^{90}Zr	^{92}Zr	^{94}Zr	^{96}Zr
Number of neutrons N	50	52	54	56
$E(2^+, 1)$ [keV]	2186.50	934.48	918.75	1750.47

Table 2. Energies of the first 2^+ states in even–even Ca isotopes

Nucleus	^{40}Ca	^{42}Ca	^{44}Ca	^{46}Ca	^{48}Ca
Number of neutrons N	20	22	24	26	28
$E(2^+,1)$ [keV]	3904.50	1524.61	1157.02	1346.00	3831.72

for all the subshells. Here, $S^{\mp}_{nlj}$ are sums of the individual spectroscopic factors $S^{\mp}_{nlj}(E_x)$ of levels with energies E_x; the upper signs "+" and "−" denote nucleon stripping and pickup, respectively; the sum in (3) is taken over valent and upper subshells in the first term and over the lower subshells in the second one; A is a total number of corresponding nucleons (protons or neutrons) in a nucleus. The essence of Eq. (3) is that a residual interaction does not change the total number of nucleons in a nucleus. To this aim, two degrees of freedom are used: (i) a new normalization condition for experimental data is introduced ($S^{+}_{nlj}(E_x) \to n^{+}S^{+}_{nlj}(E_x)$, $S^{-}_{nlj}(E_x) \to n^{-}S^{-}_{nlj}(E_x)$); (ii) the whole known information about spins of the final states is taken into account, and moreover, all possibilities should be investigated for states with unknown spins.

The codes ARES were developed on the basis of the described procedures.

As a result, intervals for factors n^+ and n^- as well as for j values are determined. More reliable values of spectroscopic factors allow one to avoid a discrepancy between various experimental data, both pickup data and stripping data. Nucleon occupation probabilities of single-particle orbitals

$$N_{nlj} = \frac{[S^{-}_{nlj} + (2j + 1 - S^{+}_{nlj})]}{2(2j + 1)} \qquad (4)$$

and single-particle energies

$$-E_{nlj} = (1 - N_{nlj})[B(A + 1) - e^{+}_{nlj}] + N_{nlj}[B(A) + e^{-}_{nlj}] \qquad (5)$$

are determined by using the improved spectroscopic factors. In Eq. (5), $B(A)$ and $B(A+1)$ are separation energies of a corresponding nucleon in a target nucleus and in a nucleus with one added nucleon; e^{+}_{nlj} are centroids of the spectroscopic factor distributions.

Such kinds of results were obtained for nuclides ^{40,42,44,46,48}Ca, ^{46,48,50}Ti, ^{50,52,54}Cr, ^{54,56,58}Fe, ^{58,60,62,64}Ni, ^{64,66,68,70}Zn, ^{90,92,94,96}Zr, and ^{116,118,120}Sn, both for neutron and proton orbitals.

3. IS ^{96}Zr A MAGIC NUCLEUS?

In Table 1, we show the energies of the first 2^+ states in ^{90,92,94,96}Zr isotopes. Their maximal values for $N = 50$ and $N = 56$ are seen very clearly. The maximum at $N = 50$ has an ordinary explanation, because $N = 50$ is a well-known magic number. However, the maximum at the neutron number $N = 56$ requires a special explanation.

Both neutron and proton subshells were a subject of investigation from the point of view of one-nucleon transfer reaction data with the method described above. Neutron single-particle energies are displayed in Fig. 1. With increasing in N, one can see a lowering of the $2d_{5/2}$ subshell from the upper shell $N = 50$–82, so that, in ^{96}Zr, the subshell becomes well separated from it. Since in ^{96}Zr the neutron subshell $2d_{5/2}$ is closed, $N = 56$ becomes somewhat like a magic number. It is necessary to note that a similar

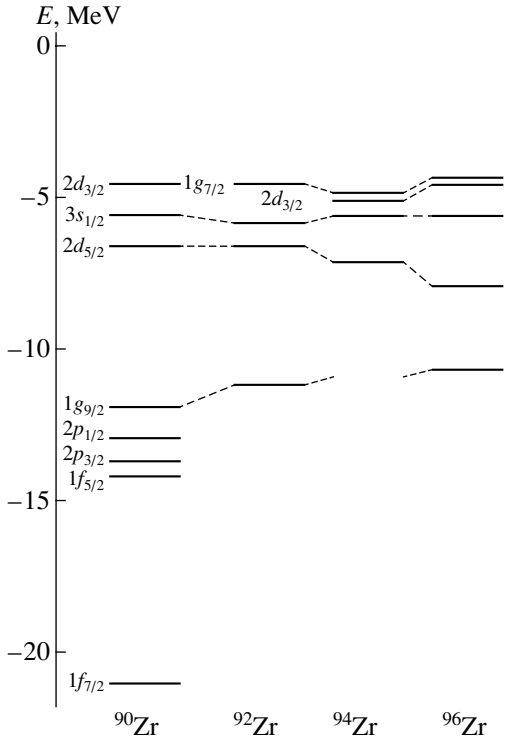

Fig. 1. Neutron subshells in ^{90,92,94,96}Zr isotopes.

Table 3. Nucleon occupation probabilities N_{nlj} and single-particle energies $-E_{nlj}$ (in MeV) of proton orbits in nuclei ^{90,92,94,96}Zr

nlj		^{90}Zr	^{92}Zr	^{94}Zr	^{96}Zr
$1g_{9/2}$	N_{nlj}	0.06(5)	0.08(5)	0.09(5)	0.00(0)
	$-E_{nlj}$	5.41(54)	4.98(142)	6.74(80)	7.48(75)
$2p_{1/2}$	N_{nlj}	0.58(5)	0.49(3)	0.75(5)	0.81(5)
	$-E_{nlj}$	6.97(70)	7.66(77)	9.37(94)	10.59(106)
$1f_{5/2}$	N_{nlj}	1.00(2)	1.00(2)	1.00(2)	0.94(5)
	$-E_{nlj}$	10.37(110)	10.93(110)	11.49(115)	12.17(122)
$2p_{3/2}$	N_{nlj}	–	–	0.87(5)	–
	$-E_{nlj}$	–	–	11.11(112)	–

picture of a separation of the subshell $1f_{7/2}$ in Ca isotopes was found earlier [4]. The neutron number $N = 28$ was suggested for consideration as a magic one (Fig. 2). Correspondingly, the two maxima of the energies of the first 2^+ states at the neutron numbers $N = 20$ and $N = 28$ are observed in Ca isotopes as well (see Table 2).

In Table 3, we present results of our investigations of proton subshells in Zr isotopes. Here, the essential peculiarity is seen in occupation probabilities of the proton $1g_{9/2}$ orbital. Whereas the occupation probabilities in ^{90,92,94}Zr are close to 0.1 (thus corresponding to one proton in the $1g_{9/2}$ orbital), this probability appears to be exactly zero in ^{96}Zr. This follows from distributions of single-proton spectroscopic factors over final states in Y isotopes. While in ^{89,91,93}Y one can observe one-proton transfers with $l = 4$, $j = 9/2$ and spectroscopic factors $S^-(E_x) = 0.9$–1.3 to levels in the excitation energy range 0.5–0.9 MeV, similar transfers to the states of ^{95}Y are not observed at all. It means that a rearrangement of nuclear structure takes place in ^{96}Zr so that this nucleus becomes stiffer and, probably, its shape becomes closer to a spherical one. This feature is typical for a magic nucleus; thus, we conclude that $N = 56$ is a magic number in the nucleus with $Z = 40$.

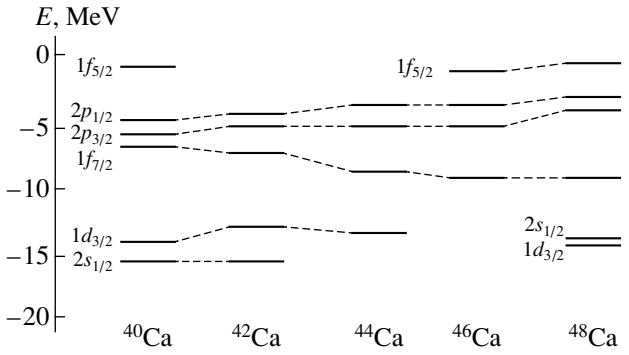

Fig. 2. Neutron subshells in ^{40,42,44,46,48}Ca isotopes.

It is worthwhile to stress that the number $N = 56$ is not a magic one combining with other Z values, i.e., in Mo, Ru isotopes, etc. This fact forces us to pay attention to a relation between numbers 40 and 56. Let us note that 56 is equal to 2×28, and 40 is equal to 2×20, and then we follow along the way of an analogy between ^{96}Zr and ^{48}Ca. Indeed, the analogy goes quite far if we consider data on decays of these two nuclei. For example, both nuclei, ^{48}Ca and ^{96}Zr, decay via the $2\beta^-$ mode—quite rare decay—which exhausts less than 1% of all types of decay, and $T_{1/2}(^{48}\mathrm{Ca}) = (4.2^{+3.3}_{-1.3}) \times 10^{19}$ yr [5] and $T_{1/2}(^{96}\mathrm{Zr}) = (2.1^{+0.8(\mathrm{stat.})}_{-0.4(\mathrm{stat.})} \pm 0.2(\mathrm{syst.})) \times 10^{19}$ yr [6]. This is really a fantastic coincidence: one nucleus is twice as large as the other one, and both of them decay via the same rare mode. Moreover, the half-life of the heavier nucleus is exactly equal to one-half of the lighter.

All these facts can be explained if one supposes the existence of an additional interaction between closed structures $Z = 20$ and $N = 28$ in the nuclei ^{48}Ca and ^{96}Zr. The nucleus ^{48}Ca is known as a neutron-rich nucleus, although it is quite stable. Interaction between the proton $Z = 20$ and the neutron $N = 28$ closed structures can be responsible for this specific stability.

At least two heuristic schemes of a coupling between proton and neutron subsystems can be proposed in the framework of the above assumption: a compound cluster model and a "nuclear crystal" model. The first model (see Fig. 3) supposes two levels of interactions of cluster-like structures. The interaction $\mathcal{A}$ couples $Z = 20$ and $N = 28$ structures to ^{48}Ca, and its destruction leads to $2\beta^-$ decay with

Table 4. Nucleon occupation probabilities N_{nlj} (upper numbers) and single-particle energies $-E_{nlj}$ (in MeV) (lower numbers) of proton subshells in nuclei ^{40,42,44,46,48}Ca

nlj	^{40}Ca	^{42}Ca	^{44}Ca	^{46}Ca	^{48}Ca
$1f_{5/2}$	–	–	–	–	0.00
	–	–	–	–	3.81 (12)
$2p_{1/2}$	0.00	–	–	–	0.01 (1)
	−2.38 (24)	–	–	–	2.35 (68)
$2p_{3/2}$	0.09 (0.02)	0.02 (1)	0.05 (2)	–	0.01 (1)
	0.73 (29)	1.30 (18)	4.99 (51)	–	3.95 (53)
$1f_{7/2}$	0.06 (2)	0.08 (3)	0.13 (3)	0.02 (2)	0.02 (2)
	1.67 (22)	4.09 (45)	7.68 (78)	7.89 (99)	8.62 (100)
$1d_{3/2}$	0.97 (3)	0.76 (7)	0.72 (7)	0.94 (4)	0.94 (5)
	9.52 (152)	10.03 (150)	10.81 (108)	13.53 (138)	15.96 (100)
$2s_{1/2}$	1.00	0.90 (5)	0.77 (7)	0.93 (4)	0.84 (9)
	10.94 (109)	>11.29	11.39 (114)	13.94 (139)	14.41 (158)
$1d_{5/2}$	0.96 (2)	–	–	–	–
	14.32 (143)	–	–	–	–

the half-life 4.2×10^{19} yr. The interaction $\mathcal{B}$ couples "clusters" ^{48}Ca to the ^{96}Zr nucleus. The interaction $\mathcal{B}$ is supposed to be stronger than the interaction $\mathcal{A}$, and destroying one of the two $\mathcal{A}$ interactions leads to destruction of the whole system and to $2\beta^-$ decay with the total half-life 2.1×10^{19} yr. The second model supposes a two-valent coupling between $Z = 20$ and $N = 28$ structures in ^{48}Ca (Fig. 4*a*). The ^{96}Zr nucleus is constructed from these two-valent structures like a molecule (Fig. 4*b*). Thus, in both cases, ^{48}Ca and ^{96}Zr, one gets systems with additional stiffness that could be characterized as "nuclear crystal."

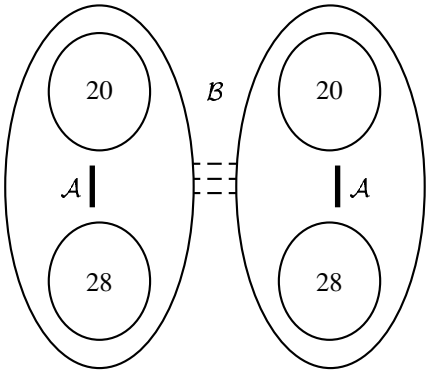

Fig. 3. A compound cluster model of ^{96}Zr.

4. PROTON SUBSHELLS IN Ca ISOTOPES

In Table 4, one-nucleon occupation probabilities as well as single-particle energies of proton orbitals in nuclides ^{40,42,44,46,48}Ca are displayed. One can observe the inversion of the $1d_{3/2}$ and $2s_{1/2}$ subshells in the ^{48}Ca isotope. This peculiarity explains irregularities in spin-parity values of the ground states of K isotopes: in nuclei ^{39,41,43,45}K, the ground states have $J^\pi = 3/2^+$, whereas in ^{47}K the ground state has $J^\pi = 1/2^+$. To describe the placement of proton subshells in ^{48}Ca and, in particular, the inversion of

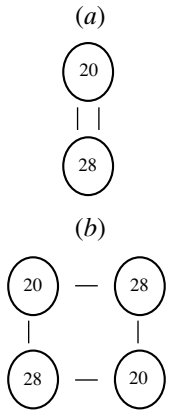

Fig. 4. A two-valent coupling model: (*a*) ^{48}Ca and (*b*) ^{96}Zr.

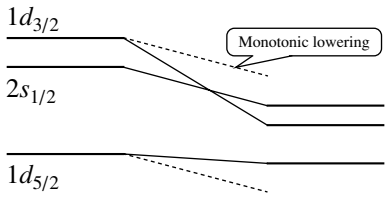

Fig. 5. For the explanation of the inversion of proton $1d_{3/2}$ and $2s_{1/2}$ orbitals in ^{48}Ca.

$1d_{3/2}$–$2s_{1/2}$ subshells, it was assumed that proton spin–orbit splitting decreases in this nucleus (see Fig. 5). This hypothesis was tested by calculations within a dispersion optical model for ^{40,42,44,46,48}Ca [7] and it was shown that this assumption allows one to describe the inversion adequately.

5. CONCLUSIONS

On the basis of the nuclear spectroscopy data bank ENSDF, new interesting information about the single-particle structure of Zr and Ca isotopes is obtained.

The most important conclusions are the following:

(i) The behavior of the energies of the first 2^+ levels in Zr isotopes is explained in the framework of a shell-model approach. A strong separation of the neutron $2d_{5/2}$ subshell in ^{96}Zr (as is with the $1f_{7/2}$ subshell in ^{48}Ca) is found, so that the neutron number $N = 56$ can be considered as a magic one in the nucleus with $Z = 40$. To explain some correlations in decay properties of ^{48}Ca and ^{96}Zr, an additional interaction between closed structures of 20 and 28 nucleons is proposed.

(ii) Irregularities of the ground-state spins along the K isotopic chain are explained in the framework of a shell-model approach by the inversion of the $1d_{3/2}$ and $2s_{1/2}$ proton orbitals.

ACKNOWLEDGMENTS

We acknowledge fruitful discussions with and help from Prof. E.A. Romanovsky and Dr. O.V. Bespalova.

Our research was carried out at the MSU SINP Department of Electromagnetic Processes and Atomic Nuclei Interaction and supported in part by the President of Russia grant no. SS-1619.2003.2 and the Russian Foundation for Basic Research, project no. 03-07-90431.

REFERENCES

1. T. W. Burrows, Nucl. Instrum. Methods Phys. Res. A **286**, 5953 (1990).
2. I. N. Boboshin, V. V. Varlamov, B. S. Ishkhanov, and I. M. Kapitonov, Nucl. Phys. A **496**, 93 (1989).
3. C. F. Clement, Nucl. Phys. A **213**, 469 (1973).
4. O. V. Bespalova, I. N. Boboshin, V. V. Varlamov, *et al.*, Izv. Ross. Akad. Nauk, Ser. Fiz. (in press).
5. V. B. Brudanin, N. I. Rukhadze, Ch. Briançon, *et al.*, Phys. Lett. B **495**, 63 (2000).
6. R. Arnold, C. Augier, J. Baker, *et al.*, Nucl. Phys. A **658**, 299 (1999).
7. O. V. Bespalova, I. N. Boboshin, V. V. Varlamov, *et al.*, Yad. Fiz. **66**, 673 (2003) [Phys. At. Nucl. **66**, 644 (2003)].

Physics of Atomic Nuclei, Vol. 67, No. 10, 2004, pp. 1851–1859. From Yadernaya Fizika, Vol. 67, No. 10, 2004, pp. 1877–1884.

Proceedings of the International Conference "Nuclear Structure and Related Topics"

Breakup Reactions of Halo Nuclei*

S. N. Ershov**

Bogolyubov Laboratory of Theoretical Physics, Joint Institute of Nuclear Research, Dubna, Moscow oblast, 141980 Russia

Received January 21, 2004

Abstract—Different reaction mechanisms of breakup reactions are discussed and the microscopic reaction model for two-neutron halo dissociation is presented. Some examples of halo breakup in reactions with electrons, nucleons, and nuclei are given. © *2004 MAIK "Nauka/Interperiodica".*

1. INTRODUCTION

In recent years, significant progress was achieved in investigations of radioactive ion beam physics. Many new and exciting issues were explored: exact locations of the neutron and proton drip lines, productions of the heaviest bound nuclei, evolution of shell structure (vanishing of magic numbers, new magic numbers), resonances beyond drip lines—just to name few of them. In particular, the discovery of a neutron halo has been made [1]. A halo is a new type of structure which appears in weakly bound nuclei at the limits of stability. It can be characterized by clustering into an ordinary core nucleus and a veil of halo neutrons forming dilute neutron matter. One-neutron halo nuclei (^{11}Be, ^{14}B, ^{19}C, ...) break into two fragments and their locations on the nuclear map are shifted by a few neutrons to the stability region away from the limit of nuclear existence. Two-neutron halo nuclei (^{6}He, ^{11}Li, ^{14}Be, ^{17}B, ...) break into three fragments and appear at the very end of nuclear stability. Thus, a one-neutron halo gradually transforms to a two-neutron halo in the process of nuclear structure evolution on the way to the edges of the nuclear landscape. Also, all two-neutron halo nuclei have the "Borromean" properties [2]. This means that any pair of fragments (two neutrons, neutron and core) cannot create a bound system while the bound state of three fragments exists. Therefore, three-body correlations are the most important for a two-neutron halo since their existence itself as a bound system is due to such correlations. In general, the two-neutron halo structure is a typical drip-line phenomenon in light nuclei.

Breakup reactions with fast beams of exotic nuclei are a powerful tool for investigations of halo nuclei (see the recent review [3] and references therein). In particular, measurements of fragments in coincidence are providing basic information about the structure of a number of neutron-rich nuclei. We present a reaction model which allows calculations of a variety of observables in fragmentation processes leading to the low-energy excitations of two-neutron halo nuclei. Some calculations of halo breakup in collisions with different probes are given. We start with electron scattering, where the reaction mechanism is the simplest and most transparent, and continue the discussion of more complicated reaction mechanisms going from fragmentation on nucleons to nuclei.

2. BASIC STRUCTURE OF HALO NUCLEI

Halo nuclei, in most cases, have only one bound state (the ground state), in which the valence nucleons are in low relative angular-momentum states with respect to the rest of the nucleons that make the more bound core. Due to the very weak binding of the last neutrons, the wave function describing their relative motion has a spatial distribution that extends far beyond the range of binding potential. In addition to the specific structure of the bound state, halo nuclei have peculiarities in the low-energy continuum: concentration of a transition strength near the breakup threshold. This follows from experimental cross sections on electromagnetic dissociation, which are larger by two orders of magnitude for halo nuclei [4]. Since we understand the reaction mechanism of electromagnetic dissociation, at least qualitatively, the only possibility to describe such a huge enhancement is an accumulation of transition strength near the breakup threshold. It is interesting to compare the magnitude of this effect with other indications of halo structure. The interaction cross sections of halo nuclei are larger by tens of percent [5]. The width of fragment momentum distributions is a few times

*This article was submitted by the author in English.

**e-mail: ershov@thsun1.jinr.ru

narrower than for stable nuclei [6]. However, for electromagnetic dissociation, the difference with stable nuclei increases up to two orders of magnitude. It means that nuclear processes and observables, where a transition from the ground state to the low-energy continuum plays a dominant role, are the most sensitive to the presence of halo structure.

The basic dynamics of halo nuclei can be characterized as a coexistence of two subsystems: one which consists of core nucleons and other of halo neutrons moving around the core center of mass. Some arguments support such decoupling of core and halo degrees of freedom. The fact that a weakly bound system breaks into fragments is evidence that the fragment components must dominate in the ground-state wave function. The interaction cross section of high-energy halo nuclei on light targets, which is approximately equal to the sum of the interaction cross section of the core nucleus and two-neutron removal cross section [5], indicates that the reaction process goes separately on the core and halo subsystems. The large changes in the total cross sections are accompanied by essentially constant charge-changing cross sections [7]. The core and halo nucleus both have similar magnetic dipole and quadrupole moments. These arguments support the assumption that the core is not significantly perturbed by the valence neutrons located far away from it. It means that with good accuracy the wave function $|\psi\rangle$ of the halo nucleus can be written as a product of two functions:

$$|\psi\rangle = |\varphi_{\rm core}\rangle|\psi_{\rm halo}\rangle.$$

One, $|\varphi_{\rm core}\rangle$, describes the internal structure of the core and the other, $|\psi_{\rm halo}\rangle$, describes the relative motion of halo neutrons around the core center of mass. Such factorization is a starting point for application of three-body models to description of the halo structure [2, 8–10]. Few-body models avoid the complicated and still open questions on development of nuclear clustering and concentrate attention on the halo wave function $|\psi_{\rm halo}\rangle$. Within such models, it is possible to give a consistent description of the main properties of both the ground-state and the low-energy continuum wave functions. Few-body models of halo structure will be used in our analysis of breakup reactions below. The bound and continuum three-body wave functions are calculated by the method of hyperspherical harmonics and a detailed description of the applied formalism can be found in [9].

3. BREAKUP REACTIONS OF HALO NUCLEI

3.1. Breakup Reaction Mechanism

Fragmentation reactions have complicated dynamics, where the nuclear structure and reaction mechanism are tightly intertwined. The focus of current discussion is on investigations of the halo structure in breakup reactions. Hence, the processes that are the most sensitive to halo are singled out from a variety of breakup phenomena. It means that our discussion is confined to dissociation reactions with undestroyed core and low-energy halo excitations. Thus, only peripheral reactions are considered since in the central collisions a core can be destroyed with a big probability. Two breakup scenarios are possible under such conditions. The first is the elastic fragmentation if a target is left in the ground state after collision with a halo nucleus. The second is inelastic breakup if a target is excited. The cross section of the breakup reaction $a + A \to 1 + 2 + C + A^*$, involving collision of projectile a (two-neutron halo nucleus that breaks up into three fragments 1, 2, and C) with target A, is given by

$$\sigma = \frac{(2\pi)^4}{\hbar v_i}\sum_\alpha \int d\mathbf{k}_1 d\mathbf{k}_2 d\mathbf{k}_C d\mathbf{k}_{A^*} \times \delta(E_i - E_f)\delta(\mathbf{P}_i - \mathbf{P}_f)\,|T_{fi}|^2, \quad (1)$$

where v_i is the relative velocity of colliding systems in the initial channel, $\mathbf{k}_{1,2,C}$ are the wave numbers of neutrons and core, $\mathbf{k}_{A^*}$ is the target wave number in the final channel. The sum on α is done on all quantum numbers that are necessary to characterize the reaction and includes, if particles have spin, the averaging on initial spin projections and sum on final spin projections. The δ functions ensure the conservation of energy and momentum. The exact transition matrix T_{fi} in the prior form can be written as

$$T_{fi} = \left\langle \Psi_\alpha^{(-)}(\mathbf{k}_x, \mathbf{k}_y, \mathbf{k}_f)\middle| \sum_{p,t} V_{pt} - U_{aA}\middle|\psi_0, \Phi_A, \chi_i^{(+)}(\mathbf{k}_i)\right\rangle, \quad (2)$$

where $\Psi_\alpha^{(-)}$ is the full scattering solution with ingoing wave boundary condition, and ψ_0 and Φ_A are ground-state wave functions of the halo and the target, respectively. The distorted wave $\chi_i^{(+)}$ describing the relative motion of nuclei in the initial channel is a solution of the Schrödinger equation with optical potential U_{aA}. V_{pt} is NN interaction between the projectile and target nucleons. Due to the translational invariance, only relative wave numbers can characterize reaction

dynamics. $\mathbf{k}_x$, $\mathbf{k}_y$, and $\mathbf{k}_{i,f}$ are relative wave numbers between a pair of fragments, between the center of mass of a pair and the third fragment, and between the center of masses of halo and target nuclei in the initial and final channels, respectively. In the halo rest frame, $\hbar\mathbf{k}_y$ corresponds to the momentum of the third fragment. We know that the translational invariance or the recoil effects are very important in light nuclei. In halo nuclei, a correct treatment of the translational invariance is even more significant due to larger spatial extension of these systems. The exact T matrix (2) cannot be calculated without approximations. Our main goal is a study of halo structure. Therefore, the reactions will be considered under conditions that allow a simplified treatment of the reaction mechanisms making them both tractable and transparent. Hence, we study the collisions at high enough energy (large momentum $\hbar\mathbf{k}_i$) where one-step processes dominate. The excitation energy of halo nucleus,[1)]

$$E_x = \frac{\hbar^2 k_x^2}{2\mu_x} + \frac{\hbar^2 k_y^2}{2\mu_y},$$

where $\mu_{x,y}$ are reduced masses, can be used for further classification of reaction mechanisms. The reason is that, for large relative momentum $\hbar k_x$ ($\hbar k_y$), the interaction between the first and second fragments (between the third one and the rest of the halo system) can be neglected. Three reaction scenarios are possible. Two are for large values of E_x and the third one corresponds to the low-energy halo excitations. If at large E_x both relative momenta, $\hbar k_x$ and $\hbar k_y$, are large, then the final-state interactions can be neglected completely and plane waves can be used for description of the halo continuum. The reaction matrix is proportional to the Fourier image of the halo ground state, $T_{fi} \sim \langle e^{i(\mathbf{k}_x\cdot\mathbf{x})} e^{i(\mathbf{k}_y\cdot\mathbf{y})} | \psi_0 \rangle$. These approximations correspond to the Serber model of fragmentation reactions. The second scenario has large $\hbar k_y$ and small $\hbar k_x$ momenta and corresponds to a knockout of the third fragment (participant) from the halo system, while the two remaining fragments (spectators) move away and continue to interact between themselves. The full scattering wave function in this participant–spectator picture can be approximated by the product of the subsystem wave functions, and the T matrix (2) is given by

$$T_{fi} = \left\langle \chi^{(-)}_{3A^*}(\mathbf{k}_{3A^*}), \Phi_{A^*}, e^{i(\mathbf{k}_y\cdot\mathbf{y})}\psi^{(-)}(\mathbf{k}_x) \middle| \sum_{p,t} V_{pt} - U_{aA} \middle| \psi_0, \Phi_A, \chi^{(+)}_i(\mathbf{k}_i) \right\rangle, \quad (3)$$

where $\chi^{(-)}_{3A^*}(\mathbf{k}_{3A^*})$ is the participant–target distorted wave depending on the relative momentum $\hbar\mathbf{k}_{3A^*}$ between the knockout fragment and target, Φ_{A^*} is the target final state, and the continuum wave function $\psi^{(-)}(\mathbf{k}_x)$ describing the two-body spectator subsystem is obtained by solving the Schrödinger equation with the appropriate two-body interaction. In this scenario, only part of the final-state interactions are included in the consideration. The third scenario is realized at the low-energy halo excitations when the relative momenta $\hbar k_{x,y}$ are both small. Therefore, the halo fragments spend some time together and interact between themselves. There are no spectators and all fragments are participants. Under such conditions, a distorted-wave treatment of reaction dynamics can be used and the exact scattering wave function $\Psi^{(-)}_\alpha(\mathbf{k}_x, \mathbf{k}_y, \mathbf{k}_f)$ can be written as a product of wave functions: projectile, target, and their relative motion. Then reaction amplitude (2) reduces to the next expression

$$T_{fi} = \left\langle \chi^{(-)}_f(\mathbf{k}_f), \Phi_{A^*}, \psi^{(-)}(\mathbf{k}_x, \mathbf{k}_y) \middle| \sum_{p,t} V_{pt} \middle| \psi_0, \Phi_A, \chi^{(+)}_i(\mathbf{k}_i) \right\rangle, \quad (4)$$

where $\chi^{(-)}_f(\mathbf{k}_f)$ is the distorted wave describing relative motion of nuclei in the final channel, and $\psi^{(-)}(\mathbf{k}_x, \mathbf{k}_y)$ is the halo three-body continuum wave function. In calculation of $\psi^{(-)}(\mathbf{k}_x, \mathbf{k}_y)$, all fragment pairwise interactions must be taken into account, or, in other words, final-state interactions must be included in full scale. The term with optical potential U_{aA} does not give a contribution to the T matrix (4) due to the orthogonality between halo bound ψ_0 and continuum $\psi^{(-)}(\mathbf{k}_x, \mathbf{k}_y)$ wave functions. This

[1)] Excitations of the core bound states, if they exist, were omitted for simplicity. Near the three-body breakup threshold, they are not allowed energetically. At high excitation energy, they have a small effect on the value of relative momenta $k_{x,y}$.

low-energy region of nuclear excitations is the most sensitive to the three-body correlations and, consequently, the most useful for a study of halo structure. Such investigations require the special selection of experimental data. It can be done by performing kinematically complete experiments where energies and momenta of all halo fragments are measured in coincidence. Then it is possible to restore the energy spectrum of a halo nucleus and select only events corresponding to the low-energy excitations. Simultaneously, a variety of different energy and angular correlations become available and the possibility of describing them within the same model is a thorough test for our understanding of nuclear structure and reaction dynamics. These experiments are kinematically complete only with respect to the halo system. The energy transferred to the target is known from measurements, but if the target is a complex nucleus, it is unknown how this energy distributes between the center-of-mass motion and the internal target excitations. Then inelastic breakup must be included in theoretical calculations. The reaction model based on approximation (4) was applied successfully [11–15] for description of many reactions with halo nuclei.

3.2. Electron Scattering

Electron scattering is one of the most powerful and proven methods for nuclear structure investigations. The electromagnetic interactions of electrons with nuclear charges and currents are well known and weak. Thus, in principle, the reaction mechanism can be disentangled from the nuclear structure effects. Ultrarelativistic electrons are used in the study of nuclear structure. Since the charge on halo nuclei is only a few units, multiple scattering effects can safely be neglected and the interactions can be well described by one-photon exchange terms. Then the initial and final electron states are known and described by plane wave Dirac spinors. In electron scattering, the breakup cross section (1) is traditionally expressed in the following way:

$$d\sigma = d\mathbf{k}_f d\mathbf{k}_1 d\mathbf{k}_2 d\mathbf{k}_C \delta(E_i - E_f) \times \delta(\mathbf{P}_i - \mathbf{P}_f)\frac{(\hbar c)^2}{\varepsilon_f^2}\sigma_{\mathrm{M}} \sum V_{ij} W_{ij}, \quad (5)$$

where ε_f and $\hbar\mathbf{k}_f$ are the final electron energy and momentum; σ_{M} is the Mott cross section, which describes electron scattering on a pointlike nucleus; and V_{ij} and W_{ij} are the electron and hadron tensors, respectively. The sum in (5) for unpolarized electrons includes four different terms. For small energy and momentum transfers that we consider here, the contributions from convection and magnetization currents can be neglected in comparison with the Coulomb interaction. Thus, only one term from four is important in (5) and the corresponding tensors are given by

$$V_{00} = \frac{Q^4}{|\mathbf{q}|^4}, \quad (6)$$

$$W_{00} = \frac{1}{\hat{J}_a^2}\sum |\langle\psi^{(-)}(\mathbf{k}_x, \mathbf{k}_y)|\hat{\rho}(\mathbf{q})|\psi_0\rangle|^2, \quad (7)$$

where $\mathbf{q} = \mathbf{k}_i - \mathbf{k}_f$ is the three-dimensional momentum transfer, $Q = \left(\frac{\varepsilon_i - \varepsilon_f}{\hbar c}, \mathbf{q}\right)$ is the Lorentz-invariant four-momentum transfer, $\hat{\rho}(\mathbf{q})$ is the charge operator, and J_a is the ground-state spin of the halo nucleus. The sum in hadron tensor (7) is over all spin projections in the halo initial and final states. We recall that all final-state interactions must be taken into account in calculation of $\psi^{(-)}(\mathbf{k}_x, \mathbf{k}_y)$ in (7). Then any exclusive or inclusive cross sections can be calculated from (5).

At the present moment, there are no ready installations for performing electron scattering experiments with unstable nuclei. But due to the new developments for intense beams of radioactive isotopes, electron–nucleus collider experiments will become feasible in the future at the new installations in RIKEN and GSI. The first measurements will be done for the processes with the largest cross sections: elastic and inclusive inelastic electron scattering. Here, the calculations of inelastic electron scattering on ^{6}He are shown. Using the three-body model for the description of the ^{6}He bound and continuum structure [15], the inclusive cross section can be explicitly written as

$$\frac{d^3\sigma}{d\mathbf{k}_f dE_x} = \frac{4\varepsilon_f^2\alpha^2}{(\hbar c)^2} \times \frac{\cos^2(\theta/2)}{1 + (1 - |\mathbf{k}_i|\cos\theta/|\mathbf{k}_f|)\varepsilon_f/(M_a c^2)}\frac{2E_x^2}{|\mathbf{q}|^4}\frac{4\pi}{\hat{J}_a^2} \times \sum |\rho^{l0l}_{\gamma,\,\mathrm{c.m.}}(\mathbf{q})\rho_C(\mathbf{q})|^2, \quad (8)$$

where θ is the electron scattering angle, α is the fine structure constant, $\rho_C(\mathbf{q})$ is the charge density of the α-particle core, and $\rho^{lsj}_{\gamma,\,\mathrm{c.m.}}(\mathbf{q})$ is the transition density of the core center-of-mass motion. The index γ includes all quantum numbers that are necessary to describe uniquely the ^{6}He continuum state at excitation energy E_x. The quantum numbers l, s, and j in transition density $\rho^{lsj}_{\gamma,\,\mathrm{c.m.}}(\mathbf{q})$ correspond to the orbital, spin, and total angular-momentum transfers, respectively. The sum is done over all possible fragment motion modes and all modes give independent contributions in (8). Since the α-particle core has zero spin and the core is not destroyed in the reaction,

only excitations of the natural parity states ($l = j$) in ^{6}He with the spin transfer $s = 0$ are possible. Figure 1 shows the spectra of the ^{6}He low-energy excitations in the inelastic electron scattering for $E_e =$ 200 MeV and various scattering angles θ. The solid, dashed, and dotted curves correspond to the total, dipole, and quadrupole excitations of ^{6}He, respectively. The absolute values of cross sections depend strongly on the momentum transfer $|\mathbf{q}|$ and decrease rapidly with increasing electron scattering angle θ. A multipole composition of excitation spectra depends on properties of the Coulomb interaction and the nuclear structure. In multipole decomposition of the Coulomb interaction, the monopole term decreases the most slowly with distance between the electron and the nuclear center of mass; then follow terms with higher angular momenta, dipole, quadrupole, and so on. At small momentum transfer, a reaction amplitude gets the main contribution from large distances, where the monopole excitations are strongly suppressed by the orthogonality of the ground and continuum halo states. As a result, the dipole excitations dominate at low-excitation energies for small $|\mathbf{q}|$ (Fig. 1*a*). With increasing momentum transfer, the well-known three-body 2^+ resonance at $E_x =$ 1.8 MeV appears (Fig. 1*b*) and soon becomes a dominant feature (Fig. 1*c*) in the low-energy spectrum. If part of the final-state interactions are neglected in calculations, then two effects happen. The first is that orthogonality of the ground and continuum states is lost and the monopole excitations dominate in the spectrum near the breakup threshold, which is a physically wrong result for electromagnetic processes. And the second is that the 2^+ resonance disappears from spectra. Thus, the final-state interactions are the essential part of reaction dynamics of the low-energy excitations. The concentration of the dipole transition strength near the threshold does not mean that these excitations have a collective nature and represent a resonance. As seen from Figs. 1*a*–1*c*, the energy position and the shape of dipole excitations show a strong dependence on transferred momentum, while for a genuine resonance, like the 2^+ at $E_x =$ 1.8 MeV, the peak position is fixed. In principle, to reveal the nature of an observed peak, more complicated energy correlations of the fragments must be studied.

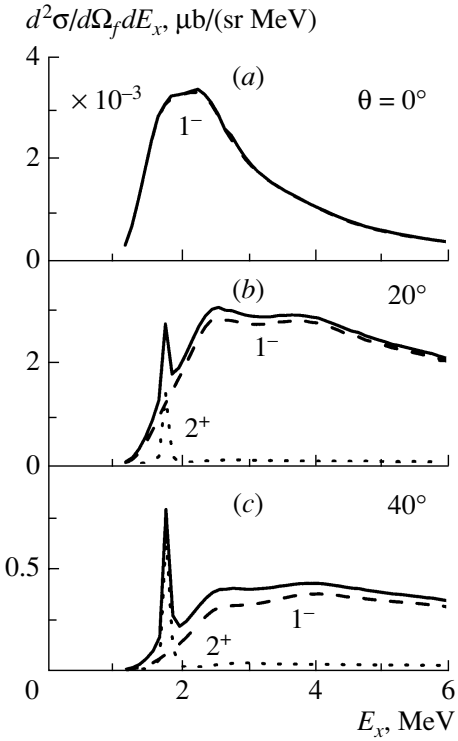

Fig. 1. Inclusive inelastic electron scattering on ^{6}He for $E_e = 200$ MeV and various scattering angles. The solid, dashed, and dotted curves are the total, dipole, and quadrupole cross sections, respectively.

3.3. Halo Breakup on Nucleons

A knowledge of nuclear structure or, more explicitly, a knowledge of transition densities from ground to continuum states is necessary for description of fragmentation reactions induced by electron scattering. From expression (4), it follows that, in addition to nuclear structure, the effective interaction V_{pt} between the projectile and target nucleons and the distorted waves $\chi^{(\pm)}_{i,f}(\mathbf{k}_{i,f})$ describing the relative motion of colliding systems must be known for calculations of breakup reactions on nucleons. The best way to fix new parameters and reduce their number is to apply the condition of self-consistency when effective interaction V_{pt} is used for calculation of optical potentials that are necessary for distorted-wave calculations. Then experimental data on elastic scattering and total reaction cross sections can be used to define the effective interaction V_{pt} and check the accuracy of distorted-wave calculations. This procedure strongly reduces the freedom of the V_{pt} modifications in breakup-reaction calculations. Unlike electron scattering, where only interactions with the core protons are important, the interactions with all (core and halo) nucleons must be taken into account in nucleon breakup. Therefore, the interplay between the core and halo degrees of freedom becomes very essential and has a strong impact on reaction dynamics.

As an example of such an approach, we consider the calculation of the ^{11}Li breakup reaction on protons at collision energy $E/A = 68$ MeV. This reaction has been studied experimentally at RIKEN [16] by correlational measurements of emitted particles. The structure of ^{11}Li was calculated in the framework of a three-body model neglecting the spin of

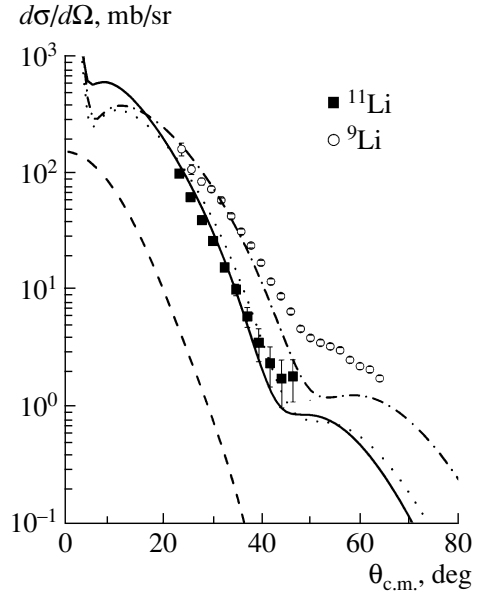

Fig. 2. Angular distributions for the elastic scattering of ^{11}Li and ^{9}Li on a proton. The solid and dash-dotted curves show the theoretical calculations for ^{11}Li and ^{9}Li, respectively. The dashed and dotted curves show contributions in elastic scattering of ^{11}Li from halo neutrons and core nucleons, respectively.

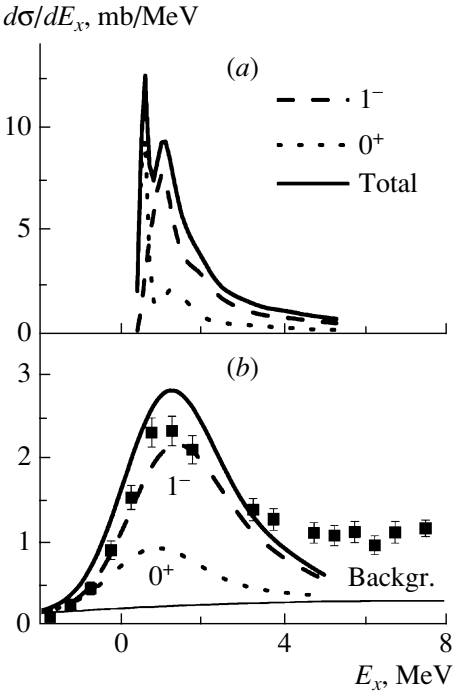

Fig. 3. The energy spectrum of ^{11}Li on a proton at collision energy $E/A = 68$ MeV. (a) The theoretical spectrum. (b) Comparison of the experimental data with the theoretical spectrum corrected for experimental conditions of the detection system. The solid, dashed, and dotted curves are the total, dipole, and monopole cross sections, respectively. In (b), the thin solid line shows the experimental background from materials other than protons in the target.

the ^{9}Li core [17]. The parameters of NN and n–core potentials correspond to the (P2) model of the ^{11}Li ground state [18] having a superposition of $(0p_{1/2})^2$ and $(0s_{1/2})^2$ components with relative weights of 45 and 31%, respectively. The distorted waves $\chi^{(\pm)}_{i,f}$ were obtained by solving the Schrödinger equation with microscopic optical potential $U_{^{11}\mathrm{Li}}$. The optical potential has been calculated in the single folding model and has two parts, U_{core} and U_{halo}, created by interactions of protons with core nucleons ($V_{pt} = V_{NN}$) and halo neutrons ($V_{pt} = t_{NN}$),

$$U_{^{11}\mathrm{Li}}(\mathbf{r}) = U_{\mathrm{core}}(\mathbf{r}) + U_{\mathrm{halo}}(\mathbf{r}) \qquad (9)$$
$$= \int d\mathbf{r}' V_{NN}(\mathbf{r}-\mathbf{r}')\rho_{\mathrm{core}}(\mathbf{r}') + \int d\mathbf{r}' t_{NN}(\mathbf{r}-\mathbf{r}')\rho_{2n}(\mathbf{r}'),$$

where ρ_{core} and ρ_{2n} are the ground-state densities of core nucleons and halo neutrons, respectively. In the calculations, we have used the GLM interaction [19] (complex, energy and density dependent) as V_{NN} and the free NN t-matrix interaction [20] (complex and energy dependent) for t_{NN}. The core density $\rho_{\mathrm{core}}(\mathbf{r})$ is a convolution integral of the ^{9}Li density $\rho_{^{9}\mathrm{Li}}(\mathbf{r})$ and the density $\rho_{\mathrm{c.m.}}(\mathbf{r})$ describing the core center-of-mass motion. In momentum space, this relation reduces to the product form $\rho_{\mathrm{core}}(\mathbf{q}) = \rho_{^{9}\mathrm{Li}}(\mathbf{q})\rho_{\mathrm{c.m.}}(\mathbf{q})$. The ^{9}Li density has been described by a Gaussian distribution with a range parameter chosen to reproduce the rms radius of ^{9}Li, $\langle r^2\rangle^{1/2} = 2.32$ fm. Thus, simultaneously with $U_{^{11}\mathrm{Li}}$, we can calculate the optical potential for proton scattering on ^{9}Li,

$$U_{^{9}\mathrm{Li}}(\mathbf{r}) = \int d\mathbf{r}' V_{NN}(\mathbf{r}-\mathbf{r}')\rho_{^{9}\mathrm{Li}}(\mathbf{r}'). \qquad (10)$$

The solid and dash-dotted curves in Fig. 2 show a comparison of experimental data [16, 21] with theoretical calculations of proton elastic scattering on the ^{11}Li and ^{9}Li nuclei, respectively. The theoretical calculations describe reasonably well both the shape and the absolute values of elastic angular distributions. It is interesting to understand in detail what dynamical features of the model are responsible for the correct reproduction of changes in character of ^{11}Li elastic scattering in comparison with scattering of ^{9}Li. The dotted and dashed curves show separately elastic scattering due to two different parts of optical potentials in (9), U_{core} and U_{halo}, created by interactions with core nucleons and halo neutrons, respectively. Elastic scattering from core nucleons domi-

nates at all angles. Only in the forward direction is the scattering on halo neutrons important as a result of the constructive interference with core contribution. Owing to the core center-of-mass motion, the space occupied by the ^{9}Li core in ^{11}Li is larger than when ^{9}Li is free. Thus, the slope of the angular distribution from a moving core (dotted curve) is steeper than one from a free core (dash-dotted curve). The calculated reaction cross section for ^{11}Li (398 mb) is significantly larger than that for ^{9}Li (234 mb). But contributions to the reaction cross section from two halo neutrons (from U_{halo}) and nine core nucleons (from U_{core}) are about the same, 231 and 226 mb, respectively. These examples clearly demonstrate the importance of interplay of the core and halo degrees of freedom.

Figure 3*a* shows the theoretical excitation spectra of ^{11}Li. The excitation spectra corrected for distortions from the detection system are compared with experimental data [16, 18] in Fig. 3*b*. The dashed and dotted curves in these figures represent the dipole and monopole contributions, respectively. The calculations show an accumulation of transition strength from different multipolarities near the breakup threshold, and experimental data support such a concentration even when the fine structure of the theoretical spectrum is washed out by the experimental finite-energy resolution. At higher excitation energy, the theoretical calculations underestimate the experimental spectrum. This indicates that new effects, like the ^{9}Li core excitations, have to be included in the model for a correct description of the ^{11}Li high-energy excitations. The inelastic angular distributions obtained by integration of the double differential cross sections $d^2\sigma/d\Omega dE_x$ over the experimentally defined section of the energy spectrum [16] are plotted in Figs. 4*a*–4*c*. Again, we have reasonable descriptions (Fig. 4*a*) of both the shape and the absolute values of experimental cross sections. Also, from Fig. 4*a*, it follows that the dipole excitations dominate at large scattering angles and the experimental data at small angles are needed to reveal the monopole contribution. The interplay of the core (dotted curve) and halo (dashed curve) degrees of freedom in inelastic scattering are shown in Figs. 4*b* and 4*c* for the dipole and monopole excitations, respectively. Similar to the elastic case, the core contributions dominate at large scattering angles. At small angles, both contributions are important and the total angular distribution shows the strong destructive (constructive) interference of the dipole (monopole) excitations.

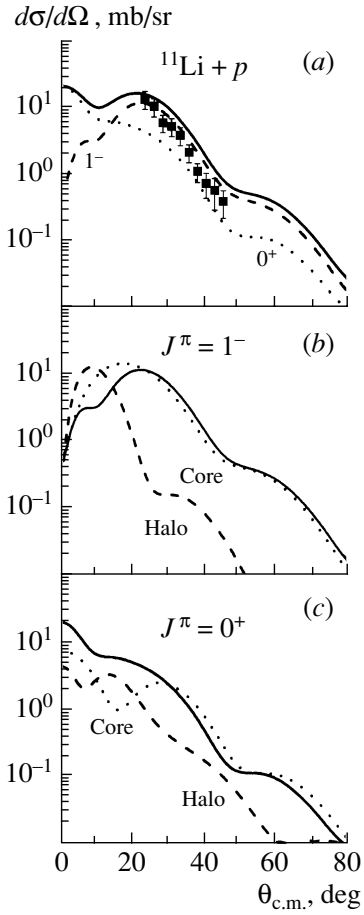

Fig. 4. Angular distributions for inelastic scattering of $^{11}\text{Li} + p$ at collision energy $E/A = 68$ MeV. (*a*) Comparison of the experimental data with theoretical calculations. The solid, dashed, and dotted curves show the total, monopole, and dipole angular distributions, respectively. In (*b*) and (*c*), the solid curves show angular distributions for monopole and dipole excitations, respectively. The dashed and dotted curves are contributions from halo neutrons and core nucleons, respectively.

3.4. Halo Breakup on Nuclei

At least two new features can be mentioned in breakup reactions on nuclei in comparison with fragmentation on a nucleon target. The first one is that, simultaneously with projectile breakup, target excitations are possible and the mechanism of inelastic breakup must be considered. The second one is that the target charge can be varied and this possibility gives additional freedom in changing the proportion between the long-range Coulomb and short-range strong interactions. Hence, Coulomb and nuclear breakup must be treated on equal footing. Both new features can be taken into account within the four-body distorted-wave theory (see [15] and references therein) discussed here. We present one example of calculations [15] of ^{6}He breakup at 240 MeV/A on ^{208}Pb and ^{12}C targets. Figure 5 shows the comparison of the ^{6}He excitation spectra with experimental data from GSI [22]. The calculations correctly describe absolute values and spectral shapes for both

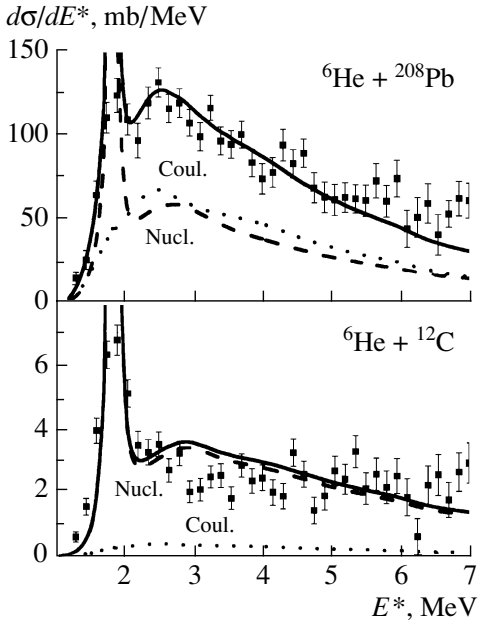

Fig. 5. Comparison of the theoretical ^{6}He excitation spectrum for ^{6}He breakup at 240 MeV/A on ^{208}Pb and ^{12}C with experimental data [22]. The dotted (dashed) curve shows calculations with only Coulomb (nuclear) interactions.

reactions, in spite of their different reaction mechanisms. The dotted and dashed curves additionally show the calculations with only Coulomb or nuclear interaction. On a carbon target, the inclusive excitation spectrum is completely defined by nuclear interaction, while on a lead target the half cross section is due to Coulomb fragmentation. The excitation of the 2^+ resonance is connected mainly with nuclear interaction. Although on a lead target the elastic fragmentation dominates the low-energy part of the spectrum, for a quantitative description the elastic and inelastic breakup have to be taken into account simultaneously. On carbon, the contributions from elastic and inelastic fragmentation are approximately equal. The Coulomb interaction is responsible for a dominance of elastic fragmentation over inelastic fragmentation on a lead target in comparison with reaction on carbon.

4. CONCLUSIONS

The characteristic of halo phenomena in light Borromean nuclei is present in properties of both bound and continuum states near the three-body breakup threshold. The reaction mechanism intertwines bound and excited states and reveals the peculiarities of the halo structure via transitions to the low-lying excited states that subsequently decay into fragments. Due to the small relative fragment velocities at low halo excitation energies, no interactions between fragments can be neglected and the final-state interactions have to be taken into account in full scale. For definite physical conditions, simplification of the reaction mechanism makes it possible to develop a viable approach. At intermediate energies, the one-step reaction mechanism dominates and the distorted-wave approximation can be applied. These approaches contain, as a main part, the microscopic three-body structure of the ground state and the exact three-body continuum. This enables us to study, in principle, the internal halo structure via all possible fragment correlations.

Breakup of halo nuclei in reactions with different probes reveals a different sensitivity to details of reaction mechanisms and halo correlations. Three examples of halo breakup reactions (with electrons, nucleons, and nuclei) leading to the low-energy halo continuum have been considered in order of increasing complexity of the reaction mechanism. It was demonstrated that the combined analysis of different breakup reactions using the same structure model can be a viable tool for discovering the genuine nature of halo nuclei. The simultaneous analysis of a variety of observables within the same model can be used to reduce the ambiguity of model assumptions on reaction dynamics. Kinematically complete experiments at intermediate energies with domination of one-step processes in the reaction mechanism are most promising and reliable spectroscopic instruments for investigation of the structure of halo nuclei.

ACKNOWLEDGMENTS

I am deeply indebted to Prof. B.V. Danilin, Prof. A.A. Korsheninnikov, Prof. I.J. Thompson, Prof. J.S. Vaagen, and Prof. M.V. Zhukov for collaborations and fruitful discussions.

REFERENCES

1. I. Tanihata, J. Phys. G **22**, 157 (1996).
2. M. V. Zhukov, B. V. Danilin, D. V. Fedorov, *et al.*, Phys. Rep. **231**, 151 (1993).
3. J. Al-Khalili and F. Nines, nucl-th/0306071.
4. T. Kobayashi, in *Proceedings of the 1st International Conference on Radioactive Nuclear Beams,* Ed. by W. D. Myers, J. M. Nitschke, and E. B. Norman (World Sci., Singapore, 1990), p. 325.
5. I. Tanihata *et al.*, Phys. Rev. Lett. **55**, 2676 (1985).
6. I. Tanihata *et al.*, Phys. Lett. B **297**, 307 (1992).
7. B. Blank *et al.*, Z. Phys. A **343**, 375 (1992).
8. B. V. Danilin and M. V. Zhukov, Yad. Fiz. **56** (4), 67 (1993) [Phys. At. Nucl. **56**, 460 (1993)].
9. B. V. Danilin, I. J. Thompson, M. V. Zhukov, and J. S. Vaagen, Nucl. Phys. A **632**, 383 (1998).
10. D. V. Fedorov, A. S. Jensen, and K. Riisager, Phys. Rev. C **50**, 2372 (1994).

11. B. V. Danilin, M. V. Zhukov, S. N. Ershov, *et al.*, Phys. Rev. C **43**, 2835 (1991).
12. S. N. Ershov, T. Rogde, B. V. Danilin, *et al.*, Phys. Rev. C **56**, 1483 (1997).
13. S. N. Ershov, B. V. Danilin, T. Rogde, and J. S. Vaagen, Phys. Rev. Lett. **82**, 908 (1999).
14. S. N. Ershov, B. V. Danilin, and J. S. Vaagen, Phys. Rev. C **62**, 041001 (2000).
15. S. N. Ershov, B. V. Danilin, and J. S. Vaagen, Phys. Rev. C **64**, 064609 (2001).
16. A. A. Korsheninnikov *et al.*, Phys. Rev. Lett. **78**, 2317 (1997).
17. I. J. Thompson and M. V. Zhukov, Phys. Rev. C **49**, 1904 (1994).
18. R. Crespo, I. J. Thompson, and A. A. Korsheninnikov, Phys. Rev. C **66**, 021002(R) (2002).
19. J.-P. Jeukenne, A. Lejeune, and C. Mahaux, Phys. Rev. C **16**, 80 (1977).
20. M. A. Franey and W. G. Love, Phys. Rev. C **31**, 488 (1985).
21. C.-B. Moor *et al.*, Phys. Lett. B **297**, 39 (1992).
22. T. Aumann *et al.*, Phys. Rev. C **59**, 1252 (1999).

Physics of Atomic Nuclei, Vol. 67, No. 10, 2004, pp. 1860–1865. From Yadernaya Fizika, Vol. 67, No. 10, 2004, pp. 1885–1890.

Proceedings of the International Conference "Nuclear Structure and Related Topics"

New Data on the Ternary Fission of ^{252}Cf from the Gammasphere Facility*

G. M. Ter-Akopian[1)], A. V. Daniel[1)], A. S. Fomichev[1)], G. S. Popeko[1)], A. M. Rodin[1)], Yu. Ts. Oganessian[1)], J. H. Hamilton[2)], A. V. Ramayya[2)], J. Kormicki[2)], J. K. Hwang[2)], D. Fong[2)], P. Gore[2)], J. D. Cole[3)], M. Jandel[4)], J. Kliman[4)], L. Krupa[4)], J. O. Rasmussen[5)], I. Y. Lee[5)], A. O. Macchiavelli[5)], P. Fallon[5)], M. A. Stoyer[6)], R. Donangelo[7)], S.-C. Wu[8)], and W. Greiner[9)]**

Received January 21, 2004

Abstract—Ternary fission of ^{252}Cf was studied at Gammasphere using eight $\Delta E \times E$ particle telescopes. Helium, beryllium, boron, and carbon light charged particles (LCPs) emitted with kinetic energy more than 9, 21, 26, and 32 MeV, respectively, were identified. The 3368-keV γ transition from the first 2^+ excited state in ^{10}Be was found and the population probability ratio $N(2^+)/N(0^+) = 0.160 \pm 0.025$ was estimated. No evidence was found for 3368-keV γ rays emitted from a triple molecular state. For the first time, charge distributions are obtained for ternary fission fragments emitted with helium, beryllium, and carbon LCPs.

1. INTRODUCTION

Spectroscopic γ-ray measurements are known for their effectiveness in getting essential characteristics for low-energy binary fission. Such are data on fragment-independent yields [1] and the measured yields of individual fragment pairs obtained at particular charge splits of the fissile nucleus [2, 3]. Until recently, such measurements could not be made for the nuclear fission accompanied by light charged particle (LCP) emission. The reason is that this process, often called ternary fission, is rare. In the case of ^{252}Cf ternary fission, one ternary fission event comes about only one time per ~ 260 binary fission events [4]. However, with the advent of contemporary 4π Ge detector arrays, such as the Gammasphere facility [5, 6], the $\gamma-\gamma-\gamma$ coincidence technique could show its full potential for the study of such rare events. Using this technique, the authors of [7, 8] for the first time obtained data on the yields of fragment pairs emitted in cold (neutronless) ternary fission of ^{252}Cf associated with ^{4}He and ^{10}Be LCPs.

It will be interesting to extend these data to the independent yields of other fragment pairs and/or individual fragments appearing in ^{252}Cf ternary fission accompanied by different LCPs. Such data will be useful for specifying initial ternary fission configurations realized by the nuclear system just before the instant when the acceleration of the three bodies (the two main fragments and the LCP) begins in the Coulomb field. The lack of experimental data characterizing these configurations led the authors of theoretical papers to make speculative assumptions when treating the problem of different LCP rates [9–12] and doing trajectory calculations for LPCs (see [4, 9, 13]).

On the other hand, the spectroscopy of ternary fission γ rays is interesting because it could be helpful in filling the gap in our knowledge about the population probability of excited states in LCPs emitted in ternary fission. Existing data of this type are scarce. Just recently, the population of a particle unstable level lying in ^{8}Li at $E^* = 2.26$ MeV was reported for the ternary fission of ^{252}Cf [14]. However, one should

*This article was submitted by the authors in English.

[1)]Flerov Laboratory of Nuclear Reactions, Joint Institute for Nuclear Research, Dubna, Moscow oblast, 141980 Russia.
[2)]Department of Physics, Vanderbilt University, Nashville, USA.
[3)]Idaho National Engineering and Environmental Laboratory, Idaho Falls, USA.
[4)]Department of Nuclear Physics, Slovak Academy of Sciences, Bratislava, Slovak Republic.
[5)]Lawrence Berkeley National Laboratory, Berkeley, USA.
[6)]Lawrence Livermore National Laboratory, Livermore, USA.
[7)]Instituto de Fisica Unversidade Federal do Rio de Janeiro, Rio de Janeiro, Brazil.
[8)]National Tsing Hua University, Hsinchu, Taiwan.
[9)]Institut für Theoretishe Physik, J.W. Goethe Universität, Frankfurt/Main, Germany.
**e-mail: Gurgen.TerAkopian@jinr.ru

not come to anything more than the observation of particle unstable states because, apart from the large statistical error of the yield value reported in [14], the ambiguity is inherent to the population ratios measured for particle unstable states.

Among LCPs with $Z > 2$, ^{10}Be has the largest yield. If its first excited state ($J^\pi = 2^+$) is populated, 3368-keV γ rays will be emitted as a result of $2^+ \to 0^+$ transition. The authors of [15, 16] reported on the observation of a 3.37-MeV peak in the γ spectrum recorded in coincidence with ^{10}Be LCPs emitted in ^{252}Cf ternary fission. They also furnished evidence that this peak did not show Doppler broadening. Taking into consideration the short, 125-fs, lifetime of ^{10}Be in its 2^+ state, the authors of [15, 16] concluded that it could either mean an emission of γ rays preferentially perpendicular to the ^{10}Be momentum vector or a substantial delay in the release of the excited ^{10}Be nuclei resulting in the fact that these nuclei stay at rest for an unusually long time before the beginning of their acceleration in the Coulomb field of the two main fragments. The result was open to question because of the poor energy resolution of the NaI detectors used in this experiment. To test this idea, a $\gamma-\gamma-\gamma$ coincidence experiment was conducted at Gammasphere with a high energy resolution [8, 17]. The data gave support to the observation reported in [15, 16], but with limited statistics and without a direct LCP identification. The possibility that the ^{10}Be nucleus may stay between two fission fragments for a long time ($\sim 10^{-13}$ s) to create a so-called triple nuclear molecule opens up an exciting possibility discussed in [18].

Thus, the observation of γ rays emitted by LCPs became important both for the deeper penetration into the dynamics of ternary fission and for examining this process for quasi-molecular states appearing presumably at the scission point.

2. EXPERIMENT

Keeping this in mind, we performed a new experiment at Gammasphere providing that events showing the coincidence of γ rays and LCPs originating from the spontaneous fission of ^{252}Cf were detected. Gammasphere was set to record γ rays with energy less than 5.4 MeV. The detection efficiency varied from a maximum value of 17% typical for the low-energy part of the γ-ray spectrum to 4.6% at 3368 keV. A ^{252}Cf sample giving $\sim 4 \times 10^4$ spontaneous fissions per second was installed in the center of a reaction chamber placed in a hollow sphere inside Gammasphere. The source was deposited on a 1.8-μm Ti foil and was tightly covered by gold foils on both sides. These foils had the least thickness that could stop

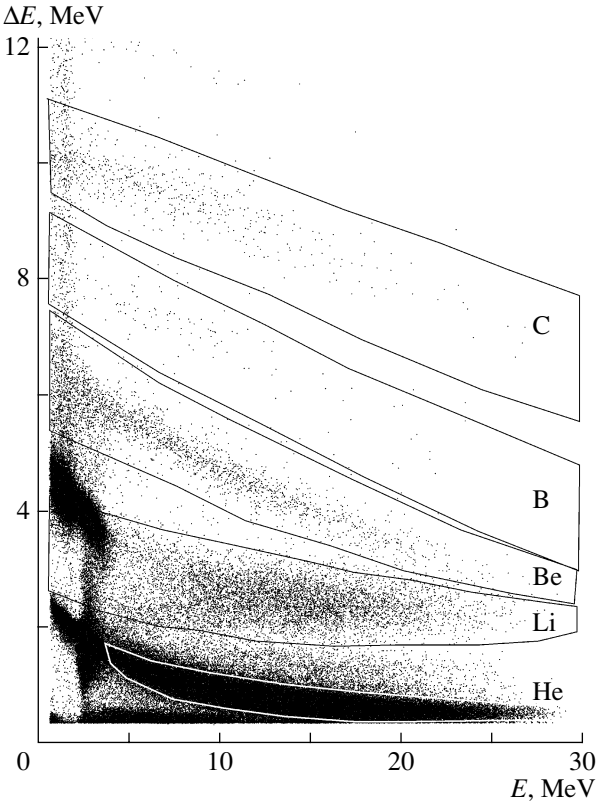

Fig. 1. $\Delta E \times E$ plot. The data were collected by the first telescope during the whole time of the experiment.

the two main fragments originating in ternary fission. The fragment deceleration time was less than 1 ps, ensuring one that γ rays were emitted by the fission fragments mainly when these fragments were at rest.

Eight $\Delta E \times E$ detector telescopes were used for the LCP detection. Four telescopes were centered at polar angle $\theta = 30°$ ($\varphi = 45°$, 135°, 225°, and 315°). The other four telescopes were at $\theta = 150°$ (azimuth angles were the same). The telescopes were inclined so that the lines connecting the centers of two opposite ΔE detectors and going through the center of the source were orthogonal to the detector surfaces. Each ΔE detector had an area of 10×10 mm and thickness varying between 9.0 and 10.5 μm. Each E detector was 400 μm thick and was 20×20 mm in area. All ΔE detectors were at a distance of 27 mm from the source. The distance between the ΔE and E detectors was 13 mm.

Data acquisition was triggered by ΔE or E signals with amplitudes above the threshold values, which were set to prevent the detection of twofold pileups of α particles emitted in ^{252}Cf radioactive decay. A ternary fission event was stored under the condition that at least one γ ray was detected within a 100-ns time interval. During a period of two weeks

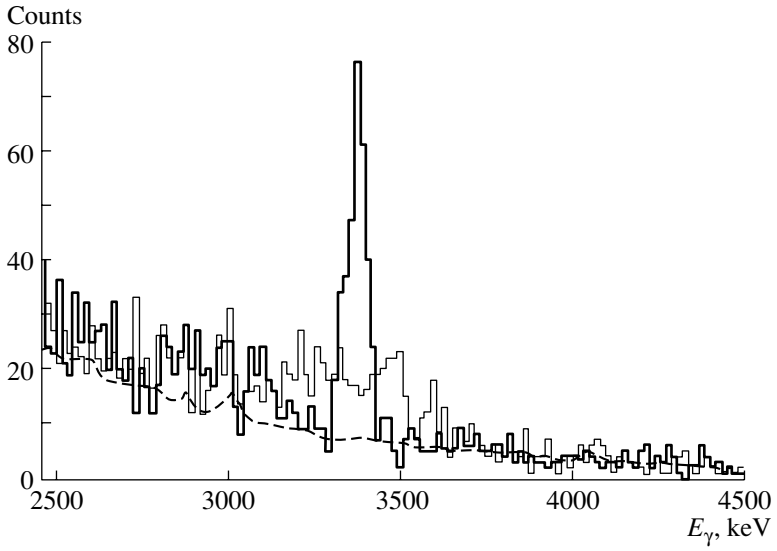

Fig. 2. Spectra of γ rays coinciding with Be LCPs obtained before and after the Doppler shift correction (histograms drawn with thin and thick solid lines, respectively). The dashed line shows the spectrum of γ rays observed in coincidence with He LCPs. The last spectrum was normalized to the total number of counts obtained in the whole spectrum associated with Be LCPs ($E_\gamma = 90-5000$ keV).

when measurements were made continuously, approximately 1.6×10^7 events were recorded.

3. RESULTS AND DISCUSSION

The resolution achieved for the $\Delta E \times E$ telescopes allowed us to identify helium, beryllium, boron, and carbon nuclei well in each of the eight two-dimensional plots created from the data recorded by the telescopes. One such plot is shown in Fig. 1. Only the lithium region was shadowed by the random coincidences of helium LCPs with α particles appearing from the radioactive decay of ^{252}Cf. We separated He, Be, B, and C LCPs using the loci shown in Fig. 1 and applying a condition that the energy deposited in the E detectors was greater than 5 MeV. Thus, the lower primary energy of the recorded LCPs was 9, 21, 26, and 32 MeV for He, Be, B, and C LCPs, respectively.

Parameters of the energy spectra and yields of LCPs obtained by fitting our experimental data (the yields are normalized to 10^4 He LCPs)

	LCP			Reference
	Be	B	C	
$\langle E \rangle$ [MeV]	18.0(4)	20.5(1.0)	23.4(1.0)	[19]
	17.5(1.0)	21.2(1.0)	26(1)	[20]
FWHM [MeV]	17.03(8)	19.8(2)	18.7(2)	Present work
	18(1)	19.3(1.0)		[20]
Yield	166(10)	16(3)	103(15)	Present work
	126(30)	6.3(4.0)		[20]

In the case of Be, B, and C LCPs, only high-energy parts of the full energy spectra were measured. Even under a usual assumption that the LCP energy distributions are Gaussians, it is impossible to estimate the mean values and widths of LCP energy distributions from these data. Therefore, we used the mean values estimated in another experiment conducted in Dubna with an open ^{252}Cf source [19]. This allowed us to estimate the FWHM values by fitting the LCP energy distributions obtained with higher statistics in the present experiment. These fits gave the yields of LCPs occurring in ^{252}Cf ternary fission. The obtained results are summarized in the table.

The histogram shown in Fig. 2 with a thin line represents the energy spectrum of prompt γ rays recorded in coincidence with Be LCPs. The thick solid line histogram is the same spectrum obtained after applying a correction for Doppler shift. A distinct peak dominating in the last spectrum at 3368 keV corresponds to the $2^+ \to 0^+$ transition in ^{10}Be. The peak width, FWHM $= 65.7 \pm 4.5$ keV, was estimated by using a Gaussian fit. This width is compatible with the value FWHM $= 62.1$ keV obtained by the Monte Carlo simulation of the correction procedure made for γ rays emitted from moving ^{10}Be nuclei. The dashed line in Fig. 2 shows the spectrum of γ rays detected in coincidence with helium nuclei. To some extent, this spectrum reflects the background from γ rays emitted by fission fragments.

In the raw spectrum of γ rays recorded in coincidence with Be LCPs, we do not see any distinct peak near 3368-keV which could be associated with γ emission from stationary ^{10}Be nuclei. A thorough analysis made with the selection of γ rays emitted in a nearly perpendicular direction to the trajectories of Be LCPs showed that there is a lack of any γ line which could be attributed to the emission from ^{10}Be standing in a triple nuclear molecule.

The number of counts obtained in the 3368-keV γ line is 263 ± 22. Taking into consideration the Gammasphere efficiency ($\simeq 4.6\%$), the total number of 3368-keV γ rays emitted by ^{10}Be nuclei becomes $I_\gamma = 5700 \pm 480$. After correction for the number of beryllium LCPs escaping detection due to the lack of recorded signals from γ rays, we estimated the total number of Be LCPs recorded by the $\Delta E \times E$ telescopes as $N_{\mathrm{Be}} = 51800 \pm 5000$. The energy resolution of the ΔE detectors did not allow us to directly separate the loci of beryllium isotopes in the $\Delta E \times E$ plot (see Fig. 1). Comparing the loci obtained by Monte Carlo simulations for ^{9}Be, ^{10}Be, and ^{11}Be with the experimental $\Delta E \times E$ distributions, we estimated the yield of ^{10}Be nuclei at $\sim 80\%$ of all beryllium LCPs emitted in the ternary fission of ^{252}Cf. This observation is in agreement with the experimental data presented in [11].

Based on these results, we estimated the population ratio of the excited 2^+ and the ground-state 0^+ levels in ^{10}Be as $N(2^+)/N(0^+) = 0.160 \pm 0.025$. The upper limit for the probability that ^{10}Be emits its γ rays while being at rest makes up only 4% of this ratio. We note, however, that these results are valid for ^{10}Be LCPs obtained at infinity with kinetic energy more than 21 MeV. In particular, one cannot exclude that the hypothetical triple molecules decay in a way leading mainly to a low kinetic energy for the ^{10}Be LCPs which was beyond the reach of the present experiment. Since the earlier Gammasphere experiment [8, 17] relied solely on the observation of $\gamma-\gamma-\gamma$ coincidence events, a possibility still remains open that a narrow γ peak characteristic of the motionless ^{10}Be can be found if the low-energy part of the energy distribution of ^{10}Be LCPs is detected. At the same time, the present result excludes any possibility that an effect of a triple quasi-molecular state involving beryllium LCPs could be observed in [15, 16], where the energy cutoff was 26 MeV for these clusters.

Using raw data, we built a 4096×4096 channel two-dimensional spectrum for events involving twofold or higher γ-ray signals recorded in coincidence with He ternary LCPs. This spectrum spanned an energy range from 50 to 2700 keV along the two axes. We also built three linear spectra extending from 50 to 5500 keV separately for γ rays coinciding with helium, beryllium, and carbon ternary LCPs.

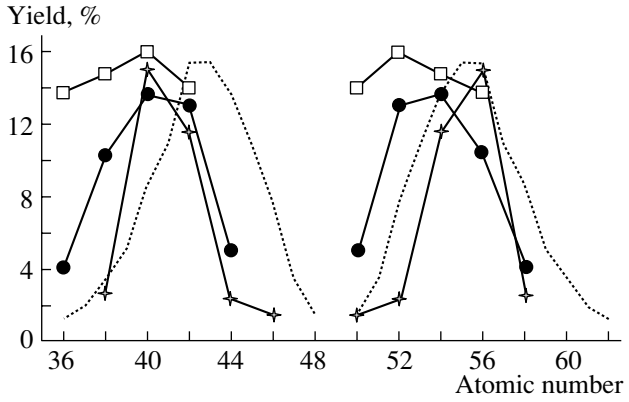

Fig. 3. The charge distributions obtained for main fragments emitted in the ternary fission of ^{252}Cf accompanied, respectively, by He (stars), Be (circles), and C (squares) LCPs. The dotted lines show the charge distribution known for the binary fission of ^{252}Cf.

In the two-dimensional spectrum, we identified more than 170 $\gamma-\gamma$ coincidence peaks originating from fission fragments appearing in the He ternary fission of ^{252}Cf. Some of these peaks corresponded to the coincidences of ground-state transitions occurring in complementary fragments entering into different fragment pairs. From these peak values, corrected for detection efficiency and electron conversion, we calculated independent yields for 63 fragment pairs corresponding to four charge splits of the main part of the ^{252}Cf nucleus remaining after the going out of the ternary He LCP. In addition, we estimated independent yields for two tin isotopes (^{130}Sn and ^{132}Sn) from their γ-peak values obtained in the linear spectrum built for the He ternary fission events.

In the γ-ray spectra observed in coincidence with Be LCPs, we identified 72 peaks as due to transitions occurring in 38 fission fragments and estimated independent yields for these fission fragments. In the case of C LCPs, 70 γ peaks were identified, and independent yields were estimated for 35 fission fragments.

These results allowed us to present, for the first time, charge distributions obtained for fission fragments appearing in the ternary fission of ^{252}Cf in coincidence with helium, beryllium, and carbon LCPs. These charge distributions are presented in Fig. 3. For comparison, we showed in Fig. 3 the fragment charge distribution known for the binary fission of ^{252}Cf.

From the comparison made for the two charge distributions, one obtained for the He ternary fission and another one known for the binary fission of ^{252}Cf, we see that two protons entering the He LCPs come

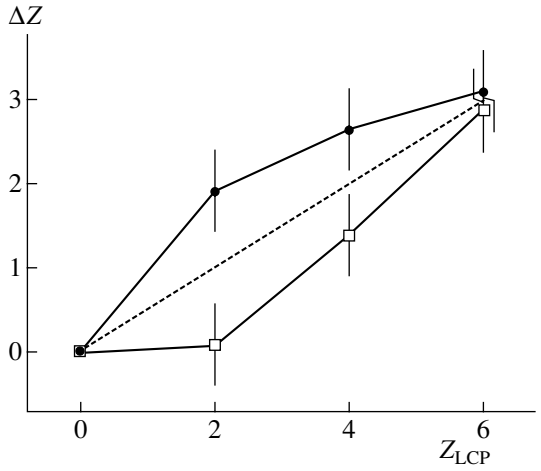

Fig. 4. The average numbers of protons removed from the heavy (squares) and light (circles) ternary fission fragments which otherwise could be obtained as those emitted in binary fission.

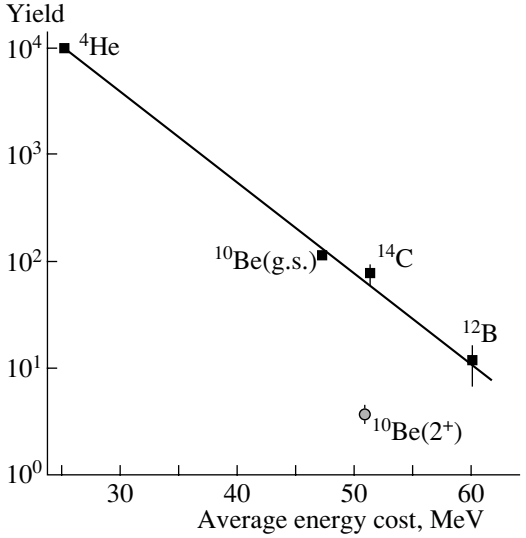

Fig. 5. Correlation plot showing the relative yields of various LCPs as a function of the average energy cost (see text).

from the light fragments, otherwise obtained as those emitted in binary fission. Similar considerations show that Be nuclei take, on average, ~ 2.7 protons from the light fragment with the rest of the charge coming from the heavy fragment. Finally, we see that both fission fragments contribute about the same proton number in the formation of carbon LCPs. The average proton numbers removed from the light and heavy binary fission fragments by He, Be, and C LCPs are presented in Fig. 4. It will be natural to say that, on average, the parts of nuclear matter contributing in these LCPs from the light and heavy binary fission fragments keep the same proportions as those established for protons. These observations seem to be more direct in their nature, and, hence, more correct, than analogous conclusions made on the basis of energy and mass distributions of primary fragments (before neutron evaporation) deduced, in turn, by iterative procedures from the measured energy ratios of correlated fragments emitted in ternary fission [20].

It is of interest to see how measured LCP yields correlate with the "average energy cost" for the production of various third particles. The correlation plot presented in Fig. 5 was obtained using the relative yield values presented in the table for Be, B, and C with respect to He LCPs. The average energy cost values were calculated following the prescription given in [9] and with the use of our results presented in Fig. 4. We assumed that ^{4}He, ^{12}B, and ^{14}C exhaust the full yield values measured for the helium, boron, and carbon LCPs. This approximation seems to be natural in view of relatively low rates reported for LCPs representing heavy helium isotopes [20] and abundance ratios measured for boron and carbon nuclei emitted in ternary fission [4, 9, 13]. As for Be LCPs, shown in Fig. 5 is the ground-state yield of ^{10}Be obtained after a correction was made to the value given in the table. This correction takes into account the measured ratio $N(2^+)/N(0^+) = 0.160 \pm 0.025$ and the 80% proportion which we have estimated for ^{10}Be LCPs emitted in the ternary fission of ^{252}Cf. Figure 5 shows that the LPC yields fall exponentially with an increase in the average energy cost.

Figure 5 shows one point representing the relative yield of ^{10}Be(2^+) nuclei emitted in the excited state. This estimate involves the measured ratio $N(2^+)/N(0^+) = 0.160 \pm 0.025$ reduced by a factor of 5 to take into account the spin factor which actually enhanced the 2^+ state yield. In the energy scale of Fig. 5, we just added the excitation energy of the 2^+ state in ^{10}Be, 3368 keV, to the average energy cost estimated for ^{10}Be(g.s.). The two points representing ^{10}Be(g.s.) and ^{10}Be(2^+) show a remarkably more rapid decrease in the yield as compared with the exponential fitting of the yields of other LCPs, taken with the exception of ^{10}Be(2^+).

4. CONCLUSION

In summary, He, Be, B, and C LCPs emitted in ^{252}Cf ternary fission with kinetic energy more than 9, 21, 26, and 32 MeV, respectively, were identified and their relative yields and energy distribution parameters were obtained. The extraordinary capability of Gammasphere in probing rare γ rays combined with $\Delta E \times E$ detector telescopes allowed us to measure for the first time the ratio of population probabilities, $N(2^+)/N(0^+) = 0.160 \pm 0.025$, for ^{10}Be nuclei

emitted in their excited (2^+) and ground (0^+) states. Assuming that a kind of statistical equilibrium is set at some stage in the ternary fission process (e.g., as discussed in the dynamical model [11]) and taking into account the statistical factor brought about by the spin, this ratio suggests a value of 1.0 ± 0.16 MeV for the temperature parameter. Our results do not show any hint that the γ rays are emitted from ^{10}Be nuclei occurring at rest as a part of a triple nuclear molecule presumably formed at the scission point.

For the first time, we presented charge distributions obtained for fission fragments appearing in the ternary fission of ^{252}Cf in coincidence with helium, beryllium, and carbon LCPs. Based on the measured charge distributions, we obtained data showing the average proton numbers removed from the light and heavy binary fission fragments by He, Be, and C LCPs and presented a correlation plot showing how the measured LCP yields correlate with the average energy cost for the production of various third particles.

ACKNOWLEDGMENTS

Work at the Joint Institute for Nuclear Research was supported in part by the US Department of Energy contract no. DE-AC011-00NN4125, BBW1 agreement no. 3498 (CRDF grant no. RPO-10301-INEEL) and by a joint RFBR–DFG grant (RFBR no. 02-02-04004, DFG no. 436RUS 113/673/0-1(R)). Work at Vanderbilt University, Lawrence Berkeley National Laboratory, Lawrence Livermore National Laboratory, and Idaho National Engineering and Environmental Laboratory was supported by the US Department of Energy under grant no. DE-FG05-88ER40407 and contract nos. W-7405-ENG48, DE-AC03-76SF00098, and DE-AC07-76ID01570.

REFERENCES

1. E. Cheifets *et al.*, Phys. Rev. C **4**, 1913 (1971).
2. J. H. Hamilton *et al.*, Prog. Part. Nucl. Phys. **35**, 635 (1995).
3. G. M. Ter-Akopian *et al.*, Phys. Rev. C **55**, 1146 (1997).
4. C. Wagemans, in *The Nuclear Fission Process,* Ed. by C. Wagemans (CRS, Boca Raton, 1991), Chap. 12.
5. P. J. Nolan, F. A. Beck, and D. B. Fossan, Annu. Rev. Nucl. Part. Sci. **45**, 561 (1994).
6. R. V. F. Janssens and F. S. Stephens, Nucl. Phys. News **6** (4), 9 (1996).
7. A. Ramayya *et al.*, Phys. Rev. C **57**, 2370 (1998).
8. A. Ramayya *et al.*, Phys. Rev. Lett. **81**, 947 (1998).
9. I. Halpern, Annu. Rev. Nucl. Sci. **21**, 245 (1971).
10. G. V. Val'skii, Yad. Fiz. **24**, 270 (1976) [Sov. J. Nucl. Phys. **24**, 140 (1976)].
11. V. A. Rubchenya and S. G. Yavshits, Z. Phys. A **329**, 217 (1988).
12. G. A. Pik-Pichak, Yad. Fiz. **57**, 966 (1994) [Phys. At. Nucl. **57**, 906 (1994)].
13. M. Mutterer and J. P. Theobald, *Nuclear Decay Modes,* Ed. by D. Poenaru (IOP, Bristol, 1996), Chap. 12.
14. Yu. N. Kopach *et al.*, Phys. Rev. C **65**, 044614 (2002).
15. P. Singer *et al.*, in *Proceedings of the 3rd International Conference DANF'96, Casta Papernicka, Slovakia, 1995*, Ed. by J. Kliman and B. Pustylnik (JINR, Dubna, 1996), p. 262.
16. M. Mutterer *et al.*, in *Proceedings of the International Conference on Fission and Properties of Neutron-Rich Nuclei,* Ed. by J. H. Hamilton and A. V. Ramayya (World Sci., Singapore, 1998), p. 119.
17. J. H. Hamilton *et al.*, Acta Phys. Slovaca **49**, 31 (1999).
18. W. Greiner, Acta Phys. Slovaca **49**, 9 (1999).
19. G. M. Ter-Akopian *et al.*, in *Proceedings of the International Conference on Fission and Properties of Neutron-Rich Nuclei, Sanibel Island, Florida, 2002*, Ed. by J. H. Hamilton, A. V. Ramayya, and H. K. Carter (World Sci., Singapore, 2003), p. 535.
20. M. Mutterer *et al.*, in *Proceedings of the 3rd International Conference DANF'96, Casta Papernicka, Slovakia, 1995*, Ed. by J. Kliman and B. Pustylnik (JINR, Dubna, 1996), p. 250.

Physics of Atomic Nuclei, Vol. 67, No. 10, 2004, pp. 1866–1872. From Yadernaya Fizika, Vol. 67, No. 10, 2004, pp. 1891–1897.

Proceedings of the International Conference "Nuclear Structure and Related Topics"

Nature of the Pygmy Resonance in Continuous γ Spectra*

A. V. Voinov[1)], A. Schiller[2)], E. Algin[2),3),4),5)], L. A. Bernstein[2)], P. E. Garrett[2)], M. Guttormsen[6)], R. O. Nelson[7)], J. Rekstad[6)], and S. Siem[6)]**

Received January 21, 2004

Abstract—Two-step-cascade spectra of the ^{171}Yb$(n,\gamma\gamma)^{172}$Yb reaction have been measured using thermal neutrons. They are compared to calculations based on experimental values of the level density and radiative strength function obtained from the ^{173}Yb(^{3}He, $\alpha\gamma)^{172}$Yb reaction. The multipolarity of a 6.5(15) μ_N^2 resonance at 3.3(1) MeV in the strength function is determined to be $M1$ by this comparison.

Excited nuclei decay often by a cascade of γ rays. While the decay between discrete states is determined by the details of the nuclear wave functions, unresolved transitions are best described by statistical concepts like a continuous radiative strength function (RSF) and level density. The RSF (reviewed in [1]) provides the mean value of the decay probability for a given γ-ray energy E_γ. For hard γ rays (~ 7–20 MeV), the RSF is governed by the giant electric dipole resonance whose parameters are determined from photoabsorption [2]. The soft tail of the RSF has been investigated by a variety of methods, most notably by primary γ rays [3]. Recently, systematic studies of the soft RSF have been performed at the Oslo Cyclotron Laboratory using a method based on sequential extraction. With this method, it is possible to obtain both the level density and RSF by a deconvolution of a set of primary γ spectra from a range of excitation energies [4]. Total RSFs (summed over all multipolarities) of rare-earth nuclei can be extracted for $B_n > E_\gamma > 1$ MeV [5]. Their common, most striking feature is a resonance at $E_\gamma \sim 3$ MeV, which is believed to be of dipole multipolarity but whose electromagnetic character is unknown. It has been shown for all investigated rare-earth nuclei that the total RSF is most readily decomposed into a sum of the Kadmenskiĭ–Markushev–Furman (KMF) $E1$ model [6], a spin-flip $M1$ model [7], and the aforementioned soft dipole resonance [5]. The knowledge of the character of this resonance is essential for its theoretical interpretation. Experimentally, it can be determined from an auxiliary two-step-cascade (TSC) measurement [8].

The TSC method is based on the observation of decays from an initial state i to a final state f via an intermediate level m [9–11]. A convenient initial state is that formed in thermal or average resonance capture (ARC); the final state can be any low-lying discrete state. TSC spectra are determined by the branching ratios of the initial and intermediate states (expressed as ratios of partial to total widths Γ) and by the level density ρ of intermediate states with spin and parity J_m^π:

$$I_{if}(E_1,E_2) = \sum_{XL,XL',J_m^\pi} \frac{\Gamma_{im}^{XL}(E_1)}{\Gamma_i}\rho(E_m,J_m^\pi)\frac{\Gamma_{mf}^{XL'}(E_2)}{\Gamma_m} + \sum_{XL,XL',J_{m'}^\pi} \frac{\Gamma_{im'}^{XL}(E_2)}{\Gamma_i}\rho(E_{m'},J_{m'}^\pi)\frac{\Gamma_{m'f}^{XL'}(E_1)}{\Gamma_{m'}}. \quad (1)$$

The sums in Eq. (1) are restricted to give valid combinations of the level spins and parities and the transition multipolarities XL. They arise since one determines neither the ordering of the two γ rays, nor the multipolarities of the transitions, nor the spins and parities of the intermediate levels; hence, one has to include all possibilities. The two transition energies are correlated by $E_1 + E_2 = E_i - E_f$; thus, TSC spectra can be expressed as spectra of one transition energy E_γ only. TSC spectra are symmetric around $E_\gamma^{\rm sym} = (E_i - E_f)/2$; integration over E_γ yields twice the total TSC intensity I_{if} (if both γ rays are counted

*This article was submitted by the authors in English.

[1)]Frank Laboratory of Neutron Physics, Joint Institute for Nuclear Research, Dubna, Moscow oblast, 141980 Russia.
[2)]Lawrence Livermore National Laboratory, Livermore, USA.
[3)]North Carolina State University, Raleigh, USA.
[4)]Triangle Universities Nuclear Laboratory, Durham, USA.
[5)]Department of Physics, Osmangazi University, Meselik, Turkey.
[6)]Department of Physics, University of Oslo, Oslo, Norway.
[7)]Los Alamos National Laboratory, Los Alamos, USA.
**e-mail: voinov@nf.jinr.ru

in the spectrum). The knowledge of the parities π_i[8] and π_f ensures that I_{if} depends, roughly speaking, on the product of two RSFs around $E_\gamma^{\rm sym}$ [8] (i.e., $f_{E1}^2 + f_{M1}^2$ for $\pi_i = \pi_f$ and $2f_{E1}f_{M1}$ for $\pi_i \neq \pi_f$, the latter case being more sensitive to the character of the soft resonance). I_{if} depends also on the level density. This usually prevents one from drawing firm conclusions from TSC experiments alone [11]. A combined analysis of Oslo-type and TSC experiments, however, will enable one to establish the sum and product, respectively, of all contributions to f_{M1} and f_{E1} at energies of the soft resonance, thus determining its character. For this goal, the partial widths of Eq. (1) are expressed via

$$\Gamma_{x\to y}^{XL}(E_\gamma) = f_{XL}(E_\gamma)E_\gamma^{2L+1}D_x \qquad (2)$$

in terms of RSFs and level spacings D_x. Equation (2) actually gives only the average value of the Porter–Thomas distributed partial widths [12]. The total width Γ is the sum of all partial widths. Again, the sum is only the sum of mean values; however, the distribution of total widths with many components is almost δ-like [12]. The level density for a given spin and parity is calculated from the total level density by [13]

$$\rho(E_x, J_x^\pi) = \rho(E_x)\frac{1}{2}\frac{2J_x+1}{2\sigma^2}\exp\left[-\frac{(J_x+1/2)^2}{2\sigma^2}\right], \qquad (3)$$

where σ is the spin cutoff parameter, and we assume equal numbers of positive and negative parity levels. This assumption and Eq. (3) have been verified from the discrete level schemes of rare-earth nuclei. Thus, all quantities for calculating TSC spectra are based on experimental data.

The combined analysis is applied to the nucleus ^{172}Yb, which has been investigated by the ^{173}Yb(^{3}He, $\alpha\gamma$)^{172}Yb reaction in Oslo and by the ^{171}Yb$(n,\gamma\gamma)^{172}$Yb reaction at the Lujan Center of the Los Alamos Neutron Science Center (LANSCE). The Oslo data have been reported in [4, 5]. Thus, only a short summary is given. The experiment was performed using a 45-MeV ^{3}He beam on a metallic, enriched, self-supporting target. Ejectiles were detected and their energies were determined using particle telescopes at 45°. In coincidence with α particles, γ rays were detected in an array of NaI detectors. From the reaction kinematics, α energy is converted into E_x, and γ-cascade spectra are constructed for a range of E_x bins. The γ spectra are unfolded [14] and the primary γ spectra are extracted using a subtraction method [15]. The spectra are deconvoluted into a level density and a total RSF by applying the Brink–Axel hypothesis [16]. The level density is normalized by comparison to discrete levels at low E_x and to the average neutron resonance spacing at B_n [4]. The RSF is normalized using the average total width of neutron resonances and is decomposed into the KMF $E1$ model [6], a spin-flip $M1$ model [7], and a soft dipole resonance [5]. Here, we have improved on the normalization of the level density and the RSF and included an isoscalar Lorentzian $E2$ model [17], giving

$$f_{\rm tot} = K(f_{E1} + f_{M1}) + E_\gamma^2 f_{E2} + f_{\rm soft}, \qquad (4)$$

where K is a scaling factor of the order of one. Since quadrupole transitions populate levels within a broader spin interval than dipole transitions, Eq. (4) is of an approximative nature. Given the weakness of quadrupole transitions and the level of experimental uncertainties, however, this approximation is believed to be sufficient. The improved data, the fit to the total RSF, and its decomposition into different multipolarities are given in Fig. 1. The parameters for the $E1$ RSF are taken from [5], and those for the $M1$ and $E2$ RSFs from [7], where we use the f_{E1}/f_{M1} systematics at ~ 7 MeV, giving values in agreement with ARC work [19]. The fitted parameters are the constant temperature of the KMF model $T = 0.34(3)$ MeV, the normalization coefficient $K = 1.7(1)$, and the three parameters of the soft resonance $E = 3.3(1)$ MeV, $\Gamma = 1.2(3)$ MeV, and $\sigma = 0.49(5)$ mb.[9]

For the ^{171}Yb$(n,\gamma\gamma)^{172}$Yb experiment, we used $\sim$1 g of enriched, dry Yb_2O_3 powder encapsulated in a glass ampule, mounted in an evacuated beam tube and irradiated by collimated neutrons with a time-averaged flux of $\sim 4\times10^4$ neutrons/(cm^2 s) at a distance of $\sim$20 m from the thermal moderator. Gamma rays were detected by two 80% and one shielded and segmented $\sim$ 200% clover Ge(HP) detector, placed $\sim$12 cm from the target in a geometry to minimize angular correlation effects and contributions from higher multiplicity cascades. Single and coincident γ rays were recorded simultaneously, including n time-of-flight and $\gamma-\gamma$ coincidence time. The experiment ran for $\sim$150 h, yielding $\sim 10^7$ coincidences. The relative detector efficiencies from 1–9 MeV were determined by two separate runs of $\sim$12 h each, before and after the ^{171}Yb$(n,\gamma\gamma)^{172}$Yb experiment, using the ^{35}Cl$(n,\gamma)^{36}$Cl reaction and its known γ intensities [20]. Also, a standard calibrated ^{60}Co source has been measured to adjust the relative curves to an absolute scale. The energy-summed coincidence spectrum (Fig. 2, upper panel) shows distinct peaks

[8] One assumes that only neutron s capture occurs.

[9] The cited parameters are mean values obtained from the ^{173}Yb(^{3}He, $\alpha\gamma$)^{172}Yb and ^{172}Yb(^{3}He, ^{3}He$'\gamma$)^{172}Yb reaction data.

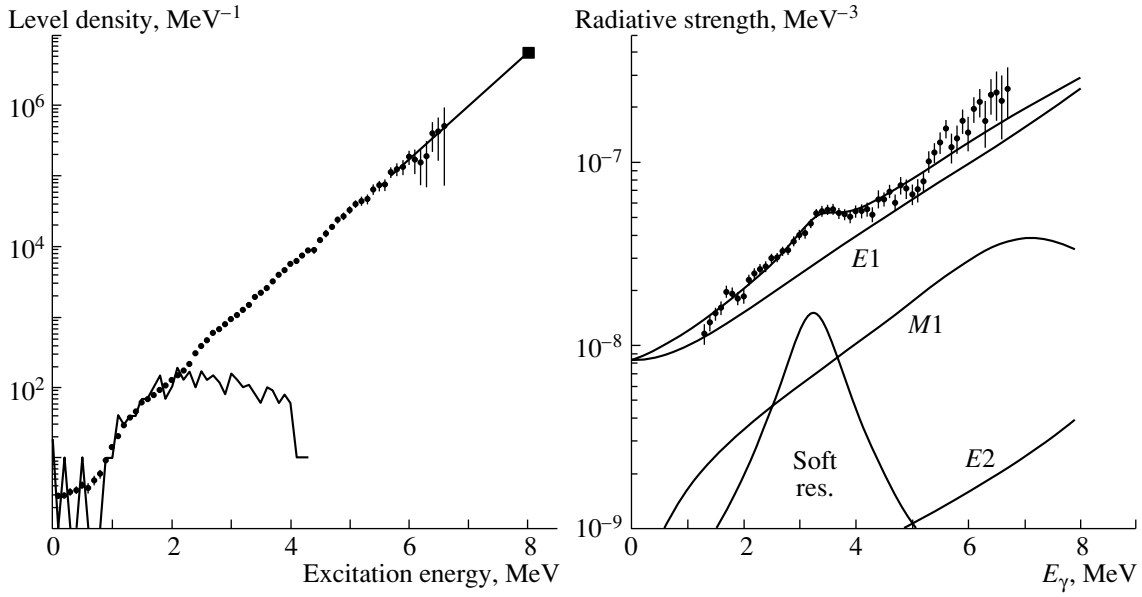

Fig. 1. (Left) Total level density (circles), constant-temperature extrapolation (solid line), level density at B_n derived from the average neutron resonance spacing (square) [7], and level density from counting of discrete levels (jagged line) [18]. (Right) Total RSF (circles), fitted to the data, and decomposition into RSFs of different multipolarities (solid curves). The inclusion of the soft resonance in the fit decreases $\chi^2_{\rm red}$ from $\sim$7.4 to $\sim$1.3. Since this value is close to unity, inclusion of additional nonstatistical structures cannot significantly improve the fit.

corresponding to TSCs between B_n and several low-lying states. The two strongest peaks have $\sim$4000 counts each. TSC spectra (lower panels) were obtained by gating on three peaks, using the background subtraction method of [21], thereby avoiding spurious structures. Relative intensities of primary versus secondary γ rays were determined from the singles spectra and are in agreement with [19]. Absolute intensities were determined by using new data on absolute secondary γ-ray intensities [22] and scaling primary intensities to these values using the relative intensities of [19]. These absolute intensities are $\sim$20% higher than in [19]. TSC intensities are normalized (i) to absolute primary intensities and secondary branching ratios of individual TSCs and (ii) by effectively estimating the number of neutron captures during the experiment from singles spectra, absolute (secondary) intensities, and absolute detector efficiencies. Both methods give equal results to within 10%.

TSC spectra are compared to calculations according to Eq. (1) assuming either electric or magnetic character for the soft resonance [8]. Due to the large Porter–Thomas fluctuations of TSC intensities, TSC spectra are compressed to 300-keV energy bins and only a 2.5-MeV broad energy interval in the middle of the spectra is taken into account [11] for the comparison. Corrections due to nonisotropic angular correlations of TSCs have been applied. They can be up to $\sim$ 20%, depending on the initial and final spins and parities involved in the respective TSCs. The contributions to the thermal radiative neutron capture cross section $\sigma^{\rm th}_{(n,\gamma)}$ from the two possible spins (0^- and 1^-) involved in neutron s capture on ^{171}Yb are uncertain. The compilation [23] assumes 0^- for the subthreshold resonances, which contribute 88% to $\sigma^{\rm th}_{(n,\gamma)}$. Another 4% comes from 0^- resonances above threshold, giving in total a 92% contribution of 0^- states. On the other hand, there is no strong evidence that all contributing subthreshold resonances have 0^-. Examination of hard primary γ rays [19, 24] reveals many strong transitions populating 2^+ levels, indicating that a sizeable portion of $\sigma^{\rm th}_{(n,\gamma)}$ stems from 1^- resonances. Therefore, we performed calculations for a set of ratios $R = \sigma^{\rm th}_{(n,\gamma)}(0^-)/\sigma^{\rm th}_{(n,\gamma)}$. These calculations show, however, that only the TSC intensity to the 0^+_1 state has a strong dependence on this ratio. Total experimental and calculated TSC intensities are shown in the left panels of Fig. 3. The calculations assuming $E1$ for the soft resonance do not reproduce the experimental intensities for any value of R. Good agreement is achieved assuming $M1$, with the additional condition of $R \sim 0.5$ for the 0^+_1 final state. However, it has to be emphasized that the conclusion of an $M1$ multipolarity for the soft resonance can be established from the TSC intensities to the 2^+_1 state and the 1^-_1 state independently, irrespective of

the value of R. Possible systematic uncertainties in the absolute normalization cannot change this conclusion, since, in the case of the final states 0_1^+ and 2_1^+, one would need a decrease while, at the same time, for the 1_1^- final state one would need an increase in the experimental TSC intensities in order to accommodate the $E1$ hypothesis. The combined $\chi^2_{\rm red}$ for all three TSC intensities as function of R is also given. The $M1$ hypothesis yields the global minimum for $R = 0.5 \pm 0.2$ with $\chi^2_{\rm red} < 1$, whereas the minimal $\chi^2_{\rm red}$ for the $E1$ hypothesis is ~ 6 for $R = 1$. Finally, we show the TSC spectra to two final states compared to calculations using the $M1$ hypothesis at $R = 0.5$ and the $E1$ hypothesis at $R = 1$. No further conclusions have been drawn from this comparison, however.

The integrated strength of the soft resonance is expressed as

$$B^{\uparrow}(M1) = \frac{9\hbar c}{32\pi^2}\left(\frac{\sigma\Gamma}{E}\right)_{\rm soft}, \qquad (5)$$

giving a value of 6.5(15) μ_N^2, which is entirely determined from the Oslo-type experiment after $M1$ multipolarity has been established. This is in agreement with the sum-rule approach for soft, orbital $M1$ strength [25] but is more than twice the strength from nuclear resonance fluorescence (NRF) [26]. However, in [11, 27], several limitations in determining $B^{\uparrow}(M1)$ using NRF are discussed, all resulting in possible underestimation. Concerns are that (i) too few 1^+ levels are observed in NRF experiments compared to level density estimates (eight candidates for 1^+ levels have been observed in the NRF experiment within the 2–4 MeV energy interval, whereas ~ 120 such levels are expected from experimental level densities); (ii) the assumption in NRF experiments is not fulfilled that the total radiative width is given by the sum of the partial radiative widths for transitions to the ground state and the first excited state only; and (iii) the energy-region coverage is insufficient. Hence, in NRF experiments, weak unobserved excitations from the ground state, weak unobserved decays to excited levels above the ground-state rotational band, and excitations outside the investigated energy range might all contribute to an increased summed $B^{\uparrow}(M1)$ value in better agreement with the present value [27]. Also in [11] $B^{\uparrow}(M1) \sim 7\mu_N^2$ is required in order to reproduce TSC spectra in ^{163}Dy.

In order to investigate the above-mentioned concerns and to better compare the present result with the NRF observations, we have performed a simulation of the ^{172}Yb(γ,γ') experiment on the basis of the statistical model. The main assumption of this approach is that the mean value of partial radiative widths does not depend on concrete initial and final nuclear levels, but that it is determined by global nuclear characteristics such as the RSF and the level density. Each individual radiative width is, according to the statistical model, randomly distributed around this mean value and the probability for having any specific value is given by the Porter–Thomas distribution. The main observable in NRF experiments is the energy-integrated cross section I_{0+1} of resonantly scattered γ rays populating an intermediate state at excitation energy E and then decaying

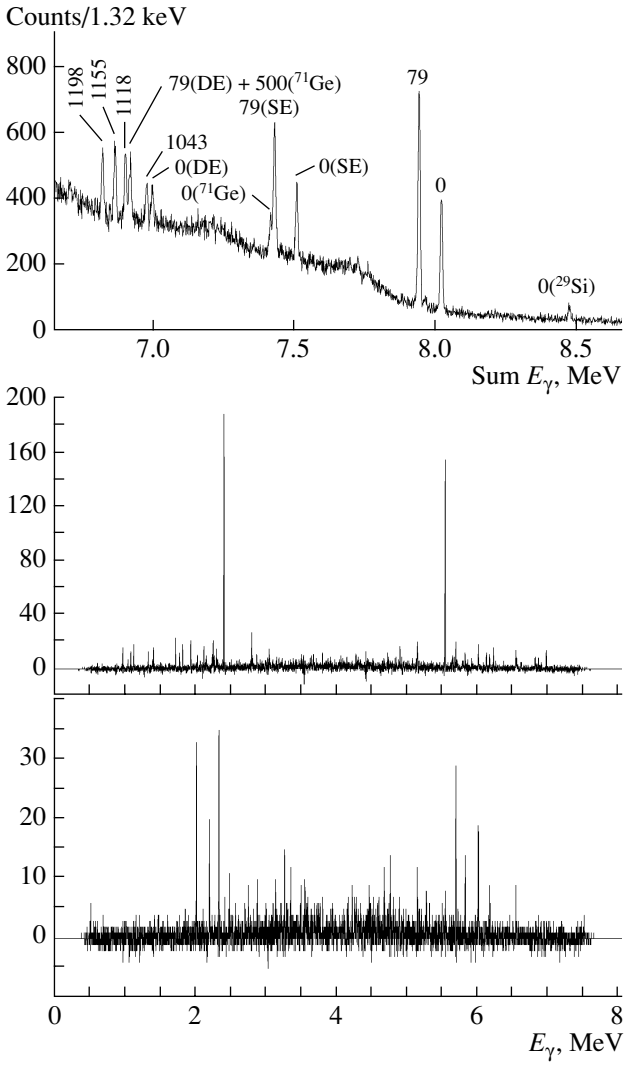

Fig. 2. (Upper panel) Energy-summed coincidence spectrum from the ^{171}Yb$(n,\gamma\gamma)^{172}$Yb reaction. The peaks are labeled by energy (in keV) of the final state. Those denoted by ^{71}Ge and ^{29}Si are due to n capture in the detector and in the glass ampule, respectively. "SE" and "DE" stands for single and double escape peaks, respectively. TSC spectra to the 2_1^+ state at 79 keV (middle panel) and the 0_1^+ state at 0 keV (lower panel). The slight asymmetry is due to the energy-dependent resolution of the detectors.

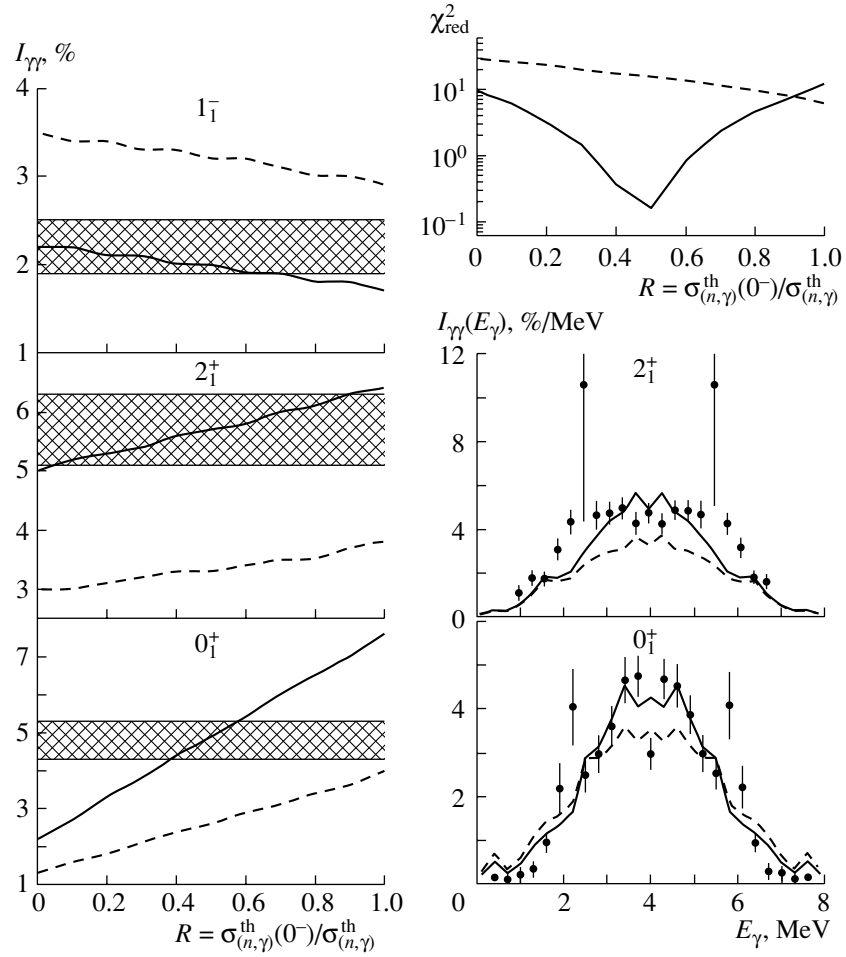

Fig. 3. (Left) Experimental values (hatched areas) for TSC intensities to final states 1_1^- at 1155 keV, 2_1^+, and 0_1^+ compared to calculations as a function of R. Solid and dashed curves correspond to the $M1$ and $E1$ hypotheses for the soft resonance. (Right) Combined $\chi^2_{\rm red}$ for all three TSC intensities as a function of R for the $M1$ and $E1$ hypotheses (upper panel). Experimental (circles) and calculated TSC spectra to the 2_1^+ state (middle panel) and 0_1^+ state (lower panel) for the $M1$ hypothesis (solid lines) at $R = 0.5$ and the $E1$ hypothesis (dashed lines) at $R = 1$. On the edges of the experimental spectra, the influence of Porter–Thomas fluctuations becomes visible.

down to either the ground state or the first excited state. This partial, energy-integrated, photoabsorption cross section is given by

$$I_{0+1} = \frac{3\pi^2\hbar^2c^2}{E^2}\frac{\Gamma_0\,(\Gamma_0+\Gamma_1)}{\Gamma}. \qquad (6)$$

Here, Γ_0 and Γ_1 are the partial decay widths to the ground state and first excited state, respectively, and Γ is the total radiative width of the intermediate state with energy E. Similar partial cross sections to higher lying final states f can be calculated by replacing $\Gamma_0 + \Gamma_1$ with the appropriate Γ_f.

The information from the ^{172}Yb(γ,γ') experiment consists of the energies E and the partial, energy-integrated, photon-absorption cross sections I_{0+1} of eight candidates for 1^+ states and of thirteen 1^- states [26]. Under the assumption that $\Gamma = \Gamma_0 + \Gamma_1$ and that all candidates for 1^+ states are, in fact, 1^+ states, the authors of [26] have deduced a summed $B^\uparrow(M1)$ value for all eight candidate states of $2.4(10)\mu_N^2$.

Since, within the statistical model, the mean values of radiative widths can be expressed in terms of level densities and RSFs according to Eq. (2), we can use experimental values of these quantities from Oslo-type experiments to simulate a random set of NRF observable using Eq. (6). In order to properly take into account the detection threshold in NRF experiments, partial radiative widths for all possible γ transitions connecting intermediate 1^+ states with final states by dipole or quadrupole radiation have been simulated as random, Porter–Thomas distributed values with mean values determined by Eq. (2). Each set of simulated radiative widths has

been used to calculate the partial, energy-integrated, photon-absorption cross sections I_{0+1} for 1^+ states. The energy dependence of the detection threshold has been introduced according to [28]. Here, we would like to point out that the estimated energy dependence of the detection threshold in NRF experiments is only valid for the cases where the scattered γ ray has roughly the same energy as the incoming γ ray. Due to the $\sim 1/E_\gamma$ shape of the bremsstrahlung spectrum typically used in NRF investigations and the presence of nonresonantly scattered γ rays, the experimental γ background for low-energy decays to excited states above the ground-state rotational band can be substantially higher. It is thus difficult to adjust the absolute scale of the detection threshold for different experiments due to a lack of information. Therefore, we have scaled the detection threshold in the simulation such that we observe, on average, eight levels above threshold in the energy range of 2–4 MeV. We have performed a total of 100 simulations from which summed mean values of partial, energy-integrated, photon-absorption cross sections I_{0+1} are obtained.

Without taking into account the detection threshold, the simulation yields a mean value of integrated cross section for the sum of all 1^+ excitations in the energy region 2–4 MeV of ~ 0.8 MeV mb. If one takes into account only the eight levels above threshold, this value reduces to 0.30(9) MeV mb. This value can be translated into $B^\uparrow(M1) = 2.6(8)\ \mu_N^2$, which is in good agreement with the reported value of $B^\uparrow(M1) = 2.4(10)\mu_N^2$ from NRF experiments. The remaining $M1$ strength is hidden in the background according to our simulation. Calculations also show that the assumption made in NRF experiments $\Gamma_0 + \Gamma_1 = \Gamma$ is only fulfilled for states with large values of I_{0+1} (i.e., transitions above threshold). This is in good agreement with [29], where the lifetimes of the most strongly populated 1^+ states in ^{162,164}Dy have been measured independently by inelastic neutron scattering. It turns out that there exists a strong positive correlation between I_{0+1} and $(\Gamma_0 + \Gamma_1)/\Gamma$, indicating that decay branches to higher lying states become more important the weaker the state is populated to begin with. This result of the simulation could probably be tested experimentally at the quasi-monoenergetic, 100% polarized High Intensity Gamma Source (HIGS) at the Duke University Free Electron Laser Laboratory and Triangle Universities Nuclear Laboratory.

In conclusion, the soft resonance found in the RSF of ^{172}Yb in Oslo-type experiments has been determined to be of $M1$ multipolarity by an auxiliary TSC measurement. The strength of the $M1$ resonance is $B^\uparrow(M1) = 6.5(15)\mu_N^2$, which is entirely determined by the former experiment. This value agrees with a sum-rule approach for orbital strength, but is more than twice the value reported by NRF experiments. However, this difference has been explained tentatively on the basis of the statistical model. Our simulation hints that a possible source for underestimation of $B^\uparrow(M1)$ strength in NRF experiments can arise from weakly excited states and weak decays to excited states above the ground-state rotational band. Those weak transitions might be missed in NRF experiments due to the presence of an experimental detection threshold. Additional experimental data to resolve this question are highly desirable. Assuming $M1$ multipolarity for similar soft resonances in other rare-earth nuclei gives consistent strengths of $\sim 6\mu_N^2$ for various even and odd Dy, Er, and Yb nuclei and quenched strengths of $\sim 3\mu_N^2$ for the more spherical Sm nuclei [30]. The centroids of the resonances increase weakly with mass number.

ACKNOWLEDGMENTS

This work has benefited from the use of the Los Alamos Neutron Science Center at the Los Alamos National Laboratory. This facility is funded by the US Department of Energy under contract W-7405-ENG-36. Part of this work was performed under the auspices of the US Department of Energy by the University of California, Lawrence Livermore National Laboratory under contract W-7405-ENG-48, and Los Alamos National Laboratory under contract W-7405-ENG-36. Financial support from the Norwegian Research Council (NFR) is gratefully acknowledged. A.V. acknowledges support from a NATO Science Fellowship under project no. 150027/432. E.A. acknowledges support by US Department of Energy grant no. DE-FG02-97-ER41042.

We would like to thank Gail F. Eaton for making the targets.

REFERENCES

1. G. A. Bartholomew *et al.*, Adv. Nucl. Phys. **7**, 229 (1973).
2. Samuel S. Dietrich and Barry B. Berman, At. Data Nucl. Data Tables **38**, 199 (1988).
3. J. Kopecky and M. Uhl, in *Proceedings of a Specialists' Meeting on Measurement, Calculation and Evaluation of Photon Production Data, Bologna, Italy, 1994*, Rep. No. NEA/NSC/DOC(95)1, p. 119.
4. A. Schiller *et al.*, Nucl. Instrum. Methods Phys. Res. A **447**, 498 (2000).
5. A. Voinov *et al.*, Phys. Rev. C **63**, 044313 (2001).
6. S. G. Kadmenskiĭ, V. P. Markushev, and V. I. Furman, Yad. Fiz. **37**, 277 (1983) [Sov. J. Nucl. Phys. **37**, 165 (1983)].

7. *Handbook for Calculations of Nuclear Reaction Data* (IAEA, Vienna, 1998).
8. A. Voinov *et al.*, Nucl. Instrum. Methods Phys. Res. A **497**, 350 (2003).
9. A. M. Hoogenboom, Nucl. Instrum. Methods Phys. Res. **3**, 57 (1958).
10. S. T. Boneva *et al.*, Fiz. Élem. Chastits At. Yadra **22**, 497 (1991) [Sov. J. Part. Nucl. **22**, 232 (1991)].
11. F. Bečvář *et al.*, Phys. Rev. C **52**, 1278 (1995).
12. C. E. Porter and R. G. Thomas, Phys. Rev. **104**, 483 (1956).
13. A. Gilbert and A. G. W. Cameron, Can. J. Phys. **43**, 1446 (1965).
14. M. Guttormsen *et al.*, Nucl. Instrum. Methods Phys. Res. A **374**, 371 (1996).
15. M. Guttormsen, T. Ramsøy, and J. Rekstad, Nucl. Instrum. Methods Phys. Res. A **255**, 518 (1987).
16. D. M. Brink, PhD Thesis (Oxford University, 1955); P. Axel, Phys. Rev. **126**, 671 (1962).
17. W. V. Prestwich, M. A. Islam, and T. J. Kennett, Z. Phys. A **315**, 103 (1984).
18. R. Firestone and V. S. Shirley, *Table of Isotopes,* 8th ed. (Wiley, New York, 1996).
19. R. C. Greenwood, C. W. Reich, and S. H. Vegors, Jr., Nucl. Phys. A **252**, 260 (1975).
20. C. Coceva, A. Brusegan, and C. van der Vorst, Nucl. Instrum. Methods Phys. Res. A **378**, 511 (1996).
21. E. V. Vasilieva *et al.*, Bull. Russ. Acad. Sci., Phys. Ser. **57**, 1549 (1993).
22. R. Firestone, private communication.
23. S. F. Mughabghab, *Neutron Cross Sections* (Academic Press, New York, 1984), Vol. I, Part B.
24. W. Gelletly *et al.*, J. Phys. G **11**, 1055 (1985).
25. E. Lipparini and S. Stringari, Phys. Rep. **175**, 103 (1989).
26. A. Zilges *et al.*, Nucl. Phys. A **507**, 399 (1990); **519**, 848 (1990).
27. A. Schiller *et al.*, nucl-ex/0011018.
28. A. Nord *et al.*, Phys. Rev. C **54**, 2287 (1996).
29. E. L. Johnson *et al.*, Phys. Rev. C **52**, 2382 (1995).
30. S. Siem *et al.*, Phys. Rev. C **65**, 044318 (2002).

Physics of Atomic Nuclei, Vol. 67, No. 10, 2004, pp. 1873–1875. From Yadernaya Fizika, Vol. 67, No. 10, 2004, pp. 1898–1900.

Proceedings of the International Conference "Nuclear Structure and Related Topics"

Time Characteristics and Odd–Even Effects in Nucleus Deexcitation Process*

O. V. Fotina**, **V. A. Drozdov, D. O. Eremenko, S. Yu. Platonov, and O. A. Yuminov**

Institute of Nuclear Physics, Moscow State University, Moscow, Russia

Received January 21, 2004

Abstract—An approach based on the statistical theory of nuclear reactions and Monte Carlo method is used for evaluations of excited nuclear system characteristics like probability of decay channel (light particle, γ-quanta emission, or fission), energy, emission angle of decay products, and time characteristics of deexcitation processes. This method permits the direct simulation of the experimental situation, in particular, nuclear-lifetime measurements by the crystal blocking technique. Decay times of compound nuclei formed in the fusion reactions $^{12}\mathrm{C} + ^{28}\mathrm{Si} \rightarrow {}^{40}\mathrm{Ca}$ and $^{19}\mathrm{F} + ^{28}\mathrm{Si} \rightarrow {}^{47}\mathrm{V}$ are estimated.

The present work is devoted to the modification of the statistical approach to describe both the traditional observables of nuclear reactions (cross sections, energy spectra, etc.) and the kinematic characteristics. The necessity of modification of the standard method is mainly motivated by the widening area of experimental information concerning nuclear reactions at high excitation energies of compound nuclei. As the experimental data show [1], the same residual nucleus can be formed as a result of various chains of particle evaporations (n, p, α, and γ) with generation of different daughter nucleus sets. In the case of fission, the situation becomes more complicated because of particle evaporation from deformed nuclear states.

This work is based on the statistical theory of nuclear reactions and Monte Carlo method, which is used to simulate a number of characteristics of excited nuclear system like the decay channel (light particle, γ emission, or fission), energy, momentum, and emission angle of the decay products. This provides an optimal consideration of the stochastic nature of nuclear deexcitation processes. The approach was realized in various computer programs and in the code PACE [2], in particular. Here, the approach is adapted for the analysis of nuclear reaction lifetimes. Universality of the approach allows the analysis of the experimental data on the energy spectra of secondary particles and γ quanta as well as the time characteristics of the reactions for excitation energies up to hundreds of MeV (for example, a fission lifetime). In addition, the Monte Carlo method for selection of decay characteristics permits the direct simulation of experimental situation, in particular, time measurements by the crystal blocking technique. This method determines really measured mean characteristics of nuclear reactions taking into account the experimental conditions.

Here, we present only a brief description of the method (for details, see [3, 4]). In the framework of this model, an evaporation particle chain is randomly selected. The standard equation for the mean lifetime of each intermediate nucleus, denoted by k, with energy E and momentum J is used:

$$\tau_k(E, J) = \hbar/\Gamma_k(E, J), \tag{1}$$

where $\Gamma_k(E, J)$ is the total decay width. It can be shown that the full production time T_i of the final reaction product for the given decay chain, denoted by i, is determined as a sum of the mean lifetimes:

$$T_i = \sum_k \tau_k(E, J). \tag{2}$$

Thus, the lifetime T_i of "decay event" i is introduced. A decay event is characterized by the type (n, p, or α), energy, momentum, and emission angle of evaporated particles and kind of finishing process (evaporation residue or fission). The obtained set of decay events can be analyzed and averaged taking into account the given experimental situation.

In earlier approaches (see [5–7]), an intermediate nucleus lifetime $\langle\tau_k\rangle$ was determined as a value averaged by ensemble $(E, J)_k$. This averaging was realized for $\tau_k(E, J)$ weighted by the evaporation probability of the given decay channel k. Such a method of averaging assumes that the mean lifetime $\tau_k(E, J)$ at each evaporation step is substantially smaller than

*This article was submitted by the authors in English.

**e-mail: fotina@p8-inr.sinp.msu.ru

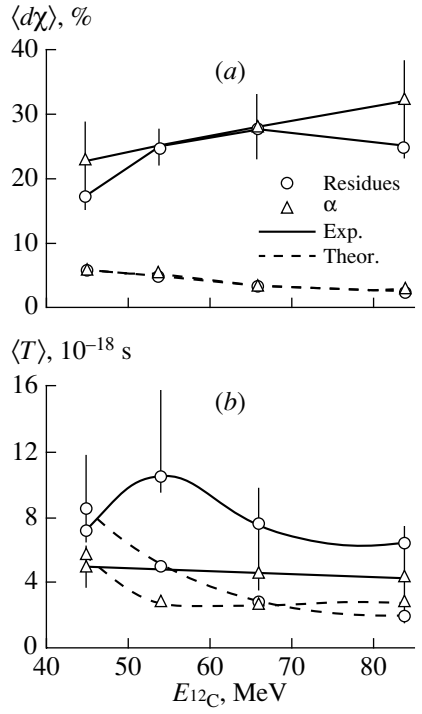

Fig. 1. Experimental results and theoretical estimations for (*a*) $\langle d\chi \rangle$ and (*b*) $\langle T \rangle$ of compound nuclei formed in the $^{12}C + ^{28}Si \rightarrow ^{40}Ca$ fusion reaction. These experimental data were obtained using the blocking of both evaporation residues and low-energy α particles [1].

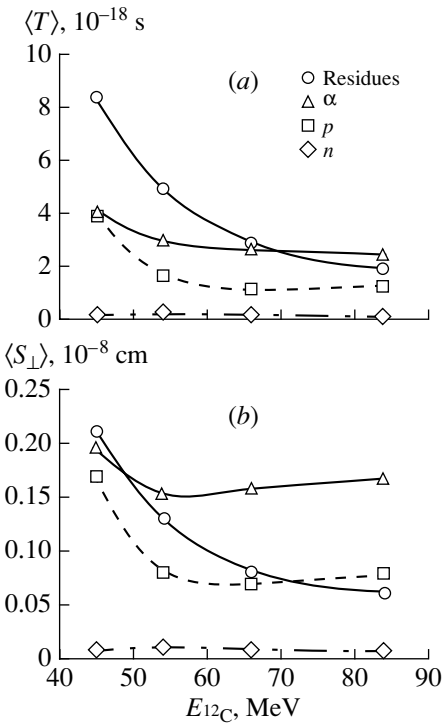

Fig. 2. Time and $\langle S_\perp \rangle$ dependences on the kind of particles registered in the blocking technique.

$\tau_{k+1}(E, J)$ at the next step. The main feature of our model is rejection of this assumption. Moreover, in the developed model, it is easy to obtain relative positions of nuclear residues or relative positions of particle evaporation events (surely taking into consideration the uncertainty relations). This permits us to analyze exotic experimental data, in particular, the nuclear lifetimes measured by the crystal blocking technique. The generality of this model allows us to perform simultaneous analysis of such experimental data as lifetimes, a particle spectrum, and various cross sections in an energy range up to hundreds of MeV.

The method was used in analysis of the time characteristics of a compound nucleus decay in the reactions $^{12}C + ^{28}Si \rightarrow ^{40}Ca$ and $^{19}F + ^{28}Si \rightarrow ^{47}V$. The results of calculations are compared with experimental data [1].

First of all, we obtain good agreement between the experimental and the theoretical lifetime values [see Fig. 1*b* (data for $\langle T \rangle$)]. For the relative yields in the minima of blocking dips, $\langle d\chi \rangle$ (see Fig. 1*a*), measured simultaneously in the experiment [1], such good agreement is not observed. Obviously, it can be explained by using the same rough relation between the nuclear lifetime and the changes in the blocking dips as in [1]. Nevertheless, relative positions of compound nuclei inside of a crystal lattice $\langle S_\perp \rangle$ and kinematic characteristics of evaporated particles were obtained by our model. In the future, it will allow us to perform a complete analysis for a particle transport through the crystal.

In our previous work [3], the time characteristic dependence on registration angle of evaporated particles forming the blocking pattern was demonstrated. This dependence becomes more pronounced with increasing energy. In the present work, the calculations show that the time value (Fig. 2*a*) and the mean position depend on the kind of particles recorded in the blocking technique (Fig. 2*b*).

Last but not least, the most interesting result is presented in Fig. 3. In the framework of our approach, a pronounced difference between production times for even Z and odd Z evaporation residue is detected. This effect is certainly related to the even–odd difference in the nuclear level densities. As one can understand from Eq. (1), the nuclear lifetime is directly proportional to the nuclear level density. Thus, the even–odd difference in the nuclear level density should be directly recorded by measurements of nuclear lifetimes. We hope that this result will be confirmed experimentally. This effect is more pronounced for the even–even compound nucleus ^{40}Ca

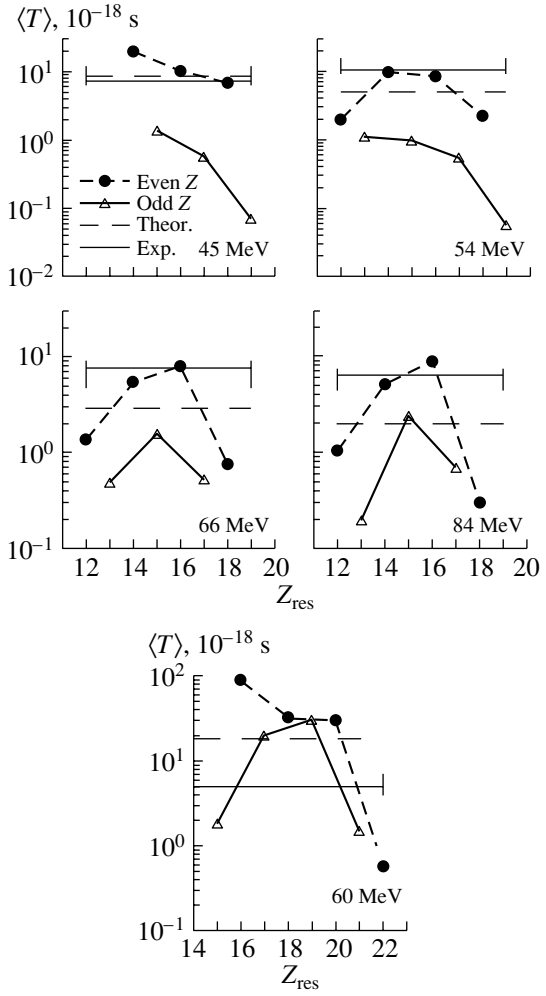

Fig. 3. Even–odd differences in the time characteristics for the reactions $^{12}C + ^{28}Si \rightarrow {}^{40}Ca$ ($E(^{12}C) = 45$, 54, 66, 84 MeV) and $^{19}F + ^{28}Si \rightarrow {}^{47}V$ ($E(^{19}F) =$ 60 MeV). The registration angle of evaporated residues is 20° in the laboratory system.

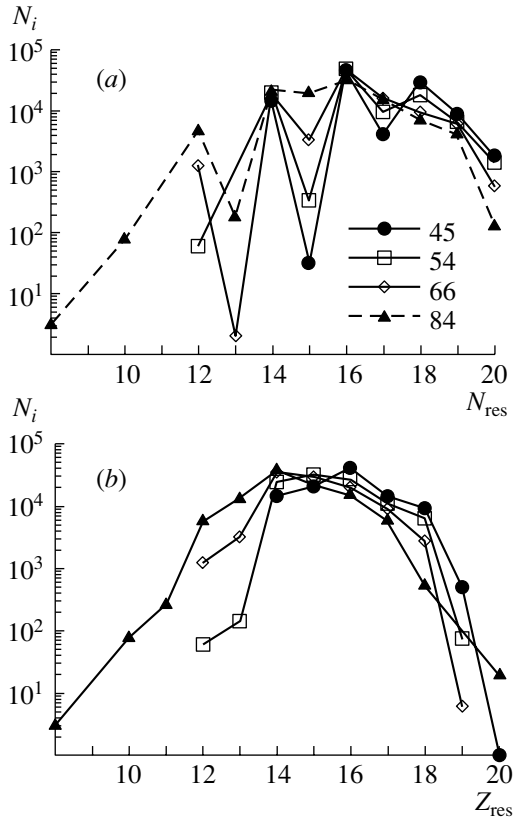

Fig. 4. Yields of evaporation residue N_i with the given N_{res} and Z_{res}.

than for ^{47}V (see Fig. 3). It is seen in Fig. 4 that, for the $^{12}C + {}^{28}Si \rightarrow {}^{40}Ca$ reaction, the evaporation probability for neutrons is substantially smaller than that for protons or α particles. Because to this, the Z-even–N-even and Z-odd–N-even daughter nuclei are more probable for this reaction. In the case of ^{47}V deexcitation, even N in daughter nuclei is more probable, but deexcitation processes start from the Z-odd nucleus. Therefore, in the case of the ^{40}Ca deexcitation, the even–even nuclei have higher excitation energies on average than that for the decay of ^{47}V. Perhaps this difference in the excitation energies is responsible for a decrease in the odd–even effects in the production time of residues.

ACKNOWLEDGMENTS

This work was supported in part by the Russian Foundation for Basic Research (project no. 02-02-17077) and the State Program "Russian Universities" (grant no. UR.02.03.014).

REFERENCES

1. Vandana Nanal *et al.*, Phys. Rev. C **51**, 2439 (1995).
2. R. Michel and P. Nagel, *International Codes and Model Intercomparison for Intermediate Energy Activation Yields* (OECD/NEA, Paris, 1997), MSC/DOC(97)-1, NEA/P&T, No. 14, p. 34.
3. D. O. Eremenko *et al.,* Bull. Russ. Acad. Sci., Phys. Ser. **65**, 667 (2001).
4. D. O. Eremenko *et al.,* Bull. Russ. Acad. Sci., Phys. Ser. **66**, 1471 (2002).
5. D. O. Eremenko *et al.,* Bull. Russ. Acad. Sci., Phys. Ser. **61**, 18 (1997).
6. D. O. Eremenko *et al.,* Phys. At. Nucl. **61**, 695 (1998).
7. Yu. L. Parfenova *et al.,* Bull. Russ. Acad. Sci., Ser. Phys. **63,** 952 (1999).

Physics of Atomic Nuclei, Vol. 67, No. 10, 2004, pp. 1876–1883. From Yadernaya Fizika, Vol. 67, No. 10, 2004, pp. 1901–1907.

Proceedings of the International Conference "Nuclear Structure and Related Topics"

Beta-Decay Strength Measurement, Total Beta-Decay Energy Determination, and Decay-Scheme Completeness Testing by Total Absorption γ-ray Spectroscopy*

I. N. Izosimov[1)], A. A. Kazimov[1)], V. G. Kalinnikov[2)], A. A. Solnyshkin[2)], and J. Suhonen[3)]**

Received January 21, 2004

Abstract—Applications of total absorption γ-ray spectroscopy and its combination with high-resolution nuclear spectroscopy methods for measurements of a β-decay strength function $S_\beta(E)$, determination of the total β-decay energy Q_β, and testing of decay-scheme completeness are presented.

1. INTRODUCTION

Total absorption γ-ray spectroscopy (TAGS) is based on summation of cascade gamma-quantum energies in 4π geometry [1–11]. TAGS may be applied for measurements of a β-decay strength function $S_\beta(E)$, determination of the total β-decay energy Q_β, and testing of decay-scheme completeness. The combination of TAGS with high-resolution γ spectroscopy may be applied in studies of $S_\beta(E)$ fine structure as well as in constructing detailed decay schemes [3, 10, 11].

Total absorption spectrometers (TAS) are used in many laboratories and their constructions are based on large-size NaI(Tl) crystals [1–11]. Comparing the TAGS spectra with the existing data on decay schemes, one may estimate the degree of decay scheme completeness. It was shown that more than 30–50% of β decays to the high-lying nuclear levels (i.e., levels with excitation energies higher than 2–3 MeV) in medium and heavy nuclei may not have been identified in decay schemes [1, 5, 7, 10, 11]. The principles of construction of more complete decay schemes by using the combination of TAGS spectroscopy with high-resolution γ spectroscopy are presented for both neutron-deficit (β^+/EC decay) and neutron-rich nuclei (β^- decay). The possibilities of TAGS applications in testing of completeness of decay schemes of fission products and more complete data using decay-heat calculations [6] are discussed.

2. β^+/EC- AND β^--DECAY STRENGTH FUNCTIONS

For the Gamow–Teller beta transition, the level occupancy $I(E)$ with the excitation energy E of the daughter nucleus after β^+/EC and β^- decay and the half-life $T_{1/2}$ can be written as [1]

$$I(E) = S_\beta(E) T_{1/2} f(Q-E), \tag{1}$$

$$\left(T_{1/2}\right)^{-1} = \int_0^Q S_\beta(E) f(Q-E) dE, \tag{2}$$

where $S_\beta(E)$ describes the nuclear part of the transition; $f(Q-E)$ is the Fermi function, which describes the lepton part of the transition; and Q is the total energy of the β decay. The function $S_\beta(E)$ is proportional to the squared matrix elements of β-decay type between the initial i and final f nuclear states

$$\int_{\Delta E} S_\beta(E) dE = \sum_{\Delta E} 1/(ft) = \left[D(g_V^2/g_A^2)\right]^{-1} \sum_{\Delta E} B(\mathrm{GT}, E), \tag{3}$$

$$B(\mathrm{GT}, E) = \left[D(g_V^2/g_A^2)\right]/(ft) = 4\pi B_\pm(\mathrm{GT}, E)/g_A^2 = \left| \left\langle I_f \middle\| \sum_{k,\mu} t_\pm(k)\sigma_\mu(k) \middle\| I_i \right\rangle \right|^2 \Big/ (2I_i+1). \tag{4}$$

In Eqs. (3), (4), I_i and I_f are nuclear spins, g_A and g_V are the constants of the axial-vector and vector components of the β decay, $D = 6147 \pm 7$ s, and $t_\pm\sigma$ is the product of the isospin and spin operators.

*This article was submitted by the authors in English.

[1)]Khlopin Radium Institute, St. Petersburg, Russia.
[2)]Dzhelepov Laboratory of Nuclear Problems, Joint Institute for Nuclear Research, Dubna, Moscow oblast, 141980 Russia.
[3)]Department of Physics, University of Jyväskylä, Finland.
**e-mail: izosimov@atom.nw.ru

The value $S_\beta(E)$ is in units of $\mathrm{MeV}^{-1}\ \mathrm{s}^{-1}$, whereas $B(\mathrm{GT}, E)$ is in $g_A^2/4\pi$ units and ft is in seconds.

The Fermi function $f(Q-E)$ decreases with increasing E. As a rule, the more intensive beta decays populate the levels with low (lower than 2–3 MeV) excitation energies. But from the nuclear structure point of view, the most interesting beta transitions populate the levels with excitation energies higher than 3–4 MeV, where strong resonances or at least their tails may be observed in $S_\beta(E)$. Also, a lot of nuclear levels and γ transitions may not be identified in decay schemes because of relatively weak beta transitions to the levels with high excitation energies. To study beta transitions to the high-lying levels, total absorption γ spectroscopy may be used [1–11]. The combination of TAGS with high-resolution γ spectroscopy can be applied to study a fine structure $S_\beta(E)$ as well as a detailed decay-scheme construction [3, 4, 10]. To this end, it is necessary to have Z-separated (element separation) and M-separated (mass separation) sources. For nuclei with $T_{1/2} > 30$ min, we applied radiochemistry methods of element separation and after them a mass separator for production of isobaric pure sources [5, 11].

In our experiments, a total absorption γ-ray spectrometer (Fig. 1) is used, which consists of two NaI(Tl) crystals with the sizes 200×110 mm and 200×140 mm. The larger crystal has a 70×80 mm well, into which nuclei under investigation are supplied and where a Si(Au) detector is installed for β-particle detection [5]. Isolating total absorption peaks in the TAS spectrum, one can find the occupancy of levels $I(E)$ and then using (1)–(4) find the strength function $S_\beta(E)$ [1, 5]. The end-point energy of the TAS spectrum is related to the total β-decay energy Q_β [1–4]. The TAS spectrum and $S_\beta(E)$ can be calculated from decay-scheme data. For decay-scheme construction, high-resolution nuclear spectroscopy methods are used [11]. Comparing the TAGS spectroscopy data (TAS spectrum and $S_\beta(E)$) with the data obtained from decay schemes, one may estimate the degree of decay-scheme completeness and determine the energy regions where a decay scheme is not sufficiently complete [1, 3, 7, 10].

Beta-decay strength functions $S_\beta(E)$ for β^+/EC and β^- decays are schematically shown in Fig. 2. The strength functions of β^+/EC and β^- Gamow–Teller decays are qualitatively different [1]. According to the Ikeda sum rule [12], the total sums S_+ and S_- are related to each other as

$$S_- - S_+ \approx 3(N-Z),$$

where $S_\pm = \sum_i B_\pm(\mathrm{GT}, E_i)$. The total sum of β^- transitions in $N > Z$ nuclei is larger than that for

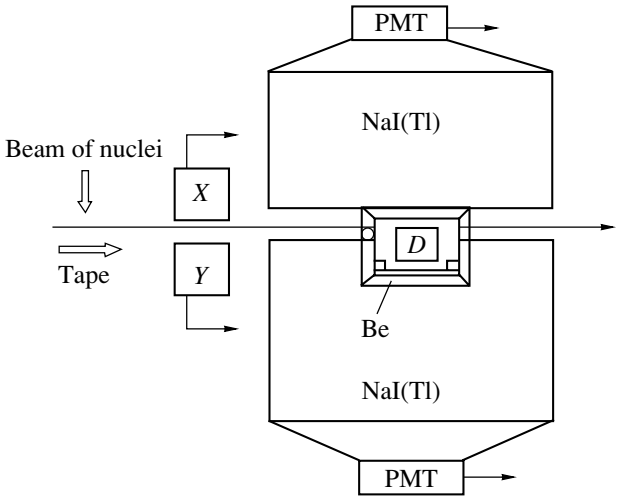

Fig. 1. Total absorption γ-ray spectrometer: D—β-particle detector, X—X-ray detector, Y—γ-ray detector.

β^+/EC transitions. However, a large part of the total strength of β^- transitions is concentrated in the Gamow–Teller resonance with $\mu_\tau = -1$ (i.e., in the state which is a coherent superposition of simple excitations with isospin projection $\mu_\tau = -1$, e.g., proton-particle–neutron-hole ones) and is out of the Q_β energy window, where the observed strengths of β^+/EC decay and β^- decay may be comparable. The Gamow–Teller resonance with $\mu_\tau = -1$ is in principle unattainable in β^- decay of $N > Z$ nuclei, whereas the Gamow–Teller resonance with $\mu_\tau = +1$ or its tail may be observed in β^+/EC decay of $N > Z$ nuclei. In β^- decay of $N > Z$ nuclei, so-called satellites of the Gamow–Teller resonance (back spin-flip and/or core polarization states) may be observed (Fig. 2).

3. β^+/EC DECAY

Using our TAGS spectrometer, we detected [3, 5, 10] the Gamow–Teller resonance with $\mu_\tau = +1$ (Fig. 3) in ^{147g}Tb ($T_{1/2} \approx 1.6$ h) as a strong peak at $E \approx 4$ MeV. The β^+/EC transitions to levels with excitation energies higher than 2 MeV were not identified in the decay scheme (Fig. 4) from [13]. This means that the decay scheme of ^{147g}Tb ($T_{1/2} \approx 1.6$ h) in [13] is very incomplete. The more complete decay scheme of ^{147g}Tb ($T_{1/2} \approx 1.6$ h) was constructed in [11] (Fig. 5). The most interesting region for study of the beta-strength function is at an excitation energy higher than 3–4 MeV. The β^+/EC-decay strength function (Fig. 6) deduced from the more complete decay scheme was constructed in [3, 10]. The strength functions (Figs. 3 and 6) are in good

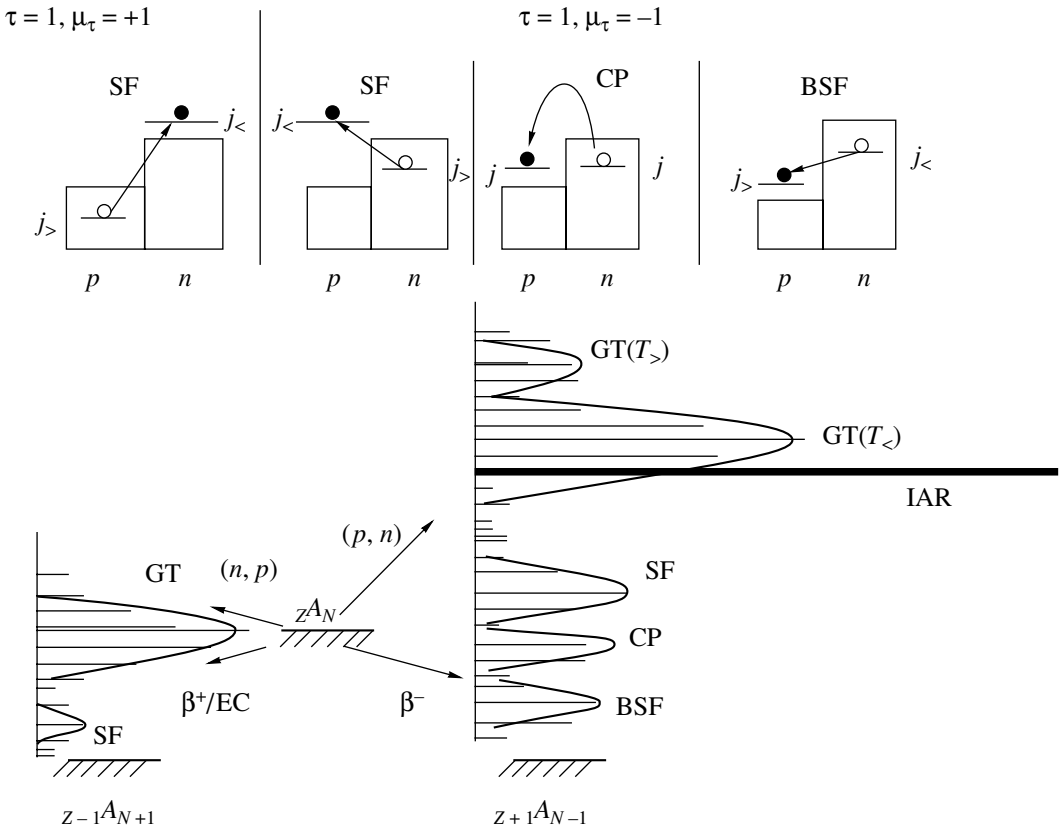

Fig. 2. A scheme of β-decay strength function in nuclei with $N > Z$. The strength function of Fermi-type transitions is concentrated at the isobar-analog resonance (IAR). The components of the Gamow–Teller resonance with different isospins ($T_<$, $T_>$) and the configurations forming the strength function of Gamow–Teller β transitions are indicated [1, 10]. BSF is a back spin-flip configuration; CP, a core polarization configuration; SF, a spin-flip configuration. Isovector excitations are characterized by isospin τ and isospin projection μ_τ (● denotes a particle, and ○ denotes a hole).

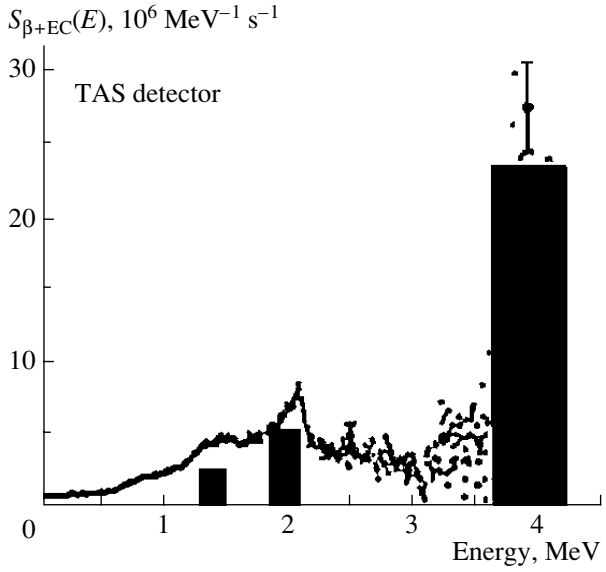

Fig. 3. The β^+/EC-decay strength function for ^{147g}Tb ($T_{1/2} \approx 1.6$ h) deduced from the TAGS spectra [3, 5, 10]. The Gamow–Teller $\mu_\tau = +1$ resonance was observed as a strong peak at $E \approx 4$ MeV.

agreement and one may conclude that the decay scheme of ^{147g}Tb ($T_{1/2} \approx 1.6$ h) β^+/EC decay in [11] is sufficiently complete. This demonstrates that the decay schemes for transitions to the levels with excitation energies higher than 2–3 MeV in medium and heavy nuclei may be very incomplete. To estimate the degree of incompleteness of the decay scheme by using TAGS spectroscopy, it is necessary to have Z- and M-separated sources and about one day for measurements and data analysis. For detailed decay-scheme construction, it is necessary to have a much longer time of measurements and data analysis.

Theoretical analysis of the observed Gamow–Teller resonance with $\mu_\tau = +1$ and its fine structure was done in [3]. Only qualitative agreement between experimental and theoretical fine structure (Fig. 6) was observed. Theory predicts more strength than was experimentally observed. This is a typical situation for both β^+/EC and β^- decays. In β^+/EC-decay of ^{147g}Tb, not all the strength is in Q_{EC} window. For a more detailed analysis of β^+/EC-decay strength in this region, experimental data on $S_\beta(E)$ in nuclei,

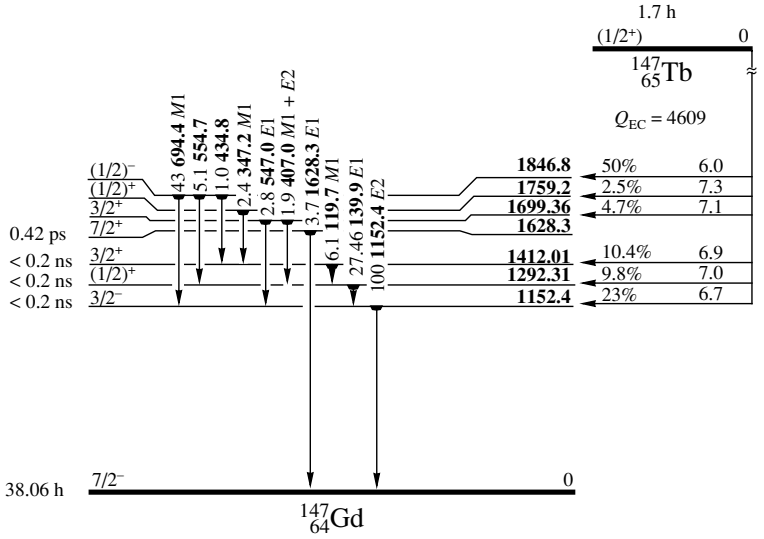

Fig. 4. ^{147g}Tb decay scheme from [13]. The β^+/EC transitions to the region where the excitation energy is higher than 2 MeV are not indicated. This decay scheme is not complete and does not agree with TAGS data. (Level energies and Q_{EC} are in keV.)

where all the β^+/EC strength lies within the Q_{EC} window, are needed. Such a possibility exists for β^+/EC decays of ^{145,143,141}Tb nuclides.

The end point of the TAS spectrum is connected with the total energy Q_β of the β decay. TAG spectroscopy can be used for measurements of Q_β with accuracy up to 20 keV [1, 4]. As a rule, the most informative region for determination of the TAS spectrum end point has a low counting per channel and determining it directly is very difficult. The part of the TAS spectrum with sufficiently high statistics is not so informative for this purpose. So there is an optimal interval of the TAS spectrum for a determination of Q_{EC}. We use the χ^2 criterion for selecting the optimal energy interval [4]. In the fitted region, the errors of the intensity determination δI were more than the maximum value of the pileup spectrum intensity. The results of determination of Q_{EC} from TAS spectra of β^+/EC decay of ^{156}Ho ($T_{1/2} \approx 56$ min) using the maximum-likelihood method [4] are presented in Figs. 7 and 8. The obtained value $Q_{EC} = 5.05 \pm 0.02$ MeV for ^{156}Ho ($T_{1/2} \approx 65$ min) is in good agreement with the systematics [14].

4. β^- DECAY, COMPLETENESS OF DECAY SCHEMES OF FISSION PRODUCTS, AND DECAY-HEAT CALCULATIONS

The population of levels at excitation energies higher than 2–3 MeV after β^- decay is related to the resonance structure in $S_\beta(E)$ (Fig. 2). Information about the β^--decay strength function and the possibility of testing decay-scheme completeness is very important for correct calculations of decay heat especially for fission products [6]. The β- and γ-decay energies realized through the natural decay of fission products may exhaust up to 13% of the total energy generated during the fission process and becomes a dominate component following a reactor shutdown [6, 15].

This energy source is commonly called decay heat. There exist some discrepancies between calculations of decay heat with different libraries like JNDC, JEF2.2, ENDF/B-VI and experiments connected with γ and β radiation of the fission products. This discrepancy is seen in equivalent studies of ^{239}Pu (Fig. 9) and ^{233,235,238}U fission products [6, 15].

Correct calculations of decay heat is a very important factor in operation with radioactivity. In [7], by using TAG spectroscopy, it was demonstrated that more than 50% of the intensity of β^- decay to high-lying states was not identified for some fission products in nuclear spectroscopic studies. To improve agreement between calculations and experiments, more complete decay schemes of fission products are needed. The combination of TAGS with high-resolution nuclear spectroscopy methods may be effectively used for construction of more complete decay schemes of fission products and understanding of the reason of the γ discrepancy in decay heat (Fig. 9).

5. CONCLUSION

In many fundamental and applied studies, sufficiently complete decay schemes of nuclei and data

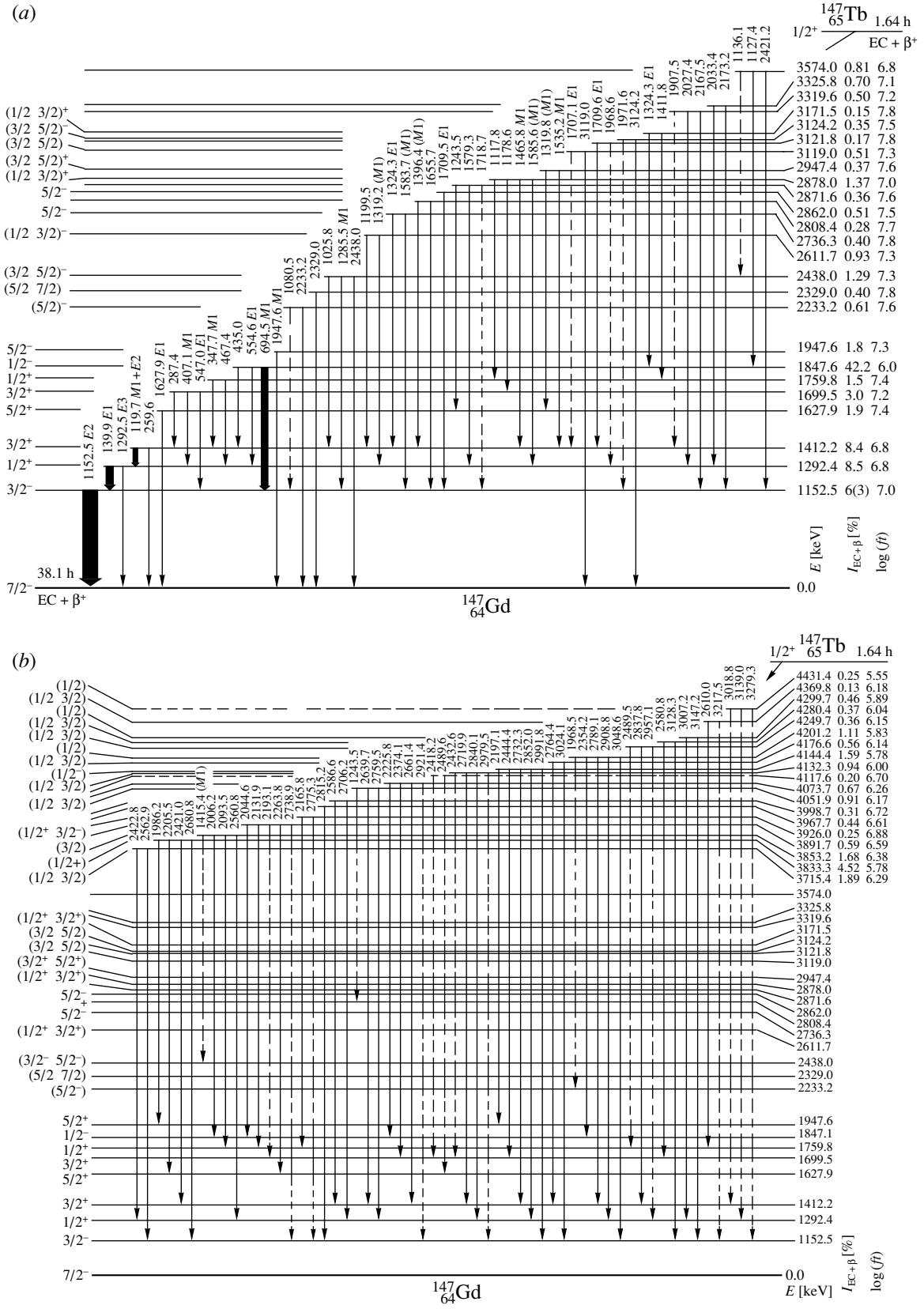

Fig. 5. ^{147g}Tb decay scheme from [11]. (*a*) Low energy levels of ^{147}Gd. (*b*) High energy levels of ^{147}Gd. There are many β_+/EC transitions to the region where the excitation energy is higher than 2 MeV. This decay scheme is quite complete and is in good agreement with the TAGS data.

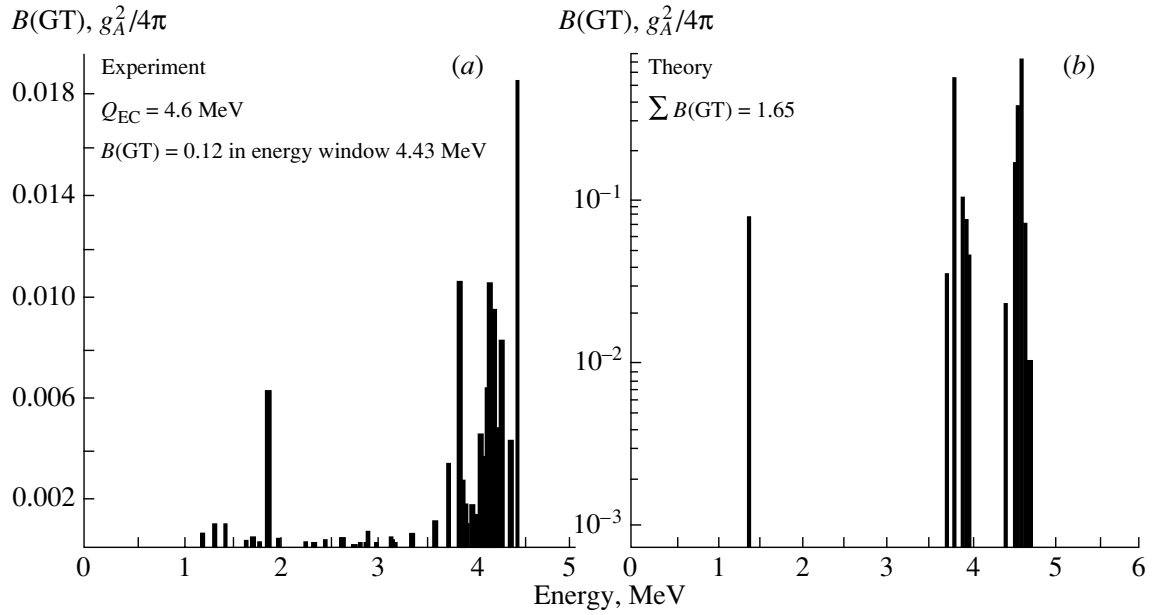

Fig. 6. (*a*) A strength function $S_\beta(E)$ of β^+/EC decay deduced in [3, 10] from the more complete decay scheme [11]. (*b*) A theoretical fine structure of $S_\beta(E)$ [3].

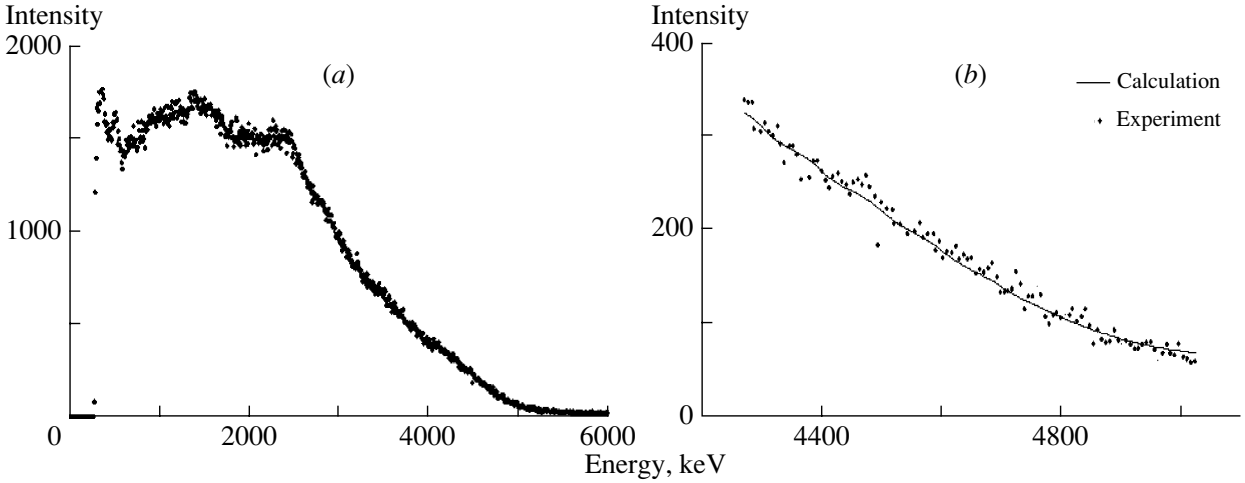

Fig. 7. Experimental (*a*) and fitted (*b*) TAS spectra of ^{156}Ho ($T_{1/2} \approx 56$ min) β^+/EC decay.

on $S_\beta(E)$ and Q_β are needed. This information may be obtained by using TAGS or TAGS in combination with high-resolution nuclear spectroscopy methods.

The degree of decay-scheme incompleteness may be quite high at excitation energies higher than 2–3 MeV in medium and heavy nuclei.

The degree of the decay-scheme completeness and energy regions where the decay scheme is incomplete can be effectively estimated by a comparison of the experimental TAS spectra with the TAS spectra calculated from the decay scheme and by a comparison of the β-decay strength functions deduced from the TAS spectra and the decay scheme. For a more complete decay-scheme construction, the combination of TAGS with high-resolution γ-spectroscopy methods must be used.

To use TAG spectroscopy, it is necessary to have both Z(element)- and M(mass)-separated sources.

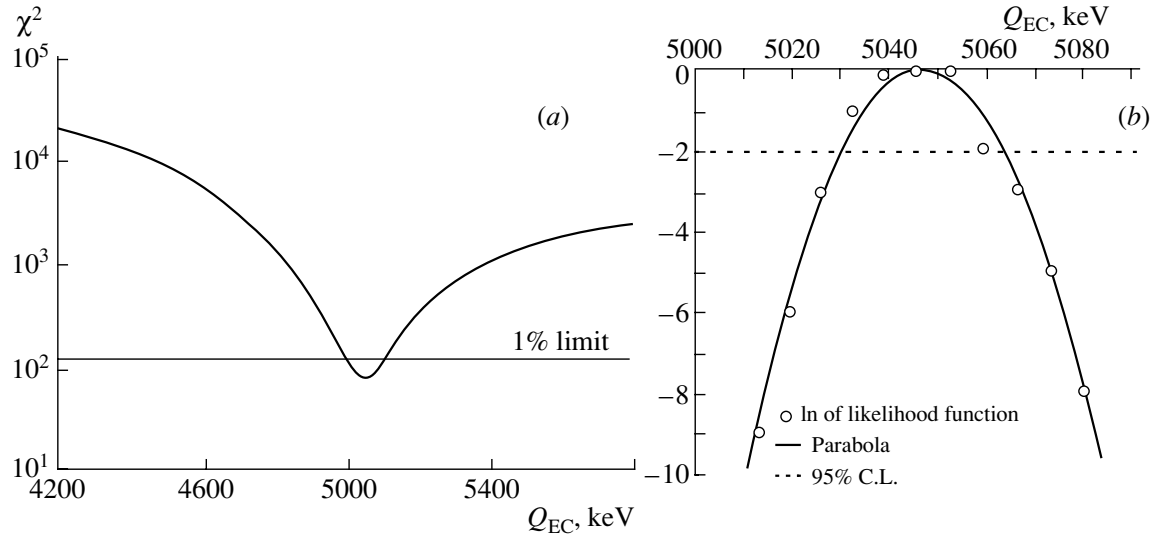

Fig. 8. (*a*) χ^2 and (*b*) natural logarithm of a likelihood function versus the total EC energy in ^{156}Ho. The number of degrees of freedom for the fitted region is $\nu = 105$, $\chi^2_{min}/\nu = 0.81$.

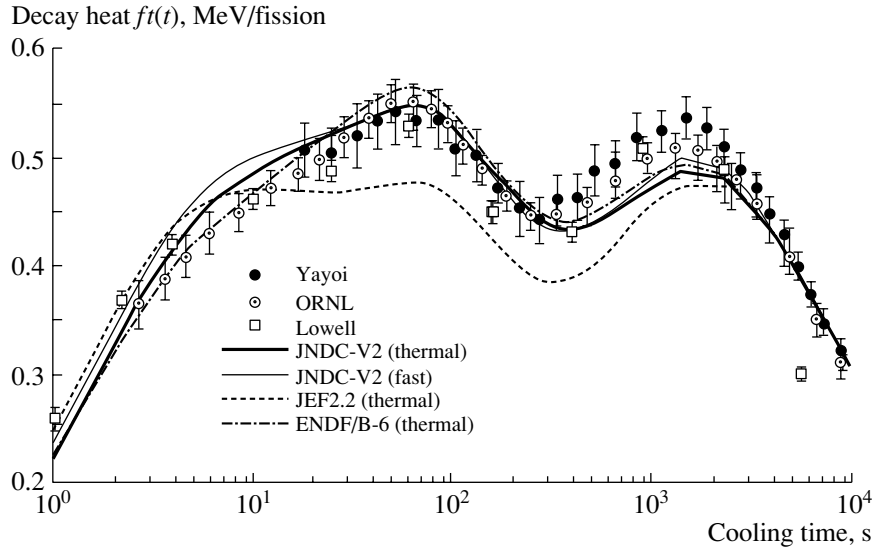

Fig. 9. Gamma-decay heat (multiplied by cooling time) for ^{239}Pu fission products as a function of cooling time after fission [6]. The curves represent results of calculations using a different database. There is a γ discrepancy in the cooling period 300–3000 s. Results are from [6, 15, 16] and references therein.

ACKNOWLEDGMENTS

This work is supported by the Russian Foundation for Basic Research, project nos. 00-02-16695 and 03-02-17395.

REFERENCES

1. Yu. V. Naumov, A. A. Bykov, and I. N. Izosimov, Fiz. Élem. Chastits At. Yadra **14**, 420 (1983) [Sov. J. Part. Nucl. **14**, 175 (1983)].
2. G. D. Alkhazov, A. A. Bykov, V. D. Witmann, *et al.*, Nucl. Phys. A **438**, 482 (1985).
3. I. N. Izosimov, V. G. Kalinnikov, A. A. Solnyshkin, and J. Suhonen, Phys. Part. Nucl., Lett., No. 2 [101], 40 (2000).
4. I. N. Izosimov, A. A. Kazimov, V. G. Kalinnikov, and A. A. Solnyshkin, Phys. Part. Nucl., Lett., No. 4 [111], 36 (2002).
5. I. N. Izosimov, V. G. Kalinnikov, M. Yu. Myakushin, *et al.*, J. Phys. G **24**, 831 (1998).
6. A. Algora, J. L. Tain, B. Rubio, *et al.*, JYFL-177 Proposal (2002).
7. R. C. Greenwood, R. G. Helmer, M. H. Putnam, and K. D. Watts, Nucl. Instrum. Methods Phys. Res. A **390**, 95 (1997).

8. M. Karny, J. M. Nitschke, L. F. Archambault, *et al.*, Nucl. Instrum. Methods Phys. Res. B **126**, 411 (1997).
9. Ph. Dessagne, B. Rubio, *et al.*, IS370 ISOLDE and INTC-P-144 Proposals.
10. I. N. Izosimov, Fiz. Élem. Chastits At. Yadra **30**, 321 (1999) [Phys. Part. Nucl. **30**, 131 (1999)].
11. J. Wawryszczuk, M. B. Yldashev, K. Yu. Gromov, *et al.*, Z. Phys. A **357**, 39 (1997).
12. K. Ikeda, Prog. Theor. Phys. **31**, 434 (1964).
13. *Tables of Isotopes,* Ed. by R. B. Firestone *et al.*, 8th ed. (Wiley-Intersci., New York, 1996).
14. G. Audi and A. H. Wapstra, Nucl. Phys. A **595**, 409 (1995).
15. T. Yoshida *et al.*, J. Nucl. Sci. Technol. **36**, 135 (1999).
16. H. V. Nguyen *et al.*, in *Proceedings of the International Conference on Nuclear Data for Science and Technology, Trieste, Italy, 1997*, p. 835.

Physics of Atomic Nuclei, Vol. 67, No. 10, 2004, pp. 1884–1891. Translated from Yadernaya Fizika, Vol. 67, No. 10, 2004, pp. 1908–1915.

NUCLEI
Experiment

Employing $(n, n'\gamma)$ Reactions to Exclude Nuclear Levels Erroneously Introduced in Other Investigations: On the 3_1^- Level in ^{56}Fe

A. M. Demidov, L. I. Govor, V. A. Kurkin*, and I. V. Mikhailov

Russian Research Centre Kurchatov Institute, pl. Akademika Kurchatova 1, Moscow, 123182 Russia

Received July 16, 2003; in final form, December 29, 2003

Abstract—Reactions of the $(n, n'\gamma)$ type proceed through a compound-nucleus stage; therefore, the excitation cross section is usually independent of the level nature. Accordingly, all of the excited states must manifest themselves in such reactions through γ transitions (with allowance for their internal conversion). In comparing the energy-level and γ-transition diagrams obtained in investigating γ rays from the inelastic scattering of fast reactor neutrons with the diagrams published in the last issues of Nuclear Data Sheets, it was found that 120 levels in 34 nuclei must be excluded from compiled data because the γ transitions expected from them were not observed. The case of the questionable first 3_1^- level in ^{56}Fe at 3076 keV is considered by way of example. It is concluded that there is no such level in ^{56}Fe.

Comprehensive and reliable experimental data on excited states of nuclei are required for developing nuclear models. However, results deduced from a comparison of model calculations with experimental data are adversely affected by the incompleteness of such data and especially by the erroneous introduction of levels. In subsequent studies, it is rather difficult to exclude such levels by using the majority of reactions because the excitation cross sections depend on the nature of the final level and its quantum numbers.

A feature peculiar to the inelastic scattering of fast neutrons is that it proceeds predominantly through a compound-nucleus stage involving a large number of overlapping resonances. As a result, the cross sections for the excitation of levels generally appear to be insensitive to the nature of the excited states and depend, in a well-known way, only on the neutron energy, the energy of the level, and its angular momentum. Up to an excitation energy of about 4 MeV, this dependence is well described on the basis of the statistical model with the aid of the Hauser–Feshbach–Moldauer formalism [1, 2]. Thus, this reaction is expected to reveal all of the actually existing levels. These excited states deexcite via γ transitions of total intensity (with allowance for electron and pair conversion) corresponding to the expected cross sections. Direct processes, whose contribution is observed for low-lying collective states, only somewhat increase the excitation cross section.

In this study, the results of our investigations into $(n, n'\gamma)$ reactions induced by fast reactor neutrons in even–even nuclei are employed to disprove or prove the existence of a level.

We performed our experiments in fast-neutron beams from a PWR reactor of the IR-8 type. The neutron beam extracted from the horizontal channel was filtered by 1 mm of Cd, 10 mm of B_4C, 50 mm of metal uranium, and a replaceable filter from 10 mm of ^{10}B [3]. For a first approximation, the spectrum of the resulting fast-neutron beam can be represented in the form of an exponential function of energy [$\Phi(E_n) \sim \exp(-0.7E_n)$, where E_n is measured in MeV]. In this case, it is natural to use the concept of the population of a level to describe quantitatively the photon yield in the deexcitation of an excited level. The primary population P_S (without taking into account the cascade population by γ transitions from higher lying states) is given by

$$P_S(\text{theor.}) = \int \sigma(E_n)\Phi(E_n)dE_n,$$

where the cross section $\sigma(E_n)$ for the excitation of a level is calculated on the basis of the statistical model [1]. If use is made of the spectrum of fast reactor neutrons, the mean energy of neutrons exciting the level is $\bar{E}_n = E_{\text{lev}} + (\approx 0.7\ \text{MeV})$. Experimentally, the value of P_S is found from the relation

$$P_S(\text{expt.}) = \sum I_\gamma(\text{out}) - \sum I_\gamma(\text{in}),$$

that is, as the difference of the sum of the intensities of γ transitions from the level and the sum of the intensities of γ transitions proceeding to it (owing to the cascade deexcitation of higher lying states). We consider relative values of P_S, the total population $[\sum I_\gamma(\text{out})]$

*e-mail: kurkin@polyn.kiae.su

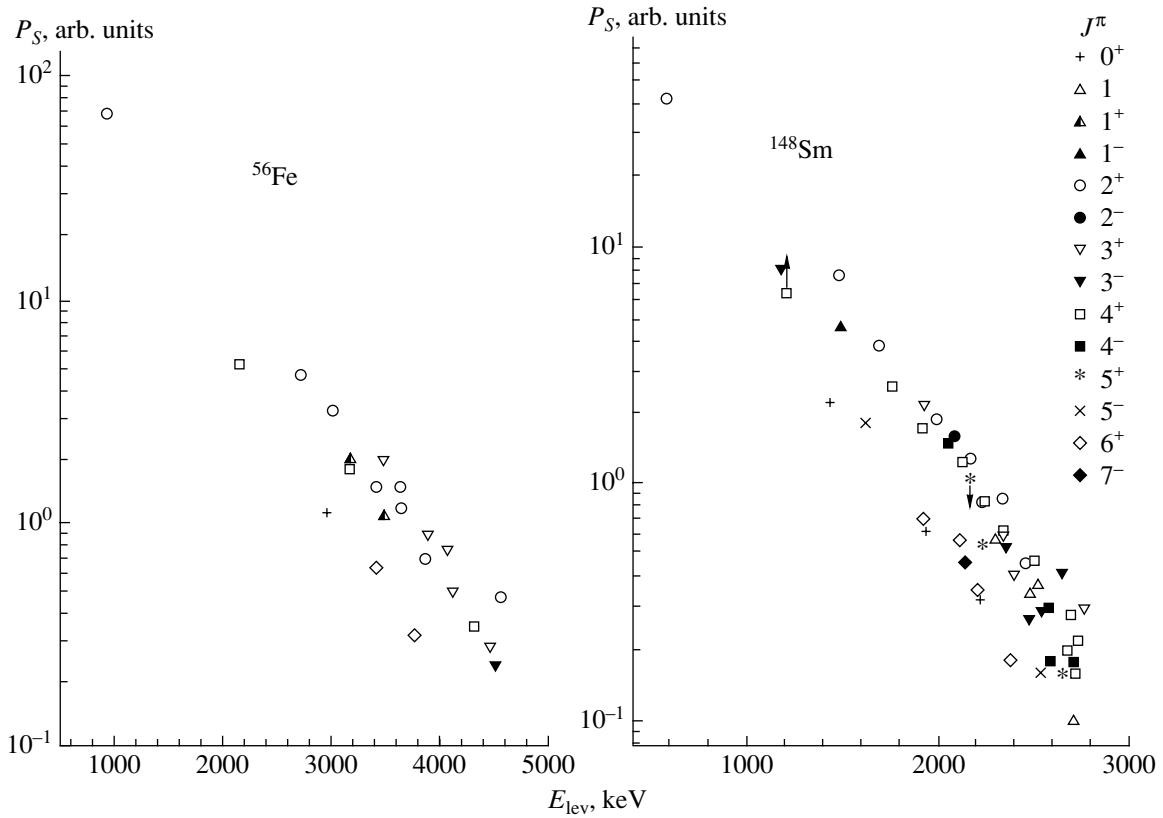

Population P_S of levels in ^{56}Fe and ^{148}Sm as a function of excitation energy.

of the first 2^+ level being taken for 100 in even–even nuclei. A comparison of P_S(expt.) and P_S(theor.) [3] showed that the inelastic scattering of fast reactor neutrons proceeds predominantly through a compound nucleus. Using relative experimental values for the γ-transition intensity I_γ for reliably established levels, one can plot the primary population as a function of excitation energy for states of various angular momenta. In calculating P_S, we took into account the level-deexcitation diagram published in Nuclear Data Sheets; that is, we included low-intensity and low-energy transitions (with allowance for their electron conversion), which did not manifest themselves in the investigation of $(n, n'\gamma)$ reactions.

In the figure, we show the populations P_S(expt.) of levels in ^{56}Fe and ^{148}Sm versus the excitation energy. The dependences $P_S(E_{\mathrm{lev}})$ for $J = 2$ and $J = 3$ levels in even–even nuclei are close; the values of P_S for $J = 1$ and $J = 4$ levels and those for $J^\pi = 0^+$ levels are less than their counterparts for $J^\pi = 2^+$ states by, respectively, a factor of 1.5 and a factor of 2 to 3. A sharp decrease in P_S is observed for $J > 5$ levels. The experimental dependences obtained in this way enable us to determine readily the P_S value expected in experiments (that is, the expected total γ-transition intensity) for an arbitrary hypothesized level. If the nuclear-level diagram below this state is well known and complete and if the spectrum of γ rays from the respective $(n, n'\gamma)$ reaction was measured with a high resolution (for example, by a germanium detector), it is straightforward to find out whether there are (or are not) γ transitions from the hypothesized level to lower lying states and, if any, whether their total intensity corresponds to the expected P_S value. This is precisely the approach that we employed in verifying the correctness of the introduction of a level.

The resulting experimental dependence $P_S(E_{\mathrm{lev}})$ obviously imposes a constraint on the arrangement of intense γ transitions in the energy-level diagram. For a specific excitation energy and a specific angular momentum of a level, this dependence gives, in addition, a lower limit on the total intensity of transitions through which this level can deexcite. If, in the spectrum generated by $(n, n'\gamma)$ reactions, such reasonably intense γ transitions not arranged in the energy-level diagram are absent, this means the completeness of this diagram up to a specific excitation energy and a specific angular momenta of the states.

Using the dependence of P_S on E_{lev} and considering combinations of γ transitions, one can introduce new levels that satisfy the requirement on the

P_S value, and this was done in many of our previous studies. Resorting to data on the population of levels makes it possible to disentangle complicated situations where there are two closely spaced levels such that γ transitions from them are not resolved in the spectra measured by germanium detectors. Within this method of investigation, an approximately doubled value of P_S must be observed if there are two such levels whose angular momenta are $J = 1$, 2, 3, 4. A typical example is provided by the case of two levels in ^{124}Te at 2039.38(6) ($J^\pi = 2^+$) and 2039.30(3) keV ($J^\pi = 3^+$); here, the total population is $P_S = 6.33$ arb. units, whereas a value of $P_S \approx 3$ arb. units is expected for a single level [4]. Unfortunately, this argument is ignored in [5], and only one level is left there in the diagram for ^{124}Te, notwithstanding additional facts that favor two levels.

In recent years, we have investigated more than 50 even–even isotopes in relevant $(n, n'\gamma)$ reactions induced by fast reactor neutrons. In each of them, we established the diagrams of level deexcitation up to an excitation energy of 3 to 4 MeV and found the quantum numbers of respective levels from the measurement of the angular distributions and linear polarizations of photons. In addition, the energy-level and γ-transition diagrams were compared with those published in Nuclear Data Sheets. No contradictions were observed in the majority of the cases. It should be noted, however, that, for some levels included in the diagram presented in Nuclear Data Sheets, we did not observe any γ transitions from them or found that their total intensity was much lower than the expected value of P_S (the distinction being in excess of fluctuations of P_S for given J^π); this circumstance could not be explained either by the internal electron conversion or by the possible very high angular momentum of a level. In our publications, we indicated, as a rule, that levels from which γ transitions were not found (without reasons) should be excluded from the diagram, but only some of the authors of the reviews in Nuclear Data Sheets took this into account. Looking through the last issues of Nuclear Data Sheets and comparing the level diagrams given there with our results obtained by investigating $(n, n'\gamma)$ reactions, we arrived at the conclusion that the levels listed in Table 1 must be excluded from the level diagrams. (In this consideration, we frequently had to analyze the γ spectrum in order to set an upper limit on the intensity of unobserved γ transitions.) Below, we give some comments to Table 1.

(i) We restricted our consideration to modest excitation energies up to about 3 MeV, in which case the γ-transition intensity is reasonably high and, accordingly, the errors in measuring energies and intensities are small, while the deexcitation diagrams are not very complicated.

(ii) In principle, the excitation-energy range being considered can be extended if the study where the level in question was introduced indicates its deexcitation diagram. In this case, a test for the consistency of the total intensity of transitions from this level with the expected value of P_S is significantly facilitated.

(iii) If there are no data on the angular momentum and parity of a level, the possible versions were considered for these quantum numbers. In doing this, it was assumed that no angular momenta above $J = 7$ were expected in even–even spherical nuclei at low excitation energies.

(iv) In drawing a conclusion on whether a level should be excluded, we paid proper attention to the possible existence of transitions whose energies are below 100 keV and which can have a high conversion coefficient. As a rule, this energy region was not investigated in $(n, n'\gamma)$ reactions. The existence of such transitions must lead to an increased population of the corresponding lower lying levels, and we took this into account.

(v) Since, in arranging all transitions of rather high intensity, the statement that the energy-level diagram is complete up to a certain excitation energy is valid, there is one more argument in favor of excluding additional levels up to these energies.

(vi) In many cases, the excluded levels were found in nuclear reactions where the energies of levels were established with large errors. In such cases, γ transitions appropriate for their deexcitation are sought in the energy range corresponding to the error in determining the energy of a level. If there are no suitable transitions of expected total intensity, the level being considered is excluded.

(vii) Particular attention was given to 0^+ levels because $0^+ - 0^+$ transitions are fully convertible. Usually, these levels are readily established in $(n, n'\gamma)$ reactions by an isotropic transition to a 2^+ level and by a P_S value that is three times less than that expected for a 2^+ level at the same energy. However, a rare case where such an $E2$ transition is fully forbidden is known in the literature for the ^{204,206}Pb nuclei, which are close to the doubly magic nucleus ^{208}Pb. The energy-level diagram for ^{204}Pb in Nuclear Data Sheets [63] contains 0_2^+ 1582.5(6)- and 0_3^+ 1729.97(12)-keV states {in ^{206}Pb [60], there is a 0_2^+ level at 1165(2) keV}, from which we observed no γ transitions. In ^{204}Pb, the 0_2^+ level is virtually coincident in energy with the $J^\pi = 2^+$ level at 1582.69(4) keV, but the value of P_S suggests that the 683.57-keV $2_3^+ - 2_1^+$ transition can contain a contribution from the $0_2^+ - 2_1^+$ transition ($P_S = 6.5$ arb. units is expected, but $P_S = 8.5$ arb. units is observed). At the same time, the 0_3^+ level in ^{206}Pb

Table 1. List of excluded levels

Isotope	Level, keV (from NDS)	J^π (from NDS)	References		Isotope	Level, keV (from NDS)	J^π (from NDS)	References	
			$(n, n'\gamma)$	NDS				$(n, n'\gamma)$	NDS
^{104}Pd	1941.2(5)		[6]	[7]	^{120}Sn	2173		[21]	[22]
	1999.1(4)	(1, 2)				2297(15)	$0^+, 1^+$		
	2125.5(1)					2540(10)	(5^-)		
^{106}Pd	1904.31(10)	$2^-, 3^-$	[6]	[8]		2751(3)	4^+		
^{106}Cd	2338.55(21)	(4^+)	[9]	[8]	^{122}Sn	2260(10)		[23]	[24]
	2521.9(3)	$(4, 5^+)$				2971.2(4)	$0^+, 1, 2$		
^{110}Cd	1809.484(18)	(2^+)	[10]	[11]		3041.4(8)			
	2000					3235.7(10)			
	2184(2)	(1^-)				3477.01(13)			
	2198(2)	$2^+, 3^+$			^{124}Sn	2109(5)	5^-	[25]	[5]
	2365(2)	2^+				2129.3	(0^+)		
	2377(2)	4^+				2366.5(5)			
	2381(2)					2706(10)	(4^+)		
	2385(2)	(2^+)			^{122}Te	1750(8)	(0^+)	[26]	[24]
	2405(2)	$(0^+, 2^-)$				2091(10)	+		
	2432(2)	2^+			^{124}Te	2134.82(18)	4	[4]	[5]
	2451(2)					2273.97(15)			
^{112}Cd	2167(1)	$2^+, 3^-$	[12]	[13]		2282.43(17)			
	2305(23)				^{126}Te	2350.8(12)		[27]	[28]
	2335(20)				^{128}Te	1972(2)		[29]	[30]
	2424(8)					2440(20)			
^{114}Cd	1784(5)	(2^+)	[14]	[15]		2485(2)	3^-		
	2317.1(7)	2^+			^{130}Te	2418(10) ?	$(1^+, 2^+)$	[31]	[32]
^{116}Cd	2188.7(6)		[16]	[17]	^{136}Ba	2153.55(8)		[33]	[34]
	2194.9(5)					2349.5(5)			
^{114}Sn	2576 (4)?	2^+	[18]	[15]		2392.1(6)	$(1^+, 2^+)$		
	2738.4(5)					2562(10)			
	2759.7(5)				^{138}Ba	2340	0^+	[35]	[36]
^{118}Sn	2120(15)	(2^+)	[19]	[20]		2582.81(13)	4^+		
	2408(3)	4^+				2794.46(12)	$1, 2^+$		
	2530					2916.36(11)	$1, 2^+$		
	2577(3)	2^+			^{140}Ce	2658.3(15)		[37]	[38]
	2725(3)	$1^+, 2^+, 3^+$				3040	3^-		
	2934(10)	(2^+)				3168.3(15)?			
	2972(3)	4^+			^{142}Ce	1742.0(8)	(4^+)	[39]	[40]
	2991(3)					1742(3)	5^-		
						2014.5(3)			

Table 1. (Contd.)

Isotope	Level, keV (from NDS)	J^π (from NDS)	References		Isotope	Level, keV (from NDS)	J^π (from NDS)	References	
			$(n, n'\gamma)$	NDS				$(n, n'\gamma)$	NDS
^{142}Nd	2244(4)	1^-	[41]	[40]	^{158}Gd	1414		[47]	[48]
	2340(25)					1440(5)			
	2515(4)	(1^-)				1554(7)			
	2529(3)				^{162}Dy	1091.6(3)		[49]	[50]
	2656(3)	0^+				1131(3)			
	2873(3)	(4^+)			^{168}Er	1266.07		[51]	[52]
^{144}Nd	2321.9(3)		[3]	[42]	^{170}Er	1332(1)	2^+	[53]	[54]
	2399.5(10)					1335	(4^+)		
	2464	1				1371	(3^-)		
	2508.42(20)				^{184}W	1283.6(3)	$(1^-, 2^-)$	[55]	[56]
^{146}Nd	915.5(4)	0^+	[43]	[44]	^{186}W	1014.97(10)	$(2^+, 3, 4^+)$	[57]	[58]
	1303.1(4)	2^+				1279.19(23)	(1, 2, 3)		
	1572(2)	(0^+)			^{206}Pb	2391.32(8)?		[59]	[60]
	1769.4(8)					2960(2)			
^{148}Sm	1434.0(8)		[45]	[46]	^{208}Pb	4045(5)	$(5^-, 6^-)$	[61]	[62]
	1461.1	$(1, 2^+)$				4106(3)	(3^-)		
	1659.4(8)	$(2, 3, 4^+)$				4141(3)	(2^+)		
	1717.8(10)					4159(4)	(2^+)		
	2041(8)					4230(2)	$(4)^-$		
	2142.5(20)	(2, 3, 4)				4403(2)	$3^-, 4^+$		
	2277(3)					4444(4)	(5^-)		
	2318.5(5)	+				4463(4)	(2^+)		
	2344(3)	$3^-, 4^-$				4577(5)			

is deexcited via a γ transition only to the 1_1^+ level, and this may be indicative of a particular structure of 0^+ states in these lead isotopes. The analogous $0_3^+ - 1_1^+$ transition in ^{204}Pb must be of energy 48.9 keV; that is, it falls within the region that has not yet been investigated in $(n, n'\gamma)$ reactions.

(viii) In connection with considering 0^+ levels, we dwell on the case that takes place in the ^{124}Sn isotope, where $0^+ - 2^+$ transitions between low-lying states are not expected to be fully forbidden. Nuclear Data Sheets [5] present two levels there, a $J^\pi = 2_2^+$ one at 2129.597(25) keV and a $J^\pi = (0^+)$ one at 2129.3 keV. We have excluded the latter from the energy-level diagram. The 997.8-keV line corresponding to the transition to the first 2^+ level is not broadened in the relevant $(n, n'\gamma)$ reaction and ensures the population of $P_S = 7.0$ arb. units, which is necessary only for the 2^+ level [25]. The ratio of the intensities of the $2_2^+ - 2_1^+$ and $2_2^+ - 0_1^+$ transitions takes the same value in the $(n, n'\gamma)$ reaction and in the β decay of ^{124}In. In the latter case, the population of the 0^+ level is expected to be low. In [5], a 2129.3-keV level was introduced on the basis of the systematics of 0^+ states in tin isotopes. However, we established the spin–parity 0^+ for the level at 2192.13 keV; this assignment is reliably confirmed by a low value of $P_S = 1.59$ arb. units and by an isotropic distribution of 1060.42-keV photons corresponding to the transition to the first 2^+ level [25]. The 2192.13-keV level is a link in the systematics of 0^+ levels in tin isotopes.

(ix) Since the existing experimental errors give no way to rule out the possibility that part of a highly intense 839.49-keV transition is associated with the deexcitation of a hypothetical level at 2426.7 keV, we cannot be positive about excluding the 2418(10)-keV level in ^{130}Te, and the question mark for this level in Table 1 reflects this situation. The main location of the 839.49-keV γ line corresponds to the deexcitation of the first 2^+ level.

To give a more detailed account of the procedure used to exclude levels, we dwell on the case of ^{56}Fe. In the relevant $(n, n'\gamma)$ reaction induced by fast reactor neutrons, this isotope was investigated in [64, 65]. Despite this, we repeated the measurement of the γ spectrum with the aim of setting an upper limit on the intensity of unobserved transitions. In Table 2, the energy-level and γ-transition diagrams for ^{56}Fe are given up to the excitation energy of 3.4 MeV [66]. In the figure, the population of the ^{56}Fe levels in the $(n, n'\gamma)$ reaction is shown as a function of excitation energy. The energy-level diagram obtained by investigating the $(n, n'\gamma)$ reaction does not contain a 3076.2-keV level [64, 65]. In the deexcitation of the 3076.2-keV level, the possible transitions are expected to have the energies of 3076.2, 2229.4, 991.1, 418.6, 134.6, and 116.3 keV. Our measurements revealed that all of these transitions have an intensity less than 0.1 arb. units (the 991-keV transition has an intensity of about 0.08 arb. units). Thus, the total intensity of the relevant γ transitions cannot exceed 0.6 arb. units in contrast to an expected value of $P_S \approx$ 2.5 arb. units. Since there are no reasons to assume that the allowed γ transitions may be forbidden in the ^{56}Fe nucleus or that the inelastic scattering of fast neutrons in the excitation of this level does not proceed through a compound nucleus, we state that there is no 3076.2-keV level in ^{56}Fe.

In the vicinity of 2229 keV, the γ spectrum obtained in the relevant $(n, n'\gamma)$ reaction exhibits a 2223.3-keV background γ line associated with neutron capture in hydrogen. We performed dedicated experiments where the contribution of this background line was reduced and where an iron sample was replaced by a copper one. As a result, it was found that this background line receives no significant contribution from a γ transition associated with the reaction ^{56}Fe $(n, n'\gamma)$.

The 3076.2-keV level in ^{56}Fe was not revealed even in a detailed inspection of the γ spectra in the β^- decay of ^{56}Mn $(J^\pi = 3^+)$ and β^+ decay of ^{56}Co $(J^\pi = 4^+)$ [66].

We now consider the reasons for the introduction of the 3076.2-keV level in [66]. These are (a) the assumption that the energy of the level is 3076.2(4) keV, that its spin–parity is $J^\pi = 3^-$, and that it is deexcited by the 2229- and 991-keV γ transitions {data from [67] on the (p, γ) reaction were used} and (b) the detection of the 3100-keV level of orbital angular momentum $L = 3$ in the relevant (e, e') reaction, the 3070-keV $L = (3)$ level in the (α, α') reaction, the 3090-keV $L = 1$ level in the (d, t) reaction, and the 3070(30)-keV level in the (^{3}He, ^{7}Be) reaction.

It can be assumed that the energy of the level is somewhat different from 3076 keV, but the point is that all of the γ lines whose intensity satisfies the condition $I_\gamma > 0.2$ arb. units and which could ensure a required value of $P_S \approx 2.5$ arb. units have already been reliably distributed. Therefore we can state that there are no other levels of $J \leq 6$ at an excitation energy lower than 3.4 MeV in ^{56}Fe. The 2229- and 991-keV γ transitions found in [67] are likely to proceed between higher lying states.

The problem of the existence of the 3^-_1 level is of importance since it concerns the octupole excitation of a nucleus. The reliably established 3^-_1 level in ^{56}Fe has an energy of 4509.64(12) keV [66].

Table 2. Energy-level and γ-transition diagram for ^{56}Fe

E_{lev}, keV	J^π_{lev}	E_γ, keV	I_γ, %
846.776(5)	2^+	846.771	100
2085.076(7)	4^+	1238.282	100
2657.562(10)	2^+	2657.45	3.2
		1810.772	100
2941.50(3)	0^+	2094.9	100
2959.923(9)	2^+	2959.77	2.14
		2113.123	100
3076.2(4)	(3^-)	2229	100
		991	47
3120.11(5)	(1^+)	3120	4.82
		2273.2	100
3122.927(7)	4^+	2276.36	0.89
		1037.940	100
3369.84(4)	2^+	3369.60	17
		2522.88	100
3388.55(5)	6^+	1303.4	100
		265.5	1.3

ACKNOWLEDGMENTS

We are grateful to F.E. Chukreev for placing the last issues of Nuclear Data Sheets at our disposal.

REFERENCES

1. W. Hauser and S. Feshbach, Phys. Rev. **109**, 1295 (1958).
2. P. A. Moldauer, Phys. Rev. **123**, 968 (1961).
3. A. M. Demidov, L. I. Govor, and K. A. Baskova, in *Investigation of Excited Nuclear States* (Nauka, Alma-Ata, 1986), p. 70.
4. L. I. Govor, A. M. Demidov, and I. V. Mikhailov, *Problems of Nuclear Physics and Cosmic Rays* (Kharkov Univ., Kharkov, 1989), No. 32, p. 3.
5. H. Iimura, J. Katakura, K. Kitao, and T. Tamura, Nucl. Data Sheets **80**, 896 (1997).
6. L. M. Demidov, L. I. Govor, Yu. K. Cherepantsev, *et al.*, *Atlas of Gamma-Ray Spectra from the Inelastic Scattering of Fast Reactor Neutrons* (Atomizdat, Moscow, 1978), Part 2.
7. J. Blachot, Nucl. Data Sheets **64**, 1 (1991).
8. D. DeFrenne and E. Jacobs, Nucl. Data Sheets **72**, 1 (1994).
9. S. A. Berendakov, L. I. Govor, A. M. Demidov, and I. V. Mikhailov, Vopr. At. Nauki Tekh., Ser. Yad. Konstanty **4**, 26 (1988); INDC(CCP)299/G (1988).
10. A. M. Demidov, S. M. Zlitni, V. A. Kurkin, *et al.,* Izv. Akad. Nauk, Ser. Fiz. **56** (1), 11 (1992).
11. D. DeFrenne and E. Jacobs, Nucl. Data Sheets **89**, 481 (2000).
12. S. Yu. Araddad, M. M. Dufani, S. M. Zlitni, *et al.,* Vopr. At. Nauki Tekh., Ser. Yad. Konstanty **1**, 47 (1991).
13. D. DeFrenne and E. Jacobs, Nucl. Data Sheets **79**, 639 (1996).
14. S. Yu. Araddad, A. M. Demidov, O. K. Zhuravlev, *et al.,* Yad. Fiz. **46**, 40 (1987) [Sov. J. Nucl. Phys. **46**, 25 (1987)].
15. J. Blachot, Nucl. Data Sheets **97**, 593 (2002).
16. S. Yu. Araddad, A. M. Demidov, S. M. Zlitni, *et al.,* Yad. Fiz. **54**, 309 (1991) [Sov. J. Nucl. Phys. **54**, 181 (1991)].
17. J. Blachot, Nucl. Data Sheets **92**, 455 (2001).
18. S. Yu. Araddad, A. M. Demidov, M. M. Dyufani, *et al.,* Izv. Akad. Nauk SSSR, Ser. Fiz. **54**, 1824 (1990).
19. I. V. Mikhailov and A. M. Demidov, Izv. Akad. Nauk SSSR, Ser. Fiz. **53**, 892 (1989).
20. K. Kitao, Nucl. Data Sheets **75**, 99 (1995).
21. A. M. Demidov and I. V. Mikhaĭlov, Yad. Fiz. **55**, 865 (1992) [Sov. J. Nucl. Phys. **55**, 481 (1992)].
22. K. Kitao, Y. Tendow, and A. Hashizume, Nucl. Data Sheets **96**, 241 (2002).
23. A. M. Demidov and I. V. Mikhailov, Izv. Akad. Nauk SSSR, Ser. Fiz. **55**, 2112 (1991).
24. T. Tamura, Nucl. Data Sheets **71**, 461 (1994).
25. A. M. Demidov and I. V. Mikhailov, Izv. Akad. Nauk SSSR, Ser. Fiz. **54**, 2126 (1990).
26. S. A. Berendakov, L. I. Govor, A. M. Demidov, and I. V. Mikhailov, Vopr. At. Nauki Tekh., Ser. Yad. Konstanty **3**, 80 (1990).
27. S. A. Berendakov, L. I. Govor, A. M. Demidov, and I. V. Mikhailov, Izv. Akad. Nauk SSSR, Ser. Fiz. **52**, 1020 (1988).
28. J. Katakura and K. Kitao, Nucl. Data Sheets **97**, 765 (2002).
29. L. I. Govor, A. M. Demidov, and I. V. Mikhailov, Vopr. At. Nauki Tekh., Ser. Yad. Konstanty **3**, 42 (1988); INDC (CCP) 310/G (1988), p. 42.
30. M. Kanbe and K. Kitao, Nucl. Data Sheets **94**, 227 (2001).
31. S. A. Berendakov, L. I. Govor, A. M. Demidov, and I. V. Mikhailov, Izv. Akad. Nauk SSSR, Ser. Fiz. **52**, 1028 (1988).
32. B. Singh, Nucl. Data Sheets **93**, 33 (2001).
33. M. M. Al-Hamidi, A. M. Demidov, M. M. Dufani, *et al.,* Yad. Fiz. **57**, 579 (1994) [Phys. At. Nucl. **57**, 545 (1994)].
34. A. A. Sonzogni, Nucl. Data Sheets **95**, 837 (2002).
35. L. I. Govor, A. M. Demidov, and I. V. Mikhailov, Yad. Fiz. **66**, 19 (2003) [Phys. At. Nucl. **66**, 17 (2003)].
36. J. K. Tuli, Nucl. Data Sheets **69**, 69 (1993); **74**, 349 (1995).
37. L. I. Govor, A. M. Demidov, and V. A. Kurkin, Yad. Fiz. **56** (12), 15 (1993) [Phys. At. Nucl. **56**, 1625 (1993)].
38. L. K. Peker, Nucl. Data Sheets **73**, 261 (1994).
39. M. M. Al-Hamidi, A. M. Demidov, M. M. Dufani, *et al.,* Yad. Fiz. **55**, 890 (1992) [Sov. J. Nucl. Phys. **55**, 496 (1992)].
40. J. K. Tuli, Nucl. Data Sheets **89**, 641 (2000).
41. L. I. Govor, A. M. Demidov, and V. A. Kurkin, Yad. Fiz. **59**, 1733 (1996) [Phys. At. Nucl. **59**, 1675 (1996)].
42. A. A. Sonzogni, Nucl. Data Sheets **93**, 599 (2001).
43. T. J. Al Janabi, J. D. Jafar, H. M. Youhana, *et al.,* J. Phys. G **9**, 779 (1983).
44. L. K. Peker and J. K. Tuli, Nucl. Data Sheets **82**, 187 (1997).
45. L. I. Govor, A. M. Demidov, and Yu. A. Cherepantsev, Yad. Fiz. **60**, 1733 (1997) [Phys. At. Nucl. **60**, 1579 (1997)].
46. M. R. Bhat, Nucl. Data Sheets **89**, 797 (2000).
47. L. I. Govor, A. M. Demidov, and I. V. Mikhailov, Yad. Fiz. **64**, 1329 (2001) [Phys. At. Nucl. **64**, 1254 (2001)].
48. R. G. Helmer, Nucl. Data Sheets **77**, 471 (1996).
49. L. I. Govor, A. M. Demidov, and V. A. Kurkin, Yad. Fiz. **65**, 819 (2002) [Phys. At. Nucl. **65**, 785 (2002)].
50. R. G. Helmer and C. W. Reich, Nucl. Data Sheets **87**, 317 (1999).
51. S. A. Berendakov, L. I. Govor, E. P. Grigoriev, *et al.,* Yad. Fiz. **61**, 389 (1998) [Phys. At. Nucl. **61**, 329 (1998)].
52. V. S. Shirley, Nucl. Data Sheets **71**, 261 (1994).
53. S. A. Berendakov and A. M. Demidov, Izv. Akad. Nauk, Ser. Fiz. **56** (11), 28 (1992).
54. Coral M. Baglin, Nucl. Data Sheets **77**, 125 (1996).
55. V. D. Avchukhov, M. R. Ahmed, K. A. Baskova, *et al.,* Izv. Akad. Nauk SSSR, Ser. Fiz. **42**, 1937 (1978).
56. R. B. Firestone, Nucl. Data Sheets **58**, 243 (1989).
57. L. I. Govor, A. M. Demidov, I. V. Mikhailov, and Yu. K. Cherepantsev, Vopr. At. Nauki Tekh., Ser. Yad. Konstanty **4**, 33 (1988); INDC(CCR)299/G(1988), p. 33.

58. Coral M. Baglin, Nucl. Data Sheets **86**, 455 (1999).
59. S. A. Berendakov, A. M. Demidov, and I. V. Mikhailov, Izv. Akad. Nauk Kaz., Ser. Fiz.-Mat. **2** (153), 14 (1999).
60. E. Brown, Nucl. Data Sheets **88**, 29 (1999).
61. L. I. Govor, A. M. Demidov, and V. A. Kurkin, Izv. Akad. Nauk SSSR, Ser. Fiz. **54**, 526 (1990).
62. M. J. Martin, Nucl. Data Sheets **47**, 797 (1986).
63. M. R. Schmorak, Nucl. Data Sheets **72**, 409 (1994).
64. M. R. Ahmed, S. Al-Najjar, M. A. Al-Amili, *et al.*, *Atlas of Gamma-Ray Spectra from the Inelastic Scattering of Fast Reactor Neutrons* (Atomizdat, Moscow, 1978), Part 1.
65. Yu. G. Kosyak, D. K. Kaipov, and L. V. Chekushina, Izv. Akad. Nauk SSSR, Ser. Fiz. **47**, 2118 (1983); **49**, 2118 (1985).
66. Huo Junde, Nucl. Data Sheets **86**, 315 (1999).
67. Z. Guo, C. Alderliesten, C. Van der Leun, and P. M. Endt, Nucl. Phys. A **540**, 117 (1992).

Translated by V. Bukhanov

Physics of Atomic Nuclei, Vol. 67, No. 10, 2004, pp. 1892–1899. Translated from Yadernaya Fizika, Vol. 67, No. 10, 2004, pp. 1916–1922.

NUCLEI
Experiment

Reactor as a Source of Antineutrinos: Thermal Fission Energy

V. I. Kopeikin, L. A. Mikaelyan, and V. V. Sinev*

Russian Research Centre Kurchatov Institute, pl. Kurchatova 1, Moscow, 123182 Russia

Received September 15, 2003

Abstract—Deeper insight into the features of a reactor as a source of antineutrinos is required for making further advances in studying the fundamental properties of the neutrino. The relationship between the thermal power of a reactor and the rate of the chain fission reaction in its core is analyzed.

INTRODUCTION

Experiments aimed at studying the fundamental properties of the neutrino and at testing the standard model of electroweak interactions are being performed at reactors. A collaboration of researchers from the Kurchatov Institute and the Petersburg Nuclear Physics Institute (PNPI, Gatchina) are conducting, at the Krasnoyarsk reactor, an experiment devoted to searches for the neutrino anomalous magnetic moment [1]. A group of physicists from the Institute of Theoretical and Experimental Physics (ITEP, Moscow) and the Joint Institute for Nuclear Research (JINR, Dubna) are preparing a similar experiment at the reactor of the Kalinin atomic power plant [2]. The CHOOZ experiment [3], completed quite recently, set constraints on the neutrino-mixing-matrix element U_{e3}. The KamLAND Collaboration, which is recording antineutrinos at a distance of a few hundred kilometers from reactors, is able to determine the remaining two mixing-matrix elements U_{e1} and U_{e2} and to test the LMA MSW hypothesis of solar-neutrino oscillations [4]. In addition, it should be noted that a program of neutrino studies at the reactors on the island of Taiwan is being developed [5] and that interesting proposals concerning searches for neutrino oscillations were put forth in Germany [6]. (More details on the motivation of those investigations, their status, and their prospects can be found, for example, in the review articles cited in [7].)

Differing in many respects, the aforementioned experiments possess one common feature: the results obtained in these experiments are analyzed by an absolute method—specifically, the measured counting rates for neutrino events and their spectral distributions are contrasted against their counterparts calculated on the basis of the theory of electroweak interactions. For input data in these calculations, use is made of the set of features of neutrino radiation that, together with other data, form a metrological basis of the experimental physics of neutrinos at nuclear reactors.

The spectral density $f(E_\nu)$ ($\mathrm{cm}^{-2}\ \mathrm{s}^{-1}\ \mathrm{MeV}^{-1}$) of the flux of reactor electron antineutrinos ($\bar{\nu}_e$) incident on a detector is given by

$$f(E_\nu) = N_f \rho_f(E_\nu)/4\pi R^2, \qquad (1)$$

where N_f is the number of fission events in a reactor per second, $\rho_f(E_\nu)$ (MeV^{-1} fiss.$^{-1}$) is the spectrum of reactor electron antineutrinos that is normalized to a fission event, and R (cm) is the distance between the reactor and the detector used.

In the fission of uranium and plutonium nuclei and in the subsequent radioactive decay of fission fragments, as well as in accompanying neutron reactions, energy is released, its major part being absorbed in the reactor, whereby it is converted into heat. Denoting by E_f (MeV/fiss.) the energy absorbed in the reactor on average per fission event, we can represent the chain-reaction rate N_f in the form

$$N_f = W/E_f. \qquad (2)$$

The present study is devoted to exploring the quantity E_f, which relates the fission-reaction rate N_f (fiss./s) to the thermal power W of a reactor. First of all, we consider this relationship for the example of a standard operating period of a reactor belonging to the PWR type, in which case isotopes undergoing fission include ^{235}U, ^{239}Pu, ^{238}U, and ^{241}Pu. The method developed here and, upon introducing some specific corrections, the results presented below can be used in neutrino experiments, both those that are being presently performed and those that are planned, at reactors of any other type.

The reactor staff determines the current value of the thermal power to a precision of about 1 to 2%. In order to avoid increasing the error in determining the

*e-mail: sinev@polyn.kiae.su

1063-7788/04/6710-1892$26.00

ratio in (2), we will try to calculate the energy E_f to a higher precision.

1. COMPONENTS OF THE ENERGY E_f

The energy E_f can be represented as the sum of four terms; that is,

$$E_f = E_{\rm tot} - \langle E_\nu \rangle - \Delta E_{\beta\gamma} + E_{nc}, \qquad (3)$$

where $E_{\rm tot}$ is the total energy released in nuclear fission from the instant at which the neutron inducing this fission process is absorbed to the completion of the beta decays of product fragments and their transformation into beta-stable neutral atoms, $\langle E_\nu \rangle$ is the mean energy carried away by the antineutrinos that are produced in the beta decay of fission fragments ($\sim 6\bar{\nu}_e$/fiss.), $\Delta E_{\beta\gamma}$ is the energy of beta electrons and photons from fission fragments that did not decay at a given instant of time, and E_{nc} is the energy absorbed upon neutron capture (without fission) in various materials of the reactor core.

That part of the total energy $E_{\rm tot}$ which remains in the reactor and which transforms into heat forms the effective fission energy $E_{\rm eff}$,

$$E_{\rm eff} = E_{\rm tot} - \langle E_\nu \rangle - \Delta E_{\beta\gamma}. \qquad (3a)$$

The expression for $E_{\rm eff}$ can then be represented in the form

$$E_f = E_{\rm eff} + E_{nc}. \qquad (3b)$$

The above concerns the energy released in a single nuclear-fission event, but the chain fission reaction in a reactor proceeds over a finite time interval. For this reason, we consider a chain fission reaction that begins at the instant $t = 0$ and proceeds at the rate of $N_f = 1$ fiss./s. We denote by $E(t)_{\rm tot}$ the energy released per second at the instant t reckoned from the commencement of the process being considered. The quantity $E(t)_{\rm tot}$ includes all kinds of energy, with the exception of E_{nc}, which is the energy that is released in various materials upon the absorption in them of neutrons not involved in the fission process. We will now consider the function $f_{\rm tot}(t)$ determining the energy released per unit time after the lapse of the time t since a single fission event. It is obvious that

$$E(t)_{\rm tot} = \int_0^t f_{\rm tot}(t')dt', \quad f_{\rm tot}(t) = \frac{dE(t)_{\rm tot}}{dt}. \qquad (4)$$

The energy $E(t)_{\rm tot}$ grows with increasing fission-process time t, tending to the limiting value $E(\infty)_{\rm tot}$,

$$E(\infty_{\rm tot}) = \int_0^\infty f_{\rm tot}(x)dx \equiv E_{\rm tot}. \qquad (4a)$$

The above equations relate the energy release in a single fission event to the energy release per unit time in a continuous process.

Neutrino investigations are performed at reactors where use is made of uranium whose enrichment in ^{235}U is low. As this isotope burns out, ^{239}Pu and ^{241}Pu are accumulated in the core of such a reactor. Just like ^{235}U, these isotopes undergo fission induced by thermal neutrons. There is also a contribution to the total number of fission events from ^{238}U, which is fissile under the effect of fast neutrons. Therefore, we have

$$E_f = \sum \alpha_i E_{fi}, \quad \sum \alpha_i = 1, \qquad (5)$$

where α_i ($i = 5, 9, 8, 1$) are the contributions of the ^{235}U, ^{239}Pu, ^{238}U, and ^{241}Pu isotopes to the total number N_f of fission events at a given instant of time. Information about α_i values, which change in the course of reactor operation, is provided by the reactor staff with a relative error of 5%. The α_i values typical of PWR reactors are

$$\alpha_5 = 0.59, \ \alpha_9 = 0.29, \ \alpha_8 = 0.07, \ \alpha_1 = 0.05. \qquad (6)$$

It should be emphasized that the energy E_f and the calculated number W/E_f of fission events occurring in a reactor at a given instant of time are not determined exclusively by the current reactor state, which is specified by the level of the reactor power and by the isotopic composition of the burning nuclear fuel, but they are dependent on the prehistory of the reactor. This dependence is controlled by the terms E_{nc} and $\Delta E_{\beta\gamma}$, which appear in (3). The quantity E_{nc} changes along with the composition of the materials in the reactor core in the course of reactor operation. Both terms involve a contribution from long-lived beta emitters and depend on the duration of the irradiation of the fuel.

For the isotopes undergoing fission, the energies E_{fi} in (5) for the whole reactor exceed 200 MeV/fiss. Going somewhat ahead, we note that, for a PWR reactor, the absolute values of the terms appearing in expression (3) for the energy E_f are in the following ratio:

$$E_{\rm tot} : \langle E_\nu \rangle : \Delta E_{\beta\gamma} : E_{nc} \approx 200 : 9 : 0.3 : 10. \qquad (7)$$

2. TOTAL ($E_{\rm tot}$) AND EFFECTIVE ($E_{\rm eff}$) FISSION ENERGY

2.1. Total Fission Energy E_{tot}

The energy $E_{\rm tot}$ can be calculated by summing the mean values of various components of the energy release, such as the fragment kinetic energy, the energy of prompt and delayed fission gamma rays, and the neutron and beta-electron kinetic energies. However,

Table 1. Mass excesses and total fission energy $E_{\rm tot}$ (in MeV/fiss.)

Fissile nucleus	Mass excess $m(A_0, Z_0)$	Mass excess for fission products, $\sum y_A m(A, Z_A)$	Number of fission neutrons, n_f	$(n_f - 1)m_n$	Total fission energy, $E_{\rm tot}$
^{235}U	40.914 ± 0.002	-173.43 ± 0.05	2.432 ± 0.0036	11.55 ± 0.03	202.79 ± 0.06
^{238}U	47.304 ± 0.002	-173.39 ± 0.10	2.829 ± 0.011	14.76 ± 0.09	205.93 ± 0.13
^{239}Pu	48.584 ± 0.002	-173.87 ± 0.07	2.875 ± 0.0060	15.13 ± 0.05	207.32 ± 0.08
^{241}Pu	52.951 ± 0.002	-173.72 ± 0.10	2.937 ± 0.0073	15.63 ± 0.06	211.04 ± 0.12

much more precise results are obtained by directly applying the energy-conservation law to the fission process; that is,

$$M(A_0, Z_0) + M_n = \sum y_A M(A, Z_A) + n_f M_n + E_{\rm tot}, \quad (8)$$

where $M(A_0, Z_0)$ is the atomic mass of the isotope undergoing fission (the speed of light is set to unity, $c = 1$); A_0 and Z_0 are its mass and charge numbers, respectively; M_n is the neutron mass; summation is performed over the mass numbers A of beta-stable fission products; $M(A, Z_A)$ are the masses of these products; y_A are their total yields, $\sum y_A = 2$; and n_f is the mean total number of prompt and delayed fission neutrons (for the obvious reason, the notation ν, which is usually used for the mean number of fission neutrons, is replaced here by n_f.)

Using the condition requiring that the number of nucleons be conserved in the fission process and introducing the mass excesses for atoms, $m(A, Z)$, we can recast relation (8) into the form

$$E_{\rm tot} = m(A_0, Z_0) - \sum y_A m(A, Z_A) - (n_f - 1)m_n, \quad (9)$$

where $m(A, Z) = M(A, Z) - Am_0$ (m_0 is an atomic mass unit) and $m_n = M_n - m_0 = 8.0713 \pm 0.0001$ MeV is the neutron mass excess.

The calculated total energy $E_{\rm tot}$ and the quantities appearing in relation (9) are given in Table 1 for all four nuclei undergoing fission. In computing these results, we employed data on the mass excesses for the atoms involved [8] and on the yields of fission fragments [9] whose mass numbers took values in the range between 66 and 172 (see Fig. 1). The data on the number of fission neutrons were borrowed from [10].

For the fissile nuclei being considered, the values of $E_{\rm tot}$ differ from one another by a few MeV, increasing in the order of their positions in the first column of Table 1. These distinctions are caused, above all, by an increase in the mass excess for the atoms of the fissile isotopes and, to a lesser extent, by an increase in the number n_f of fission neutrons. At the same time, it can be seen from Table 1 that, for the set of stable fission fragments, the total mass excess $\sum y_A m(A, Z_A)$ is virtually independent of the nucleus undergoing fission. This is because the quantity $m(A, Z_A)$ is approximately constant over the region of high fragment yields y_A, sizably increasing only for products originating from highly asymmetric fission, where the yields in question are relatively low (see Fig. 1). Therefore, even significant distinctions between the mass distributions of fragments produced in the fission of uranium and plutonium nuclei have but a slight effect on the sums $\sum y_A m(A, Z_A)$.

The error in the mass excess $\sum y_A m(A, Z_A)$ (see the third column in Table 1) depends on the uncertainty in the yields y_A, since the overwhelming majority of values of $m(A, Z_A)$ are known to a precision not poorer than 5 keV. In order to find this error, each of the yields y_A was varied individually, irrespective of the others, under the assumption that it obeys the a Gaussian distribution. Upon each variation, there arises a new set of y_A values, and we calculated the value of $\sum y_A m(A, Z_A)$ for this set. As a result, the total number $\sum y_A A$ of nucleons contained in fission products changed somewhat. On the basis of the relation

$$A_0 + 1 = \sum y_A A + n_f, \quad (10)$$

which expresses the law of nucleon-number conservation, we calculated the corresponding number n_f of neutrons. A point in the plane spanned by the variables $\sum y_A m(A, Z_A)$ and n_f was associated with the pair of values found in this way for the mass excess and the number of neutrons. The results of one such computational experiment performed for ^{235}U, where use was made of a Gaussian distribution characterized by a FWHM value of 0.12, are illustrated in Fig. 2 (10 000 points). From Fig. 2, it can be seen that the uncertainties in the yields of fission products introduce an error of about 35 keV in the mass excess and that available experimental data on the yields of fission products and on the number of neutrons are quite consistent.

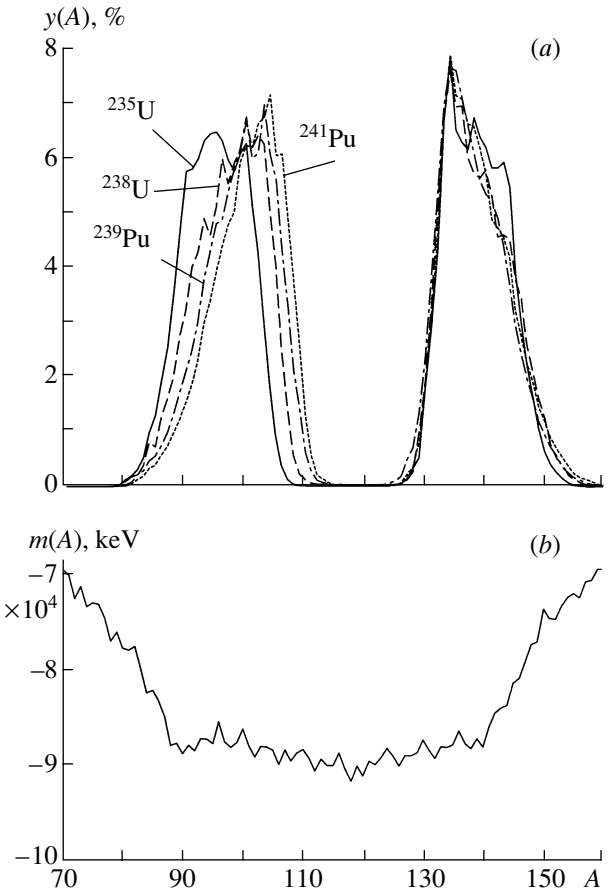

Fig. 1. (a) Total yield $y(A)$ of beta-stable fragments originating from the fission of uranium and plutonium isotopes; (b) mass excess $m(A)$ for beta-stable atoms as a function of the mass number A.

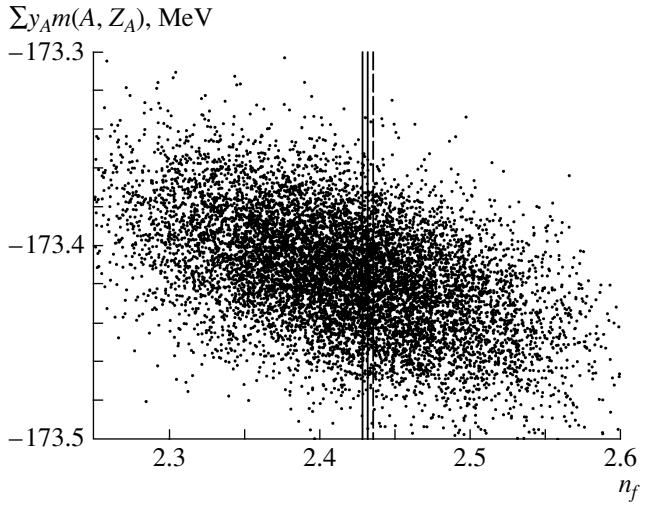

Fig. 2. Effect of the errors in the yield of products originating from ^{235}U fission on the mass defect $\sum y_A m(A, Z_A)$ (see main body of the text). The vertical band corresponds to the experimental value of the number n_f of neutrons.

That the calculation of the total energies E_{tot} on the basis of applying the energy-conservation law to the fission process was highly precise was due to the above features.

We also note that, in fact, the quantity $\sum y_A m(A, Z_A)$ is independent of the incident-neutron energy until the yields y_A change significantly near the humps of the mass distributions. The calculations reveal that, in ^{235}U and ^{239}Pu fission induced by neutrons of the fission spectrum, the deviation of $\sum y_A m(A, Z_A)$ from the values presented in Table 1 does not exceed 0.1 MeV.

The values of E_{tot} were obtained without taking into account ternary fission. Ternary fission accompanied by the emission of a long-range alpha particle occurs approximately in one of 500 cases; other types of ternary fission are much less probable. According to estimates, the change in E_{tot} upon taking into account ternary fission does not exceed 0.02%.

In calculating E_{tot}, we disregarded the alpha decays of ^{144}Nd, ^{147}Sm, and ^{149}Sm nuclei, which are formed upon the completion of beta-decay processes. The total yield of these alpha-particle emitters is about 10%; however, their half-lives exceed 10^{11} yr, so that they make no significant contribution to the energy release.

2.2. Effective Energy E_{eff}

In this subsection, we describe schematically a procedure for calculating the energies $\langle E_\nu \rangle$ carried away by antineutrinos and the corrections $\Delta E_{\beta\gamma}$ and present the results of these calculations, along with the values found for the effective energies E_{eff} according to relation (3a).

1. Along with electron antineutrinos ($\bar{\nu}_e$) emitted by fission fragments, a considerable number of electron antineutrinos are generated in a reactor that are emitted in the beta decay of nuclei produced upon the activation of the materials occurring in the reactor by neutrons. In calculating the energy $\langle E_\nu \rangle$, we take into account only those reactor antineutrinos that are emitted by fission fragments not perturbed by the interaction with neutrons rather than all of them.

The $\bar{\nu}_e$ spectrum decreases fast with increasing energy E_ν, virtually vanishing at $E_\nu \approx 10$ MeV. In this spectrum, the hard section $E_\nu \geq 2$ MeV contains about 60% of the energy $\langle E_\nu \rangle$ that is carried away by antineutrinos.

In the case of ^{235}U, ^{239}Pu, and ^{241}Pu, the $\bar{\nu}_e$ spectra necessary for calculating $\langle E_\nu \rangle$ were determined in the following way:

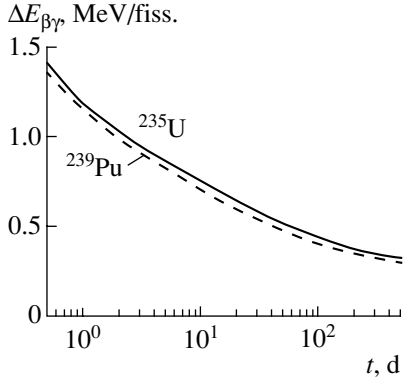

Fig. 3. Energy $\Delta E_{\beta\gamma}$ of beta and gamma radiation from fission fragments that did not decay as a function of the chain-reaction time t.

For the region of energies above 1.8 MeV, use was made of the spectra found in the Laue–Langevin Institute (ILL) by reconstructing the measured spectra of beta electrons emitted by fission fragments [11], small corrections of about 2.5% that correspond to the contributions of long-lived beta emitters [12] and which were disregarded in [11] being introduced in these spectra.

The $\bar{\nu}_e$ spectra that we calculated for the energy range 0–3 MeV were smoothly matched in the segment between 2 and 2.5 MeV with the corrected ILL spectra. As a result, the calculated values changed by 2 to 3%.

In the case of ^{238}U, the energy $\langle E_\nu \rangle$ was found on the basis of the $\bar{\nu}_e$ spectrum calculated in the present study.

In the region $E_\nu < 2$ MeV, it is not easy to estimate the error in the energy carried away by electron antineutrinos. The database used in the relevant calculation includes information about 571 fission fragments. For them, the overwhelming majority of decay diagrams is well known. The error in determining this part of $\langle E_\nu \rangle$ is likely to be within 4%.

We recall that, in fission, nuclei emit about $6\bar{\nu}_e$ of mean energy approximately equal to 1.5 MeV. For the fissile isotopes in question, the $\langle E_\nu \rangle$ values (in MeV/fiss.) found in the way outlined above are

$$^{235}\mathrm{U}:\ 9.07 \pm 0.32, \quad ^{238}\mathrm{U}:\ 11.00 \pm 0.80, \qquad (11)$$
$$^{239}\mathrm{Pu}:\ 7.22 \pm 0.27, \quad ^{241}\mathrm{Pu}:\ 8.71 \pm 0.30.$$

We note that the errors in our knowledge of the outgoing-neutrino energies $\langle E_\nu \rangle$ are much greater than the errors in determining the energies E_{tot}.

Part of the energy carried away by antineutrinos of energy $E_\nu \geq 1.8$ MeV can be directly compared with data obtained in an experiment at the reactor of the Rovno atomic power plant [13]. In that experiment, the positron spectrum was measured in the inverse-beta-decay reaction $\bar{\nu}_e + p \to e^+ + n$, and the $\bar{\nu}_e$ spectrum was reconstructed in the energy region $E_\nu > 1.8$ MeV. The value found with the aid of this spectrum for the energy that is carried away is in satisfactory agreement with that which was calculated in the present study; that is,

$$X_{\mathrm{Rovno/calc}} = 4.679/4.815 = 0.972. \qquad (12)$$

2. We recall that the energy $E_{\beta\gamma}$ released upon the complete beta decay of a pair of fission fragments is contained in the total fission energy E_{tot}. The correction $\Delta E_{\beta\gamma}(t)$ takes into account the fact that, at the instant of observation t, the decay processes have not yet been completed,

$$\Delta E_{\beta\gamma}(t) = E_{\beta\gamma}(\infty) - E_{\beta\gamma}(t) = \int_0^\infty dt' f_{\beta\gamma}(t'), \qquad (13)$$

where $E_{\beta\gamma}(t)$ is the energy released per second at the instant t reckoned from the beginning of the fission process proceeding at a rate of 1 fiss./s and $f_{\beta\gamma}(t)$ is the energy released per unit time after a lapse of time t from a single fission event [compare with the analogous expressions in (4) for E_{tot}].

The energy $\Delta E_{\beta\gamma}(t)$ of fission fragments that did not decay first decreases fast with increasing duration of the irradiation of the fuel used; this decrease gradually becomes slower, with the result that, at an irradiation time of about 1.5 yr, $\Delta E_{\beta\gamma}(t)$ virtually reaches a plateau (see Fig. 3). The formation of this plateau is associated with fragments whose lifetime exceeds 30 yr. Presented immediately below are the values of $\Delta E_{\beta\gamma}(t)$ (in MeV/fiss.) at the fuel-irradiation time corresponding to the midpoint of the standard operating period of a PWR reactor:

$$^{235}\mathrm{U}:\ 0.35 \pm 0.02, \quad ^{238}\mathrm{U}:\ 0.33 \pm 0.03, \qquad (14)$$
$$^{239}\mathrm{Pu}:\ 0.30 \pm 0.02 \quad ^{241}\mathrm{Pu}:\ 0.29 \pm 0.03.$$

It is useful to have an analytic expression for the energy $\Delta E_{\beta\gamma}(t)$. Over a wide interval of the times t, the expression

$$^{\mathrm{fit}}\Delta E_{\beta\gamma}(t) = E_0 \exp(-\lambda_0 t^\alpha) + \epsilon, \qquad (15)$$

Table 2. Parameters of the functions $^{\mathrm{fit}}\Delta E_{\beta\gamma}(t)$

Fissile nucleus	E_0, MeV	λ_0	α	ϵ, MeV
^{235}U	8.80	2.15	0.108	0.185
^{238}U	9.20	2.22	0.106	0.165
^{239}Pu	8.50	2.18	0.109	0.155
^{241}Pu	8.20	2.16	0.105	0.135

Table 3. Balance of the absorption of neutrons not involved in the chain reaction and of the thermal energy E_{nck} released upon the absorption of a single neutron in a given material (midpoint of the operating period)

Material	Capture probability η_k, %	E_{nc}, MeV/neutron	Material	Capture probability η_k, %	E_{nc}, MeV/neutron
^{235}U	11.6	6.54	^{149}Sm	0.8	7.99
^{238}U	38.4	5.72	Other fragments	6.8	7.88
^{239}Pu	10.5	6.53	Zirconium	7.0	8.11
^{240}Pu	6.1	5.24	^{10}B	5.6	2.79
^{241}Pu	3.6	6.31	Water	4.4	2.22
^{135}Xe	3.4	7.49	Other materials	1.8	5.67

$$0.5 < t < 500 \text{ days},$$

at the E_0, λ_0, α, and ϵ values given in Table 2 agrees with the results of the precise calculation to within 2%. The first term in (15) describes an exponential decay with a decay probability decreasing with time, while the second term corresponds to the plateau.

3. To conclude this section, we present the values of the effective fission energy E_{eff} (in MeV/fiss.) that correspond to the midpoint of the reactor operating period:

$$^{235}\text{U: } 193.37 \pm 0.33, \quad ^{238}\text{U: } 194.60 \pm 0.81, \quad (16)$$
$$^{239}\text{Pu: } 199.80 \pm 0.28, \quad ^{241}\text{Pu: } 202.04 \pm 0.32.$$

3. TOTAL THERMAL ENERGY E_f

In this section, we quote the results obtained by calculating the energy E_{nc} (in MeV/fiss.) absorbed in a reactor upon the capture of neutrons not involved in the chain reaction, determine the total thermal energy E_f, and consider its variation within the reactor operating period.

1. Of the total number n_f of neutrons emitted in a fission event, only one contributes to the chain reaction. The remaining neutrons are absorbed almost completely in the reactor core, reflector, and vessel. The probabilities of the absorption of these neutrons by various substances and the energies E_{nk} released in the capture of one neutron in those substances are given in Table 3.

From those data, it can be seen that more than 80% of $n_f - 1$ neutrons are absorbed in the fuel and in the accumulated fission fragments. In all cases, with the exception of that of ^{10}B, the neutrons are absorbed via (n, γ) reactions. The energies E_{nk} include the energy of photons emitted in radiative neutron capture and, if beta-radioactive nuclei are formed, the energy of beta electrons and photons originating from the subsequent transformations of these nuclei.

The mean energy absorbed in the reactor in the capture of one neutron, $E_{n1} = \sum \eta_k E_{nck}$, and calculated on the basis of the data given in Table 4 is $E_{n1} = 5.97 \pm 0.15$ MeV/neutron, its variation within the interval from 1 day to the end of the operating period being 0.55 MeV/neutron.

At the midpoint of the reactor operating period, the energies $E_{nci} = E_{n1} \cdot (n_{fi} - 1)$ (in MeV/fiss.) entering into the total thermal energy of the fission of uranium and plutonium isotopes are

$$^{235}\text{U: } 8.55 \pm 0.22, \quad ^{238}\text{U: } 10.92 \pm 0.28, \quad (17)$$
$$^{239}\text{Pu: } 11.19 \pm 0.28, \quad ^{241}\text{Pu: } 11.56 \pm 0.29.$$

2. We now present the values obtained for the total thermal energies E_{fi} of fissile isotopes by summing the components found above.

The total thermal energy $E_f = \sum \alpha_i E_{fi}$ and the contributions of fissile isotopes to the total number of fission events within the operating period of a PWR reactor are given in Fig. 4 versus the time of reactor operation. At the midpoint of the operating period, we have $E_f = 205.3$ MeV/fiss. The errors in the values of E_f are estimated at 0.6 MeV, which corresponds to about 0.3%. They include both the errors in E_{tot}, $\langle E_\nu \rangle$, $\Delta E_{\beta\gamma}$, and E_{nc} and the errors in α_i. It is assumed that the latter are 5% (relative errors). The increase in E_f

Table 4. Thermal fission energies E_{fi} at the midpoint of the reactor operating period

Isotope	E_{fi}, MeV/fiss.
^{235}U	201.92 ± 0.46
^{238}U	205.52 ± 0.96
^{239}Pu	209.99 ± 0.60
^{241}Pu	213.60 ± 0.65

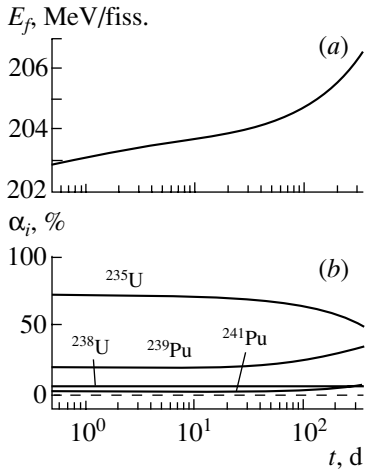

Fig. 4. (*a*) Total thermal energy E_f and (*b*) contributions α_i of fissile isotopes to the total number of fission events within the standard operating period of a PWR reactor versus the reactor-operation time t.

over the segment from 0.5 d after the start-up to the end of the operating period is 3.75 MeV. This increase is due to three reasons: the growth of the energy E_{nc} released in neutron capture, a decrease in the fraction of ^{235}U and an increase in the contributions of ^{239}Pu and ^{241}Pu in the process of reactor operation, and the "start-up effect" that is associated with the growth of the beta- and gamma-radiation energy and which is the most sizable within the first week after the start-up (see Fig. 4).

4. CONCLUDING COMMENTS

The energy E_f, which relates the number of fission events occurring in a reactor to its thermal power, has been calculated with an error of $\delta E_f/E_f \approx 3 \times 10^{-3}$. The high precision of the calculation of this energy has been achieved owing to the possibility of finding its main component $E_{\rm tot}$ with a relative error as small as about 5×10^{-4}. The three other components, $\langle E_\nu \rangle$, $\Delta E_{\beta\gamma}$, and E_{nc}, have been computed to a poorer precision, but they are relatively small, not exceeding 5% of E_f.

The energy E_f increases throughout the operating period. At a constant thermal power, the number of fission events in the reactor decreases from the beginning to the end of the operating period.

We note that all of the components appearing in expression (3) for the energy E_f, with the exception of E_{nc}, are characteristics of the fission of the nuclei being considered, so that their calculation is based on nuclear-physics data—in particular, data associated with the physics of fission.

The special features of a reactor manifest themselves in the following:

Use is made of the chain-reacting condition, which implies that one of the fission neutrons from the preceding generation induces one new fission process in the next generation.

Numerical data on the fission branching fractions α_i and on their time dependence are employed.

The term E_{nc} is calculated with the aid of data on the balance of neutron absorption in a reactor.

As a typical example, we have presented results (see Fig. 4) concerning a standard operating period of PWR reactors, which are widely used in Europe, the United States of America, and Japan. However, an actual operating period of a PWR reactor may differ from a standard one significantly. There also exist other high-power reactors at which neutrino investigations are presently being performed or are planned. These reactors differ from their PWR counterparts in the duration of the operating period, the enrichment of the nuclear fuel used, and some other special features. In all such cases, the method developed in the present study and the results obtained here can be used in neutrino investigations to perform a quantitative analysis of the relationship between the level of power and the rate of the chain reaction in the reactor core.

Thermal fission energies were calculated for the first time more than 30 years ago [14]. Later on, a new calculation was performed [15] in connection with neutrino investigations at the Rovno atomic power plant. In the present study, we have employed the most recent data concerning the issue being considered and, for the first time, have traced the dynamics of thermal fission energy throughout the reactor operating period.

ACKNOWLEDGMENTS

We are grateful to M.S. Yudkevich, V.D. Sidorenko, and S.N. Bolshagov for consultations on problems in the physics of nuclear reactors.

This work was supported by the Russian Foundation for Basic Research (project no. 03-02-16055) and was also funded with a grant in support of leading scientific schools.

REFERENCES

1. Yu. Kozlov *et al.*, Nucl. Phys. B (Proc. Suppl.) **87**, 514 (2000).
2. A. G. Beda, E. V. Demidova, A. S. Starostin, and M. B. Voloshin, Yad. Fiz. **61**, 72 (1998) [Phys. At. Nucl. **61**, 66 (1998)].
3. M. Appolonio *et al.* (CHOOZ Collab.), Phys. Lett. B **420**, 397 (1998); **466**, 415 (1999).

4. KamLAND Collab., Phys. Rev. Lett. **90**, 021802 (2003).
5. H. T. Wong and J. Li, hep-ex/0201001.
6. S. Schoenert, T. Lassere, and L. Oberauer, hep-ex/0203013.
7. A. V. Derbin, Fiz. Élem. Chastits At. Yadra **32**, 739 (2001); L. A. Mikaelyan, Yad. Fiz. **65**, 1206 (2002) [Phys. At. Nucl. **65**, 1173 (2002)].
8. G. Audi and A. H. Wapstra, Nucl. Phys. A **595**, 409 (1995).
9. T. R. England and B. F. Rider, LA-UR-94 3106, ENDF-349, LANL (Los Alamos, 1994).
10. L. P. Abagyan *et al.,* Vopr. At. Nauki Tekh., Ser.: Fiz. At. Reaktorov, No. 3, 50 (2001).
11. K. Schreckenbach *et al.*, Phys. Lett. B **160B**, 325 (1985); A. Hahn *et al.*, Phys. Lett. B **218**, 385 (1989).
12. V. I. Kopeikin, L. A. Mikaelyan, and V. V. Sinev, Yad. Fiz. **64**, 914 (2001) [Phys. At. Nucl. **64**, 849 (2001)].
13. V. I. Kopeikin, L. A. Mikaelyan, and V. V. Sinev, Yad. Fiz. **60**, 230 (1997) [Phys. At. Nucl. **60**, 172 (1997)].
14. M. F. James, J. Nucl. Energy **23**, 517 (1969).
15. V. I. Kopeikin, Preprint No. IAÉ-4305/2 (Kurchatov Institute of Atomic Energy, Moscow, 1986).

Translated by A. Isaakyan

Physics of Atomic Nuclei, Vol. 67, No. 10, 2004, pp. 1900–1917. Translated from Yadernaya Fizika, Vol. 67, No. 10, 2004, pp. 1923–1939.

ELEMENTARY PARTICLES AND FIELDS
Experiment

Energy Spectrum of Cosmic Rays and Multiparticle Generation of Hadrons at Ultrahigh Energies

S. I. Nikolsky[†] **and V. G. Sinitsyna**

Lebedev Institute of Physics, Russian Academy of Sciences, Leninskiĭ pr. 53, Moscow, 117924 Russia

Received January 26, 2004

Abstract—None of the presently known local sources of photons whose energy exceeds 10^{12} eV is incompatible with the universal energy spectrum $F(>E_\gamma) \sim E_\gamma^{-1.36\pm0.15}$. The power of extragalactic sources is 10^6 to 10^{12} times higher than the power of galactic sources since the respective distances are longer in the former case, while the observed flux intensities are approximately identical in the two cases. A much higher power of extragalactic sources is indicative of an extragalactic cosmic-ray origin and of the existence of a universal (for all energies of protons and cosmic-ray nuclei) process that is responsible for the energy loss in the Metagalaxy and which forms the observed energy spectrum of protons and nuclei ($\sim E_0^{-2.72}$). It is shown that there is no break in the energy spectrum of primary protons in the energy range 10^{15}–10^{16} eV and that the break in the spectrum of extensive air showers with respect to the number of electrons is due to a change in the process of multiparticle hadron generation in the first event of extensive-air-shower production, this being confirmed by a change in the extensive-air-shower absorption length from $\lambda_a < 90$ g/cm^2 before the break to $\lambda_a > 150$ g/cm^2 after the break.

By the region of ultrahigh energies, one most frequently means an energy region that is not covered by investigations at present-day proton accelerators. Therefore, investigation of primary cosmic radiation and analysis of multiparticle hadron generation at energies in excess of accelerator energies are the main lines of research in dealing with the propagation of primary cosmic rays through the atmosphere, where there occurs the development and absorption of extensive air showers of electrons, hadrons, and muons.

As far back as 1958, the observation of extensive air showers [1–12, 14–16] generated by cosmic-ray protons and nuclei revealed a boundary between cosmic rays of high and ultrahigh energies, which manifests itself as a break in the spectrum of extensive air showers with respect to the number N_e of electrons at $N_e \cong 10^6$ [1]. Near the maximum of the development of extensive air showers, this value corresponds to primary-proton energies in the range 3×10^5–2×10^6 GeV. So broad an interval for the primary-particle energy at a rather clear-cut break in the spectrum of extensive air showers with respect to the number of electrons is a consequence of the uncertainty in the reasons for the break in the spectrum of extensive air showers. If, as has been generally accepted since the discovery of the break, it reflects a change in the energy spectrum of cosmic-ray protons, the energy corresponding to the break in the spectrum of primary cosmic rays must be virtually coincident with the total energy of extensive air showers since, under this assumption, the relation between the observed number of electrons in a shower and the energy of a primary particle undergoes no change upon passing the break. If, however, a change in the process of multiparticle hadron generation at some primary-proton energy is the reason behind the break in question, then the point of the break in the observed spectrum of extensive air showers corresponds to the sum of the flux of showers developing in accordance with processes characteristic of showers having lower energies and the flux of showers initiated by some unknown multiparticle-hadron-generation process for which showers involve a smaller number of electrons at the observation level because of enhanced absorption in the upper atmosphere. The latter point of view is less popular, partly because it entails a problem that is difficult for an experimental investigation—the mechanism behind the change in processes that occur in the first shower-production event must be reconstructed on the basis of information about the subsequent development of a shower in the depth of the atmosphere.

A detailed investigation into the development of extensive air showers in the the region where their spectrum with respect to the number of electrons undergoes a break begins from selecting showers that

[†] Deceased.

are generated by primary protons. The flux of primary cosmic rays is dominated by protons, the depth to which they penetrate into the atmosphere prior to undergoing the first inelastic collision being the greatest. Showers generated by nuclei are averaged over the number of nucleons and nuclear fragments produced near the upper atmosphere in a collision of a primary-cosmic-radiation nucleus with the nucleus of an air atom.

In order to study in detail showers generated by primary protons, an experimental facility for analyzing the central region of showers had been created by 1970 at the Tien Shan mountain station of the Lebedev Institute of Physics [2]. This made it possible to distinguish between showers generated by primary protons and nuclei by using the properties of the development of the electron–photon component of extensive air showers. An ionization calorimeter of area 6×6 m^2, where the fluxes of the energies associated with the electron–photon and the hadron component of extensive-air-shower cores were determined on the basis of data on absorption, the resolution of the jet structure of the energy fluxes being $\gtrsim 0.3$ m, was at the center of the facility. The symmetry axis of the lateral distribution of the electron–photon component of extensive air showers was determined to a precision not poorer than 1 m within a radius of 8 m from the calorimeter center and to a precision of about 2 m at distances not longer than 20 m from the calorimeter. Detailed information about the lateral distribution of the electron–photon component in each shower up to distances of about 70 m for the case where the total number of electrons in an extensive air shower was in excess of 10^5 at the observation level made it possible to break down the extensive air showers being studied into groups corresponding to different values of the parameter S characterizing the cascade development of the electron–photon component[1] (see Fig. 1). The experimental data in this figure, which shows, for two observation levels, the fluxes of extensive air showers characterized by different values of the parameter S, corroborate the correctness of employing this parameter of the theory of electron–photon showers in analyzing extensive air showers generated by protons and cosmic-ray nuclei. The absorption of the electron flux in extensive air showers having S values in the regions $S \leq 0.75$ and $0.75 < S \leq 1.05$ and belonging to the spectral section before the break is approximately consistent with the generation of these showers by protons whose absorption length is $\lambda \cong 80 \pm 5$ g/cm^2, this being in accord with the effective cross section for proton scattering on the nuclei of air atoms if one considers that the depth corresponding to the maximum of the development of extensive air showers increases with increasing primary energy. It is of importance that both primary nuclei and 80% of primary protons transfer more than 70% of their energy to the respective electron–photon shower in the upper half of the atmosphere. For this reason, subsequent interactions of hadrons deep in the atmosphere have but a small effect on the development of the electron–photon component of extensive air showers generated by protons.

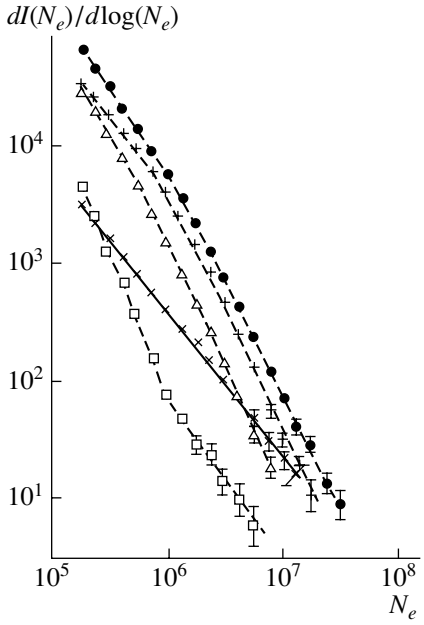

Fig. 1. Total spectrum of extensive air showers with respect to the number of electrons at the depth of 760 g/cm^2 in the atmosphere for $N_e = 1 \times 10^5 - 3 \times 10^7$ (•) and four components of this spectrum that correspond to various values of the parameter S: (right crosses) $S = 0.75-1.05$, (open triangles) $S = 1.05-1.35$, (inclined crosses) $S = 0.35-0.75$, and (open boxes) $S = 1.35-1.95$.

The group of showers occurring at the maximum of their development ($0.75 < S \leq 1.05$) contains the greatest number of showers. All of the showers that are responsible for the break in the spectrum of extensive air showers at the point where the number of electrons in a shower is $N_e \cong 10^6$ belong to this group. In order to explain the break in the spectrum of extensive air showers, one can assume either a change in the energy spectrum of primary protons or a considerable increase in the multiplicity of secondary hadrons in events of extensive-air-shower generation in a collision of a primary proton with nucleons of nuclei of air atoms. The threshold energy at which the process of multiparticle hadron generation is expected to undergo a change is estimated at 4×10^3 GeV

[1] The possibility of reconstructing the degree of the development of an extensive air shower above the observation level was demonstrated by B. Rossi in the report presented at the ICRC of 1960 [3].

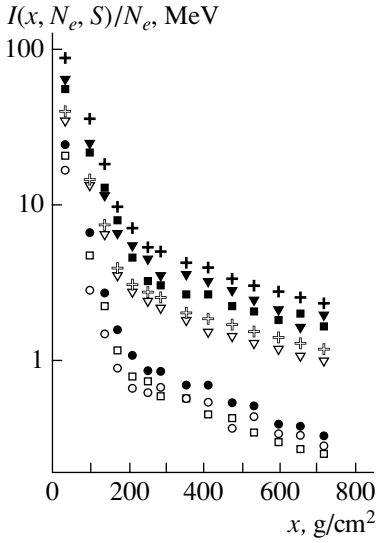

Fig. 2. Absorption in the ionization-calorimeter lead of the electron–photon component of the cores of extensive air showers featuring (closed and open crosses) (1–3) $\times 10^5$, (closed and open inverted triangles) (3–10) $\times 10^5$, (closed and open boxes) (1–3) $\times 10^6$, and (closed and open circles) (3–10) $\times 10^6$ electrons each for (closed symbols) $S > \bar{S}$ and (open symbols) $S < \bar{S}$, where $\bar{S}$ is the mean number of the parameter S for a given group of showers containing a specific number of electrons in a shower.

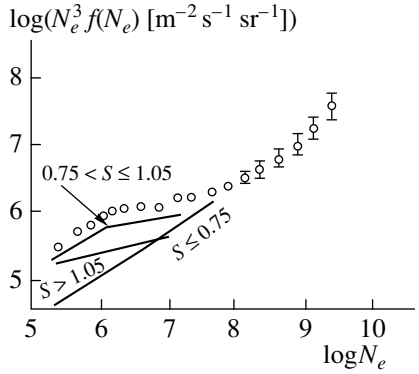

Fig. 3. Differential spectrum of extensive air showers (open circles) from [16] (the ordinates of the spectrum were multiplied by N_e^3, where N_e is the number of electrons corresponding to the abscissa). The solid lines represent the result obtained by decomposing the total spectrum of extensive air showers within the interval $N_e = 2 \times 10^5 - 2 \times 10^7$ into three components: showers generated predominantly by primary nuclei in the upper atmosphere ($S > 1.05$), showers generated by protons deep in the atmosphere ($S \leq 0.75$), and the group that was generated by primary protons and helium nuclei in the upper atmosphere (that is, at an altitude greater than that corresponding to 200 g/cm^2) and which contains the greatest number of showers.

in the c.m. frame of colliding hadrons. Extensive air showers generated by primary nuclei in the upper atmosphere (that is, at an altitude greater than that corresponding to 100 g/cm^2) are averaged during their development over the number of nucleons and nuclear fragments after the first interaction event. With increasing energy of a primary nucleus, the averaging and subsequent absorption of the hadronic shower are enhanced in relation to what one has for the hadronic shower from a primary proton. In the lower half of the atmosphere, the fraction of showers that are generated by nuclei and which contain not less than 10^6 electrons in a shower is less than 10% of the total flux of extensive air showers involving the above number of electrons.

It is reasonable to expect that the multiplicity of hadrons produced in inelastic nucleon–nucleon collisions is maximal in the case where a single excited lump of gluons and quarks is formed in the c.m. frame of colliding nucleons. Similar models of multiparticle hadron production were theoretically considered by Heisenberg, Fermi, and Landau in the period between 1950 and 1953, but observations of inelastic collisions in cosmic rays and at accelerators revealed that a discrete excited system is not formed at energies less than 3×10^7 GeV in the c.m. frame of colliding nucleons. As will be shown below, available experimental data give sufficient grounds to believe that, over the entire range of primary-cosmic-radiation energy studied thus far, the energy spectrum of primary protons has no breaks up to energies of the presumed relic cutoff of primary nuclei and protons and that the observed break in the spectrum of extensive air showers with respect to the number of electrons in a shower is due to a considerable increase in the multiplicity of product hadrons in the formation of a discrete excited hadron system (quark–gluon plasma) at energies in excess of 4 TeV in the c.m. frame of colliding nucleons. This manifested itself experimentally in calorimetric data on the energies of hadrons and of the electron–photon component in extensive-air-shower cores, since these data provide an unambiguous indication of an increase in the energy loss in the upper atmosphere with respect to the electron flux at the observation level (see Fig. 2).

1. ENERGY SPECTRUM AND NUCLEAR COMPOSITION OF PRIMARY COSMIC RAYS

In order to solve the problem of the origin of cosmic rays, it is of importance to determine the nuclear composition of primary cosmic rays. However, one can disregard the presence of nuclei in primary cosmic rays in studying the energy spectrum of primary radiation and, the more so, in examining extensive-air-shower generation with the aim of revealing changes in the process of multiparticle hadron production with

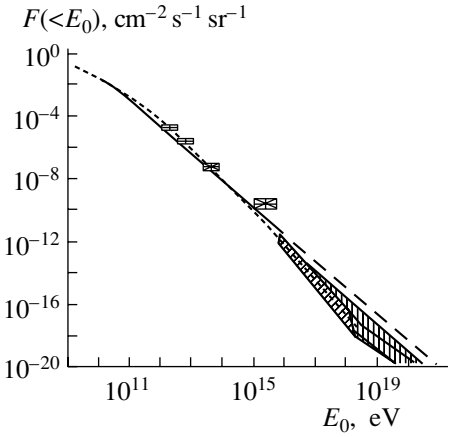

Fig. 4. Energy spectrum of primary cosmic rays. The curve (short dashes) was taken from [3]. The boxes and the band covered with inclined shading represent experimental data quoted in [3]. The solid line corresponds to experimental data obtained beyond the atmosphere and generalized in the monograph of Murzin [9], while the continuation of the straight line (long dashes) is the extrapolation of the spectrum by the present authors to higher energies. The band covered with vertical shading represent experimental data from the review article of Gaisser and Stanev [4] (see also Fig. 13 in [2]).

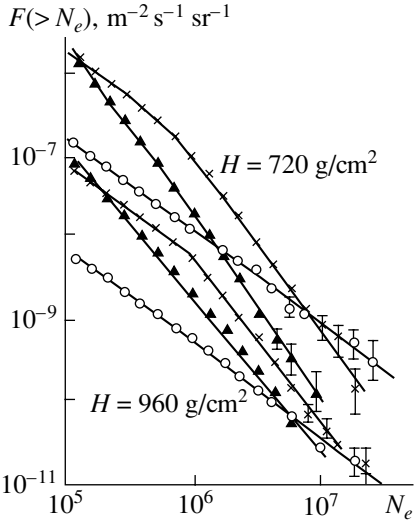

Fig. 5. Three components of the total flux of extensive air showers with respect to the number N_e of electrons at various values of the parameter S at the observation level of 720 g/cm^2 for angles smaller than 25° (three upper curves) and at the observation level of 960 g/cm^2 for angles not smaller than 25° (three lower curves): (open circles) $S \leq 0.75$, (inclined crosses) $0.75 < S \leq 1.05$, and (closed triangles) $S > 1.05$.

increasing energy of primary protons interacting with nuclei of air atoms. In primary cosmic rays of energy per nucleon in the region $E_0 \geq 2.5$ GeV, the flux of nuclei is about 8%, which is only slightly above the error in estimating the total particle flux in extensive air showers. At energies of primary particles in excess of 10^{15} eV, extensive air showers whose properties and structure are the subject of investigation may disclose, in the lower half of the atmosphere, the presence of nuclei in the primary flux of cosmic rays only if the observation method used is able to exclude information about electron fluxes in extensive air showers at distances shorter than 50 m from the shower axis, but it turns out in this case that one simultaneously removes a significant fraction of showers generated by primary protons deep in the atmosphere. The exclusion of information about the lateral distribution of electrons in each observed shower at distances of 5 to 70 m from the shower axis leads to a considerable underestimation of the number of electrons in showers generated by primary protons deep in the atmosphere, although such "young" showers form an "inverse" break (see Fig. 3), thereby returning the spectrum of extensive air showers with respect to the number of electrons to a spectrum whose exponent is $\gamma = 2.7$, which is characteristic of extensive air showers before the break at $N_e \cong 10^6$. According to all relevant publications since 1958, the energy spectrum of primary cosmic rays in the energy range 10^3–10^6 GeV can be represented in the form $F(E_0)dE_0 \sim E_0^{-\gamma}dE_0$, where the exponent is $\gamma = 2.7 \pm 0.2$. Experimental data on the break in the spectrum of extensive air showers with respect to the number of electrons in a shower at $N_e \geq 4 \times 10^5$ were first presented at the Moscow International Cosmic Ray Conference in 1958 [1] (see Fig. 4).

Experimental information about the energy spectrum of primary cosmic rays whose energy is above 10^{14} eV is based on recording extensive air showers involving various numbers of electrons at the observation level, a determination of the number of electrons as a function of the zenith angle of shower arrival to the observation level making it possible to estimate the extensive-air-shower absorption length below the observation level.

Detailed investigations of extensive air showers at the Tien Shan mountain station of the Lebedev Institute of Physics began in 1970 from creating an experimental facility for studying the structure and composition of extensive air showers in the primary-particle-energy range 10^{14}–10^{17} eV. Those investigations were completed in 1988. A determination of the energies of the electron–photon and the hadron component in the core of each shower (see Fig. 2), along with an estimation of the age parameter S of an electron–photon shower, was a feature peculiar to the investigations in question, which have not been repeated anywhere so far. Employing this information and relying on the theory of electron–photon

showers, one can then determine the energy of a shower from the known altitude of its generation, since a primary proton (the more so, a primary nucleus) transfers, in three generations of the nuclear cascade in the upper atmosphere, more than two-thirds of its energy to the electron–photon cascade, with the result that the electron–photon shower further develops independently in the middle part of the atmosphere. Figure 5 demonstrates that, for the number of electrons in the range 2×10^5–2×10^7, an analysis of the total flux of extensive air showers in terms of the age parameter S is quite efficient. That the spectrum of young showers generated by protons deep in the atmosphere and characterized by $S \leq 0.75$ is described in terms of a single value of the exponent rules out the possibility that the energy spectrum of primary protons has a break, which could be responsible for a break in the total flux of extensive air showers featuring $N_e = 10^6$ electrons. Any traces of a break similar to the break in the total spectrum of extensive air showers are absent in all intervals of the parameter S, with the exception of the interval 0.75–1.05 near the maximum of the development of the electron–photon component of extensive air showers, in which case the number of electrons reflects most precisely the energy of an electron–photon shower and cannot exceed the energy of a primary particle. If the break in the spectrum of extensive air showers is a consequence of a change in the energy spectrum of primary cosmic rays, then it must inevitably begin from a change in the energy spectrum of showers generated by primary protons. However, Figs. 1 and 5 demonstrate the absence of any changes in the spectrum of extensive air showers generated by primary protons deep in the atmosphere. But if the break in the spectrum of extensive air showers is a consequence of changes in the generation of extensive air showers, then this must be reflected in the properties of showers generated by protons. In addition to the break in the spectrum of extensive air showers, one can see an increase in the absorption length from $\lambda_a \leq 90$ g/cm^2 to $\lambda_a \geq 150$ g/cm^2 in Fig. 1 and a more than four- to fivefold decrease in the energy flux in the cores of showers in Fig. 2. The formation of the break in the spectrum of extensive air showers with respect to the number of electrons and its location on the energy scale is associated with the fact that there arises a superposition of the flux of showers whose energy spectrum has an exponent of $\gamma = 2.7$, which is characteristic of cosmic rays before the break, and the flux of showers that have a higher energy, but which involve a smaller number of electrons at the observation level (because of an enhanced absorption in the upper atmosphere after the first interaction event in view of an increase in the multiplicity of the generation of secondary hadrons). The absorption of showers in the atmosphere that have a primary energy in excess of the energy of the break corresponds to the generation of extensive air showers in which the number of hadrons from the first collision between a primary proton and the nucleus of an air atom is much larger and to the formation of a shower without single nucleons carrying particular energies that is absorbed in accordance with the neutral-pion-absorption length ($\lambda_a \cong 150$–160 g/cm^2). Thus, the absorption of showers in terms of the number of particles in the lower half of the atmosphere before the break in the spectrum of extensive air showers reflects the leading role of nucleons in the energy spectrum of secondary hadrons from the multiparticle-generation process at colliding-nucleon energies of 3 to 4 GeV in the c.m. frame, and one can see manifestations of this in the fact that the extensive-air-shower absorption length is determined primarily by nucleons. At colliding-nucleon energies higher than 4 to 6 GeV in the c.m. frame, a sharp increase in the multiplicity of secondary hadrons results in that the absorption length assumes a value of 150 g/cm^2, which is peculiar to pions.

For showers characterized by age-parameter values in the range $0.35 < S \leq 0.75$, an extrapolation of the spectrum of extensive air showers with respect to the number of particles (see Fig. 5) predicts the emergence of an "inverse" break at $N_e \cong 10^8$ electrons in a shower. An experimental observation of this break "restores" the shape that the spectrum of extensive air showers has before the break (for $N_e < 10^6$)—that is, the exponent of the differential spectrum again takes the value of $\gamma = 2.7$ (see Fig. 3). It should be noted that, for the first time, the inverse break in the spectrum of extensive air showers was observed by Khristiansen more than thirty years ago [5], but that, upon going over to investigations of extensive air showers at arrays based on widely spaced detectors, this break was lost. In the observations reported in [6], the arrangement of electron-flux detectors was much denser over the area where it had been planned to seek shower cores, and it was owing precisely to this circumstance that the inverse break in the spectrum of extensive air showers with respect to the number of electrons was rediscovered after a quarter of a century since its first observation. Unfortunately, the need for detailed information about the energy centroid of the showers under study in the case of widely spaced electron-flux detectors remains a serious problem that complicates investigations of cosmic rays whose energy exceeds 10^{18} eV. Resort to additional information about Cherenkov light or ionization luminiscence cannot always compensate for detailed data on the composition and the lateral distribution of particles in the region of a shower core or on the lateral distribution of electrons at distances

less than 50 m from the axis of the observed showers, since Cherenkov light and ionization luminiscence are observable within rather short seasonal intervals. Data on the lateral distribution of electrons in a shower at distances less than 50 m from the axis of the shower being observed are an indispensable characteristic of the distribution before the maximum of its development. If there are no such data, one can lose extensive air showers generated by primary protons deep in the atmosphere.

The conclusion that the break in the spectrum near the point $N_e \sim 10^6$ is a consequence of a considerable increase in the multiplicity of hadrons produced in inelastic collisions between protons of primary cosmic radiation and nuclei of air atoms was drawn from an analysis of the spectrum of extensive air showers with respect to the number N_e of electrons in the interval $3 \times 10^5 \leq N_e \leq 3 \times 10^8$ and of the absorption of such showers. This conclusion is dictated by the absence of breaks in the spectrum of extensive air showers generated by primary protons deep in the atmosphere ($S < 0.75$) and by its universal shape in the energy range being considered. At such S values, hadron–electron cascades reflect the total energy of neutral pions generated by primary protons in their collisions with nuclei of air atoms. In the case where a shower is generated by a primary proton near the upper boundary of the atmosphere (both at low primary energies and in generation events leading to a high multiplicity of secondary hadrons), the energy of a primary particle is spent above the level of high-mountain observations, the maximum of the development of such a shower being at an altitude greater than the respective altitudes for showers produced in collisions of nucleons whose energies are less than $(4–6) \times 10^3$ GeV in the c.m. frame of colliding nucleons.

2. MULTIPARTICLE HADRON GENERATION AT ENERGIES IN THE RANGE $(4–6) \times 10^3$ GeV IN THE c.m. FRAME OF COLLIDING NUCLEONS

The conclusion that a new process of multiparticle hadron generation produces a discrete excited lump formed by the gluons and quarks of colliding nucleons appeared as an alternative result of an analysis of the reasons behind the break at $N_e = 10^6$ in the spectrum of extensive air showers with respect to the number of electrons. Along with an analysis of the spatial and energy features of a shower with allowance for the partition of showers into groups according to values of the age parameter S (see Fig. 5), which characterizes the development of the electron–photon component of a shower, a calorimetric measurement of the energies of the electron–photon and the hadron component of the shower core and the observation of the change in the shower absorption length from the primary-proton absorption length in the atmosphere to the absorption length of the avalanche of pions having approximately the same energy (see Fig. 1) give sufficient grounds to assume that multiparticle hadron production in the first event of extensive-air-shower generation undergoes a qualitative change. An extremely high multiplicity of hadrons is a significant feature of the new multiparticle-hadron-generation process. In calorimetric measurements of the energy flux in the cores of showers generated by primary protons and observed at an initial stage of the development of the electron–photon shower, it was found that the energy flux within a radius of about 1 m from the shower axis is commensurate with the total energy flux in an extensive air shower (that is, the energy flux carried by all of its components) [6]. On average, the development of the hadron–electron cascade terminates, because of multiparticle hadron generation, in the upper half of the atmosphere, since, after the third generation of the hadron cascade, approximately 70% of the primary-hadron energy is transferred to the electron–photon shower, irrespective of the energy of primary particles, if pions carry the bulk of energy in the multiparticle-generation process.

A feature peculiar to the present analysis is the first ever use of the partition of extensive air showers into groups according to stages of the development of electron–photon showers. Extensive air showers generated by primary nuclei and averaged during their development in the upper atmosphere have already passed their maximum when they reach the lower half of the atmosphere and constitute less than 10% of the total flux of showers. A direct observation of the multiparticle-production process in cosmic rays at energies not less than 4 TeV in the c.m. frame of colliding nucleons is hardly feasible at present in satellite-borne experiments beyond the atmosphere or balloon-borne experiments at high altitudes. In the next decade, it would be the most important to investigate the development of extensive air showers within the third to the fourth generation of a hadron cascade, in which case the energy in the electron–photon shower has just exceeded the total energy of hadrons in showers. The majority of the showers (more than 70% of them) observed near the maximum of their development that involve not less than $3–5 \times 10^6$ electrons have, in their cores, a relative energy that is four to five time less (this concerns both the electron–photon and the hadron component) than that in showers featuring a smaller number of electrons at the maximum of their development. A sharp decrease in the relative flux of energy in

extensive-air-shower cores and the threefold distinction between the numbers of electrons in showers that accompanies this decrease in the energy flux in the core of an extensive air shower after the break in the spectrum (see Fig. 2) cannot be explained by a change in the energy spectrum of primary cosmic rays or by the disappearance of protons from their composition, since, for showers generated by primary protons deep in the atmosphere, there is no violation of a universal shape of the spectrum of extensive air showers with respect to the number of electrons (see Fig. 1). The break in the spectrum of extensive air showers occurring near the maximum of their development, in which case the flux of the electron–photon shower component is the most tightly related to the energy of primary particles that generated the extensive air shower in question, corresponds to more than a tenfold increase in the multiplicity of hadrons produced in an inelastic collision between a primary proton of cosmic radiation and the nucleus of an air atom. An increase in the multiplicity of secondary hadrons and the respective decrease in their energy results in that, for primary-proton energies in excess of 2×10^7 GeV, the maximum of the development of extensive air showers in the atmosphere is shifted to greater altitudes. The above increase in the multiplicity of secondary hadrons also entails a decrease in the primary-energy fraction transferred to a single pion produced in the first interaction of a cosmic-ray proton. This enhances the development of showers in the upper part of the atmosphere, where there are no direct observations. In the distribution of the maxima of the development of an electron–photon shower [7], the average altitude of the maximum in extensive air showers of primary energy in the range 5×10^7–5×10^8 GeV proved to be shifted to upper layers of the atmosphere in relation to the expected altitude. This can also be explained by a decrease in the fraction of protons in primary cosmic rays, but, in the investigations of extensive air showers at the Yakutsk array [8], the range with respect to inelastic proton interactions with nuclei of air atoms in the energy ranges 10^8–10^9 and 10^9–10^{10} GeV was determined by using the distribution of the altitudes of the maxima of the development of extensive air showers. Also, it was found that the flux of showers generated by primary nuclei disappears. Thus, we see that, for the disintegration of nuclei in collisions with microwave-background-radiation photons, the phrase the "cutoff of the spectrum" is fully adequate to the observed process.

Returning to the fact that the altitudes of the maximum in the development of extensive air showers undergo a shift, which confirms an increase in the multiplicity of hadrons generated in the first collision of protons with nuclei of air atoms, we note that, although some experimental data suggest a predominant primary-proton-induced generation of observed extensive air showers, the mean altitude of the maxima in the development of extensive air showers whose primary energies lie in the range 10^{16}–10^{18} eV corresponds to nuclei that contain 20 to 50 nucleons (see Figs. 12 and 17 in [9]).

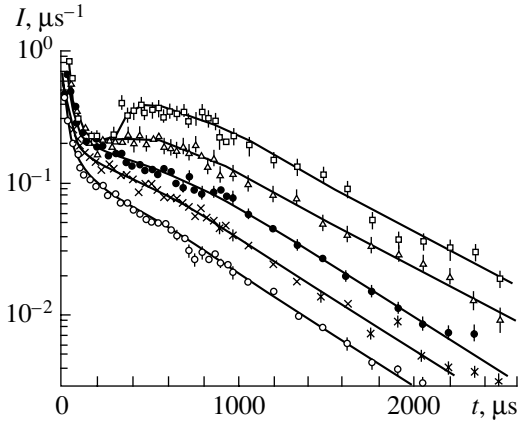

Fig. 6. Time distribution I of the number of neutrons for various values of the total multiplicity recorded by a neutron monitor: (open circles) 316–400, (inclined crosses) 500–630, (closed circles) 794–1000, (open triangles) 1284–1584, and (open boxes) 1995–2511 [6].

In the preceding section, we have demonstrated that it is necessary to assume an extremely high multiplicity of hadrons produced in inelastic collisions between primary protons and nucleons of the nuclei of air atoms at energies of 4 to 6 TeV in the c.m. frame of colliding nucleons. This is equivalent to the assumption that a hot quark–gluon plasma is formed, possibly because of the compression of colliding gluon fields. It can be hypothesized that the temperature of the hadronization of the quark–gluon plasma in the process of its cooling corresponds to the isotropic divergence of pions whose energy is about the transverse momenta of secondary particles in events of multiparticle production at primary-proton energies below 10^7 GeV. However, a simulation of the development and absorption of extensive air showers generated at an energy of 4 to 6 TeV in the c.m. frame of two colliding nucleons and a simulation of the ensuing isotropic divergence of pions having an energy of 0.5 GeV revealed that, at such multiplicities of hadrons in a shower-generation event, the development of a hadron cascade features only three generations, so that, at the altitude of the Tien Shan experiment (about 760 g/cm^2), it would be hardly possible to observe [10], in 3% of extensive air showers involving less than 10^6 electrons, anomalously high fluxes of nonrelativistic neutrons (see Fig. 6).

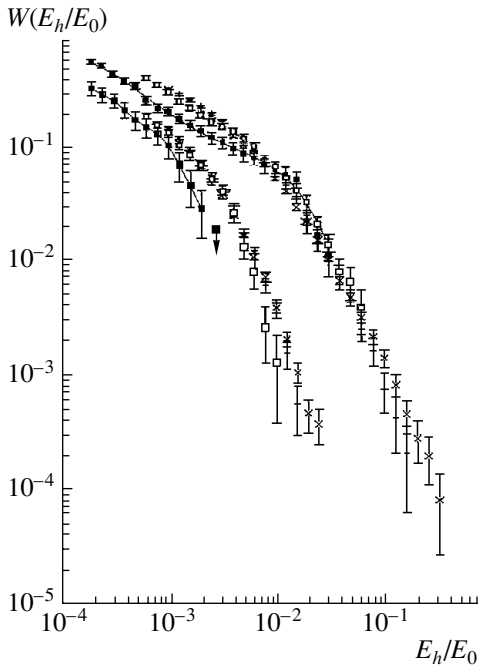

Fig. 7. Ratio of the energy E_h of hadrons in the core of an extensive air shower to the energy E_0 of the primary cosmic-ray particle for various ranges of N_e: (inclined crosses) $1.33 \times 10^5 < N_e < 3.2 \times 10^5$, (right crosses) $3.2 \times 10^5 < N_e < 10^6$, (open boxes) $10^6 < N_e < 3.2 \times 10^6$, and (closed boxes) $3.2 \times 10^6 < N_e < 10^7$. The upper group represents the spectra of jets having the highest energy, while the lower groups correspond to jets that follow it in order of decreasing energy [12].

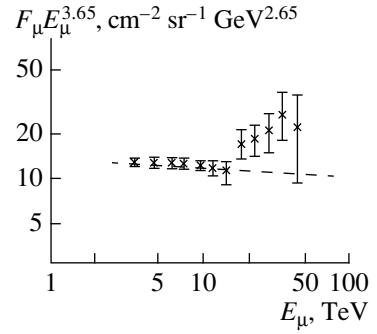

Fig. 8. Differential energy spectrum of muons from [11]. An increase in their flux corresponds to an event featuring the generation of up to 1000 hadrons (predominantly pions) at an energy not less than 4 TeV in the c.m. frame of colliding nucleons.

By and large, experimental data on nonrelativistic neutrons in showers containing more than 10^6 electrons and a four- to fivefold decrease in the flux of energy carried by hadrons in the cores of extensive air showers involving more than 3×10^6 electrons (see Fig. 7) are indicative of multiparticle hadron production within a discrete object in collisions between protons of primary cosmic radiation and nuclei of air atoms, provided that the energy of primary protons exceeds 4 TeV in the c.m. frame of colliding nucleons. In calculations of nuclear-cascade processes initiated in the atmosphere by primary protons of energy not less than 10^7 GeV, the formation of a large number of nonrelativistic neutrons does not contradict anything, but, in multiparticle-production events like those at primary-proton energies less than 10^{16} eV, a hadron shower propagates over the interior of the atmosphere, with the result that the production of nonrelativistic neutrons occurs in the major part of the atmosphere. In the laboratory frame (it should be recalled that a multiparticle-production event involving the generation of a large number of hadrons having approximately identical energies corresponding to the temperature of the hadronization of quark–gluon plasma is considered here), hadrons diverging isotropically with an energy of 4 to 5 GeV in the c.m. frame of colliding nucleons whose energy is not less than 4 TeV can be partitioned into three groups characterized by rather close energies within each group: the forward cone of generated hadrons; their backward cone turned out in the forward direction; and the group of secondary hadrons whose energy corresponds, on average, to the Lorentz factor of the center of mass of colliding hadrons (this group contains a three to four times greater number of hadrons than the first two). As was indicated above, a simulation of the process in question ruled out an isotropic divergence of a discrete system for energies less than 4 GeV, since, in that case, it would be impossible to observe, at the altitude of the Tien Shan station, showers involving a large flux of delayed neutrons [10]. Six to seven percent of extensive air showers of primary energy not less than 2×10^7 TeV that contain, in their cores, the same part of the primary-proton energy as showers generated at energies corresponding to the region before the break in the spectrum of extensive air showers with respect to the number of electrons (see Fig. 7) could not be observed either.

The long since known experimental observation [11] of a twofold increase in the flux of muons whose energy is not less than 14 TeV could not be explained in any way other than that which relies on a new multiparticle-production process yielding pions of high multiplicity, and this observation is likely to be a piece of direct evidence in favor of such a process.

Data on an increase in the flux of muons having energies in the range 10–20 TeV were reported as far back as 1981 at the Paris International Cosmic Ray Conference (see Fig. 8). The main difficulty in explaining this phenomenon is associated with the fact that, in the interior of the atmosphere, the decay of pions having such energies is next to impossible. The

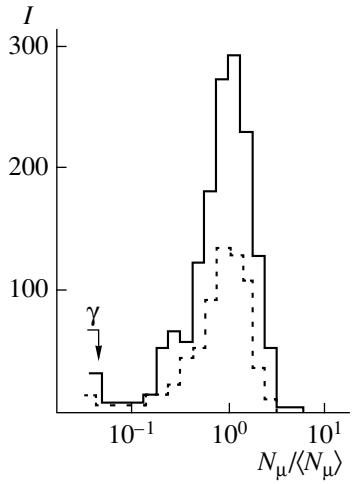

Fig. 9. Relative flux of extensive air showers generated by primary photons and selected by the absence of muons in the showers (the arrow in the figure indicates the limiting admissible value for primary photons): (dashed-line histogram) $N_e = (3–6) \times 10^5$ and (solid-line histogram) $N_e = (6–10) \times 10^5$. By way of example, we indicate that $I_\gamma(> 4 \times 10^{14}\ \text{eV}) = (3.4 \pm 1.2) \times 10^{-13}\ \text{m}^{-2}\ \text{s}^{-1}\ \text{sr}^{-1}$ and $F(> 4 \times 10^{14}\text{eV}) = 8.6 \times 10^{-10}\ \text{m}^{-2}\ \text{s}^{-1}\ \text{sr}^{-1}$.

appearance of these extra muons can be associated with the first events of nucleon interactions near the upper boundary of the atmosphere at energies above 4 TeV in the c.m. frame of colliding nucleons.

3. GALACTIC AND EXTRAGALACTIC SOURCES OF PHOTONS WHOSE ENERGY IS IN EXCESS OF 10^3 GeV

Searches for local sources of ultrahigh-energy cosmic rays on the basis of an excess of the extensive-air-shower flux within narrow angular intervals in the directions to the presumed sources began in the middle of the 20th century, but they have not yet given reliable results because of an extremely low flux of showers generated by photons, this being due to the accumulation of charged particles in the Metagalaxy, including intergalactic space. This was confirmed in experiments aimed at determining the total flux of extensive air showers initiated by photons and selected by the absence of muons and hadrons in them. Such showers were sought at the Tien Shan mountain station of the Lebedev Institute of Physics with the aid of the facility installed there for studying the structure of extensive air showers [2]. An analysis of the results obtained by observing showers of primary energy not less than 3×10^5 GeV revealed a relative rarity of such showers: $(0.5 \pm 0.1)\%$ of showers without hadrons in the total flux of extensive air showers and $(0.4 \pm 0.1)\%$ of showers without muons (see Fig. 9). The observed showers were classified as those that were generated by photons. In some cases, the coordinates of the discovered sources were coincident with those of active objects in the Metagalaxy. However, the statistical significance of such an interpretation is rather low. There are no difficulties of a conceptual character in determining a locus of photon generation, since the coordinates of many active objects in the Galaxy and Metagalaxy are available in the maps of the stellar sky. The problem is that one has to observe efficiently extensive air showers free from hadrons and muons against the background of more than 100 times higher flux of extensive air showers initiated by protons and nuclei, determining quite precisely (to within a few angular degrees) the zenith and azimuthal coordinates of a shower. The problem in question can in principle be solved with the aid of the SHALON facility (see Fig. 10), but this will require quite long-term observations.

The energy spectrum of protons and nuclei that was formed in active galactic objects is given by $F(E_h)dE_h \sim E_h^{-2.35\pm0.15}dE_h$, but this spectrum is corrected in intergalactic space because of an enormous number of elastic collisions with photons of cosmic microwave background radiation. The total energy loss is the sum of rare large energy losses (in collisions with nuclei and protons) and an indefinitely large number of small losses (in collisions with photons of cosmic microwave background radiation), this yielding the Napierian number—that is, 2.718...—a number that is extremely close to the observed exponent of the primary-proton spectrum in the energy ranges $10^{12}–10^{16}$ and $3 \times 10^{17}–10^{20}$ eV and which is reconstructed on the basis of the spectrum of extensive air showers. A weak manifestation of the relic cutoff of protons and the hard splitting of primary nuclei can be considered as a corroboration of the above assumption.

The spectrum of photons that are generated in active galactic cores in collisions between protons and nuclei and in their collisions with nonrelativistic protons and nuclei is a consequence of the fact that, prior to an ultimate formation of their energy spectrum $F(E_h)dE_h \sim E_h^{-2.718}dE_h$, cosmic-ray protons and nuclei accelerated in the magnetic fields of active galactic centers in the Metagalaxy had a spectrum whose exponent was about -2.35. During their acceleration, protons and nuclei must undergo inelastic collisions in traversing a layer of nonrelativistic protons and nuclei that has a thickness not less than some 6 g/cm^2. This is suggested by the fact that cosmic rays do not contain some of those nuclei that, according to spectral observations in the optical range of energies, are present at the surface of an active galactic core. The same layer of thickness

SHALON-1

SHALON-2

Fig. 10. High-mountain observatory SHALON in Ala Tau mountains.

about 6 g/cm^2 serves as a target for proton interactions resulting in the generation of photons whose energy spectrum reflects the spectrum of accelerated protons, the differential exponent of their power-law spectrum being -2.3.

At present, the use of mirror Cherenkov telescopes, which, apart from having a high angular resolution, enable one to reconstruct the pattern of the development of a shower over the depth of the atmosphere, thereby providing the possibility of testing the correspondence of the observed showers to the electron–photon component among ordinary extensive air showers, has become the most popular method for seeking and observing sources of photons. The table and Figs. 11–17 present data obtained by observing extragalactic and galactic photon sources with the SHALON telescope [13] (the power of photon radiation from the Crab nebula is taken to be unity). For each source, integrated spectra, a time analysis of events that arrived from the source and of background events obtained simultaneously with the observations, and the image of the source became the result of the investigation of data.

The uncertainty in the intensity of the photon flux from the Crab nebula (Fig. 11) is exaggerated since it was estimated with allowance for the distinction between the data obtained in the energy range 10^{12}–10^{14} eV with the aid of a gamma telescope and the data obtained on board cosmic vehicles for gamma-radiation fluxes in the energy range 10^8–10^{10} eV. (At the same time, this distinction may stem from the distinction between the photon-generation processes

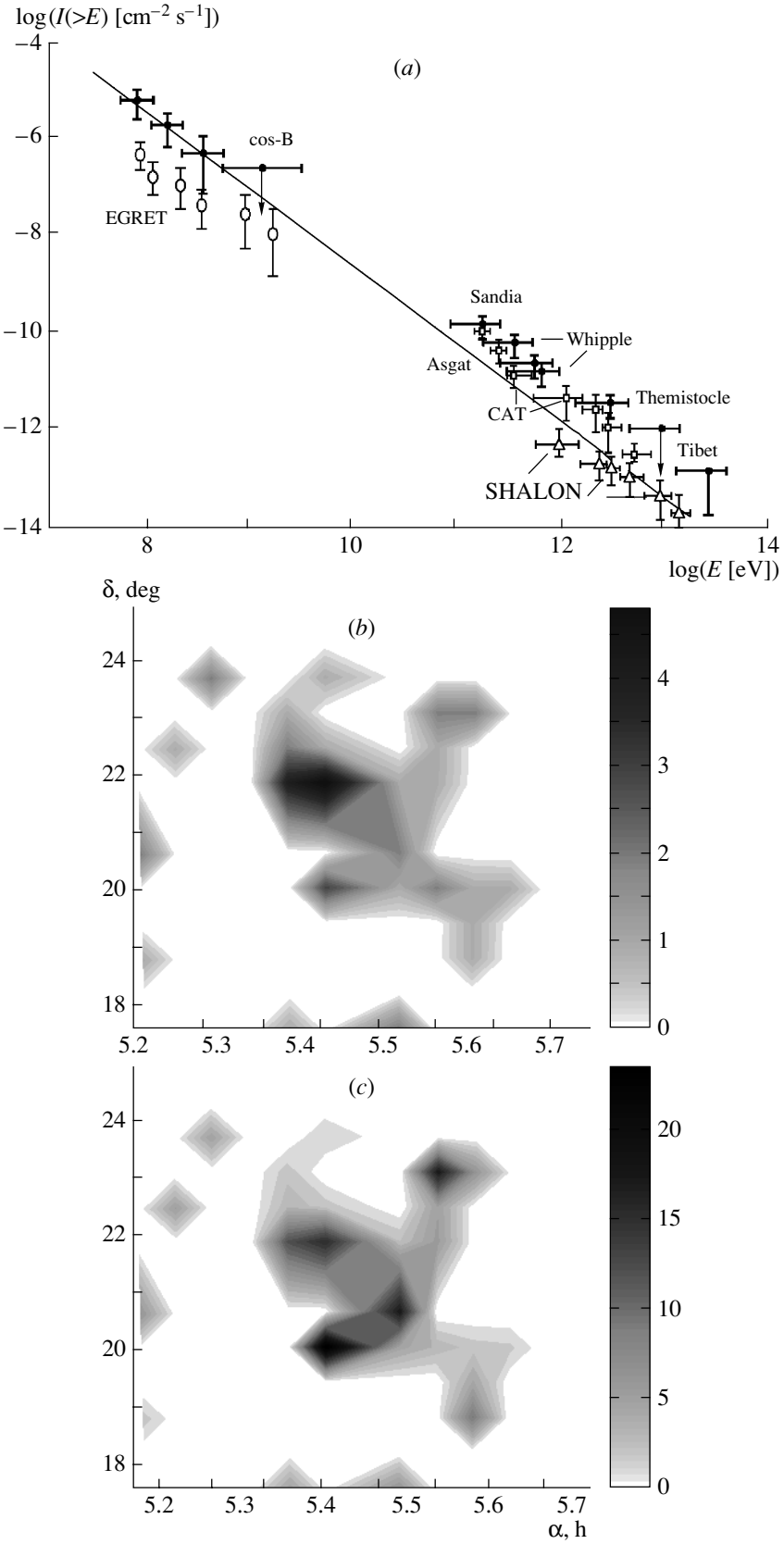

Fig. 11. (*a*) Integrated spectrum of photons ($E > 0.8$ TeV) from the Crab nebula according to SHALON data, along with data from other experiments [13]; (*b*) image obtained with the SHALON telescope for the Crab nebula pointlike source for energies in excess of 0.8 TeV; and (*c*) its energy representation.

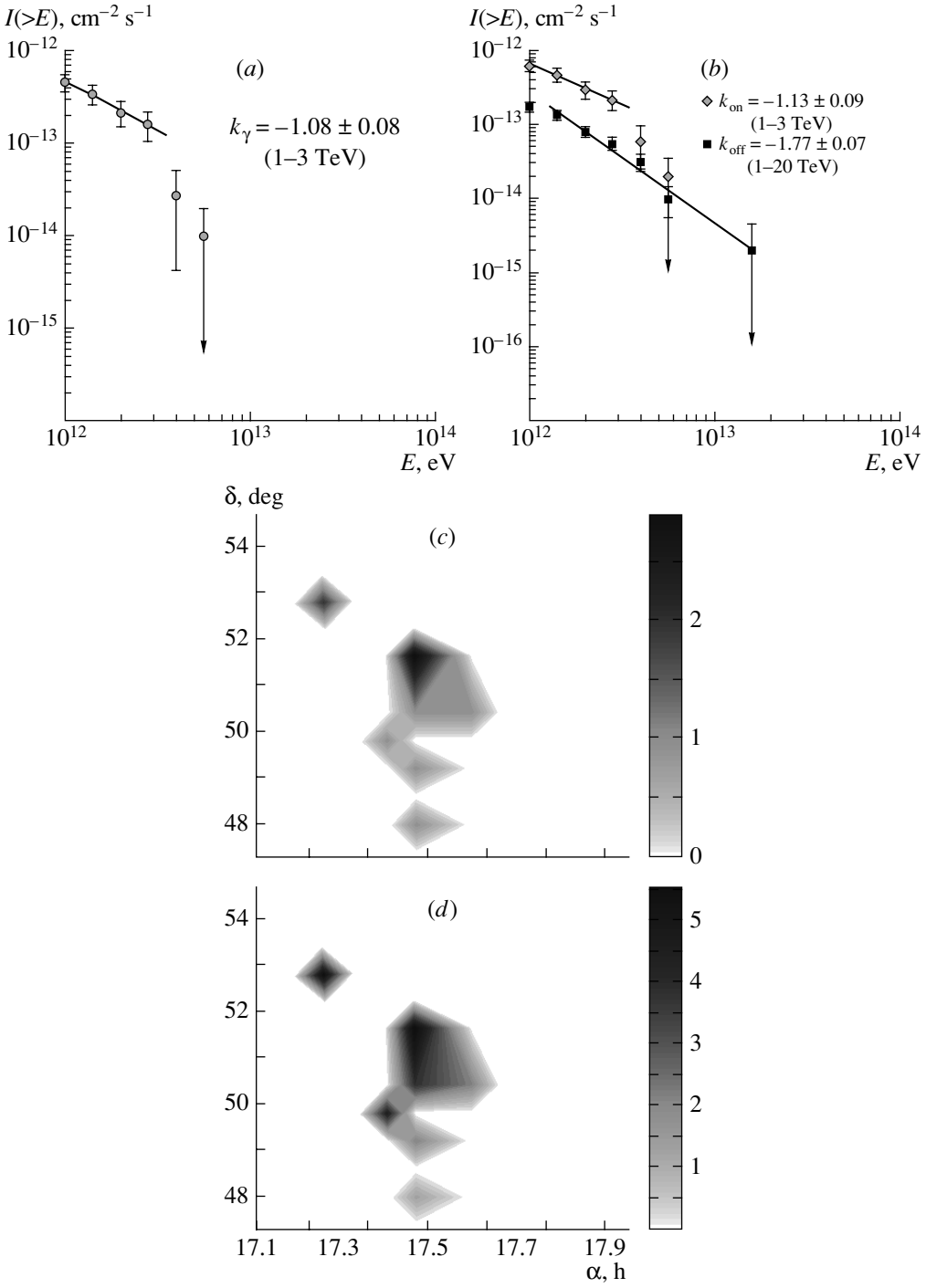

Fig. 12. (*a*) Integrated spectrum of photons ($E > 0.8$ TeV) from the $1739 + 522$ source with a power-law exponent of $k_\gamma = -1.08 \pm 0.08$ according to SHALON data; (*b*) spectrum of events from the $1739 + 522$ source that have passed selection criteria without background subtraction, $k_{on} = -1.13 \pm 0.09$, and spectrum of background events observed simultaneously with the $1739 + 522$ source, $k_{off} = -1.77 \pm 0.07$; (*c*) image obtained with the SHALON telescope for the $1739 + 522$ source for energies in excess of 0.8 TeV; and (*d*) its energy representation.

in the x-ray energy region and in the energy range 10^{11}–10^{14} eV.) The distinction between the power of sources observed in the Milky Way Galaxy and the power of extragalactic sources is the result of a formidable distinction between the distances to the observed objects, the times of observation being approximately identical. The most remote extragalactic source $1739 + 522$, which is characterized by a red-

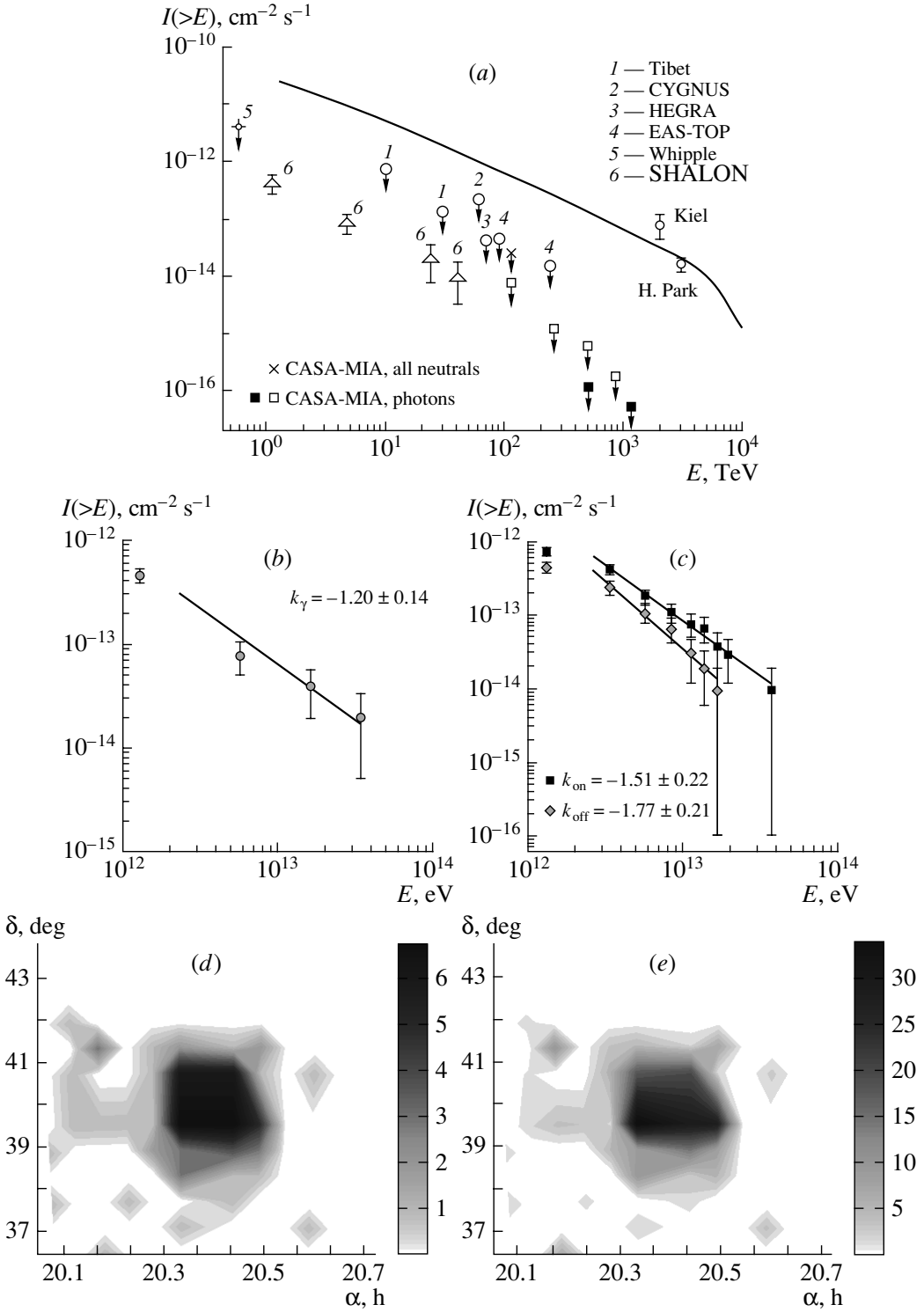

Fig. 13. (*a*) Integrated spectrum of photons ($E > 0.8$ TeV) from Swan X-3 according to SHALON data, along with data from other experiments [13]; (*b*) spectrum of gamma radiation from Swan X-3 with a power-law exponent of $k_\gamma = -1.20 \pm 0.14$; (*c*) spectrum of events from Swan X-3 that have passed selection criteria without background subtraction, $k_{on} = -1.51 \pm 0.22$, and spectrum of background events observed simultaneously with the Swan X-3 source, $k_{off} = -1.77 \pm 0.21$; (*d*) image obtained with the SHALON telescope for the Swan X-3 source for energies in excess of 0.8 TeV; and (*e*) its energy representation.

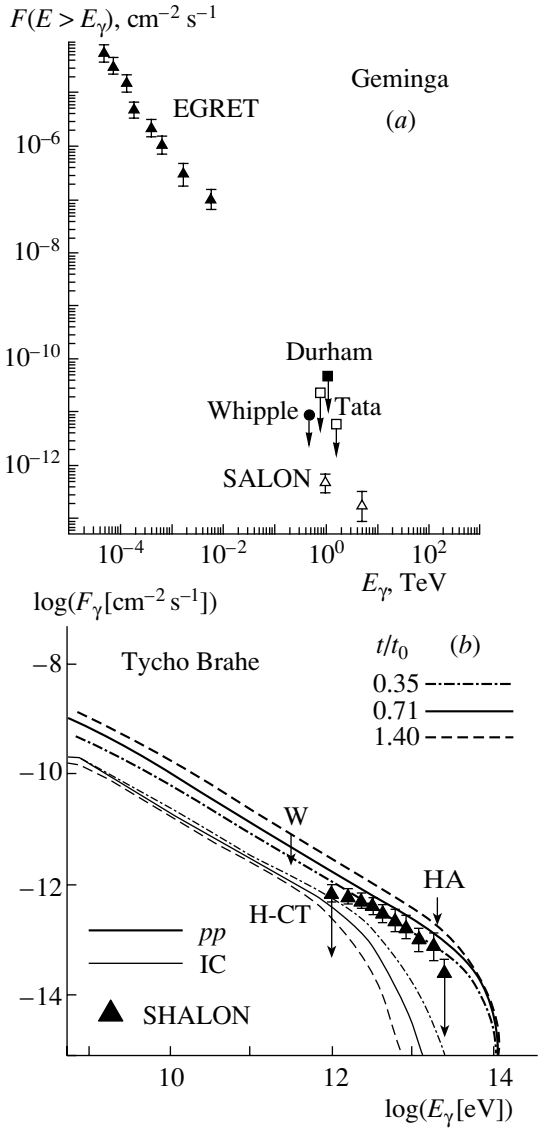

Fig. 14. (*a*) Integrated spectrum of photons ($E >$ 0.8 TeV) from Geminga according to SHALON data, along with data from other experiments [13]; (*b*) integrated spectrum of photons ($E > 0.8$ TeV) from Tycho Brahe according to SHALON data, along with data from other experiments [upper limits according to (W) Whipple, (H-CT) HEGRA IACT, and (HA) HEGRA AIROBICC] and results of the theoretical calculations due to G.F. Krymsky and E.G. Berezhko.

shift value of $z = 1.375$ in the optical range, is simultaneously the most powerful (see Fig. 12). However, the energy spectrum of gamma radiation from 1739 + 522 does not differ from the gamma-radiation spectrum averaged over the presently known extragalactic sources and two galactic ones [Swan X-3 (see Fig. 13) and Crab nebula (see Fig. 11)]; that is, it is proportional to $E_\gamma^{-1.35}$ in the integral representation.

The powers of gamma radiation from local sources in the Milky Way Galaxy (Figs. 11, 13, 14) are extremely small in relation to those of observed extragalactic sources (Figs. 12, 15–17), as can be seen from the table. This relationship will hardly change upon the accumulation of data on gamma-radiation sources in the Milky Way Galaxy. The distinction between the powers of the observed sources in the Metagalaxy and the Milky Way Galaxy fully corresponds to the scales and energies of the observed sources: these are quasars, Seifert galaxies, and active cores of galaxies in the Metagalaxy and the remnants of supernovae in the Milky Way Galaxy. Moreover, one has yet to find out conclusively whether supernovae such as the Crab nebula emit photons of energy 10^{16} eV or higher. Unfortunately, sources that emit photons of energy in excess of 10^{16} eV can hardly be observed by means of single Cherenkov telescopes, which cover only a limited area of extensive-air-shower cores. It is necessary to create facilities that ensure a large area of observation and a reliable selection of extensive air showers free from muons. The construction of large "fields" of Cherenkov gamma telescopes is hardly realistic. Searches for sources whose coordinates are a priori unknown are very cumbersome if use is made of gamma-telescope fields for this.

4. CONCLUSION

The currently available results of gamma-astronomy observations in the energy range 10^{12}–10^{14} eV put the following important problems to the fore: (i) that of explaining a sharp increase in the energy lost by a shower in the upper atmosphere, this being impossible without more than of an order of magnitude increase in the multiplicity of hadrons produced in the first nucleon-collision event; (ii) that of validating the partition of cosmic radiation into radiation of a galactic origin and radiation of an extragalactic origin; (iii) that of pinpointing processes through which the energy spectrum of cosmic rays that has a universal $E_k^{-2.72\pm0.01}$ form over the broad energy range 10^{11}–10^{19} eV arises from the radiation emitted by a great many local sources of cosmic rays, which has a harder energy spectrum of the $E_\gamma^{-2.35\pm0.10}$ form; and, finally, (iv) that of determining the fraction of photons in primary cosmic radiation.

The concept of a new process of the multiparticle production of hadrons, predominantly pions, in a discrete system of colliding nucleons at a projectile-nucleon energy of about 1 to 2×10^7 GeV makes it possible to extend, to the region of ultrahigh energies, the spectrum of protons and cosmic-ray nuclei that is observed at lower energies in the form of a power-law spectrum characterized by a differential-exponent

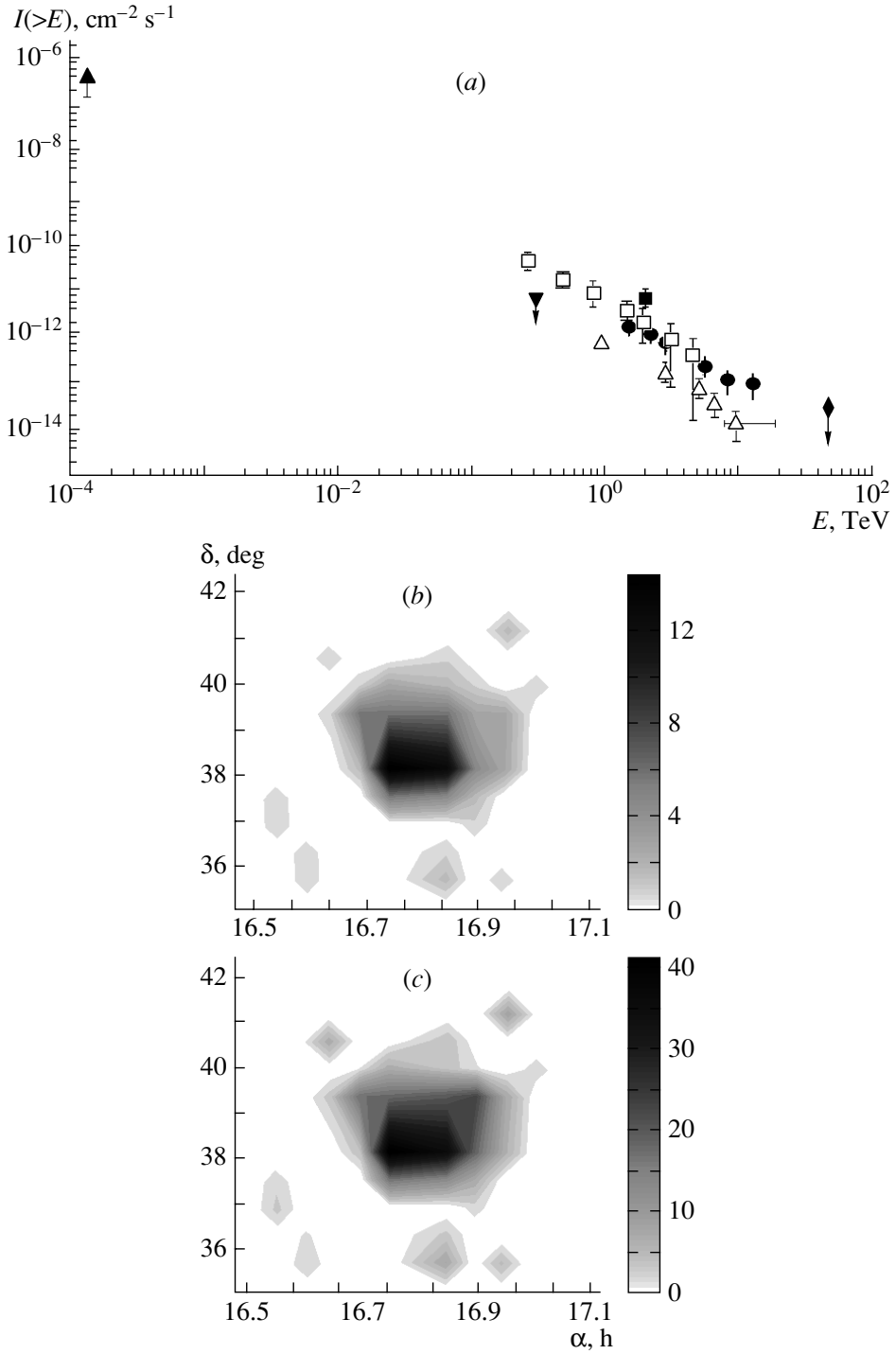

Fig. 15. (*a*) Integrated spectrum of photons ($E > 0.8$ TeV) from Markarian 501 according to SHALON data, along with data from other experiments [13]: (closed triangle) EGRET (D.J. Thompson, R. Mukherjee, *et al.*, 1997; F. Kataoka *et al.*, 1999), (closed inverted triangle) Whipple 1999 (T. Weekes *et al.*, 1999), (open boxes) CAT 97 (M. Punch *et al.*, 1997), (open triangles) SHALON 96–02 (V.G. Sinitsyna *et al.*, 2002), (closed box) TACTIC 97 (C. Bhat *et al.*, 1997), (closed circles) HEGRA CT1 96 (D. Petry *et al.*, 1997), and (closed diamond) CASA-MIA 96–97 (M. Catanese *et al.*, 1997); (*b*) image obtained with the SHALON telescope for the Markarian 501 source for energies in excess of 0.8 TeV; and (*c*) its energy representation.

Table

Sources generating photons of energy above 0.8 TeV	Observed flux, 10^{-12} cm^{-2} s^{-1}	Distance, Mpc	Relative power of a source
Galactic:			
Crab nebula	1.10 ± 0.30	2.0×10^{-3}	1
Swan X-3	0.42 ± 0.07	10.0×10^{-3}	0.12
Geminga	0.48 ± 0.17	0.25×10^{-3}	0.11
Tycho Brahe	0.19 ± 0.09	$(2.0–3.1) \times 10^{-3}$	0.3
Extragalactic:			
Markarian 421	0.63 ± 0.14	124 ($z = 0.031$)	3.8×10^9
Markarian 501	0.86 ± 0.13	135 ($z = 0.034$)	4.6×10^9
Active galactic core NGC 1275	0.78 ± 0.13	71 ($z = 0.013$)	1.2×10^9
3c4543	0.43 ± 0.17	4685 ($z = 0.859$)	5.3×10^{12}
1739 + 522	0.47 ± 0.18	7500 ($z = 1.375$)	1.4×10^{13}

value of $-\gamma = -2.72 \pm 0.001$. The experimental investigations of cosmic radiation in the region of the relic cutoff in [14, 15] support the validity of this unification of the data spaced on the energy scale by more than four orders of magnitude. It can be seen from Fig. 4 that, in the energy region above the relic cutoff (splitting of primary nuclei), the exponent of the energy spectrum of primary protons is $-\gamma = -2.72$. Such an energy spectrum corresponds to the situation where protons and nuclei travel in intergalactic space over a three orders of magnitude wider time interval, losing energy in elastic collisions with photons of cosmic microwave background radiation.

Obviously, the new process of multiparticle hadron production in the region of the observed break in the spectrum of extensive air showers has not yet received adequate study. At the present time, its description relies on two experimentally observed features of extensive air showers having energies in excess of 10^7 GeV: (i) The energy lost by a shower in the upper atmosphere increases sharply (this is impossible without more than an order of magnitude increase in the multiplicity of hadrons produced in the first nucleon-collision event); in the case of an invariable energy spectrum of primary protons, it is impossible to explain otherwise the break in the spectrum of extensive air showers. (ii) For the absorption to be characterized by a pion range to a depth of 1100 g/cm^2 in the atmosphere, the energy of secondary pions in the c.m. frame of colliding nucleons must be 5 GeV or higher. Other features of multiparticle-production events are ambiguous. There are even no grounds for choosing between the spherical and the two-cone divergence of pions in an event of their multiparticle production.

With the exception of neutrinos, only photons of high- and ultrahigh-energy cosmic rays carry information about the relationship between the observed arrival direction of extensive air showers and a galactic or an extragalactic object where these photons were generated, and this makes it possible to find, in the Metagalaxy, active cores accelerating protons and cosmic-ray nuclei. In just the same way, the directions of photon arrival point to stellar objects accelerating protons and nuclei in the Milky Way Galaxy. This relationship between the observed extensive air showers and objects where protons and nuclei are accelerated provides a link between our observations and specific objects in the Metagalaxy. In contrast to cosmic-ray protons and nuclei, photons have an energy spectrum of the form $E_\gamma dE_\gamma \sim E^{-2.3} dE$, and their contribution to the total flux of cosmic rays at energies not less than 6×10^5 GeV is rather small (4×10^{-3}). However, the contribution of photons becomes as large as 20% of the total flux of cosmic radiation as one moves toward the energy region of the relic cutoff of protons. We cannot rule out the possibility that the spectrum of photons undergoes no changes up to indefinitely high energies, remaining the only piece of information about ultrahigh-energy processes in the Metagalaxy. All of the aforesaid puts the development of experimental gamma-astronomy investigations and of methods for respective observations in the energy range 10^8–10^9 GeV to the fore.

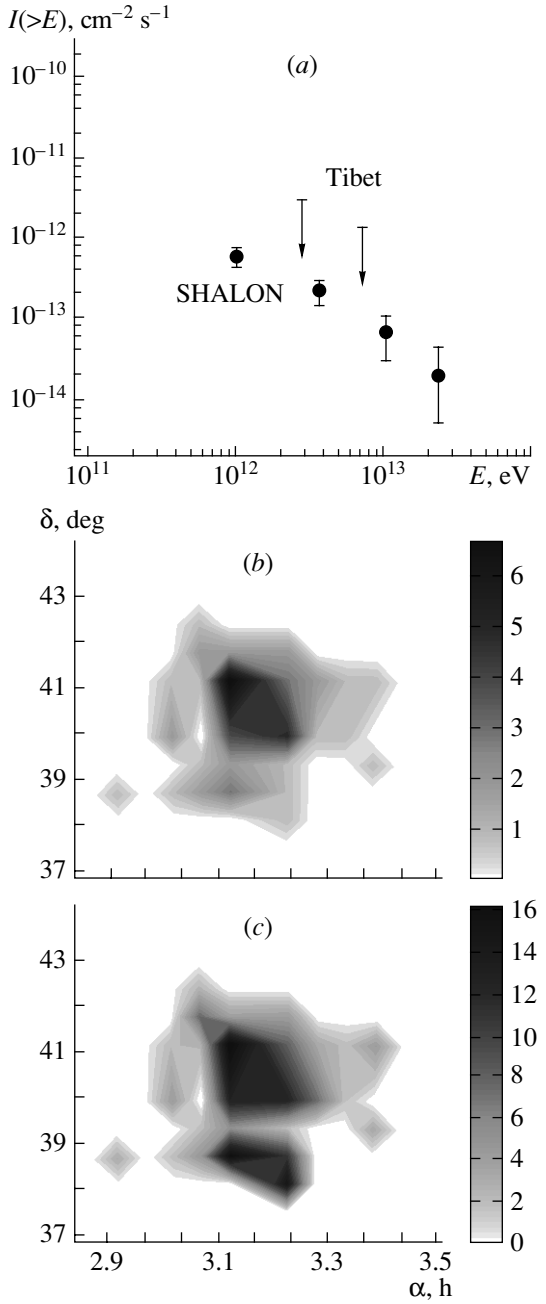

Fig. 16. (*a*) Integrated spectrum of photons ($E >$ 0.8 TeV) from NGC 1275 according to SHALON data, along with data from other experiments [13] (Tibet array); (*b*) image obtained with the SHALON telescope for the NGC 1275 source for energies in excess of 0.8 TeV; and (*c*) its energy representation.

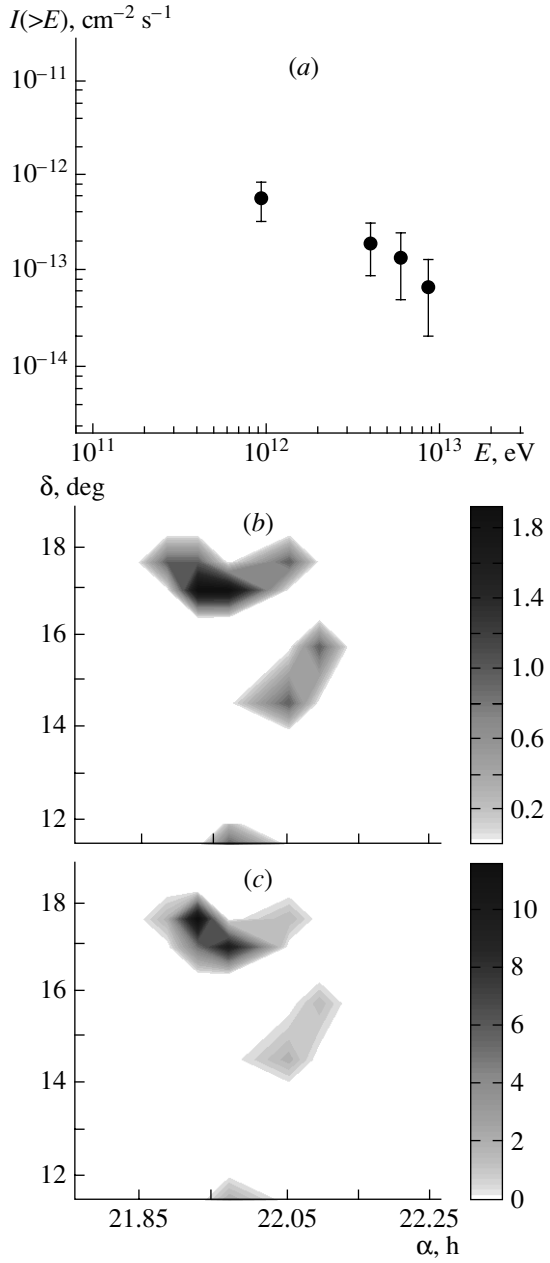

Fig. 17. (*a*) Integrated spectrum of photons ($E >$ 0.8 TeV) from 3c454.3 according to SHALON data; (*b*) image obtained with the SHALON telescope for the 3c454.3 source for energies in excess of 0.8 TeV; and (*c*) its energy representation.

REFERENCES

1. T. Kameda, T. Maeda, and I. Toioda, in *Proceedings of the International Conference on Cosmic Rays: Extensive Air Showers and Cascade Processes* (Akad. Nauk SSSR, Moscow, 1960), Vol. 2, p. 56.
2. S. I. Nikolsky and V. A. Romakhin, Yad. Fiz. **63**, 1888 (2000) [Phys. At. Nucl. **63**, 1799 (2000)].
3. B. Rossi, in *Proceedings of the International Conference on Cosmic Rays: Extensive Air Showers and Cascade Processes* (Akad. Nauk SSSR, Moscow, 1960), Vol. 2, p. 17.
4. T. K. Gaisser and T. Stanev, Phys. Rev. D **54**, 22 (1996).
5. G. B. Khristiansen, *Problems of Cosmic Rays Physics* (Nauka, Moscow, 1987), p. 226 [in Russian].

6. L. I. Vil'danova, P. A. Dyatlov, *et al.,* Izv. Akad. Nauk, Ser. Fiz. **58**, 79 (1994).
7. D. J. Bird, S. C. Colbato, *et al.*, in *Proceedings of the 21st ICRC, Adelaide, 1990*, Vol. 9, p. 252.
8. M. N. Dyakonov, V. P. Egorova, *et al.*, in *Proceedings of the 23d ICRC, Calgary, 1993*, Vol. 2, p. 38.
9. V. S. Murzin, *Introduction to Cosmic-Ray Physics* (Atomizdat, Moscow, 1979), p. 200 [in Russian].
10. V. P. Antonova, G. B. Zhdanov, *et al.,* Kratk. Soobshch. Fiz., No. 11, 60 (1997).
11. O. C. Allkofer *et al.*, in *Proceedings of the 17th ICRC*, Paris, 1981, Vol. 10, p. 32.
12. O. E. Krasnova, S. I. Nikolsky, and V. A. Romakhin, Izv. Akad. Nauk, Ser. Fiz. **65**, 1204 (2000).
13. V. G. Sinitsyna, AIP Conf. Proc. **515**, 293 (2000); **515**, 205 (2000).
14. Charles C. H. Jui, AIP Conf. Proc. **516**, 370 (2000).
15. M. Teshima, AIP Conf. Proc. **516**, 365 (2000).
16. S. I. Nikolsky, *Proceedings of the 23rd ICRC, Calgary, 1993*, Vol. 4, p. 243.

Translated by A. Isaakyan

Physics of Atomic Nuclei, Vol. 67, No. 10, 2004, pp. 1918–1922. Translated from Yadernaya Fizika, Vol. 67, No. 10, 2004, pp. 1940–1944.

ELEMENTARY PARTICLES AND FIELDS
Theory

New Possibilities for Studying Nucleon Resonances in the Production of $\pi^+\pi^-$ Pairs by Polarized Electrons on an Unpolarized Proton

V. Burkert[1], A. A. Boluchevskii[2], V. I. Mokeev[1),2)], M. Ripani[3], M. Anghinolfi[3], B. Battaglieri[3], E. N. Golovach[2], R. De Vita[3], L. Elouadrhiri[1], B. S. Ishkhanov[2),4)], M. V. Osipenko[2),3)], G. Ricco[3),5)], M. Taiuti[5], G. V. Fedotov[2], E. L. Isupov[4], N. S. Markov[4], and N. V. Shvedunov[4]

Received May 5, 2003; in final form, January 27, 2004

Abstract—The difference of the cross sections for double charged-pion production in the scattering of opposite-helicity electrons on an unpolarized proton is evaluated within the phenomenological model developed previously. The electromagnetic nucleon-resonance form factors and the parameters of nonresonance processes were taken from a fit to the latest data of the CLAS Collaboration on double charged-pion electroproduction. The effect of the longitudinal excitations of the $P_{11}(1440)$ and $D_{13}(1520)$ states on the difference of the helicity components of the cross section is studied. The sensitivity of this observable to the nucleon-resonance contribution opens the possibility of employing it both in extracting the Coulomb form factors and in seeking new baryon states. Signals from one of these states were possibly observed in the latest data of the CLAS Collaboration. © *2004 MAIK "Nauka/Interperiodica".*

1. INTRODUCTION

The application of the approach proposed in [1–3] to analyzing the first data of the CLAS Collaboration on the production of $\pi^+\pi^-$ pairs by virtual photons in the kinematical region specified by the inequalities $W < 2.1$ GeV and $Q^2 < 1.5$ GeV^2 [4–6] made it possible to obtain, for the first time, information about the electromagnetic form factors for high-lying nucleon resonances N^* ($M_{N^*} > 1.6$ GeV), the majority of them decaying to multipion final states. A structure at $W \sim 1.7$ GeV was first revealed, which had not been observed earlier in studying the exclusive channels of real- and virtual-photon interactions with a proton [4, 7]. This structure in the cross section [4–6] can be a manifestation of either the new baryon state $P_{I3}(1720)$ (I is the isospin value, which is 1/2 or 3/2; it cannot be determined unambiguously by studying the only charge channel of double pion production by photons) or an excitation of the known state $P_{13}(1720)$; in the latter case, the branching fractions of decays through the $\pi\Delta$ and ρp channels would be strongly different from those that were determined to date from an analysis of $\pi N \to \pi\pi N$ reactions. Data on electromagnetic form factors for nucleon resonances N^* of mass below 1.6 GeV were obtained by examining a few exclusive channels, such as single and double pion production and η-meson production. Thus, the investigation of various exclusive meson-electroproduction channels that was performed by the CLAS Collaboration [4–10] furnished the first pieces of information about electromagnetic form factors for the majority of nucleon resonances N^* of mass below 2 GeV.

At the same time, the analysis performed in [5, 6] revealed that experimental data involving unpolarized differential cross sections alone are sufficient for extracting only the electromagnetic form factors $A_{1/2}$ and $A_{3/2}$ for nucleon resonances, ad hoc assumptions on their longitudinal (Coulomb) form factors $C_{1/2}$ being made for this.

In order to extract information about Coulomb form factors for nucleon resonances, it is necessary to have a wider set of experimental data at our disposal. For example, the Coulomb excitations of nucleon resonances can be studied by measuring the difference $\Delta d\sigma = (d\sigma_{+1} - d\sigma_{-1})$ of the differential cross sections for the scattering of opposite-helicity electrons on a proton. This quantity is determined by the interference between the longitudinal and transverse hadron currents; therefore, the Coulomb form

[1)]Thomas Jefferson National Accelerator Facility, Newport News, VA 23606, USA.
[2)]Institute of Nuclear Physics, Moscow State University, Vorob'evy gory, Moscow, 119899 Russia.
[3)]Istituto Nazionale di Fisica Nucleare, Sezione di Genova, Italy.
[4)]Department of Physics, Moscow State University, Vorob'evy gory, Moscow, 119899 Russia.
[5)]Università di Genova, via Dodecaneso 33, I-16146 Genova, Italy.

factors $C_{1/2}$ for nucleon resonances could in principle be extracted from the difference $\Delta d\sigma$. In [11], the phenomenological model of double charged-pion production by photons was further developed, which made it possible to calculate $\Delta d\sigma$, and the sensitivity of this observable to the Coulomb excitation of the $P_{11}(1440)$ resonance was explored there.

In the present study, we analyze the possibilities for extracting information about the Coulomb excitations of nucleon resonances in the case where longitudinal photons excite a few states and examine the sensitivity of $\Delta d\sigma$ to the contribution of the new baryon state $P_{I3}(1720)$ [4–6].

2. DESCRIPTION OF THE DIFFERENCE OF THE HELICITY COMPONENTS OF THE CROSS SECTION FOR THE PRODUCTION OF $\pi^+\pi^-$ PAIRS BY POLARIZED ELECTRONS

Within the model presented in [1–3], the production of $\pi^+\pi^-$ pairs by photons on a proton is described as a superposition of a few quasi-two-body mechanisms,

$$\begin{aligned}\gamma p &\to \pi^-\Delta^{++} \to \pi^+\pi^- p,\\ \gamma p &\to \pi^+\Delta^0 \to \pi^+\pi^- p,\\ \gamma p &\to \rho^0 p \to \pi^-\pi^+ p.\end{aligned} \qquad (1)$$

The remaining mechanisms are described in terms of a complex amplitude $C(W, Q^2)$ that does not depend on either the kinematical variables of the final state or the spins of particles participating in the reaction, but which is a function of the c.m. energy W of the colliding photon and proton and the square Q^2 of the photon 4-momentum. The absolute value of this amplitude is assumed to be identical for all helicity states, while its phase is chosen to be equal to that of the amplitude for the quasi-two-body processes (1). In [11], it was shown that this parametrization corresponds to the approximation of three-body phase space, the above choice of phase ensuring that, under space reflections, the total amplitude transforms in accordance with parity conservation. Each of the quasi-two-particle mechanisms in (1) is described as a superposition of nonresonance processes and the nucleon-resonance excitations in the s-channel in a photon–proton collision that are followed by decays to the $\pi^-\Delta^{++}$, $\pi^+\Delta^0$, and $\rho^0 p$ states. The model involves all nucleon resonances of mass below 2.0 GeV that have a four-star status according to Particle Data Group and which decay through the $\pi\Delta$ or the ρp channel. Nonresonance mechanisms in the $\pi\Delta$ channels are described by a set of Reggeized Born terms, gauge invariance being restored upon Reggeization [2, 3]. The effects of initial- and final-state interaction are taken into account in the quasi-two-body channels $\gamma_v p \to \pi^-\Delta^{++}$ and $\gamma_v p \to \pi^+\Delta^0$ [1]. Nonresonance processes in the quasi-two-body channel $\gamma_v p \to \rho^0 p$ are described in the diffraction approximation [2, 3]. The model developed in [1–3, 11] relates the electromagnetic form factors for nucleon resonances to the measured differential cross sections and to the polarization asymmetry of the beam in the reaction $\gamma p \to \pi^+\pi^- p$, this enabling one to determine the electromagnetic form factors in question from a fit to these observables.

The excitation of nucleon resonances by longitudinal and transverse photons in the case where the total helicity in the photon–proton system is 1/2 $(A_{1/2}, C_{1/2})$ leads to similar angular distributions of decay products. On the basis of an experimental-data set containing only the differential cross sections for the reaction $\gamma p \to \pi^+\pi^- p$ induced by an unpolarized electron beam in an unpolarized target, it is therefore hardly possible, in this case, to determine the actual fractions of the longitudinal and transverse components in the excitation strength of nucleon resonances.

New possibilities for extracting the Coulomb form factors for nucleon resonances are provided by measurements of the difference $\Delta d\sigma$ of the polarization components of the cross section. This difference is given by

$$\Delta d\sigma/d\varphi_{\pi^-} = d\sigma_{+1}/d\varphi_{\pi^-} - d\sigma_{-1}/d\varphi_{\pi^-}, \qquad (2)$$

where $d\sigma_{+1,-1}/d\varphi_{\pi^-}$ are the angular distributions of π^- mesons off the scattering plane in the reaction $\gamma p \to \pi^+\pi^- p$ for the incident-electron helicity of $h = \pm 1$, these distributions being integrated with respect to all final-state kinematical variables presented in [11], with the exception of the π^--meson emission angle φ_{π^-}. The quantity $\Delta d\sigma/d\varphi_{\pi^-}$ and the helicity amplitudes of the reaction $\gamma p \to \pi^+\pi^- p$ that appear in the term associated with the interference between the longitudinal and transverse hadron currents (J_z and J_y, respectively) [11] are related by the equation

$$\Delta d\sigma/d\varphi_{\pi^-} = 2C_h \sin(\varphi_{\pi^-}), \qquad (3)$$

$$\begin{aligned}C_h = \int \frac{4\pi\alpha}{4K_L M_N}\sqrt{2\varepsilon_L(1-\varepsilon)}\frac{1}{4}\frac{\nu}{\sqrt{Q^2}}\frac{1}{\sqrt{2}} \qquad (4)\\ \times\left(2\mathrm{Im}\left(\sum_{\lambda_p\lambda_{p'}}\langle\lambda_{p'}\pi\pi|T|\lambda_\gamma=0,\lambda_p\rangle^*\right.\right.\\ \times\left(\langle\lambda_{p'}\pi\pi|T|\lambda_\gamma=1,\lambda_p\rangle\right.\\ \left.\left.\left.-\langle\lambda_{p'}\pi\pi|T|\lambda_\gamma=-1,\lambda_p\rangle\right)\right)\right)\frac{1}{32W^2}\frac{1}{(2\pi)^5}d\tau',\end{aligned}$$

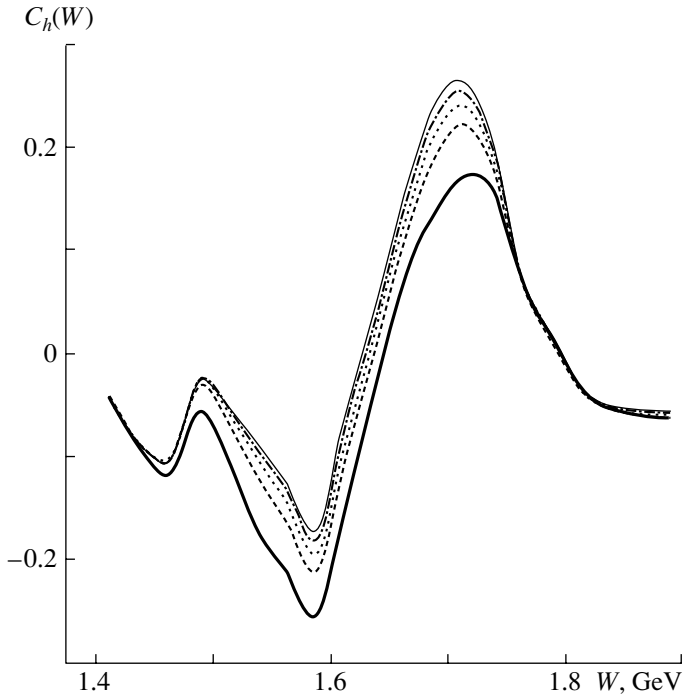

Fig. 1. Coefficients $C_h(W)$ [see (3)] calculated as a function of W for various fractions of the transverse and longitudinal components in the total excitation strength of the $D_{13}(1520)$ state for a total helicity of $1/2$. The Coulomb-excitation strength of $P_{11}(1440)$ and the electromagnetic form factors for all other nucleon resonances were extracted from data of the CLAS Collaboration [4–6] under the assumption of the excitation of the new state $P_{I3}(1720)$. Each curve corresponds to a specific set of values of the parameters α and β [see (5)]: (thick solid curve) $\alpha = 1.0$ and $\beta = 0.0$, (dashed curve) $\alpha = 0.8$ and $\beta = 0.2$, (dotted curve) $\alpha = 0.6$ and $\beta = 0.4$, (dash-dotted curve) $\alpha = 0.4$ and $\beta = 0.6$, and (thin solid curve) $\alpha = 0.2$ and $\beta = 0.8$.

where $\langle \lambda_{p'} \pi\pi | T | \lambda_\gamma \lambda_p \rangle$ are helicity amplitudes for the initial-state photon (proton) helicity λ_γ (λ_p) and the final-state proton helicity $\lambda_{p'}$; ν is the energy transfer to the virtual photon in the laboratory frame; $K_L = (W^2 - M_N^2)/(2M_N)$; $\alpha = 1/137$; ε_L and ε are the polarization parameters of the virtual photon [11]; and d' is a differential formed by final-state variables [2, 3, 11], where $d\varphi_{\pi^-}$ must be discarded.

3. EFFECT OF NUCLEON-RESONANCE EXCITATIONS ON THE HELICITY-COMPONENT DIFFERENCE

Within the approach outlined above, we have calculated the W dependence of the coefficients $C_h(W)$ [see Eqs. (3), (4)] for the reaction $\gamma p \to \pi^+\pi^- p$ at $Q^2 = 0.95$ GeV^2. For all of the resonances included in the model proposed in [1–3], with the exception of $D_{13}(1520)$, we used, for the electromagnetic form factors $A_{1/2}$ and $A_{3/2}$, the values obtained from a fit to data of the CLAS Collaboration [4–6] under the assumption of an excitation of the new baryon state $P_{I3}(1720)$.

In the present study, we explore the possibility of extracting information about the Coulomb form factors $C_{1/2}$ for nucleon resonances in the presence of longitudinal excitations of two states, $P_{11}(1440)$ and $D_{13}(1520)$. The longitudinal form factor $C_{1/2}$ for $P_{11}(1440)$ is chosen to be -0.135 GeV$^{-1/2}$, which corresponds to the best fit to the CLAS data [4–6] at $Q^2 = 0.95$ GeV^2. In order to analyze the sensitivity of the W dependence of the coefficients C_h to the Coulomb excitations of the $D_{13}(1520)$ state, the calculations were performed for a few values of the electromagnetic form factor $C_{1/2}$. In those calculations, the total strength of electromagnetic excitation of the state $D_{13}(1520)$ of total helicity $1/2$, $A^2_{1/2\,\mathrm{tot}}$, was taken to be equal to the electromagnetic form factor $A^2_{1/2}$ extracted from CLAS data [4–6]. This total strength was shared in different proportions (α and β) between the Coulomb ($C^2_{1/2}$) and the transverse ($A^2_{1/2}$) excitation strength of the $D_{13}(1520)$ state,

$$A^2_{1/2} + \varepsilon_L C^2_{1/2} = A^2_{1/2\,\mathrm{tot}}, \qquad (5)$$
$$A^2_{1/2} = \alpha A^2_{1/2\,\mathrm{tot}},$$
$$\varepsilon_L C^2_{1/2} = \beta A^2_{1/2\,\mathrm{tot}},$$
$$\alpha + \beta = 1.$$

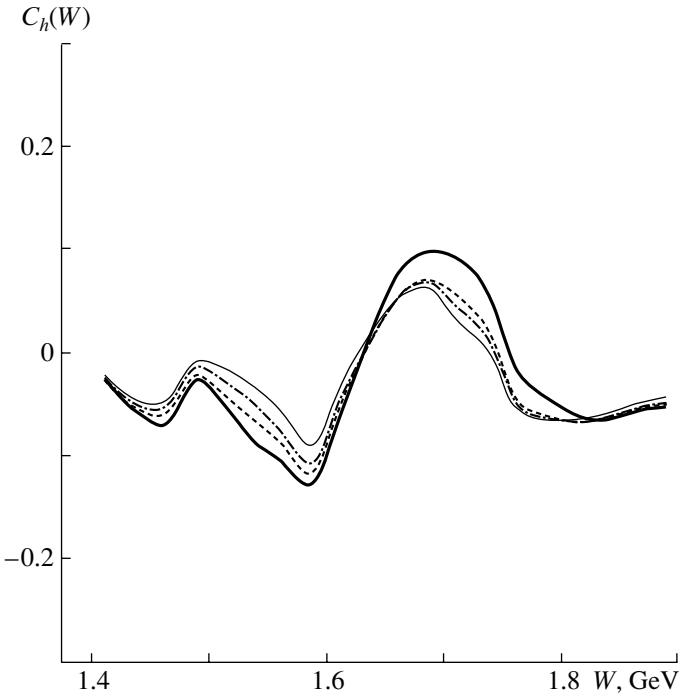

Fig. 2. Coefficients $C_h(W)$ [see (3)] calculated as a function of W for various fractions of the longitudinal and transverse components in the total excitation strength of the $D_{13}(1520)$ state for a total helicity of $1/2$. The Coulomb excitation strength of $P_{11}(1440)$ is -0.050 GeV$^{-1/2}$, and the electromagnetic form factors for all other nucleon resonances were extracted from data of the CLAS Collaboration [4–6] under the assumption that the new state $P_{I3}(1720)$ is not excited. Each curve corresponds to a specific set of values of the parameters α and β [see (5)]: (thick solid curve) $\alpha = 1.0$ and $\beta = 0.0$, (dashed curve) $\alpha = 0.8$ and $\beta = 0.2$, (dash-dotted curve) $\alpha = 0.6$ and $\beta = 0.4$ or $\alpha = 0.4$ and $\beta = 0.6$, and (thin solid curve) $\alpha = 0.2$ and $\beta = 0.8$.

Figure 1 shows the calculated W dependence of the coefficients $C_h(W)$. For the form factors $A^2_{1/2}$ and $C^2_{1/2}$, the signature was chosen to be negative.

It can be seen that the coefficients $C_h(W)$ depend greatly on the strength of the Coulomb excitation of the $D_{13}(1520)$ state. This opens the possibility of extracting data on the Coulomb excitation of $D_{13}(1520)$ in the case of a simultaneous excitation of the closely lying state $P_{11}(1440)$, with an amplitude exceeding that of the Coulomb excitation of the $D_{13}(1520)$ state.

However, the region of the highest sensitivity of $C_h(W)$ to various fractions of $A_{1/2}$ and $C_{1/2}$ in the total excitation strength of the $D_{13}(1520)$ state lies at W between 1.59 and 1.71 GeV—that is, far above the $D_{13}(1520)$ mass. In order to reveal the reasons for this behavior, we have calculated the coefficient $C_h(W)$ under the same assumptions on the Coulomb and transverse excitations of nucleon resonances for the case where there is no excitation of the new baryon state $P_{I3}(1720)$ ($A_{1/2} = A_{3/2} = C_{1/2} = 0$) and where the photocoupling $C_{1/2}$ for $P_{11}(1440)$ is reduced to become -0.050 GeV$^{-1/2}$. The results are displayed in Fig. 2.

The results in Fig. 2 show that the maximum of the sensitivity to the Coulomb excitation of the $D_{13}(1520)$ state is shifted to the W region corresponding to the mass of the $D_{13}(1520)$ state. At the same time, the sensitivity to the Coulomb excitation of the $D_{13}(1520)$ state becomes much lower. This suggests that the interference between the most highly excited states $D_{13}(1520)$ and $P_{I3}(1720)$ makes a significant contribution to $C_h(W)$. Since these states have identical spins, the interference effects survive in observables upon integration with respect to angular variables. According to (4), $C_h(W)$ is determined by the product of the Coulomb amplitude ($\lambda_\gamma = 0$) and the difference of the transverse amplitudes for opposite helicities, $\lambda_\gamma = \pm 1$. The interference between the $D_{13}(1520)$ and $P_{I3}(1720)$ states contributes to this difference. The interference effects are maximal in the range of W between 1.59 and 1.62 GeV; in response to a variation in $C_{1/2}$ for $D_{13}(1520)$, this shifts the maximum of the sensitivity from the central mass value toward the region around $W = 1.59$ GeV (see Fig. 1). In Fig. 1, another sensitivity peak is seen at $W = 1.7$ GeV. This is because the $P_{I3}(1720)$ resonance has a maximum difference of the absolute values of the electromag-

netic form factors $A_{1/2}$ and $A_{3/2}$ in relation to all other nucleon resonances, this leading to a maximum of the difference of the $\lambda = \pm 1$ transverse amplitudes at $W = 1.7$ GeV.

Thus, measurement of the difference of the polarization components of the cross section is sensitive to the contribution of the baryon state observed in [4–6], and this can be employed in seeking and studying the nature of missing resonances.

4. CONCLUSIONS

We have analyzed the possibilities for extracting information about the Coulomb excitations of nucleon resonances in measuring the difference of the helicity components of the cross sections in the angular distributions of π^- mesons off the scattering plane in the reaction $\gamma p \to \pi^+\pi^- p$. By using data of the CLAS Collaboration [4–6] on the electromagnetic form factors for the total spectrum of excited nucleon states in the mass region below 2 GeV, we have calculated the coefficients $C_h(W)$ [see Eqs. (3), (4)], which are proportional to the difference of the helicity components of the cross section. The results are the following:

(i) The W dependence of the coefficients $C_h(W)$ is sensitive to variations in the Coulomb form factor for the $D_{13}(1520)$ state even in the presence of the closely lying state $P_{11}(1440)$, which has a much larger longitudinal excitation amplitude. Owing to this, an analysis of the difference of the helicity components of the cross section is a promising method for extracting Coulomb form factors.

(ii) The interference between the $D_{13}(1520)$ and $P_{I3}(1720)$ states has a pronounced effect on the W dependence of the coefficients $C_h(W)$, making it possible to extract information about the interference between the transverse excitations of nucleon resonances from measurements of the beam polarization asymmetry.

(iii) The coefficients $C_h(W)$ are sensitive to the contribution of the baryon state $P_{I3}(1720)$. Owing to this, measurement of the beam polarization asymmetry appears to be a promising tool for seeking missing baryon states and for analyzing their nature.

REFERENCES

1. M. Ripani, V. I. Mokeev, M. Anghinolfi, *et al.*, Nucl. Phys. A **672**, 220 (2000).
2. M. Ripani, V. I. Mokeev, M. Battaglieri, *et al.,* Yad. Fiz. **63**, 2036 (2000) [Phys. At. Nucl. **63**, 1943 (2000)].
3. V. I. Mokeev, M. Ripani, M. Anghinolfi, *et al.,* Yad. Fiz. **64**, 1368 (2001) [Phys. At. Nucl. **64**, 1292 (2001)].
4. V. D. Burkert, in *Proceedings of the 9th International Conference on the Structure of Baryon, BARYON 2002,* Ed. by C. E. Carlson and B. A. Mecking (World Sci., Singapore, 2003), p. 29.
5. M. Ripani, V. D. Burkert, and V. I. Mokeev, Phys. Rev. Lett. **91**, 022002 (2003).
6. E. N. Golovach, V. D. Burkert, V. I. Mokeev, *et al.*, in *Proceedings of the ICHEP 2002 Conference* (Elsevier Sci., 2003), p. 668.
7. V. D. Burkert, Nucl. Phys. A **669**, 261 (2002).
8. R. Thompson *et al.* (CLAS Collab.), Phys. Rev. Lett. **86**, 1702 (2001).
9. K. Joo *et al.* (CLAS Collab.), Phys. Rev. Lett. **88**, 122001 (2002).
10. M. Dugger *et al.* (CLAS Collab.), Phys. Rev. Lett. (in press).
11. V. Burkert, V. I. Mokeev, M. Ripani, *et al.,* Yad. Fiz. **66**, 2199 (2003) [Phys. At. Nucl. **66**, 2149 (2003)].

Translated by O. Chernavskaya

Physics of Atomic Nuclei, Vol. 67, No. 10, 2004, pp. 1923–1927. From Yadernaya Fizika, Vol. 67, No. 10, 2004, pp. 1945–1949.

ELEMENTARY PARTICLES AND FIELDS
Theory

Lepton-Pair Production in Relativistic Ion Collisions and Its Correspondence to the Crossing Process*

E. Bartoš[1], S. R. Gevorkyan[2], and E. A. Kuraev

Joint Institute for Nuclear Research, Dubna, Moscow oblast, 141980 Russia

Received November 4, 2003

Abstract—Using the Sudakov technique, we sum the perturbation series for the process $3 \to 3$ and obtain the compact analytical expression for the amplitude of this process, which takes into account all possible Coulomb interactions between colliding particles. Comparing it to the amplitude of the lepton-pair production in heavy-ion collisions, i.e., in the process $2 \to 4$, we show that the amplitudes obtained in the high-energy limit lose the crossing-symmetry property (which holds only on the Born level).

1. INTRODUCTION

During the past decade, the interest in the process of lepton-pair production in strong Coulomb fields has risen significantly. This is connected mainly with the beginning of the operation of the relativistic heavy-ion collider RHIC (Lorentz factor $\gamma = E/m = 108$) and the new collider LHC ($\gamma = 3000$), which will operate in the near future. At such energies, the lepton-pair yield becomes huge (according to [1, 2]), so that a detailed analysis of the process

$$A + B \to A + B + e^+ + e^- \qquad (1)$$

accounting for the Coulomb corrections (CC) is required. Such work has been done in recent years and a lot of papers have been devoted to this subject [3–11]. Nevertheless, the problem turned out to be more complex than it seemed at first glance. We want only to mention the exciting result obtained in [3, 4, 7]: the CC to the process (1) enter the amplitude of this process in such a way that its cross section is determined solely by the lowest (Born) term. In our opinion, this is the result of the incorrect application of crossing symmetry to the amplitudes obtained in the high-energy limit.

As an obvious example of the crossing-symmetry violation, we want to cite the process of lepton-pair photoproduction on nuclei and its counterpart, the bremsstrahlung in lepton–nucleus scattering. The amplitudes of both processes are determined by the Coulomb phase, which is infrared stable in the case of pair photoproduction, whereas it is infrared divergent in the case of bremsstrahlung, and this difference cannot be adjusted by a trivial crossing change of the variables. Taking into account the importance of the problem and permanent interest in it from the scientific community, we calculated the full amplitude for the crossing process accounting for all possible photon exchanges among the colliding relativistic particles. Comparing it with the amplitude of the process (1) also obtained using the high-energy approximation, we have shown that the crossing-symmetry property becomes invalid when one takes into account the final-state interaction of the lepton pair with the Coulomb field of ions.

2. THE BORN AMPLITUDE OF THE PROCESS $3 \to 3$

Let us construct the amplitude of the process $3 \to 3$ represented in Figs. 1*a* and 1*b*,

$$A_1(p_1) + A_2(p_2) + C(p_3) \to A_1(p_1') + A_2(p_2') + C(p_3'). \qquad (2)$$

We consider the kinematics when all the energy invariants which determined the process (2) are large, compared with the masses of the involved particles and transfer momenta

$$s = (p_1 + p_2)^2, \quad s_1 = (p_1 + p_3)^2, \quad s_2 = (p_3 + p_2)^2, \qquad (3)$$
$$q_1^2 = (p_1 - p_1')^2, \quad q_2^2 = (p_2 - p_2')^2, \quad q_3^2 = (p_3 - p_3')^2,$$
$$p_1^2 = p_1'^2 = m_1^2, \quad p_2^2 = p_2'^2 = m_2^2, \quad p_3^2 = p_3'^2 = m^2,$$
$$s \gg s_1 \sim s_2 \gg -q_1^2 \sim -q_2^2 \sim -q_3^2.$$

*This article was submitted by the authors in English.

[1] Department of Theoretical Physics, Comenius University, Bratislava, Slovakia.

[2] Yerevan Physics Institute, Yerevan, Armenia.

1063-7788/04/6710-1923$26.00

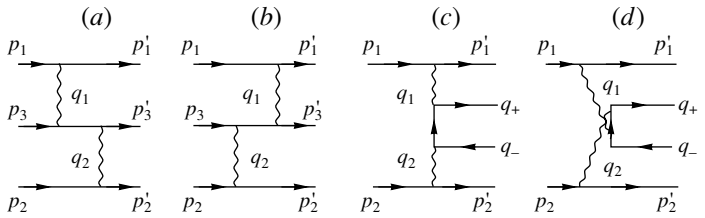

Fig. 1. Feynman diagrams for the Born amplitudes of the processes $(a, b)\ A_1 + A_2 + C \to A_1 + A_2 + C$ and $(c, d)\ A_1 + A_2 \to A_1 + A_2 + C + \bar{C}$.

For the Born amplitude of the process (2), one can write

$$M_{(1)}^{(1)} = -i(4\pi\alpha)^2 Z_1 Z_2 \bar{u}(p_1')\gamma_\mu u(p_1) \times \bar{u}(p_2')\gamma_\nu u(p_2)\frac{\bar{u}(p_3')O_{\rho\sigma}u(p_3)g^{\mu\sigma}g^{\nu\rho}}{q_1^2 q_2^2}, \quad (4)$$

where $Z_{1,2}$ are the charge numbers of the colliding nuclei. We use the Sudakov parametrization for all 4-momenta entering the problem (for details, see [10]),

$$q_1 = \alpha_1\tilde{p}_2 + \beta_1\tilde{p}_1 + q_{1\perp},\ \ q_2 = \alpha_2\tilde{p}_2 + \beta_2\tilde{p}_1 + q_{2\perp}, \quad (5)$$
$$p_1' = \alpha_1'\tilde{p}_2 + \beta_1'\tilde{p}_1 + p_{1\perp}',\ \ p_2' = \alpha_2'\tilde{p}_2 + \beta_2'\tilde{p}_1 + p_{2\perp}',$$
$$p_3 = \alpha_3\tilde{p}_2 + \beta_3\tilde{p}_1 + p_{3\perp},\ \ p_3' = \alpha_3'\tilde{p}_2 + \beta_3'\tilde{p}_1 + p_{3\perp}',$$

and the Gribov decomposition of the metric tensor into the longitudinal and transverse parts,

$$g_{\mu\nu} = g_{\perp\mu\nu} + \frac{2}{s}\left(\tilde{p}_{1\mu}\tilde{p}_{2\nu} + \tilde{p}_{1\nu}\tilde{p}_{2\mu}\right),$$

with lightlike 4-vectors $\tilde{p}_{1,2}$. For the kinematics of the process, we will use the following relations:

$$s = 2\tilde{p}_1\tilde{p}_2, \quad \beta_1 + \beta_3 = \beta_3', \quad \alpha_2 + \alpha_3 = \alpha_3', \quad (6)$$
$$g_{\mu\sigma} = \frac{2}{s}\tilde{p}_{1\sigma}\tilde{p}_{2\mu}, \quad g_{\nu\rho} = \frac{2}{s}\tilde{p}_{1\nu}\tilde{p}_{2\rho},$$
$$q_1^2 = q_{1\perp}^2 = -\mathbf{q}_1^2, \quad q_2^2 = q_{2\perp}^2 = -\mathbf{q}_2^2,$$

where $\mathbf{q}_i$ are two-dimensional vectors in the plane transverse to the z axes, which we choose along 3-vector $\mathbf{p}_1 = -\mathbf{p}_2$ in the c.m. frame of initial particles A_1, A_2.

Using the gauge-invariant condition,

$$q_{1\rho}\bar{u}(p_3')O_{\rho\sigma}u(p_3) \approx (\beta_1\tilde{p}_1 + q_{1\perp})_\rho\bar{u}(p_3')O_{\rho\sigma}u(p_3) = 0, \quad (7)$$
$$q_{2\sigma}\bar{u}(p_3')O_{\rho\sigma}u(p_3) \approx (\alpha_2\tilde{p}_2 + q_{2\perp})_\sigma\bar{u}(p_3')O_{\rho\sigma}u(p_3) = 0,$$

one gets the Born amplitude in the form

$$M_{(1)}^{(1)}(q_1, q_2) = -4isN_1N_2(4\pi\alpha Z_1) \times (4\pi\alpha Z_2)B(q_1, q_2) \quad (8)$$

with

$$B(q_1, q_2) = \frac{\bar{u}(p_3')O_{\rho\sigma}u(p_3)q_{1\perp}^\rho q_{2\perp}^\sigma}{s\alpha_2\beta_1\mathbf{q}_1^2\mathbf{q}_2^2}, \quad (9)$$
$$N_1 = \frac{1}{s}\bar{u}(p_1')\hat{p}_2u(p_1), \quad N_2 = \frac{1}{s}\bar{u}(p_2')\hat{p}_1u(p_2),$$
$$s\alpha_2\beta_1 = -q_3^2 - (\mathbf{q}_1 - \mathbf{q}_2)^2 \sim m^2.$$

The values of N_i for every polarization state of initial particles (or for spinless particles) are unity and

$$\bar{u}(p_3')O_{\rho\sigma}u(p_3)q_{1\perp}^\rho q_{2\perp}^\sigma = \bar{u}(p_3')\left[\hat{q}_{2\perp}\frac{\hat{p}_3 + \hat{q}_1 + m}{(p_3 + q_1)^2 - m^2}\hat{q}_{1\perp} + \hat{q}_{1\perp}\frac{\hat{p}_3 + \hat{q}_2 + m}{(p_3 + q_2)^2 - m^2}\hat{q}_{2\perp}\right]u(p_3). \quad (10)$$

3. THE COULOMB CORRECTIONS TO THE PROCESS $3 \to 3$

Let us consider the set of six Feynman diagrams (FDs) with one virtual photon connecting the p_3 line with the particle A_1 and two connecting the p_3 line with the particle A_2 (see Fig. 2). The loop-momentum integration in the relevant matrix element can be performed considering that

$$d^4k = (2\pi i)^2\frac{1}{2s}\frac{d(s\alpha_k)}{2\pi i}\frac{d(s\beta_k)}{2\pi i}d^2k_\perp, \quad k = \alpha_k\tilde{p}_2 + \beta_k\tilde{p}_1 + k_\perp. \quad (11)$$

It can be shown that only four FD amplitudes work (Figs. 2*a*–2*d*). Really, when one writes the denominators explicitly in Figs. 2*e* and 2*f* through longitudinal Sudakov variables, i.e.,

$$(p_3 + k)^2 - m^2 + i0 \approx s\alpha_k\beta_3 + i0, \quad (12)$$
$$(p_3 - q_2 + k)^2 - m^2 + i0 \approx s\alpha_k\beta_3 + i0,$$
$$(p_2 - k)^2 - m^2 + i0 \approx -s\beta_k + i0,$$
$$(p_2' + k)^2 - m^2 + i0 \approx s\beta_k + i0,$$

one can see that both poles in the α_k complex plane are located in the same half-plane, so their contribution to the amplitude is zero (suppressed by the factor

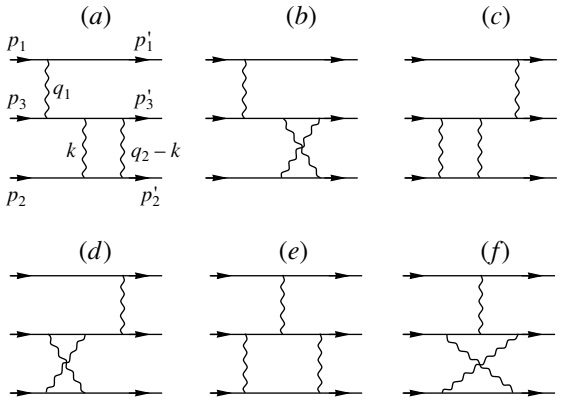

Fig. 2. Feynman diagrams for the process $A_1 + A_2 + C \to A_1 + A_2 + C$ with three-photon exchange.

$|q_3^2/s| \sim |s_1/s|$). This result is in agreement with the one obtained in [8].

It is convenient to introduce eight FDs (including the four depicted in Figs. $2a$–$2d$ and additional four FDs with interchanged photons absorbed by the nucleus A_2 line). To avoid double counting, we multiply the relevant matrix element by the statistical factor $1/2!$. This trick permits one to perform the integration over α_k, β_k with the result

$$\int\limits_{-\infty}^{\infty} \frac{d(s\alpha_k)}{2\pi i}\left(\frac{\beta_3}{s\alpha_k\beta_3+i0}+\frac{\beta_3}{-s\alpha_k\beta_3+i0}\right) \quad (13)$$

$$= \int\limits_{-\infty}^{\infty} \frac{d(s\beta_k)}{2\pi i}\left(\frac{1}{s\beta_k+i0}+\frac{1}{-s\beta_k+i0}\right) = 1.$$

Now let us show how the cancellations of the contribution arising from FD with absorption of $n+1$ exchanged photons between particle C and nucleus A_1, sandwiched between two exchanges between particle C and nucleus A_2 (Fig. 3), take place. The algebraic symmetrization procedure described above (13), with help of the relations

$$l_i = \alpha_{l_i}\tilde{p}_2 + \beta_{l_i}\tilde{p}_1 + l_{i\perp}, \quad (14)$$
$$\alpha_{l_i} < \alpha_3 < \alpha_k \le 1, \quad \beta_k < \beta_3 < \beta_{l_i} \le 1,$$

leads to the product of factors

$$\prod_{i=1}^{n}\left(\frac{\beta_3}{s\alpha_{l_i}\beta_3+i0}+\frac{\beta_3}{-s\alpha_{l_i}\beta_3+i0}\right) \quad (15)$$
$$\times \prod_{j=1}^{n}\left(\frac{1}{s\beta_{l_j}+i0}+\frac{1}{-s\beta_{l_j}+i0}\right), \qquad n \ge 1.$$

In terms of notation used in [4, 8], our assumptions (14) read

$$E = p_{1+} \gg p_{3+} \gg p_{2+} = \frac{m_2^2}{E}, \quad (16)$$

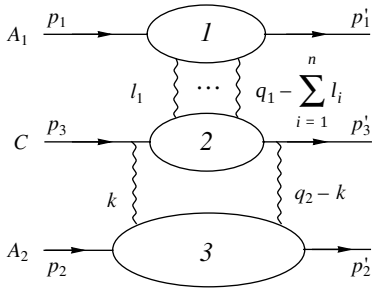

Fig. 3. Feynman diagram for the process $A_1 + A_2 + C \to A_1 + A_2 + C$ with $n+1$ exchanged photons ($n \ge 1$) between particles A_1 and C.

$$\frac{m_1^2}{E} = p_{1-} \ll p_{3-} \ll p_{2-} = E.$$

It is easy to see that, in this case, no dependence on $p_{3\pm}$ sign appears for the eikonal amplitudes corresponding to the situation in Fig. 3.

The poles of the electron Green's functions (Fig. 3) are located in the same half-plane of k_-, which allows one to safely neglect the contribution of such diagrams.

After performing the integration over longitudinal Sudakov variables α_{l_i}, β_{l_j} in blocks *1*, *2* of FD in Fig. 3, one can see that the dependence on longitudinal Sudakov variables α_k, β_k relevant to the lower loop is completely the same as in the previous case (see Figs. $2e$, $2f$); therefore, the contribution of such type of FD to the total amplitude is zero.

Further integration over transverse momentum is straightforward,

$$\int \frac{d\mathbf{k}}{\pi}\frac{1}{(\mathbf{k}^2+\lambda^2)((\mathbf{q}_2-\mathbf{k})^2+\lambda^2)} = \frac{2}{\mathbf{q}_2^2}\ln\frac{\mathbf{q}_2^2}{\lambda^2}, \quad (17)$$

where the photon mass parameter λ is introduced for the purpose of regularization.

For the amplitude $M_{(2)}^{(1)}$ (see Fig. 4) and the similar amplitude $M_{(1)}^{(2)}$, we obtained

$$M_{(2)}^{(1)} + M_{(1)}^{(2)} \quad (18)$$
$$= M_{(1)}^{(1)}(q_1,q_2)\frac{1}{2!}\left[2iZ_1\alpha\ln\frac{\mathbf{q}_1^2}{\lambda^2} + 2iZ_2\alpha\ln\frac{\mathbf{q}_2^2}{\lambda^2}\right].$$

The amplitude for an arbitrary amount of interchanged photons (see Fig. 5) is constructed in a similar way,

$$M_{(\infty)}^{(\infty)}(q_1,q_2) = M_{(1)}^{(1)}(q_1,q_2)e^{i(\varphi_1(\mathbf{q}_1)+\varphi_2(\mathbf{q}_2))}, \quad (19)$$

with the Coulomb phases

$$\varphi_1(\mathbf{q}_1) = Z_1\alpha\ln\frac{\mathbf{q}_1^2}{\lambda^2}, \quad \varphi_2(\mathbf{q}_2) = Z_2\alpha\ln\frac{\mathbf{q}_2^2}{\lambda^2}.$$

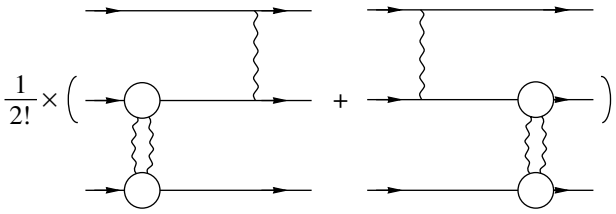

Fig. 4. Feynman diagram for the amplitude $M^{(1)}_{(2)}$.

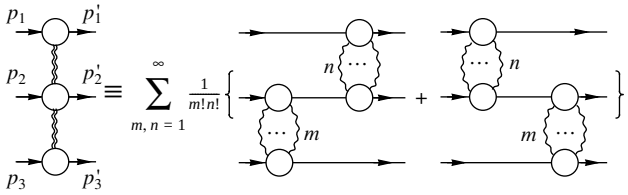

Fig. 5. Feynman diagram for the amplitude $M^{(\infty)}_{(\infty)}(q_1, q_2)$.

Consider now the case with one additional exchanged photon between two nuclei A_1 and A_2. The relevant matrix element $M_{(1\mathrm{B})}$ reads

$$M_{(1\mathrm{B})} = i\alpha Z_1 Z_2 \times \int \frac{d\mathbf{k}}{\pi(\mathbf{k}^2+\lambda^2)} M^{(1)}_{(1)}(q_1+k, q_2+k). \tag{20}$$

In the same approach, we get for the matrix element with n exchanged (between nuclei) photons (see Fig. 6*a*)

$$M_{(n\mathrm{B})} = \frac{(i\alpha Z_1 Z_2)^n}{n!}\prod_{i=1}^{n}\int \frac{d\mathbf{k}_i}{\pi(\mathbf{k}_i^2+\lambda^2)} \times M^{(1)}_{(1)}\left(q_1+\sum_{i=1}^{n}k_i, q_2+\sum_{i=1}^{n}k_i\right). \tag{21}$$

It is convenient to write this expression in the impact-parameter representation. For this aim, we use the identity

$$\int d\mathbf{k}_{n+1}\delta^{(2)}\left(k_{n+1}-q_1-\sum_{i=1}^{n}k_i\right) = \frac{1}{(2\pi)^2}\int d\mathbf{k}_{n+1}d\boldsymbol{\rho}\, e^{i(\mathbf{k}_{n+1}-\mathbf{q}_1-\sum\mathbf{k}_i)\cdot\boldsymbol{\rho}} = 1. \tag{22}$$

Thus, the matrix element with an arbitrary number of exchanged photons can be cast

$$M(3\to 3) = \sum_{n=1}^{\infty} M_{(n\mathrm{B})} = \frac{1}{4}\int \frac{d\boldsymbol{\rho}}{\pi} e^{-i\mathbf{q}_1\cdot\boldsymbol{\rho}} e^{i\alpha Z_1 Z_2\psi(\boldsymbol{\rho})}\tilde{M}^{(1)}_{(1)}(\rho, q_1, q_2) \tag{23}$$

with

$$\psi(\boldsymbol{\rho}) = \int \frac{d\mathbf{k}}{\pi}\frac{e^{-i\mathbf{k}\cdot\boldsymbol{\rho}}}{\mathbf{k}^2+\lambda^2} = 2K_0(\rho\lambda) \approx -2\ln\left(\frac{C\rho\lambda}{2}\right), \tag{24}$$

where $C \approx 1.781$ and

$$\tilde{M}^{(1)}_{(1)}(\rho, q_1, q_2) = \int \frac{d\mathbf{k}}{\pi} e^{-i\mathbf{k}\cdot\boldsymbol{\rho}} M^{(1)}_{(1)}(k, k+q_2-q_1). \tag{25}$$

This result confirms the general statement given above [see (19)] that the dependence on "photon mass" λ can be represented as a phase factor. As can be seen, the whole amplitude (23) cannot be cast solely as a Born amplitude multiplied by the phase factor. The corresponding contributions to the total cross section (except for the Born term) will be enhanced only by the first power of logarithm in energy.

Finally, taking into account all photon exchanges between particle C and nuclei A_1 and A_2, we obtain the general answer by the simple replacement in expression (25)

$$M^{(1)}_{(1)}(k, k+q_2-q_1) \to M^{(\infty)}_{(\infty)} = M^{(1)}_{(1)}(k, k+q_2-q_1)e^{i\varphi_1(\mathbf{k})+i\varphi_2(\mathbf{k}+\mathbf{q}_2-\mathbf{q}_1)} \tag{26}$$

with φ_1, φ_2 given in (19).

4. THE COULOMB CORRECTIONS TO THE PROCESS OF LEPTON-PAIR PRODUCTION

As was mentioned above, our goal is to investigate the crossing-symmetry property between the amplitudes of process (2) and the relevant process in Figs. 1*c* and 1*d*,

$$A_1(p_1)+A_2(p_2)\to A_1(p_1')+A_2(p_2')+C(q_+)+\bar{C}(q_-), \tag{27}$$

with the following kinematics:

$$s=(p_1+p_2)^2,\quad s_p=(q_++q_-)^2,\quad q_1^2=(p_1-p_1')^2,\quad q_2^2=(p_2-p_2')^2,\quad p_1^2=p_1'^2=m_1^2,\quad q_+^2=q_-^2=m_2^2,\quad q_+^2=q_-^2=m^2,\quad s\gg -q_1^2\sim -q_2^2\sim s_{12}. \tag{28}$$

Using the Sudakov technique, the Born amplitude for the process (27) can be represented in the form

$$M_p = -is\cdot 2^6\pi^2 Z_1 Z_2 N_1 N_2 B_p(q_1, q_2) \tag{29}$$

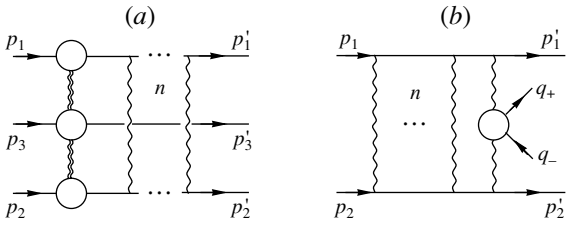

Fig. 6. Feynman diagrams for the n-photon exchange between nuclei A_1 and A_2 compared with the Born diagram for the processes (a) $3 \to 3$ and (b) $2 \to 4$ (blob in (b) corresponds to diagrams in Figs. 1c, 1d).

with

$$B_p(q_1, q_2) = \frac{e_1^\alpha e_2^\beta \bar{u}(q_-) T_{\alpha\beta} v(q_+) |\mathbf{q}_1||\mathbf{q}_2|}{\tilde{s}\mathbf{q}_1^2\mathbf{q}_2^2},$$

$$\tilde{s} = s\alpha_2\beta_1 = (q_+ + q_-)^2 + (\mathbf{q}_1 + \mathbf{q}_2)^2,$$

$$T_{\alpha\beta} = \gamma_\beta \frac{\hat{q}_1 - \hat{q}_+ + m}{(q_1 - q_+)^2 - m^2}\gamma_\alpha + \gamma_\alpha \frac{\hat{q}_2 - \hat{q}_+ + m}{(q_2 - q_+)^2 - m^2}\gamma_\beta$$

(for details, see [10]).

Generalization for the case of an arbitrary number of exchanged photons between colliding nuclei is straightforward. The same approach as was used above leads to the following form of the generalized amplitude:

$$M(2 \to 4) = \frac{1}{4}\int \frac{d\boldsymbol{\rho}}{\pi} e^{-i\mathbf{q}_1\cdot\boldsymbol{\rho} + i\alpha Z_1 Z_2 \psi(\boldsymbol{\rho})} \Phi_\mathrm{B}(\rho, q_2), \tag{30}$$

with

$$\Phi_\mathrm{B}(\rho, q_2) = \int \frac{d\mathbf{k}}{\pi} e^{i\mathbf{k}\cdot\boldsymbol{\rho}} M_p(k, q_2 - k).$$

Comparing expression (30) with the amplitude for the process $3 \to 3$ (23), one can see that the crossing-symmetry property between the considered processes takes place in the case where one neglects the multiple exchanges of particle C with nuclei. Moreover, this statement is correct even when one takes into account the screening effects between nuclei A_1 and A_2 in both processes, which manifest themselves by insertion of light-by-light scattering blocks into Feynman amplitudes. As was shown in [11], account of this effect can be provided by the universal factor

$$\exp\left\{-\frac{\alpha^2 Z_1 Z_2}{2} L A(\rho)\right\}, \quad L = \ln(\gamma_1\gamma_2), \tag{31}$$

with the complex quantity $A(\rho)$ connected with the Fourier transformation of the light-by-light scattering amplitude.

Nevertheless, crossing symmetry is broken in all orders of perturbation theory if one tries to compare the full amplitude for the process $3 \to 3$ [expression (23) with the replacement (26)] and the relevant amplitude for the process $2 \to 4$ accounting for the multiple interaction of produced particles [10].

Finally, we want to stress that the crossing symmetry is a general property of the amplitude of physical processes and its violation considered above is the result of approximations done at the high-energy limit.

ACKNOWLEDGMENTS

We are grateful to V. Serbo and N. Nikolaev for useful discussions and comments.

This work was supported by grants INTAS 97-30494, SR-2000.

REFERENCES

1. L. D. Landau and E. M. Lifshits, Phys. Zs. **6**, 244 (1934).
2. G. Racah, Nuovo Cimento **14**, 93 (1937).
3. A. J. Baltz and L. McLerran, Phys. Rev. C **58**, 1679 (1998).
4. A. J. Baltz, F. Gelis, L. McLerran, and A. Peshier, Nucl. Phys. A **695**, 395 (2001).
5. R. N. Lee, A. I. Milstein, and V. G. Serbo, hep-ph/0108014.
6. R. N. Lee and A. I. Milstein, Phys. Rev. A **61**, 032103 (2000).
7. U. Eichmann, J. Reinhardt, and W. Greiner, Phys. Rev. A **59**, 1223 (1999).
8. U. Eichmann, J. Reinhardt, and W. Greiner, Phys. Rev. A **61**, 062710 (2000).
9. D. Yu. Ivanov, A. Schiller, and V. G. Serbo, Phys. Lett. B **454**, 155 (1999).
10. E. Bartoš, S. R. Gevorkyan, E. A. Kuraev, and N. N. Nikolaev, Phys. Rev. A **66**, 042720 (2002).
11. E. Bartoš, S. R. Gevorkyan, E. A. Kuraev, and N. N. Nikolaev, Phys. Lett. B **538**, 45 (2002).

Physics of Atomic Nuclei, Vol. 67, No. 10, 2004, pp. 1928–1929. Translated from Yadernaya Fizika, Vol. 67, No. 10, 2004, pp. 1950–1952.

FUTURE PUBLICATIONS

Investigation of Spallation Reactions on ^{120}Sn and (d, xn), (d, pxn), (p, xn), and (p, pxn) Reactions on Enriched Tin Isotopes

A. R. Balabekyan, A. S. Danagulyan, G. R. Drnoyan, N. A. Demekhina, I. Adam, V. G. Kalinnikov, M. I. Krivopustov, V. S. Pronskikh, V. I. Stegailov, A. A. Solnyshkin, P. Chaloun, V. M. Tsupko-Sitnikov, and Zh. Musulmanbekov

The cross sections for (d, xn), (d, pxn), (p, xn), and (p, pxn) reactions on enriched tin isotopes are obtained at a projectile energy of 3.65 GeV per nucleon. The yields in the energy range 0.66–8.1 GeV are analyzed with resort to experimental data obtained previously. Experimental results are compared with the results of theoretical calculations performed within the cascade-evaporation model. The dependence of the yields on the number of emitted neutrons, the projectile type, and the isotopic composition of a target is investigated. The cross sections for the $(p, xpyn)$ reactions on a ^{120}Sn target are presented at a primary-proton energy of 0.66 GeV.

Magic Numbers of Superheavy Nuclei

V. Yu. Denisov

The proton and neutron shell corrections for nuclei where the number of protons lies in the interval $76 \leq Z \leq 400$ are calculated along the beta-stability line described by the Green's formula. The magic numbers of protons and neutrons are determined for superheavy nuclei. The alpha-decay half-lives and the fission barriers for superheavy doubly magic nuclei are estimated.

Magnetic Resonances of the Electroexcitation of the ^{26}Mg Nucleus

N. G. Goncharova and N. D. Pronkina

On the basis of spectroscopic information about direct pickup reactions, the multipole magnetic resonances $M2$, $M4$, and $M6$ of the ^{26}Mg nucleus are calculated within the *particle–final-nucleus state* version of the multiparticle shell model. The excitation-energy distribution of the form factors for the multipole magnetic $1\hbar\omega$ resonances is obtained for momentum transfers to a nucleus up to 2 fm^{-1}. A comparison of the results of the calculations for the $M6$ form factors with corresponding experimental data confirms that the adopted model approximations are realistic.

$J^\pi = 0^-$ Levels in the ^{156}Gd and ^{158}Gd Nuclei

E. P. Grigoriev

The 0^- states in the ^{156}Gd nucleus at $E = 1952.38$ keV and in the ^{158}Gd nucleus at E = 2269.16 keV are established on the basis of an analysis of available data on even–even deformed nuclei. From data on the deexcitation of levels and on the probability of their population by β transitions, it is found that these states have a two-particle proton structure. A comparison of the present data with information about the 0^- levels in the ^{170}Yb and ^{176}Hf nuclei makes it possible to conclude that $K^\pi = 0^-$ two-particle states exist at an excitation energy of about 2 MeV or higher.

Energy and Mass Dependence of the Parameters of the Semimicroscopic Folding Model for Alpha Particles at Low and Intermediate Energies

K. A. Kuterbekov, I. N. Kukhtina, Yu. E. Penionzhkevich, and T. K. Zholdybaev

The energy and mass dependence of the parameters of the semimicroscopic alpha-particle potential is investigated for the first time in the region of low and intermediate energies. Within the semimicroscopic folding model, both elastic and inelastic differential and total cross sections for reactions on various nuclei are well described in terms of the global parameters obtained in this study.

1063-7788/04/6710-1928$26.00

Effects of the Mixing of the Scalar–Pseudoscalar Higgs Bosons in the Process $e^+e^- \to e^+e^-bb$ at a Future Linear Electron–Positron Collider

A. A. Likhoded and A. E. Chalov

The sensitivity of data on the process $e^+e^- \to e^+e^-bb$ to a deviation of the coupling of the Higgs boson to b quarks from the Standard Model predictions owing to the presence of a pseudoscalar Higgs boson state is analyzed for a future linear electron–positron collider at $\sqrt{s} = 500$ GeV. The admixture of a new hypothetical pseudoscalar Higgs boson state at the Hbb vertex is parameterized in the form $(m_b/\nu)(a + i\gamma_5 b)$. On the basis of an analysis of differential distributions for the processes, it is shown that data from the future linear collider TESLA will make it possible to constrain the parameters $\Delta a = a - 1$ and b as $-0.056 \leq \Delta a \leq 0.055$ and $-0.32 \leq b \leq 0.32$, respectively.

Calculation of the Mass Spectrum within QED-2 in Terms of Light-Front Coordinates

S. A. Paston, E. V. Prokhvatilov, and V. A. Franke

With the aim of a further investigation of the nonperturbative Hamiltonian approach to gauge field theories, the QED-2 mass spectrum is calculated numerically by using the corrected Hamiltonian constructed previously for this theory on the light front. The calculations are performed for a wide range of the ratio of the fermion mass to the charge at all values of the parameter $\hat{\theta}$ associated with the vacuum angle θ. Our results are compared with the results of known numerical calculations on a lattice in Lorentz coordinates. A method is proposed for extrapolating the values obtained within the infrared-regularized theory to the limit where the regularization is removed. The resulting spectrum agrees well with the known results in the case of $\theta = 0$; in the case of $\theta = \pi$, there is agreement at small values of the fermion mass (below the phase-transition point).

Additional Symmetry in the Weinberg–Salam Model

B. L. G. Bakker, A. I. Veselov, and M. A. Zubkov

An additional symmetry hidden in the fermion and Higgs sectors of the Standard Model was found recently. It has a singular nature and is related to the centers of the $SU(3)$ and $SU(2)$ subgroups of the gauge group. A lattice regularization of the Standard Model was constructed that possesses this symmetry. In this paper, we report our results on a numerical simulation of its electroweak sector.

Formation of Antideuterons in Heavy-Ion Collisions

B. L. Ioffe, I. A. Shushpanov, and K. N. Zyablyuk

The antideuteron-production rate in high-energy heavy-ion collisions is calculated on the basis of the concept of $\bar{d}$ formation by antinucleons that move in the mean field of the fireball constituents (mainly pions). An explicit formula is presented for the coalescence parameter B_2 in terms of the deuteron binding energy and the fireball volume.

Physics of Atomic Nuclei, Vol. 67, No. 10, 2004, p. 1930.

ERRATA

Erratum: "Associated $\phi\Lambda^0$ Production in the EXCHARM Experiment"

[*Phys. At. Nucl.* 67, 1513 (2004)]

A. N. Aleev, N. S. Amaglobeli, V. P. Balandin, O. V. Bulekov, I. M. Geshkov, T. S. Grigalashvili, E. A. Goudzovski, D. K. Guriev, D. D. Emelianov, S. V. Eremin, A. I. Zinchenko, Z. M. Ivanchenko, I. M. Ivanchenko, M. N. Kapishin, A. A. Loktionov, V. D. Kekelidze, Z. I. Kozhenkova, V. V. Korenkov, I. G. Kosarev, N. A. Kuzmin, A. L. Ljubimov, D. T. Madigozhin, V. G. Maznyj, A. S. Mestvirishvili, N. A. Molokanova, A. N. Morozov, R. E. Pismenyj, V. D. Pose, I. A. Polenkevich, A. K. Ponosov, T. Ponta, Yu. K. Potrebenikov, F. M. Sergeev, L. A. Slepets, and V. N. Spaskov
The EXCHARM Collaboration

The surname of one of the authors should read V. D. Pose.